

Cavity Quantum Electrodynamics with Site-Controlled Pyramidal Quantum Dots in Photonic Crystal Cavities

THÈSE N° 5957 (2013)

PRÉSENTÉE LE 18 OCTOBRE 2013
À LA FACULTÉ DES SCIENCES DE BASE
LABORATOIRE DE PHYSIQUE DES NANOSTRUCTURES
PROGRAMME DOCTORAL EN PHYSIQUE

ÉCOLE POLYTECHNIQUE FÉDÉRALE DE LAUSANNE

POUR L'OBTENTION DU GRADE DE DOCTEUR ÈS SCIENCES

PAR

Milan ČALIĆ

acceptée sur proposition du jury:

Prof. V. Savona, président du jury
Prof. E. Kapon, directeur de thèse
Prof. J. Finley, rapporteur
Prof. T. Kippenberg, rapporteur
Prof. J. Mørk, rapporteur



ÉCOLE POLYTECHNIQUE
FÉDÉRALE DE LAUSANNE

Suisse
2013



Acknowledgements

Undertaking a PhD is a big challenge that not only requires hard work, determination and perseverance, but also guidance and support from others. I have been very fortunate with my PhD to have worked together with highly competent and passionate researchers, whose invaluable contributions I would like to acknowledge here.

First and foremost, I would like to express my deep gratitude to Prof. Elyahou Kapon. I am very glad to have had him as my thesis supervisor and that he granted me the opportunity to work on a fascinating research topic in his laboratory. Under Eli's guidance, I made great strides in my project and I learnt how to achieve ambitious goals through rigorous work. I am very thankful for all the exceedingly helpful feedback and inputs that he gave me for my conference presentations, for the writing of publications and especially for my dissertation. Also, I feel privileged that he allowed me to present our results at several major conferences.

Without the help from my past and present colleagues, this thesis would surely not exist. I am greatly indebted for the tremendous support and the contributions from Pascal Gallo, Benjamin Dwir, Marco Felici, Clément Jarlov, Lydie Ferrier, Kirill Atlasov and Alok Rudra. It was a very pleasant experience to interact with such motivated and committed people. Thank you for everything! My special thanks go to Pascal for his dedicated assistance and passionate involvement throughout the years, I owe him a great deal. Another extra big "thank you" is dedicated to our technological mastermind Benny, who has always been enormously helpful in the lab and whose efforts were indispensable in the "quantum dots in photonic crystals"-project.

I would also like to thank the other friendly members (past and present) of the Kapon group for enriching my experience at EPFL: Valentina Troncale, Clément Jarlov, Alexey Lyasota, Justyna Szeszko, Nicolas Volet, Alessandro Surrente, Etienne Wodey, Bruno Rigal, Zlatko Mickovic, Dalila Ellafi, Julien Delgado, Nicolas Moret, Elodie Lamothe, Romain Carron, Sanna Palmgren, Arun Mohan, Lukas Mutter, Fredrik Karlsson, Nicolas Moret, Qing Zhu, Marcin Byszewski, Christopher Long, Daniel Oberli, Marc-André Dupertuis and Vladimir Iakovlev. Last but not least, a big "merci beaucoup" to the secretaries of our group Gabriella Fuchs, Nadia Gauljaux and Céline Liniger for their kindness and their cordial services.

Merci beaucoup, grazie mille, spasiba, toda, tack så mycket to my office mates

Acknowledgements

Kirill, Valentina, Nicolas, Alexey, Sanna and Moshe Judelewicz; our office environment was enjoyable every day with such open-minded and cheerful people!

It should not be left unmentioned that our institute has the most efficient, capable and well organized technical staff that one could wish for, and they deserve all the praise for their support. Nicolas Leiser, Damien Trolliet, Yoan Trolliet et Roger Rochat, merci infiniment pour votre aide!

I feel lucky to have collaborated with Prof. Vincenzo Savona and Guillaume Tarel from the Institute of Theoretical Physics, who provided substantial theoretical backing to our experimental results. I was very happy that Vincenzo accepted to be the president of the jury at my thesis defense.

Speaking about the defense, I am honored and thankful that Prof. Tobias Kippenberg, Prof. Jonathan Finley and Prof. Jesper Mørk evaluated my work and were part of my thesis jury.

Finally, I profoundly thank my family and my friends for accompanying and encouraging me in this journey, I would not be where I am now without them.

Abstract

Cavity quantum electrodynamics encompasses the study and control of the interactions between quantum light sources and resonant modes of optical cavities. The subject of this thesis is cavity quantum electrodynamics with semiconductor quantum dots (QDs), which are light-emitting nanostructures with atom-like optical and electronic properties. Recently it has become possible to combine QDs with methods of producing cavities that have microscopically small volumes, which led to the observations of spontaneous emission enhancement, lasing, single-photon nonlinearities and vacuum Rabi splitting. These effects can potentially be exploited for applications in quantum communication, computing and metrology.

A challenging obstacle faced in current research is the lack of control over the positions of the QDs within the cavity structures, because the majority of experiments employ self-assembled QDs that nucleate randomly at unpredictable locations during the crystal growth process. The technical objective of the present thesis was to address this problem by means of an alternative approach for QD growth that utilizes metal-organic chemical vapor deposition on GaAs substrates patterned with inverted pyramidal recesses. The QDs obtained by this approach are referred to as *site-controlled pyramidal QDs*, and the technique for their growth has been refined in our research group since more than a decade.

One of the principal achievements of this thesis was to develop a deterministic and scalable fabrication procedure for integrating InGaAs/GaAs pyramidal QDs into planar photonic crystal (PhC) cavities. In particular, we succeeded in coupling single QDs and pairs of spatially separated QDs with a three-hole defect (*L3*-type) PhC cavities. Owing to the excellent site control and the few-meV inhomogeneous broadening of pyramidal QDs, we could routinely obtain a spatial alignment precision of better than 50 nm and thereby yield many effectively coupled QD-cavity devices on the same substrate. This facilitated systematic examinations of the coupling characteristics of single and pairs of QDs in cavities, without ambiguities related to the QD positions and the possible presence of spectator QDs in the cavity region.

First, we investigated the *L3* cavities containing a single QD at their centers in micro-photoluminescence and photon correlation measurements. We observed that the QD exciton line closest to the cavity mode becomes markedly enhanced

Acknowledgements

in intensity upon crossing the resonance through temperature tuning, which is a characteristic signature of the Purcell effect in the weak coupling regime. Furthermore, we performed detailed polarization-resolved studies and found that the QD exciton becomes co-polarized to the cavity only within a narrow detuning range.

Most notably, we also discovered that pyramidal QDs detuned by more than 5 meV could not couple their emission to the cavity, such that the cavity resonance was spectrally absent or negligibly small even at high pumping power. This is in striking contrast with the typical behavior of self-assembled QDs, where a spurious "cavity feeding" mechanism contaminates the emission from the cavity with uncorrelated photons and leads to far-off resonance coupling. Using theoretical modeling of the optical spectra, we were able to understand the coupling characteristics of pyramidal QDs by taking into account that longitudinal-acoustic phonons can assist the excitation transfer from the QD to the cavity. A possible explanation for the absence of cavity feeding in pyramidal QDs is that the confined excitons do not interact efficiently with charges in the barrier material, unlike the situation in self-assembled QDs.

Building on the knowledge acquired from our experiments with single QDs, we proceeded to systematically study *L3* cavities in which 2 QDs were embedded with an interdot separation of 350 nm. Here the outstanding reproducibility of the excitonic states previously evidenced in the spectra from single pyramidal QDs turned out to be a crucial advantage, permitting the spectral identification of the individual QDs from the QD pairs. The most significant finding that emerged from our measurements was the observation of mutual Purcell enhancement from a QD pair, which constitutes the first demonstration of that kind.

The results of this thesis demonstrate the benefits of site-controlled QD technology for cavity quantum electrodynamics and validate the potential of pyramidal QDs for implementing more complex architectures, such as multiple QDs in a cavity and nanophotonic integrated circuits consisting of waveguide-coupled cavities. A very interesting outlook regarding multiple QDs in a cavity is the exploration of collective effects like superradiance and multipartite entanglement. Further efforts in improving the quality factors of the cavities and reducing the linewidths of the pyramidal QDs may eventually culminate in reaching the coherent regime of strong coupling and achieving lasing.

Keywords: quantum dots, cavity quantum electrodynamics, microcavities, photonic crystals, quantum optics, photoluminescence, III-V semiconductors, nanotechnology, nanophotonics, nanostructures, quantum information science, MOCVD, Jaynes-Cummings model, Dicke model, Tavis-Cummings model, Purcell effect

Résumé

L'électrodynamique quantique en cavité englobe l'étude et le contrôle des interactions entre les sources de lumière quantique et les modes de résonance des cavités optiques. Le sujet de cette thèse est l'électrodynamique quantique en cavité avec des boîtes quantiques (BQs) semiconductrices, qui sont des nanostructures avec des propriétés optiques et électroniques similaires aux atomes et qui émettent des photons uniques. Récemment, il est devenu possible d'intégrer ces BQs à des cavités photoniques, ce qui a conduit aux observations de modification de l'émission spontanée, l'effet laser, des non-linéarités au niveau des photons uniques et des oscillations de Rabi quantiques. Ces effets peuvent potentiellement être exploités pour des applications dans la communication quantique, l'informatique quantique et la métrologie quantique.

Un obstacle difficile à surmonter dans ce domaine de recherche est le manque de contrôle sur les positions des BQs au sein des microcavités, car la majorité des expériences emploient des BQs auto-assemblées qui se forment à des endroits aléatoires pendant la croissance cristalline. L'objectif technique de la présente thèse a été d'aborder ce problème au moyen d'une approche alternative pour la croissance des BQs, en utilisant l'épitaxie en phase vapeur aux organométalliques sur un substrat de GaAs dans lequel ont été attaqués des creux pyramidaux. Les BQs obtenues par cette approche sont précisément contrôlées en position et ils sont appelés *BQs pyramidales*. La technique pour leur croissance a été améliorée dans notre groupe de recherche depuis plus d'une décennie.

L'une des principales réalisations de cette thèse est de développer un procédé de fabrication déterministe et évolutif pour l'intégration des BQs pyramidales InGaAs/GaAs dans des cavités à cristaux photoniques (ChPs) planaires. En particulier, nous avons réussi à coupler des BQs uniques et des paires de BQs séparées avec des cavités $L3$ (défaut à trois trous dans le ChP). Grâce à l'excellent contrôle du site de formation et la haute uniformité spectrale des BQs pyramidales, nous avons pu systématiquement obtenir une précision d'alignement spatial meilleure que 50 nm et ainsi produire de nombreux systèmes BQ-cavité effectivement couplés sur le même substrat. Cela a facilité l'examen des mécanismes de couplage des BQs uniques et des paires de BQs dans des cavités de manière systématique, sans ambiguïtés liées aux positions des BQs et la présence éventuelle des BQs "spectatrices" dans la région de la

Acknowledgements

cavité.

Tout d'abord, nous avons étudié des cavités $L3$ contenant une seule BQ en leur centre avec des dispositifs de micro-photoluminescence et des mesures de corrélation des photons. Nous avons observé que la transition de la BQ la plus proche du mode de la cavité est nettement améliorée en intensité en croisant la résonance, ce qui est une signature caractéristique de l'effet Purcell en régime de couplage faible. En outre, nous avons effectué des études résolues en polarisation détaillées et constaté que la BQ devient co-polarisée avec la cavité seulement dans un intervalle de désaccord énergétique très petit.

Plus particulièrement, nous avons également découvert que les BQs pyramidales désaccordées de plus de 5 meV ne pouvait pas coupler leur émission à la cavité, de telle sorte que la résonance de la cavité était absente ou négligeable, même à haute puissance de pompage. Ceci est en contraste frappant avec le comportement typique des boîtes quantiques auto-assemblées, où un mécanisme perturbant d'alimentation de la cavité contamine l'émission de la cavité avec des photons non corrélés et provoque un couplage hors résonance. Grâce à la modélisation théorique des spectres optiques, nous avons pu comprendre les caractéristiques de couplage des BQs pyramidales en tenant compte du fait que les phonons acoustiques longitudinaux peuvent contribuer au transfert d'excitation de la BQ à la cavité. Une explication possible pour l'absence d'alimentation de la cavité avec les BQ pyramidales serait que les excitons confinés n'interagissent pas efficacement avec les charges dans les barrières, contrairement à la situation dans les BQs auto-assemblées.

En s'appuyant sur les connaissances acquises de nos expériences avec les BQs uniques, nous avons procédé à l'étude systématique des cavités $L3$ dans lesquelles 2 BQs ont été intégrées avec une séparation de 350 nm. Ici, la reproductibilité remarquable des états excitoniques déjà constatée dans les spectres de BQ pyramidales uniques s'est avérée être un avantage décisif, permettant l'identification spectrale des BQs individuelles des paires de BQs. La conclusion la plus importante qui ressort de nos mesures a été l'observation de l'effet Purcell mutuel d'une paire BQs, qui constitue la première démonstration de ce genre.

Les résultats de cette thèse mettent en évidence les avantages des BQ contrôlées en position pour électrodynamique quantique en cavité et valident le potentiel des BQs pyramidales pour la mise en œuvre de systèmes plus complexes, comme des multiples BQs dans une cavité et circuits nanophotoniques intégrés constitués de cavités couplées par des guides d'onde. Une perspective très intéressante en ce qui concerne plusieurs BQs dans une cavité est l'exploration des effets collectifs comme la superradiance et l'intrication multi-particules. Des efforts supplémentaires pour améliorer les facteurs de qualité des cavités et pour réduire les largeurs de ligne des BQs pyramidales peuvent éventuellement aboutir à atteindre le régime cohérent de

couplage fort et la réalisation d'un laser.

Mots-clés : boîtes quantiques, électrodynamique quantique en cavité, microcavités, cristaux photoniques, optique quantique, photoluminescence, semi-conducteurs III-V, nanotechnologie, nanophotonique, nanostructures, informatique quantique, MOCVD, EPVOM, model de Jaynes-Cummings, model de Dicke, model de Tavis-Cummings, effet Purcell

Contents

Acknowledgements	i
Abstract (English/Français/Deutsch)	iii
1 Cavity quantum electrodynamics with quantum dots	1
1.1 Introduction to nanophotonics	1
1.2 Quantum-confined heterostructures	4
1.2.1 Semiconductors in photonics	4
1.2.2 Quantum wells, wires and dots	5
1.2.3 Fabrication of quantum dots	8
1.2.4 Excitons in quantum dots	12
1.2.5 Linewidth broadening in quantum dots	13
1.3 Photonic crystals	15
1.3.1 Photonic bandgap materials	15
1.3.2 Numerical modeling	18
1.4 Cavity quantum electrodynamics	21
1.4.1 The Jaynes-Cummings model	22
1.4.2 Strong versus weak coupling	26
1.4.3 Experimental investigations with single quantum dots	27
1.5 Thesis goal and outline	29
2 Experimental techniques	31
2.1 Fabrication of pyramidal quantum dots	31
2.1.1 Summary of the fabrication procedure	31
2.1.2 Growth mechanisms	34
2.2 Fabrication tools	36
2.2.1 Metal-organic chemical vapor deposition	36
2.2.2 Scanning electron microscopy	37
2.2.3 Atomic force microscopy	39
2.2.4 Electron beam lithography	40
2.2.5 Reactive ion etching	41
2.2.6 Inductively coupled plasma etching	42

Contents

2.3	Optical characterization techniques	43
2.3.1	Micro-Photoluminescence spectroscopy	43
2.3.2	Photon correlation measurements	45
2.4	Chapter summary	48
3	Integration of site-controlled quantum dots into photonic crystal cavities	49
3.1	State of the art	49
3.2	Combining site-controlled pyramidal quantum dots with photonic crystals	52
3.2.1	Design of our experiments	52
3.2.2	Meeting the spatial and spectral matching requirements	54
3.2.3	Growth optimization	58
3.2.4	Description of the fabrication procedure	59
3.2.5	Control over the cavity resonance position	66
3.2.6	Optical properties of non-resonant single and pairs of quantum dots	68
3.2.7	Comparison with other fabrication approaches	69
3.3	Chapter summary	71
4	Coupling characteristics of single pyramidal quantum dots	73
4.1	Review of the coupling phenomena observed with single quantum dots	75
4.1.1	Introduction	75
4.1.2	Cavity-enhanced continuum transitions associated with the quantum dot barriers	75
4.1.3	Influence of pure dephasing	77
4.1.4	Modification of spontaneous emission in a 2D photonic crystal	80
4.2	Investigation of the Purcell effect with a single quantum dot	85
4.2.1	Polarization-resolved photoluminescence	85
4.2.2	Temperature-tuning the quantum dot through resonance	90
4.2.3	Detuning-dependent polarization features	93
4.2.4	Linewidth narrowing at resonance	95
4.2.5	Photon statistics of the quantum-dot-cavity system	99
4.2.6	Excitation power dependence	101
4.3	Theoretical analysis	103
4.3.1	Mode structure of an $L3$ cavity	103
4.3.2	Modeling of phonon-assisted Purcell enhancement	105
4.3.3	Effect of pure dephasing at resonance	107
4.4	Chapter summary	112

5	Two spatially separated quantum dots in a photonic crystal cavity	113
5.1	Two quantum emitters in a cavity: An Introduction	115
5.1.1	Theory	115
5.1.2	Physical realizations	118
5.2	Two pyramidal quantum dots in a photonic crystal cavity: General ob- servations	120
5.2.1	r/a -tuning of the cavity resonances	120
5.2.2	Cavity mode intensity and Q factor	127
5.2.3	Polarization features	128
5.2.4	Power dependence of the emission spectra	130
5.3	A mutually coupled quantum dot pair	136
5.3.1	Purcell-enhancement of the intensities	136
5.3.2	Detuning dependence of the polarization features	140
5.3.3	Power dependent spectra of a resonant quantum dot pair	143
5.4	Chapter summary	149
6	Conclusions and outlook	151
A	List of publications and conferences	155
	Bibliography	177
	Curriculum Vitae	179

1 Cavity quantum electrodynamics with quantum dots

1.1 Introduction to nanophotonics

Photonics includes all technologies that enable the generation and the handling of photons, which are the fundamental particles of light. The field of photonics is very broad and cross-disciplinary, as it involves physics, optics, electronics, material science, chemistry, and other fields. There is a vast number of technical applications of photonics, which include [1, 2]:

- Lasers, light-emitting diodes (LEDs), and other light sources.
- Optical fibers, amplifiers and modulators for telecommunications.
- Photodetectors such as charge-coupled devices (CCDs), photodiodes and photomultipliers.
- High-precision metrology for the measurement of distances and frequencies based on, e.g., interferometers and frequency combs.
- Photovoltaic solar cells for the generation of electrical power from solar energy.

This non-exhaustive list gives an impression of the great influence that photonics already has in our modern day life, revolutionizing many different industries such as telecommunications (internet), health care, consumer electronics and computers [3]. The great success of photonics has been fostered by the use of semiconductor materials in many photonics components, which can be combined with electronics to serve as optoelectronic devices. The compatibility between electronics and photonics is a major advantage, since it provides a means to simultaneously control the flow of photons as well as of electrons on the same solid state platform. In fact, our society is at the verge of a new era where the information technology industry is

increasingly merging electronic circuits with photonic components. Companies like IBM or Intel are currently in the process of developing integrated photonic devices that contain modulators, detectors, waveguides and electronic circuitry on a single chip [4, 5]. These are intended to be used in computer networks and are expected to drastically improve their data transfer performance in terms of speed, volume and power consumption.

The subject of the present dissertation is situated within *nanophotonics*, a sub-field of photonics which deals with the behavior of photons in nanostructured materials and that is currently receiving a lot of attention in the research community. Broadly speaking, the technical goals of nanophotonics are to make compact light sources with engineered properties, to control the direction and the speed of propagating light signals on a microscopic scale, to trap photons within optical microresonators, and to enhance light-matter coupling through confinement of both electrons and photons. Some examples of nanophotonic materials and structures are:

- **Photonic metamaterials:** Consist of densely packed micro- and nanostructures made of metallodielectric materials with new and unusual optical properties, such as negative refractive index and invisibility within a band of frequencies [6, 7].
- **Nanoplasmonic materials:** Metallic nanostructures that strongly localize and enhance electromagnetic fields near metal/dielectric interfaces. Their nonlinear properties can be used for sensing and waveguiding [8, 9].
- **Photonic crystals:** A new class of optical materials that exhibit photonic bandgaps, i.e. energy gaps where the propagation of photons is inhibited [10, 11]. Photonic crystals are made of periodically patterned dielectric structures that can be designed to confine, guide and slow down light. The periodicity is of the order of the optical wavelength.
- **Quantum wells, quantum wires and quantum dots:** Light-emitting semiconductor structures that confine electrons and holes in one, two or all three dimensions, such that quantum confinement effects alter the electronic states and the optical properties with respect to bulk media [1, 12]. Applications include lasers, optoelectronic switches and photodetectors.
- **Optical microcavities:** These are micro- and nanostructures (typically made of semiconductors) that confine light to microscopically small volumes [13]. Examples are micropillar (or micropost) cavities [14], microtoroids [15], microdisks [16] and photonic crystal defect cavities [17].

The aim of this thesis was to fabricate and experimentally investigate site-controlled semiconductor quantum dots that were integrated into photonic crystal cavities. In such nanophotonic devices, light-matter interaction is particularly strong because both electrons and photons are confined to an ultra-small space. This leads to intriguing quantum optical phenomena, such as the enhancement of the spontaneous emission rate (referred to as the Purcell effect [18]), single-photon nonlinearities [19] and the creation of half-matter/half-light quasiparticles (so-called *exciton polaritons* [20]). These effects fall under the category of *cavity quantum electrodynamics* (cavity QED), which is the study of the interactions between single two-level systems and single photons in an optical cavity. In the following few sections of this chapter, we will briefly review the basics of quantum dots, photonic crystals and cavity QED.

1.2 Quantum-confined heterostructures

1.2.1 Semiconductors in photonics

Semiconductors are solid crystals in which atoms are periodically arranged in a lattice structure. The interatomic separation corresponds approximately to the size of the atoms, such that the atoms become covalently bound together through sharing valence electrons. The overlapping orbitals interact strongly with each other and form bands of electronic states. What distinguishes ideal semiconductors from metallic solids is that at low temperatures, electrons cannot move freely in the semiconductor crystal because they are held in place in their bonds in between atoms. Therefore, pure semiconductors are poor electrical conductors. However, with rising temperatures, electrons can gain sufficient energy to escape the covalent bonds and become mobile. When a mobile electron moves away from its bond, it leaves behind an "empty space" which is called a *hole*. After a while, a moving electron can recombine with a hole and become immobile again. This relaxation is sometimes accompanied by the emission of a photon.

In solid state physics, the electronic and optical properties of semiconductors are interpreted by means of the concepts of band theory. Electrons that are immobile occupy states in the valence band, while freely moving (unbound) electrons are in the conduction band. An energy gap separates the two bands; this is the so-called *band gap*, where no allowed electronic states exist. The size of the band gap determines the energy of the photons that are emitted upon electron-hole recombination. A more detailed description of semiconductor physics is beyond the scope of this thesis; readers unfamiliar with these concepts should refer to introductory textbooks of solid state physics, e.g. Ref. [21].

Semiconducting materials are made of elements from the groups II, III, IV, V and VI of the periodic table [1]. Elemental semiconductors such as silicon (Si) and germanium (Ge) have indirect bandgaps and are therefore not practical for light emitting purposes. However, Si is the basis of virtually all integrated circuits and computing devices. Both Si and Ge are widely used in photonics for making photodetectors, microphotonic components and photovoltaic cells. Light-emitting devices such as LEDs and lasers employ compound semiconductors that have direct bandgaps and therefore high internal quantum efficiencies [1]. Compound materials are obtained by combining elements from group III with group V, or alternatively by mixing group II with group VI. The most widely used compounds are gallium arsenide (GaAs), gallium nitride (GaN) and indium phosphide (InP), which are very efficient in generating light by virtue of their direct bandgaps. The crystal structure and the band structure of

GaAs are illustrated in Fig. 1.1. GaAs has a bandgap of 1.42 eV at room temperature, which means that its emission wavelength is centered around 873 nm in the infrared regime. The refractive index of GaAs is ~ 3.5 at a wavelength of $1\ \mu\text{m}$.

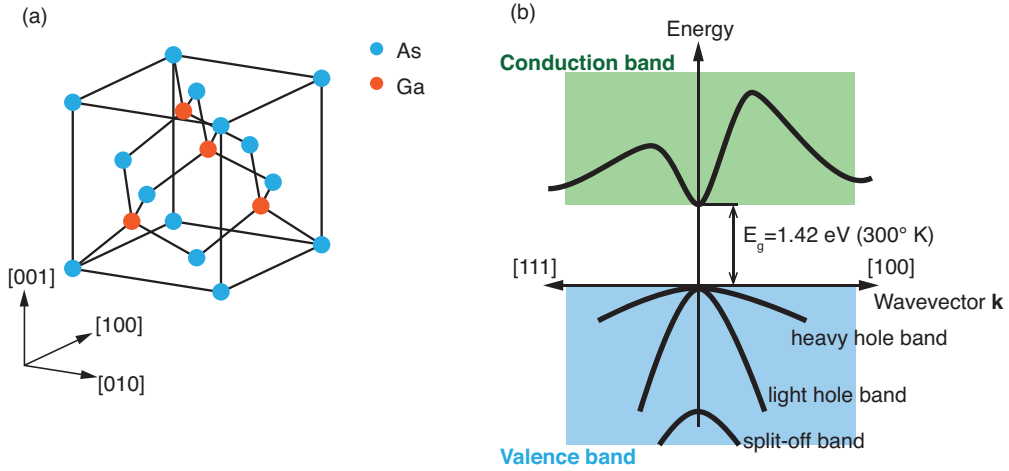


Figure 1.1: (a) Crystal structure of GaAs, which corresponds to the zinc blende lattice. The geometry is the same as for diamond, but with alternating types of atoms at the lattice sites. (b) Illustration of the band structure of GaAs near the conduction band minimum where the wavevector \mathbf{k} is equal to zero.

To fabricate compound semiconductor crystals, typically epitaxial growth methods are used. The most widely used ones are molecular beam epitaxy (MBE) and metal-organic vapor phase epitaxy (MOVPE). In MBE, beams of free atoms are directed towards a substrate that is being held under ultra-high vacuum. Under the right conditions, the free atoms attach to the substrate surface and arrange themselves in a self-organized fashion to form perfect crystal layers. In contrast to MBE, the crystal growth in MOVPE does not take place in vacuum. Instead, the crystal growth occurs in a closed chamber that is maintained under a constant flux of a hot gas mixture. The gas consists of an inert carrier gas (typically hydrogen or nitrogen) and organometallic molecules (so-called precursors), which chemically decompose and release the growth atoms on the substrate. This procedure allows growing atomically thin layers on a planar substrate. The application of MOVPE for the purpose of the present thesis work is elaborated in more detail in Chapter 2 of this thesis.

1.2.2 Quantum wells, wires and dots

Owing to the high-precision growth capabilities of MOVPE and MBE, it is possible to grow alternating layers of different semiconductor compounds on top of each other with atomically sharp interfaces between them. Such heterostructures are the

basis for fabricating *quantum-confined* structures, namely quantum wells (QWs), quantum wires (QWRs) and quantum dots (QDs) [12]. To understand the concept of quantum confinement, it is instructive to regard the example of a QW. A QW is a double heterostructure consisting of a smaller-bandgap material sandwiched in between a larger-bandgap material, for example GaAs/InGaAs/GaAs (Fig. 1.2(a)). Due to the distinct modulation of the bandgap accross the QW structure, a finite potential well is created where both electrons and holes are kept within the two-dimensional region of InGaAs layer. The thickness d of the InGaAs layer is typically 5-50 nm, which is of the same order as the de Broglie wavelength of the conduction band electrons ($\lambda \approx 20$ nm). Therefore the motion of the charge carriers within the QW is severely restricted along the x direction (see Fig. 1.2(a)), which leads to a "squeezing" of their wavefunctions. This squeezing is generally known as *quantum confinement*. In the case of QWs, quantum confinement is responsible for the formation of 2D subbands that are energetically separated from each other (Fig. 1.2(b)).

In essence, quantum confinement leads to a rearrangement of the allowed energies and reduces the number of possible states with decreasing dimensionality. This becomes evident by examining the electronic density of states (DOS) ρ , which gives the number of possible states per energy and per volume. A comparison of the DOS for the different quantum heterostructures is shown in Fig. 1.3, together with the bulk DOS. Going from the 3D bulk to the 2D QW, the DOS becomes staircase-like (Fig. 1.3(a),(b)). In the 1D QWR, a series of spikes emerge in the DOS (Fig. 1.3(c)). Finally, when the charge carriers are confined in all three directions in the QD (Fig. 1.3(d)), the DOS becomes a ladder consisting of a sequence of Dirac delta functions. This visualizes why QDs are often compared to atoms: both are characterized by a quantized energy level spectrum. However, there is a fundamental difference between an atom and a QD regarding how their peculiar energy level structure is created. In the case of an atom, it is the attractive force from the nucleus that gives rise to bound states and therefore to energy quantization, while in a QD it is (primarily) the 3D quantum confinement that leads to the equivalent result. In other words, energy quantization is intrinsic to isolated atoms, but it is extrinsic to QDs in the sense that quantum confinement is caused by the collective behavior of a large assembly of interacting atoms that make up the QD itself and its environment [22].

1.2. Quantum-confined heterostructures

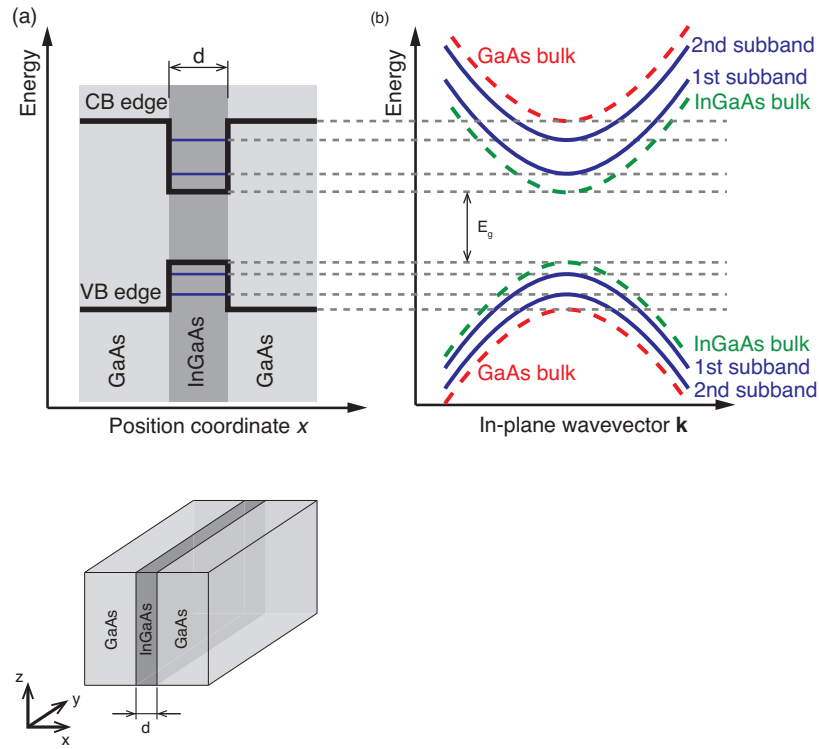


Figure 1.2: (a) Schematic band diagram of a GaAs/InGaAs/GaAs QW structure as a function of position across the QW. CB=conduction band, VB=valence band. The three-dimensional geometry of a QW is shown below. (b) Illustration of the dispersion diagram for the QW. Electrons and holes are only allowed to occupy states from the 2D subbands.

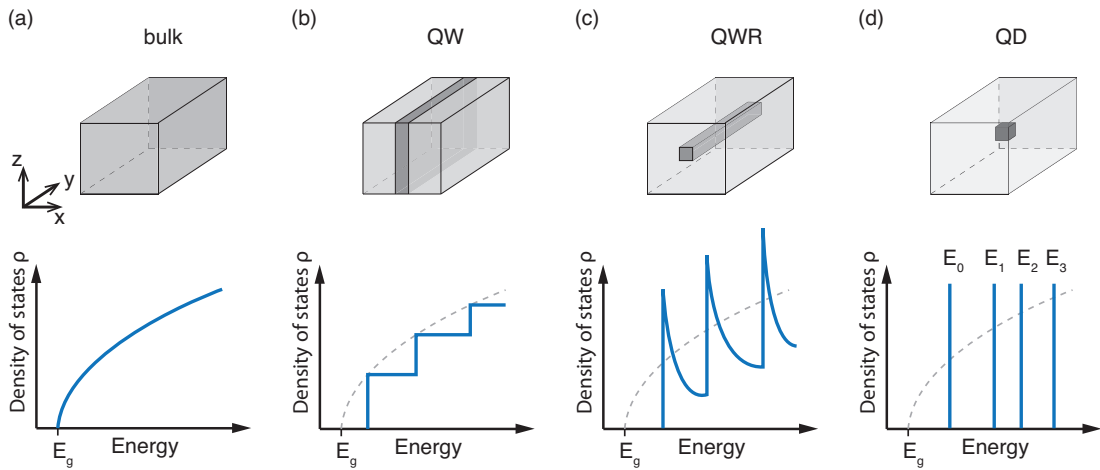


Figure 1.3: Electronic density of states ρ of (a) a bulk semiconductor, (b), a QW, (c) a QWR and (d) a QD.

1.2.3 Fabrication of quantum dots

Among the variety of methods that exists for fabricating QDs, the most common ones are chemical synthesis in colloidal solutions [23] and the Stranski-Krastanov growth mode in MBE and in MOVPE [24]. Colloidal QDs are usually not used in cavity QED experiments (although there are exceptions [25]), because of the difficulty of integrating them into cavity structures. Stranski-Krastanov QDs (SKQDs) are island-shaped structures that naturally form due to strain relaxation when a very thin layer of a semiconductor material is grown on a different, lattice-mismatched substrate material [22, 24].

For example, SK growth of QDs can be achieved by depositing few monolayers of In(Ga)As on top of a GaAs (001) substrate [22, 24], since the lattice constant of In(Ga)As is by a few percent larger than that of GaAs. As one can see in Fig. 1.4(a), the SKQDs are randomly distributed over the substrate surface. The growth of SKQDs occurs in two steps. First, single monolayers of In(Ga)As are formed on top of the flat GaAs surface during growth. After a certain critical thickness (between one and several monolayers), the built-up strain in the grown 2D In(Ga)As film becomes so large that island formation occurs at random locations to relieve strain (Fig. 1.4(b)). The 2D film on top of which the islands nucleate is called *wetting layer* (WL) [22, 24].

Typically, In(Ga)As/GaAs SKQDs are about 5 nm high and ~ 20 nm wide (Fig. 1.4 (c),(d),(e)). They are elliptically shaped in the growth plane due to the orientation-dependent strain on the substrate, with an elongation along the [110] crystal direction (visible in Fig. 1.4(d),(e)). Because of their small size, SKQDs exhibit quantum confinement effects. In(Ga)As/GaAs SKQDs grown by MBE are the most popular QD systems in the field of solid-state cavity QED, because they can easily be fabricated and incorporated into cavities. Another advantage of SKQDs is that their emission lines are very sharp, such that their linewidths can be close to the lifetime limit of few μeV . This is important, since a narrower QD linewidth ensures a more coherent coupling in cavity QED experiments [20].

A major drawback of SKQDs is the lack of position control, which makes it considerably more difficult to implement particular configurations of QDs in a cavity, e.g. a single QD in a micropillar cavity. The workaround that many research groups have adopted for this problem is to fabricate large arrays of cavity structures on the same substrate that contains randomly distributed SKQDs. Then, the sample is systematically scanned in photoluminescence (PL) measurements in order to find a cavity structure that shows signatures of QD-cavity coupling. However, there also exist more advanced approaches for integrating SKQDs into cavities, which will be discussed more explicitly in Chapter 3. Another disadvantage of SKQDs is the large spectral

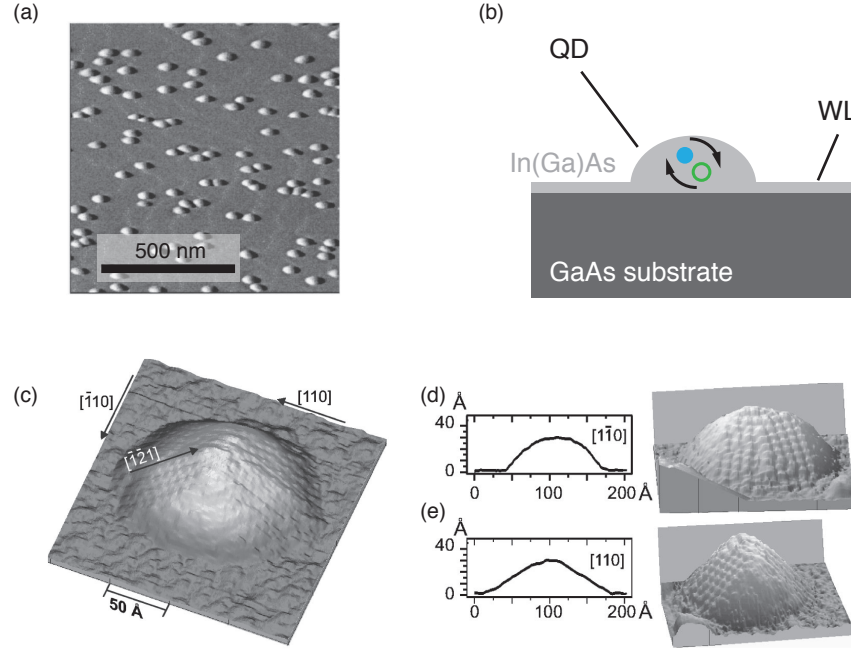


Figure 1.4: AFM image of self-assembled InGaAs/GaAs SKQDs (density $\sim 100 \mu\text{m}^{-2}$). (b) Schematic illustration of an individual SKQD with an exciton confined inside. (c) Scanning tunneling microscope image of an individual InAs/GaAs SKQD, showing the 3D profile. Height profiles along the $[1\bar{1}1]$ and $[110]$ directions are shown in (d) and (e), together with side-view images of the QD.

(a): Reprinted with permission from [26]. Copyright 2000, AIP Publishing LLC. (c),(d),(e): Reprinted with permission from [27]. Copyright 2001, AIP Publishing LLC.

non-uniformity of their emission lines, which is evidenced by typical inhomogeneous broadenings of 30-50 meV in QD ensemble spectra [28,29]. Such large spectral variations in the QD exciton wavelengths further add to the difficulty in achieving coupling of an individual QD with a cavity mode.

Last but not least, the asymmetric shape of In(Ga)As/GaAs SKQDs splits the exciton energy level into a doublet and causes the photon emission to be strongly linearly polarized along $[1\ 1\ 0]$ and $[1\ \bar{1}\ 0]$ [30]. On the one hand, the polarization anisotropy implies that the exciton dipole is preferentially oriented along the two latter crystal directions, which has to be carefully taken into account in designing cavity QED experiments [31]. On the other hand, the fine-structure splitting of the exciton level is detrimental in view of using QDs as sources of entangled photons, because it introduces a "which-path" information to the radiative decay of the excitonic

states [32].

Motivated by these issues, there have been several attempts to control the positions of the SKQDs with considerable success. One of the developed methods employs SK growth on lithographically patterned substrates [33,34] (Fig. 1.5). The substrates are first prepared by etching square mesas and cross-shaped alignment marks. Then, electron-beam lithography (EBL) is used to define a square array of circles on the mesa that are separated from each other by $1\text{ }\mu\text{m}$. The circles are subsequently transferred to the mesa through etching, which creates nanoholes. These nanoholes serve as nucleation spots for the SKQDs during MBE growth. About 90 % of the nanoholes become occupied with a single QD upon growth, and the statistical alignment accuracy of individual QDs with respect to their target positions is $\sim 50\text{ nm}$. Despite these promising advancements, the average linewidths of these site-controlled SKQDs is still too large (in the range of $\sim 1\text{ meV}$ [34]) for applications in cavity QED, and the problem of the large inhomogeneous broadening remains unresolved. Nevertheless, the successful integration of such lithographically-defined SKQDs into micropillars and PhC cavities were recently reported, together with the observation of weak coupling effects [35,36].

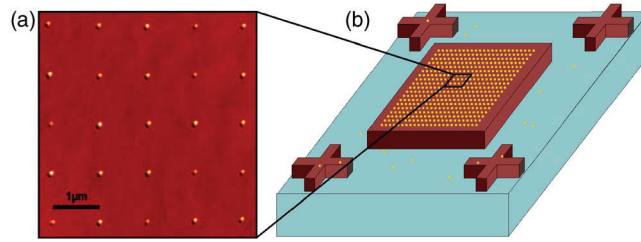


Figure 1.5: (a) Atomic force microscope (AFM) image of site-controlled InAs/GaAs QDs. (b) Schematic illustration of the mesa structure on top of which a square array of nanoholes were lithographically defined, which later served as nucleation spots for the SKQDs. The crosses depict alignment marks.

Reprinted with permission from [27]. Copyright 2008, AIP Publishing LLC.

To date, the most successful method for fabricating site-controlled QDs is based on MOVPE growth on (1 1 1)B-oriented GaAs substrates patterned with inverted pyramids Fig. 1.6) [37]. The QDs obtained by this method are referred to as *pyramidal QDs*. The regular array patterns of tetrahedral pyramids are created using electron beam lithography (EBL) and wet chemical etching. These patterned substrates are then introduced into a metal-organic vapor phase epitaxy (MOVPE) reactor for epitaxial layer growth, which results in the nucleation of a single QD in each pyramid (Fig. 1.6(c)). Since the locations of the pyramids are defined by EBL, one can control the positions of the QDs on the substrate with nanometer precision (ideally within $\pm 5\text{ nm}$).

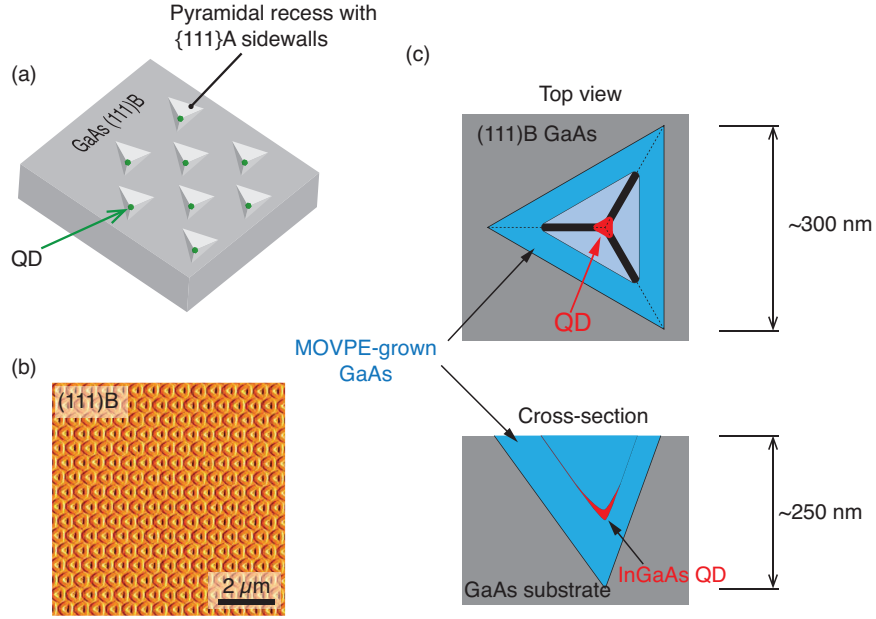


Figure 1.6: (a) Schematic illustration of a triangular array of pyramidal QDs. The pyramidal recesses are etched into the substrate prior to growth and serve as nucleation spots for QDs. (b) AFM image of an array of pyramidal QDs, where the surface was intentionally not fully planarized. (c) Schematic illustration of a pyramidal QD in top view and in cross-section.

In addition to the excellent site control, pyramidal QDs offer outstanding reproducibility. Their inhomogeneous broadening can be as low as 1 meV [38], and different QDs can exhibit almost identical spectra with equivalent excitonic transitions [39, 40]. The spectral linewidths of individual excitonic transitions is typically of the order of $\sim 100 \mu\text{eV}$. Pyramidal QDs can be grown in pyramidal recesses of different sizes, and were demonstrated for pyramid base lengths L_b ranging from $5 \mu\text{m}$ down to $\sim 100 \text{ nm}$ [39, 41, 42]. Furthermore, the material composition of the QDs and their barriers can be modified depending on the application within the InGaAs/GaAs compound system [43–45].

For the purpose of the cavity QED experiments conducted within the scope of this thesis, we utilized InGaAs/GaAs pyramidal QDs grown in pyramids with a base length of $L_b \sim 300 \text{ nm}$ (Fig. 1.6(c)). These QDs can be readily integrated into PhC cavities due to the sufficiently small pyramid size, as it was first demonstrated by Gallo *et al.* [43]. Although it is also possible to integrate even smaller pyramids into PhC cavities [46], we were able to achieve better QD uniformity and spectral quality with these slightly larger pyramids. The substrate patterning and the MOVPE growth for yielding pyramidal QDs will be described in detail in Chapter 2.

1.2.4 Excitons in quantum dots

When a free electron and a free hole come close enough to each other in a bulk semiconductor such that the attractive Coulomb force between them becomes significant, then these two oppositely charged particles can form a bound state. The bound electron-hole pair is called *exciton*, which is an electrically neutral quasi-particle [23]. Excitons also exist in QWs, QWRs and QDs. However, the binding energy of an exciton in such quantum-confined structures differs from the bulk, since the narrow confinement potential squeezes the charges close together.

The discrete energy states that a single exciton can adopt in a QD are determined by an interplay between quantum confinement and Coulomb interactions. The lowest energy state corresponds to the configuration where both the electron and the hole are in the so-called *s-shell* of the QD energy level structure (Fig. 1.7(a)). When either the hole or the electron is excited to a higher energy level, then an excited exciton state is created, e.g. when the hole is in the p-shell (Fig. 1.7(b)). In fact, a QD can accommodate several electrons and holes at the same time in its atom-like shell structure. For example, there can be charged excitons (so-called *trions*) with an excess hole or electron (Fig. 1.7(c),(d)). Furthermore, when the QD is occupied by two excitons, then a *biexciton* $2X$ is created (Fig. 1.7(e)).

Every excitonic species has different substates arising from the different spin configurations of the electrons and holes. The neutral exciton has four substates, but due to optical selection rules only two of the substates are (normally) be optically accessed [47]. The two "bright" states are usually not degenerate, but exhibit a small fine-structure splitting [48].

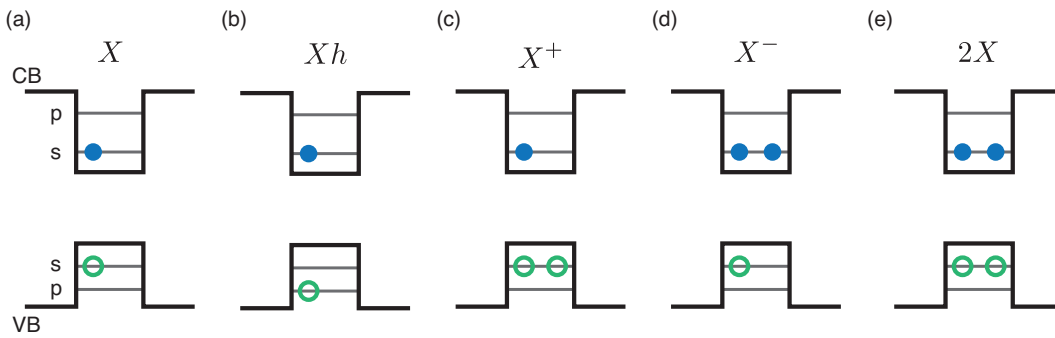


Figure 1.7: Examples of possible excitonic states in a QD: (a) neutral exciton X , (b) excited hole state of the neutral exciton Xh , (c) positive trion X^+ , (d) negative trion X^- , (e) neutral biexciton $2X$.

QDs can be charged with electrons and holes either through optical excitation

(e.g. with a laser beam) or through current injection. The operation temperature of QDs depends on their potential depth and is usually well below 100 K in the case of In(Ga)As/GaAs QDs, because their quantum confinement is lost at higher temperatures. An exciton can stay confined within a QD for about 1 ns, until it radiatively decays through the emission of a single photon. Therefore, a single QD can be used as an on-demand single-photon source [39,49]. If the QD is loaded with a biexciton, then a pair of consecutively emitted photons is generated as a result: the first photon comes from the decay of the biexciton ending at the exciton state, and the second photon is emitted subsequently after the finite lifetime of the exciton. This two-photon cascade is the basis for the generation of entangled photon pairs [32]. Recently, researchers demonstrated the realization of an electrically driven source of entangled photons that consisted of a single QD embedded within an LED structure [50].

The reason why QDs have stimulated so much interest in the quantum information science community is because they can serve as stationary quantum memories, so-called *qubits* [51]. A single electron confined in a QD carries quantum information in the form of distinct spin states. Optical manipulation allows controlling the electron spin state in a QD on a timescale of picoseconds, as it was shown in a recent work [52]. Even more excitingly, quantum information can be transmitted from a QD through the emission of a photon, which can be considered as a *flying qubit* in this case. This is the key for building quantum communication networks, where remote matter qubits are entangled with each other through photonic qubits [53]. In fact, De Greve *et al.* experimentally demonstrated that spin-photon entanglement can be realized using InAs QD [54, 55]. The next big step in this development would be the quantum state transfer between two distant QD qubits via photons.

1.2.5 Linewidth broadening in quantum dots

All real quantum systems are inevitably subject to interactions with their surroundings, which irreversibly lead to the loss of quantum coherence and the disappearance of interference effects observable otherwise. As a consequence of the quantum decoherence processes, the excited state of a quantum emitter is depopulated after a finite lifetime and the phase angle of its wave function is randomized. One generally distinguishes decoherence due to population relaxation and as a consequence of *pure dephasing*, which is the term for population-conserving mechanisms. The effect of pure dephasing is to introduce temporal modulations in the phases of the wave functions, which spectrally broaden emission lines. Recent theoretical and experimental investigations have highlighted that the effect of pure dephasing significantly modifies the coupling characteristics of QDs in cavity-QED experiments [56–71]. Since the

interpretation of the data presented in this thesis is based on the current knowledge of the different contributions to pure dephasing, we will briefly review these effects.

If no dephasing mechanisms were active in the solid state environment, then the spectral lineshape of a QD exciton would be a perfect Lorentzian with a linewidth inversely proportional to the lifetime τ_0 of the state (Fig. 1.8(a)), in accordance with the energy-time uncertainty principle $\Delta E \Delta t \approx \hbar$. In the case of III-V compound SKQDs, the measured τ_0 is about 1 ns, whereby the corresponding lifetime-limited linewidth would be of the order of $\sim 1 \mu\text{eV}$ [72, 73]. However, various PL studies of single QDs have shown that the linewidth of the zero-phonon line (ZPL) at liquid-helium temperatures is normally much larger than the radiative limit, ranging from a few μeV up to 1 meV [34, 74–76]. In addition, the spectral tails of the ZPL are extended by an asymmetric background, which is termed *phonon sidebands* (see illustration in Fig. 1.8(c)) [75–78]. The ZPL linewidth γ was observed to vary as a function of both temperature [74] and excitation power [77]. $\gamma(T)$ increases linearly for T up to 40–60 K, where a transition occurs that induces a much stronger dependence on temperature [74, 77, 79]. Simultaneously with the thermal broadening of the ZPL, the phonon sidebands gain in intensity and become more symmetric as a function of T .

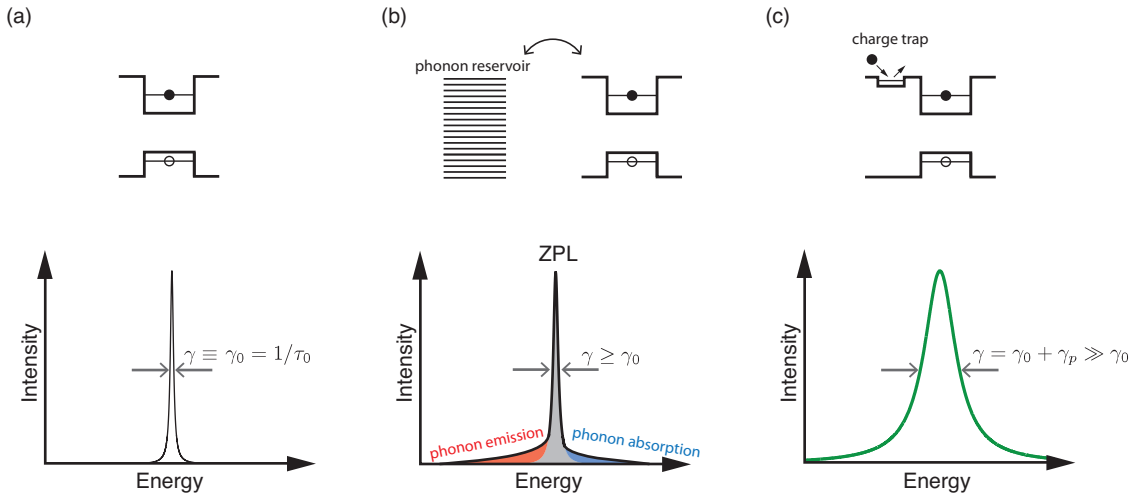


Figure 1.8: Illustration of the pure dephasing mechanisms. (a) Bare QD without any dephasing; the QD linewidth is only limited by the lifetime τ_0 . (c) Effect of carrier-phonon scattering. (b) Broadening through spectral diffusion.

In order to explain these observations, the dephasing interactions between the QD-confined excitons with the environment of the semiconductor host material have to be taken into account. Phonons perturb electrons and holes in QDs in a non-Markovian fashion, whereby the Lorentzian profile of the ZPL becomes asymmetrically (inhomogeneously) broadened (Fig. 1.8(b)) [75, 77, 78]. The non-Markovian

nature of exciton-phonon coupling is also reflected in the temporal decay QD states, which deviates from a simple exponential trend [72]. In order to realistically calculate the optical response of a QD, it is necessary to adopt a microscopic theory of carrier-phonon interactions. By extending the independent boson model with a higher order coupling term for acoustic phonons, Muljarov *et al.* [80] were able to numerically reproduce the phonon sidebands and obtained a ZPL that broadens linearly with temperature, in qualitative agreement with experimental findings. However, the quantitative contribution of exciton-phonon scattering to the ZPL width γ theoretically amounts only $\sim 1 - 10 \mu\text{eV}$ for temperatures up to 50 K [80]. However, this is rather small compared to experimentally determined values of γ , which can be $100 \mu\text{eV}$ or more [79,81].

The additional ZPL broadening is explained by the presence of randomly fluctuating local electric fields at the position of the QD, caused by the charge traps in its vicinity [79,81]. This extrinsic dephasing process is known as *spectral diffusion*. As a result of this mechanism, the ZPL of the excitonic transitions are broadened by a factor γ_p . According to Refs. [79,81], the local field fluctuations occur on a rapid timescale of ~ 10 ps in the case of InAs/GaAs SKQDs at low temperature and low excitation power. In comparison, spectral diffusion in colloidal QDs takes place on a timescale that is by several orders of magnitude slower (1 s in the case of colloidal CdSe/ZnS QDs [82]).

1.3 Photonic crystals

1.3.1 Photonic bandgap materials

Periodic material structures that suppress the propagation of light of certain frequencies are generally referred to as PhCs or photonic bandgap (PBG) structures. They are produced by structuring dielectric materials with regular patterns in one, two or all three spatial dimensions (Fig. 1.9). PBG devices have found numerous applications, such as high-capacity optical fibers [83], nanoscopic lasers [17,84] and photonic integrated circuits [11]. Of particular interest for cavity quantum electrodynamics (QED) with QDs is the ability to make nanocavities in PhCs by introducing defects in their periodic structure [85].

The core concepts behind PhC materials were proposed by Yablonovitch and John in 1987 [89,90], who basically had the idea to design a new class of materials that would allow to control spontaneous emission and to create photon localization. They suggested that this could be achieved with periodic dielectric structures: the periodic variation of the refractive index would give rise to a frequency band of inhibited optical

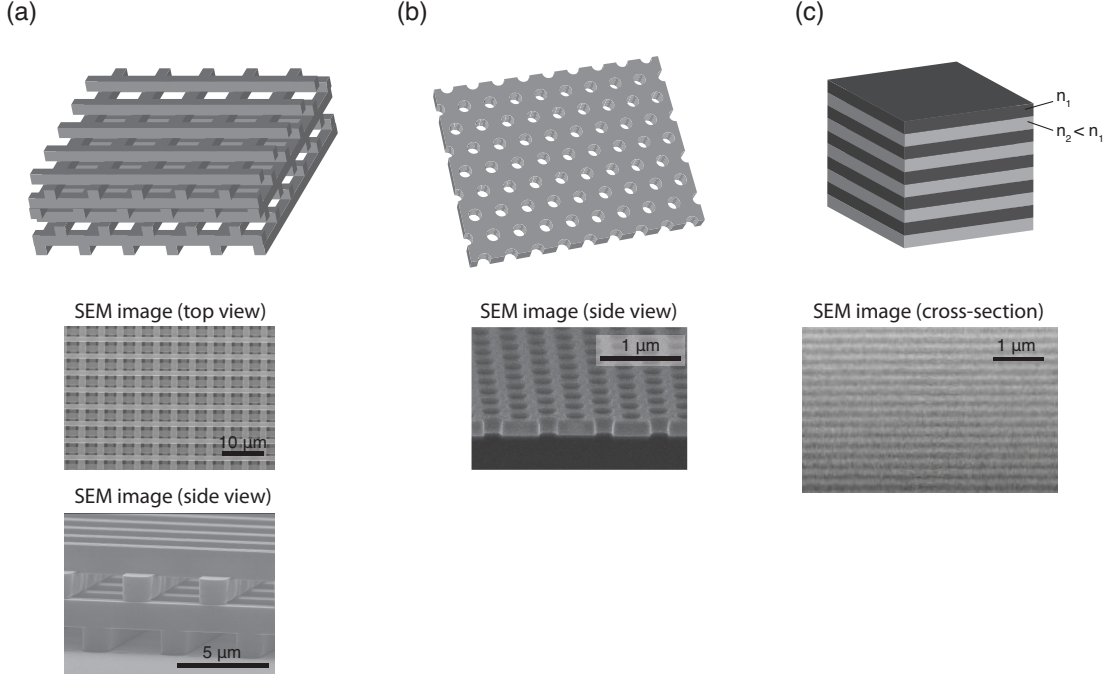


Figure 1.9: Examples of PhC structures. (a) 3D woodpile structure. Below: SEM images of a woodpile PhC made of Si; reprinted by permission from Macmillan Publishers Ltd: [Nature](#) [86]. Copyright 1998. (b) 2D PhC slab. Below: SEM image of a 2D PhC made of GaInAsP; from [87]. Reprinted with permission from AAAS. (c) 1D PhC, most commonly known as distributed Bragg reflector (DBR). Below: SEM image of a GaAs/AlGaAs DBR that was used in a vertical-cavity surface-emitting laser (VCSEL); provided by courtesy of Z. Mickovic and N. Volet [88].

modes, much like the periodic arrangement of atoms in a semiconductor crystal is responsible for the existence of an electronic bandgap. Yablonovitch was also the first to demonstrate a 3D PhC structure that had a complete PBG in the microwave region [91].

Indeed, there are several striking analogies between electron waves in a crystalline solid and light waves in a periodic dielectric structure. Upon examining the steady state equations for the two cases, one can notice similarities. While electrons in semiconductors are governed by the Schrödinger equation

$$\left[-\frac{\hbar^2}{2m^*} \nabla^2 + V(\vec{r}) \right] \psi(\vec{r}) = E\psi(\vec{r}), \quad (1.1)$$

the behavior of light waves in a non-magnetic dielectric medium is determined by

$$\nabla \times \left[\frac{1}{\epsilon(\vec{r})} \nabla \times \vec{H}(\vec{r}) \right] = \left(\frac{\omega}{c} \right)^2 \vec{H}(\vec{r}), \quad (1.2)$$

which is derived from Maxwell's equations [10, 92]. The equations (1.1) and (1.2) have similar forms; both constitute eigenvalue equations describing a wavelike function in space. In eq. (1.1), \hbar is the reduced Planck constant, m^* is the effective mass of an electron, $V(\vec{r})$ is the potential function, E is the total energy and $\psi(\vec{r})$ is the quantum mechanical wave function of an electron. Assuming a perfect crystal lattice, the translational symmetry is expressed by a periodic potential $V(\vec{r}) = V(\vec{r} + \vec{R})$, where \vec{R} can be any point of the Bravais lattice. As a consequence of this periodicity, the solutions of eq. (1.1) can be written as product between a plane wave $e^{i(\vec{k} \cdot \vec{r})}$ and a periodic amplitude function $u_{\vec{k}}(\vec{r}) = u_{\vec{k}}(\vec{r} + \vec{R})$:

$$\psi_{\vec{k}}(\vec{r}) = u_{\vec{k}}(\vec{r}) e^{i(\vec{k} \cdot \vec{r})}, \quad (1.3)$$

which constitutes a Bloch mode [21]. On the other hand, eq. (1.2) comes from classical electromagnetic theory and relates the magnetic field \vec{H} of a light wave with a medium characterized by the dielectric permittivity $\epsilon(\vec{r})$. ω is the angular frequency and c is the speed of light in vacuum. Since $\epsilon(\vec{r})$ is a periodic function in a PhC, i.e. $\epsilon(\vec{r}) = \epsilon(\vec{r} + \vec{R})$, the solutions of eq. (1.2) are also Bloch modes of the form

$$\vec{H}_{\vec{k}}(\vec{r}) = \vec{h}_{\vec{k}}(\vec{r}) e^{i(\vec{k} \cdot \vec{r})}, \quad (1.4)$$

where $\vec{h}_{\vec{k}}(\vec{r}) = \vec{h}_{\vec{k}}(\vec{r} + \vec{R})$ is a complex amplitude function. Thus, the concepts of reciprocal space, Brillouin zones and band structures are also applicable for light waves in PhCs.

In a semiconductor crystal, the electronic bandgap arises due to Bragg diffraction of electron waves from atoms arranged in a periodic lattice. Likewise, the PBG in PhCs occurs as a result of the coherent superposition of light waves that are partially scattered from the dielectric interfaces at each lattice site. Since Maxwell's equations are scale invariant, PhCs can in principle be scaled in size arbitrarily. Scaling will only change the frequency range of the PBG, but the form of the band structure will remain the same. This property is very advantageous from the fabrication point of view, as it gives the possibility to design a PhC to operate at a desired frequency.

One of the most intriguing aspects of PhCs is the possibility to reach very tight photon confinement by means of crystal defects. When the periodic structure of a PhC is disturbed by defects, localized states are introduced in the PBG region. A point defect will act like a microcavity, line defects establish narrow waveguides. Semiconductor-based PhCs are of particular interest for research and technology, because one can exploit well-established micro- and nanofabrication methods to create structures that incorporate efficient light emitters. The PhC structures can then be utilized to control spontaneous emission of light sources such as QWs, QWRs and

QDs [85].

1.3.2 Numerical modeling

In cavity QED, the observation of distinct light-matter coupling effects depends on the properties of a given cavity mode, in particular its electric field distribution, polarization, mode volume and Q factor. Therefore the realization of an experiment requires careful considerations on the design of the cavity structure and a detailed analysis of its modes. For this purpose, there exist several numerical methods in computational electromagnetism, which can generally be divided into frequency-domain and time-domain approaches.

Frequency domain approaches consist of expressing the master equation (1.2) as a generalized eigenvalue problem $A\vec{x} = \omega^2 B\vec{x}$, where A and B are matrices. By applying techniques from linear algebra, one can then find a set of eigenfrequencies ω and the associated field distributions. Since the operator $\Theta = \nabla \times (\epsilon(\vec{r})^{-1} \nabla \times \dots)$ acting on the left-hand side of eq. (1.2) is linear and Hermitian, it follows that the frequencies ω are real and the eigenmodes of the magnetic field \vec{H} are orthogonal to each other.

For periodic structures such as PhCs, the most widely used frequency-domain algorithm is the plane wave expansion (PWE) method. It exploits the periodicity of the dielectric function $\epsilon(\vec{r})$ by expanding it as a Fourier series over a finite number of reciprocal lattice vectors \vec{G}_m :

$$\epsilon^{-1}(\vec{r}) = \sum_{m=1}^N \kappa(\vec{G}_m) e^{i\vec{G}_m \cdot \vec{r}} \quad . \quad (1.5)$$

Here the $\kappa(\vec{G}_m)$ are expansion coefficients, and the dielectric function is invariant upon translation in space by an arbitrary lattice vector \vec{R} , i.e. $\epsilon(\vec{r}) = \epsilon(\vec{r} + \vec{R})$. As a consequence of this translational symmetry, one can decompose the \vec{H} field into Bloch modes [10, 92]:

$$\vec{H}_{\vec{k}}(\vec{r}) = \vec{h}_{\vec{k}}(\vec{r}) e^{i(\vec{k} \cdot \vec{r})} = \sum_{m=1}^N \vec{C}_{\vec{k}}(\vec{G}_m) e^{i(\vec{k} + \vec{G}_m) \cdot \vec{r}} \quad . \quad (1.6)$$

The $\vec{C}_{\vec{k}}(\vec{G}_m)$ are Fourier expansion coefficients, and \vec{k} is a wave vector inside the Brillouin zone. Substituting eq. (1.5) and (1.6) into the master equation (1.2) leads to an eigenvalue problem in matrix form, as mentioned above. The electric field distributions $\vec{E}_{\vec{k}}(\vec{r})$ are then simply deduced from the obtained $\vec{H}_{\vec{k}}(\vec{r})$ modes via

Maxwell's relation

$$i\omega\epsilon(\vec{r})\vec{E}_{\vec{k}}(\vec{r}) = \nabla \times \vec{H}_{\vec{k}}(\vec{r}) . \quad (1.7)$$

The PWE method is particularly effective for modeling 2D PhCs. It is used to compute the field distributions of the Bloch modes and band structures, which represent the variation of the eigenfrequencies ω versus the wave propagation vector \vec{k} .

In contrast to frequency domain methods, their time domain counterparts simulate the propagation of the fields $\vec{E}(\vec{r}, t)$ and $\vec{H}(\vec{r}, t)$ in both space and time by implementing Maxwell's equations directly. Here the most prominent technique is the finite-difference time domain (FDTD) method, which is based on approximating Maxwell's equations with central finite-difference expressions on a discretized space-time grid. In essence, the partial derivatives in

$$\mu_0 \frac{\partial \vec{H}}{\partial t} = -\nabla \times \vec{E} \quad (1.8)$$

$$\epsilon \frac{\partial \vec{E}}{\partial t} = \nabla \times \vec{H} \quad (1.9)$$

are replaced by [10]:

$$\frac{\partial}{\partial x} f|_{i,j,k}^n \approx \frac{f|_{i+1/2,j,k}^n - f|_{i-1/2,j,k}^n}{\Delta x} \quad (1.10)$$

$$\frac{\partial}{\partial t} f|_{i,j,k}^n \approx \frac{f|_{i,j,k}^{n+1/2} - f|_{i,j,k}^{n-1/2}}{\Delta t} . \quad (1.11)$$

The function $f|_{i,j,k}^n = f(i\Delta x, j\Delta y, k\Delta z, n\Delta t)$ designates any component of either \vec{E} or \vec{H} at a discrete point in space and in time, where i, j, k and n are integer numbers. The spatial grid points are separated by the intervals $\Delta x, \Delta y, \Delta z$ and the time increment is Δt . Note that the Cartesian grid points are not the same for the electric and magnetic fields; the points at which \vec{E} is computed belong to a spatial grid that is offset from the grid used for \vec{H} (Fig. 1.10). This is because according to eq. (1.7) the time derivative of \vec{E} depends on the variation of \vec{H} in space (the curl). Thus, the value of a particular component of \vec{E} at any point in space is updated using the value of \vec{H} from spatially adjacent points, which is indicated in eq. (1.10) by the increment $\pm(1/2)$ in the index i . The same principle applies for updating \vec{H} . This type of computational grid is known as the Yee lattice [10].

In FDTD, the temporal evolution of the electric and magnetic fields is computed iteratively for each point in space, where \vec{E} at time $t - \Delta t$ is used along with \vec{H} at $t - \Delta t/2$ in order to obtain \vec{E} at time t . The \vec{H} field at $t + \Delta t/2$ is updated in an

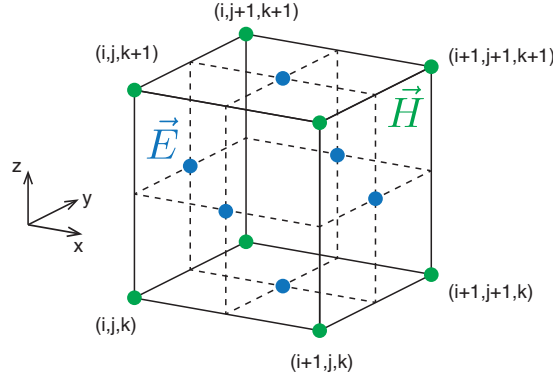


Figure 1.10: A unit cell of the Yee lattice in 3D.

analogous manner. The time difference between the update of \vec{E} and \vec{H} is thus $\Delta t/2$, such that both fields are updated after a full time step Δt . This is reflected in eq. (1.11) by the $\pm(1/2)$ increment of time index n .

In order to simulate electromagnetic wave propagation within a given structured medium using FDTD, one has to define the computational domain that sets the spatial boundaries. To avoid unphysical reflections from the boundary region, appropriate boundary conditions have to be chosen. The grid discretization has to be chosen such that the intervals between adjacent grid points is small compared to the wavelengths under consideration, and the reciprocal of the time increment has to be small in relation with the frequencies of interest. The structure to be simulated is created by assigning material properties to each point in space. Typically, all the components of the fields \vec{E} and \vec{H} are initialized to 0 throughout the computational domain, except for those spatial positions at which one defines excitation sources. These can be either continuous or transient in time. Transient sources are used whenever one is interested in acquiring the response of a system over a wide range of frequencies, while continuous sources are applied to examine the case of single-frequency excitation.

In the transient analysis, a pulse of finite duration is launched at a point of interest. For example, to compute the resonant modes of a PhC cavity, one can place a source with a Gaussian temporal profile at a non-specific point inside the cavity region. After a sufficient number of time steps (i.e. long enough so that potential spurious modes have decayed), one halts the simulation and evaluates the frequency response of the system by taking the Fourier transform

$$\tilde{f}(\vec{r}, \nu) = FT[f(\vec{r}, n\Delta t)]. \quad (1.12)$$

Here $f(\vec{r}, n\Delta t)$ is the temporal transient response of any component of either \vec{E} or

\vec{H} , at position \vec{r} . Coming back to the example of a PhC cavity, here one places one or several such field probes in the cavity region in order to capture its full mode structure. In this case, the result consists of a spectrum containing the Lorentzian profiles of the confined optical modes. By evaluating the ratio between the resonance frequency ν_c and the full-width at half maximum (FWHM) $\Delta\nu_c$ for a specific mode, one obtains the Q factor:

$$Q = \frac{\nu_c}{\Delta\nu_c}. \quad (1.13)$$

FDTD is a versatile modeling technique that allows to simulate wave propagation both in periodic and in irregular structures with complex geometries. It can be used to calculate transmission and reflection spectra as well as to evaluate eigenfrequencies, field distributions and Q factors of PhC cavity modes, in addition to computing band structures. One can also animate how \vec{E} and \vec{H} evolve in time throughout computational region, which can be helpful to gain physical insight. However, FDTD can consume a lot of computer memory, and the simulations can become very lengthy.

When it comes to analyzing the optical response of a PhC cavity, the PWE method is more straightforward and much faster for calculating the resonance frequencies and field distributions of the cavity modes as compared to FDTD. With the PWE method, only a single run cycle is needed to get the results, and one can be certain not to miss out any cavity resonance. On the other hand, PWE is not suited for assessing Q factors and for investigating temporal dynamics of the fields. For these tasks, FDTD is the method of choice. Simulating the time evolution of the fields with FDTD can be particularly insightful in the case of coupled cavities, where one can gain additional insight in the energy transfer oscillations between neighboring cavities [93]. However, FDTD is tricky insofar as special care has to be taken about what type of excitation source to select and where to position the source(s) within the structured medium in order to efficiently excite all modes. If these parameters are not chosen with prudence, there exists the risk to miss out one or several resonances.

1.4 Cavity quantum electrodynamics

Cavity quantum electrodynamics (cavity QED) is the study of the interactions between quantum light sources and resonant modes of optical cavities. It was first established by pioneering works in the field of atomic physics [94–97], before the technology for the fabrication of QDs and microcavities became advanced enough to conduct similar experiments. The theoretical foundation for describing a single QD coupled to a microcavity is the Jaynes-Cummings model, which we will review in this section. This

should also facilitate a better understanding of the differences between the strong and the weak coupling regime. In the end of this section we will briefly summarize the advances in experimental realizations of cavity QED based on QDs.

1.4.1 The Jaynes-Cummings model

In order to understand the interaction process between a single two-level emitter and a single mode of the radiation field inside a cavity (Fig. 1.11(a)), this combined light-matter system has to be treated quantum mechanically. A simplified and widely used theoretical model for this was proposed by Jaynes and Cummings [98], which is briefly summarized in the following. An introduction to the model can be found e.g. in [18, 99]. In the Jaynes-Cummings model, the two-level atom approximation is adopted by describing the uncoupled matter part as an atom with only 2 states, the ground state $|g\rangle$ and excited state $|e\rangle$. The corresponding Hamiltonian is

$$\hat{H}_A = \hbar\omega_0 |e\rangle\langle e|, \quad (1.14)$$

with $\hbar\omega_0$ being the energy separation between $|e\rangle$ and $|g\rangle$. The quantized radiation field of the cavity is represented by photon number states $|n\rangle$ and with

$$\hat{H}_R = \hbar\omega_c \hat{a}^\dagger \hat{a}, \quad (1.15)$$

where \hat{a}^\dagger and \hat{a} are the photon creation and annihilation operators, and $\hbar\omega_c$ corresponds to the energy of the quasi-resonant cavity mode. We neglect the presence of other cavity modes by assuming that they are far from resonance with respect to the atomic transition. Atom-field coupling is introduced with the interaction Hamiltonian in the dipole approximation

$$\hat{H}_I = -\hat{\mu} \cdot \hat{E}(\vec{r}_0), \quad (1.16)$$

where $\hat{\mu}$ denotes the dipole operator, \hat{E} the electric field operator and \vec{r}_0 the position of the atom inside the cavity. Expanding the dipole operator over the atomic eigenbasis, we get

$$\hat{\mu} = \mu |e\rangle\langle g| + \mu^* |g\rangle\langle e| \quad (1.17)$$

with the dipole moment $\mu = q \langle e | \hat{r} | g \rangle$, where $q = -e$ is the charge of an electron. For a given polarization \hat{e}_k , the electric field operator in (1.16) can be expressed as

$$\hat{E}_k(\vec{r}) = \sqrt{\frac{\hbar\omega_c}{2\epsilon_0 V_m}} \left(\Phi_k(\vec{r}) \hat{a} + \Phi_k^*(\vec{r}) \hat{a}^\dagger \right) \hat{e}_k. \quad (1.18)$$

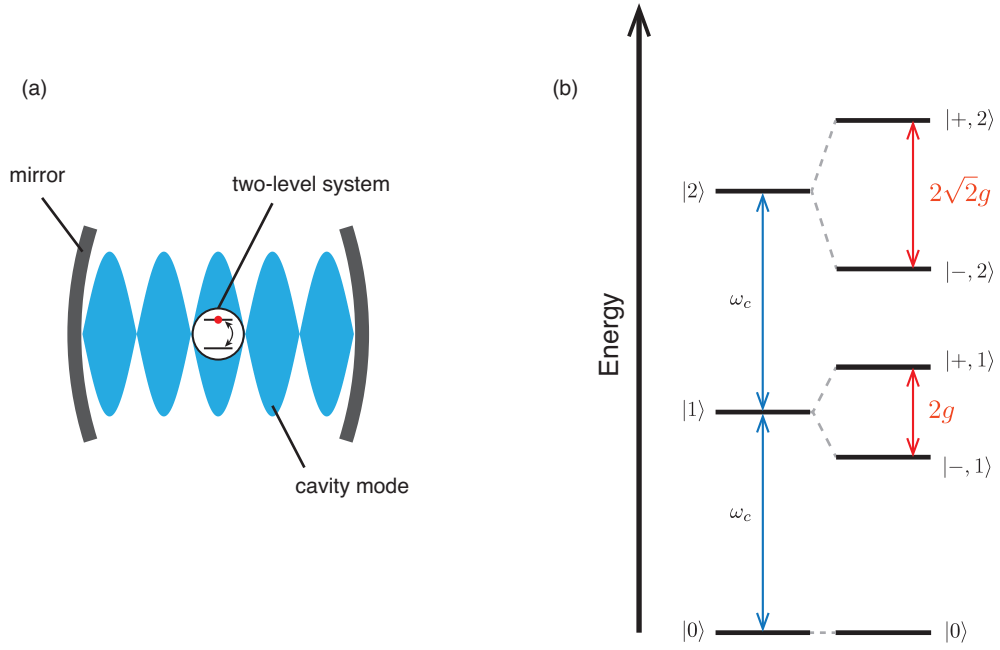


Figure 1.11: (a) Schematic illustration of a two-level system interacting with a single quantized mode of a cavity. (b) Jaynes-Cummings energy ladder for coupled emitter-cavity system at resonance, depicted here on the right for the first two manifolds ($n = 0, 1, 2$). For comparison, the energy levels of the uncoupled cavity are shown on the left, where ω_c is the bare cavity frequency.

Here the term

$$\sqrt{\frac{\hbar\omega_c}{2\epsilon_0 V_m}} = E_0 \quad (1.19)$$

can be interpreted as the electric field amplitude of a single photon inside the cavity, where ϵ_0 denotes the dielectric constant of vacuum and V_m is the mode volume. The cavity field function

$$\Phi_k(\vec{r}) = \frac{E_k(\vec{r})}{\sqrt{\max(\epsilon(\vec{r})|E_k(\vec{r})|^2)}} \quad (1.20)$$

represents the spatial distribution of the normalized electric field amplitude E_k inside the cavity with polarization \hat{e}_k , and ϵ is the relative permittivity. The mode volume V_m in (1.18) is defined by

$$V_m = \int \epsilon(\vec{r}) \Phi^2(\vec{r}) d^3\vec{r}, \quad (1.21)$$

and it determines the spatial confinement of photons inside the cavity. When there are no photons present, the radiation field is in its ground state $|0\rangle$. This is referred to as the vacuum state or also vacuum field, which has a zero-point energy equal to $(1/2)\hbar\omega_c$. Although the expectation value of \hat{E}_k equals zero in the vacuum state, its finite variance

$$(\Delta\hat{E}_k)^2 = \langle 0 | \hat{E}_k^2 | 0 \rangle = \frac{\hbar\omega_c}{2\epsilon_0 V_m} = E_0^2 \quad (1.22)$$

tells us that the vacuum state is associated with random fluctuations in the electric field. Indeed, these vacuum field fluctuations are regarded as the stimulus that triggers the spontaneous emission of a photon from an atom. According to (1.22), the fluctuations scale with the inverse of V_m , which means that they will be larger for smaller cavities. By using (1.17) and (1.18) and applying the rotating wave approximation, the interaction Hamiltonian becomes

$$\hat{H}_I = \hbar g \left(\hat{a} |e\rangle \langle g| + \hat{a}^\dagger |g\rangle \langle e| \right), \quad (1.23)$$

where we introduced the interaction coefficient g known as coupling strength or coupling constant. The interaction Hamiltonian in (1.23) is referred to as the Jaynes-Cummings Hamiltonian in the literature and is commonly used in cavity QED. The coefficient g determines the strength of atom-photon interaction at the position \vec{r}_0 of the atom, and it is defined as

$$g = \sqrt{\frac{\hbar\omega_c}{2\epsilon_0 V_m}} \Phi_k(\vec{r}_0) \mu \cdot \hat{e}_k. \quad (1.24)$$

One should notice here that the coupling strength depends on the alignment of the atom with respect to the cavity field function Φ_k , and also on the relative orientation between the atomic dipole moment μ and the polarization vector \hat{e}_k . Furthermore, g increases with decreasing mode volume, which means that the atom-field coupling is stronger in smaller cavities. We can now write the Hamiltonian of the coupled states $|i, n\rangle = |i\rangle \otimes |n\rangle$ ($i = g, e; n = 0, 1, 2, 3, \dots$):

$$\begin{aligned} \hat{H} &= \hat{H}_A + \hat{H}_R + \hat{H}_I \\ &= \hbar\omega_0 |e\rangle \langle e| + \hbar\omega_c \hat{a}^\dagger \hat{a} + \hbar g \left(\hat{a} |e\rangle \langle g| + \hat{a}^\dagger |g\rangle \langle e| \right) \end{aligned} \quad (1.25)$$

or equivalently, in matrix form

$$\hat{H} = \hbar \begin{pmatrix} n\omega_c & \sqrt{n}g \\ \sqrt{n}g & n\omega_c - \Delta\omega \end{pmatrix}. \quad (1.26)$$

with $\Delta\omega = \omega_c - \omega_0$. The corresponding energy eigenvalues of (1.26) are

$$E_{\pm,n} = \hbar \left(\omega_c n - \frac{\Delta\omega}{2} \pm \sqrt{ng^2 + \frac{\Delta\omega^2}{4}} \right), \quad (1.27)$$

and the hybridized eigenstates are

$$\begin{aligned} |+, n\rangle &= \cos\theta_n |g, n\rangle + \sin\theta_n |e, n-1\rangle \\ |-, n\rangle &= -\sin\theta_n |g, n\rangle + \cos\theta_n |e, n-1\rangle. \end{aligned} \quad (1.28)$$

The ground state $|g, 0\rangle$ is taken to have zero energy and is not affected by the interaction Hamiltonian (1.23). The time-independent wavefunctions $|\psi_{\pm,n}\rangle$ are the so-called *polariton states* or *dressed states* of the atom-cavity system, and the angle θ_n defined by

$$\tan 2\theta_n = \frac{2g\sqrt{n}}{\Delta\omega} \quad (1.29)$$

determines the degree of atom-photon entanglement (i.e. light-matter hybridization). Maximal entanglement occurs at resonance ($\Delta\omega = 0$, i.e. $\theta_n = \frac{\pi}{4}$), where the energy levels of the eigenstates

$$|\pm, n\rangle = \frac{1}{\sqrt{2}}(|g, n\rangle \pm |e, n-1\rangle) \quad (1.30)$$

are split by a factor $2\hbar g\sqrt{n}$ for each n :

$$E_{\pm,n} = \hbar\omega_c n \pm \hbar\sqrt{n}g. \quad (1.31)$$

These energy levels define the anharmonic Jaynes-Cummings ladder, which is depicted in Fig. 1.11(b). Note that n is the number of energy quanta shared by the emitter and the cavity. Thus, when a single excitation ($n = 1$) is present in the emitter-cavity system, then the corresponding states are split in energy by $2g$. This is the so-called *Vacuum Rabi splitting*, which is induced by the vacuum field [20]. The \sqrt{n} -scaling in the energy splitting of the dressed states means that the emitter-cavity system is nonlinear at the level of single quanta. Such single-photon nonlinearities have been observed with single QDs in PhC cavity systems and could be the basis for making single-photon switches [19, 100].

1.4.2 Strong versus weak coupling

So far, we completely neglected the influence of the environment on the quantum dynamics, which is indispensable for the realistic modeling of QD-cavity systems. One common approach for taking into account dissipative and non-dissipative dephasing processes is to formulate a Liouville-von Neumann master equation in the Lindblad form for the density matrix ρ of the composite system [62, 101]:

$$\frac{\partial \hat{\rho}}{\partial t} = -\frac{i}{\hbar} [\hat{H}, \hat{\rho}] + \mathcal{L}(\hat{\rho}). \quad (1.32)$$

In this equation, the Lindblad operator \mathcal{L} consists of several terms that describe the action of the different decoherence mechanisms on the temporal evolution on the system, such as radiative losses from the cavity and from the emitters, incoherent pumping of the exciton and cavity states [102] and pure dephasing stemming from phonon interactions [103] and spectral diffusion [57]. The condition for observing Vacuum Rabi splitting in the spectral domain (i.e. the $2g$ -splitting of the $n = 1$ rung of the Jaynes-Cummings ladder) then depends on the effective broadenings induced by decoherence.

If we ignore the other dephasing mechanisms, the strong coupling regime can be defined as the situation when the coupling strength g is greater than the individual radiative loss rates γ and κ from the QD and the cavity, respectively [20]. In this regime, a quantum of energy coherently oscillates back and forth between the QD and the cavity several times before it is lost to the environment (Fig. 1.12(a)). Strong coupling manifests itself in the spectral domain by a doublet, where the splitting between the two peaks corresponds to the Rabi frequency $\Omega = 2g$ of the oscillations (Fig. 1.12(b)). The implementation of strong coupling is a prerequisite for the quantum state transfer in quantum networks [53] and also in applications that require single-photon nonlinearities [19, 100].

The weak coupling regime is defined as the situation where g is smaller than the loss rates, i.e. $g < \kappa, \gamma$. Here the energy quantum stored in the QD decays to the environment in the form of a spontaneously emitted photon instead of undergoing coherent oscillations in the QD-cavity system (Fig. 1.12(c)). Therefore the Vacuum Rabi splitting is lost, leaving a single Lorentzian-shaped peak in the spectrum at the bare cavity frequency (Fig. 1.12(d)). Nevertheless, a QD can experience a modification of its spontaneous emission in the weak coupling regime. If the QD is spectrally and spatially overlapping with a high- Q cavity mode, then its spontaneous emission rate can be drastically increased with respect to emission in a bulk medium. This phenomenon is the *Purcell effect*, which was predicted by E. Purcell for atoms in

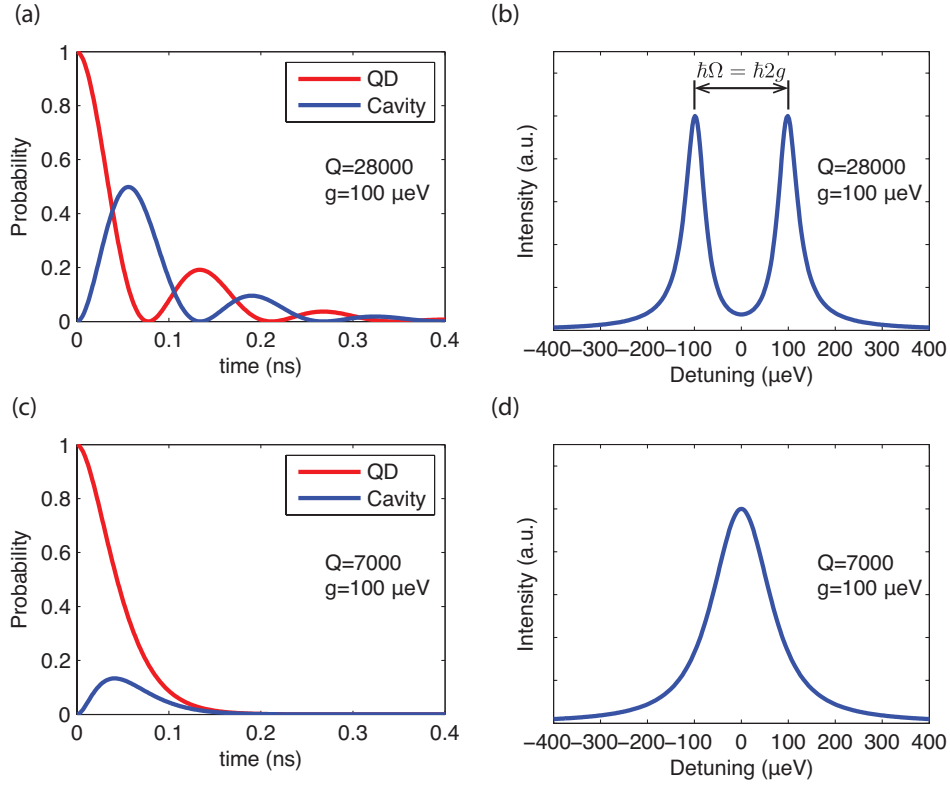


Figure 1.12: (a) Calculated population dynamics of a strongly coupled QD-cavity system at resonance. Used parameters: $g = 100 \mu\text{eV}$, $\gamma = 1 \mu\text{eV}$, $\kappa = 50 \mu\text{eV}$ (corresponding to $Q = 28000$ at 1.42 eV). (b) Emission spectrum of the strongly coupled system. (c) and (d): Population dynamics of a weakly coupled QD-cavity system and corresponding emission spectrum. Parameters: $g = 100 \mu\text{eV}$, $\gamma = 1 \mu\text{eV}$, $\kappa = 200 \mu\text{eV}$ ($Q = 7000$ at 1.42 eV). All calculations in this figure were performed using the model by Cui and Raymer [70].

1946 [104]. At the same time, the emitted photons are also geometrically channeled into the field pattern of the cavity mode, such that the QD emission is redirected. The Purcell effect can be used as a means to improve the efficiency of QD-based single photon sources [105], as well as of indistinguishable [106] and entangled photon sources [107].

1.4.3 Experimental investigations with single quantum dots

The past decade has evidenced tremendous progress in the field of cavity QED with QDs. Both weak and strong coupling phenomena were realized with self-assembled SKQDs in micropillars (also known as microposts), microdisks and PhC cavities (Fig. 1.13). An initial demonstration of spontaneous emission enhancement for QDs was achieved by Gérard in 1998 *et al.* using a micropillar (also known as micropost)

resonator [14]. Later successful experiments were conducted with micropillars and microdisks for the pulse-triggered generation of single photons from single QDs [108,109] and for the creation of indistinguishable photon sources [106]. The improvement of photon indistinguishability through weak coupling was also the basis for yielding an efficient source of entangled photon pairs [107]. Also the spontaneous emission enhancement of single SKQDs in PhC cavities was the subject of many studies, e.g. [110–112].

Strong coupling phenomena with single QDs were first observed in 2004 by Reithmaier *et al.* in micropillars [113] and by Yoshi *et al.* in PhC cavities [28]. Vacuum Rabi splitting and the anticrossing behavior of strongly coupled QDs were then examined in microdisks [114], micropillars [115] and PhC cavities [71, 116, 117]. The single-photon nonlinearities of the Jaynes-Cummings ladder were then investigated in a series of reports [16, 19, 100, 118–123].

Despite these impressive advances, there is still no practical solution to the challenging problem of controlling the positions of conventional In(Ga)As/GaAs SKQDs in cavity structures and in reducing their spectral inhomogeneity. In addition, the interaction of SKQDs with charges in the WL introduces a spurious emission background in QD-cavity coupling experiments. This latter phenomenon will be discussed in Chapter 4.

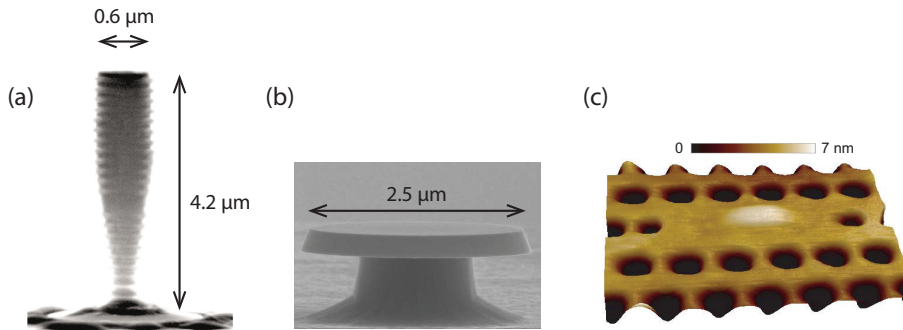


Figure 1.13:

(a) SEM image of a micropost cavity that was used to Purcell-enhance the emission rate of a single SKQD. Reprinted with permission from Physical Review Letters [109]. Copyright 2002, American Physical Society. (b) SEM image of a microdisk structure that contained a strongly coupled SKQD. Reprinted by permission from Macmillan Publishers Ltd: [Nature](#) [16], copyright 2007. (c) AFM image of a single SKQD embedded in the center of a PhC nanocavity, from which strong coupling characteristics were observed. Reprinted by permission from Macmillan Publishers Ltd: [Nature](#) [116], copyright 2007. (a) (b)

1.5 Thesis goal and outline

Broadly speaking, the objective of this thesis was to experimentally study light-matter interactions on a quantum level using single and pairs of QDs coupled to ultrasmall optical resonators. To this end, we intended to produce samples with single and pairs of pyramidal QDs placed in PhC nanocavities. The starting point for this development was established prior to this thesis by Gallo *et al.*, who successfully incorporated a single pyramidal QD made of InGaAs/GaAs into a PhC nanocavity and observed signatures of QD-cavity coupling [43]. However, at the time when the article by Gallo *et al.* was published, the method for integrating pyramidal QDs into PhCs was not mature enough to yield many well-aligned and effectively coupled devices on the same sample, which is required for conducting systematic studies. To our knowledge, none of the fabrication techniques that were reported so far are capable of achieving a scalable and deterministic integration of site-controlled QDs into cavities. By "deterministic", we do not only mean the position control for the precise placement of each individual QD within each cavity structure, but also the spectral control for matching the cavity resonances to the QD transition energies.

The chapters of this thesis are organized as follows. In Chapter 2, we describe the substrate preparation and the growth for InGaAs/GaAs pyramidal QDs. The fabrication tools and the methods for probing the PL and the photon correlations from individual QDs are briefly reviewed.

Chapter 3 summarizes the nanofabrication technique that was developed in the course of this thesis for embedding single and pairs of site-controlled pyramidal QDs within PhC nanocavities. Owing to the accurate spatial and spectral alignment features of our method, we were able to achieve the first large-scale and deterministic integration of the QD-PhC structures, which resulted in a high yield of effectively coupled devices on the same substrate. This is a significant advancement with regards to current state-of-the-art fabrication methods.

In Chapter 4, we present and analyze the PL spectra of single pyramidal QDs coupled to $L3$ PhC cavities. We investigate the signatures of the Purcell effect in the intensity, polarization and linewidth behaviors. Our results also confirm that QD-cavity coupling is influenced by the presence of the phonon reservoir, as previously predicted by theory. In addition, we demonstrate that the spurious cavity feeding mechanism, which plays a dominant role in SKQD systems, is absent with pyramidal QDs.

Chapter 5 is devoted to our studies of two spatially separated pyramidal QDs in $L3$ PhC cavities. Here, we first show and discuss the systematic properties of these

systems, which include the presence of non-resonant cavity mode emission and a characteristic polarization profile in the spectra. Then we proceed to present the detailed study from a QD pair mutually coupled to a cavity mode and demonstrate that both QDs are simultaneously subject to the Purcell effect. This represents the first realization of deterministic coupling of two QDs to a cavity. Power dependence measurements from this system manifested that the peaks from both QDs gradually disappeared from the spectrum with increasing power, leaving the cavity mode as the dominant emission channel. This could be an indication of radiative coupling effects.

Finally, in Chapter 6 we arrive at the conclusions of this thesis. Here we propose possible continuations for the research with pyramidal QDs in cavity QED.

2 Experimental techniques

The fabrication of the pyramidal QDs and their integration into PhCs is a complex process and requires the combined application of several different technologies. In this chapter, we summarize the experimental procedures employed for creating the patterned substrates and for epitaxially growing InGaAs/GaAs QDs on top of them. In addition, we discuss the mechanisms leading to QD nucleation. The specific technologies that were used in the sample fabrication process will also be reviewed. In the last part of this chapter, we introduce the working principles of photoluminescence and photon correlation measurements that were employed to study the light emission spectra of our samples.

2.1 Fabrication of pyramidal quantum dots

2.1.1 Summary of the fabrication procedure

This subsection summarizes the fabrication process for preparing regular arrays of InGaAs/GaAs QDs grown in pyramids with a base length of $L_b \sim 300$ nm, which were intended for the integration into the PhC cavities (see Chapter 3). The main steps are illustrated in Fig. 2.1. Our start material is a 2 inch GaAs (1 1 1)B wafer¹, which is misoriented towards $[-2\ 1\ 1]$ by 2° . For practical purposes, we normally cleave the wafer into 12 equal-sized pieces, each of which serves as a substrate in the processing steps described in the following.

We begin by depositing a 40 nm thick layer of SiO_2 by means of plasma-enhanced chemical vapor deposition (PECVD). Then the sample is spin-coated with a ~ 200 nm layer of Poly(methyl methacrylate) (PMMA) resist (Fig. 2.1(a)), into which regular

¹“GaAs (1 1 1)B” means that the substrate surface corresponds to the arsenic-terminated (1 1 1) crystal plane.

arrays of equilateral triangles are written with nanometer resolution by EBL. These triangles are separated by 400 nm (center to center) and are aligned on a triangular lattice. The area covered with such an array pattern is typically $300\ \mu\text{m} \times 300\ \mu\text{m}$.

After EBL writing, the exposed parts of the PMMA are developed with a Methyl isobutyl ketone (MIBK) solvent and removed by rinsing (Fig. 2.1(b)). Pattern transfer from the PMMA level to the SiO_2 mask is performed using CHF_3/Ar -based reactive ion etching (RIE). Subsequently, the PMMA resist is removed using acetone and oxygen plasma cleaning (Fig. 2.1(c)). Prior to etching the pyramidal recesses, an argon plasma treatment is performed by RIE in order to remove potentially present CHF_3 -related residues from the exposed GaAs surfaces. To etch the pyramidal recesses, the sample is then immersed into a 0.05% bromine-methanol solution for 8 s. We use a magnetic stirrer in order to facilitate homogeneous etching across the whole sample. The wet chemical etching process causes an anisotropic removal of GaAs material through the triangular openings of the SiO_2 mask, such that the perfectly flat pyramid facets become exposed (Fig. 2.1(d)). The 3 facets of each pyramid correspond to $\{1\ 1\ 1\}$ A gallium-terminated crystal planes. Aided by the high precision of the EBL in writing the triangle mask pattern and the nature of the wet chemical etching process, the pyramids are perfectly symmetric and uniform in size; the standard deviation in the size of the pyramids can be as small as 4 nm [124].

After pyramid etching, buffered HF is used to strip off the SiO_2 mask. In order to reduce the amount of contaminations on the surface, the substrate is then intentionally oxidized using oxygen plasma, followed by immersion into pure HF. This is the last substrate preparation step prior to growing the QD heterostructures. Finally, the sample is introduced into the MOVPE reactor to grow a GaAs/InGaAs/GaAs layer sequence. In this process, a single InGaAs/GaAs QD is self-formed inside each of the pyramids as a result of the interplay between growth rate anisotropy, curvature-induced capillarity and entropy of mixing effects (Fig. 2.1(e)) [125–127]. The GaAs capping layer fills up the pyramids, such that the substrate surface is planar in the end.

2.1. Fabrication of pyramidal quantum dots

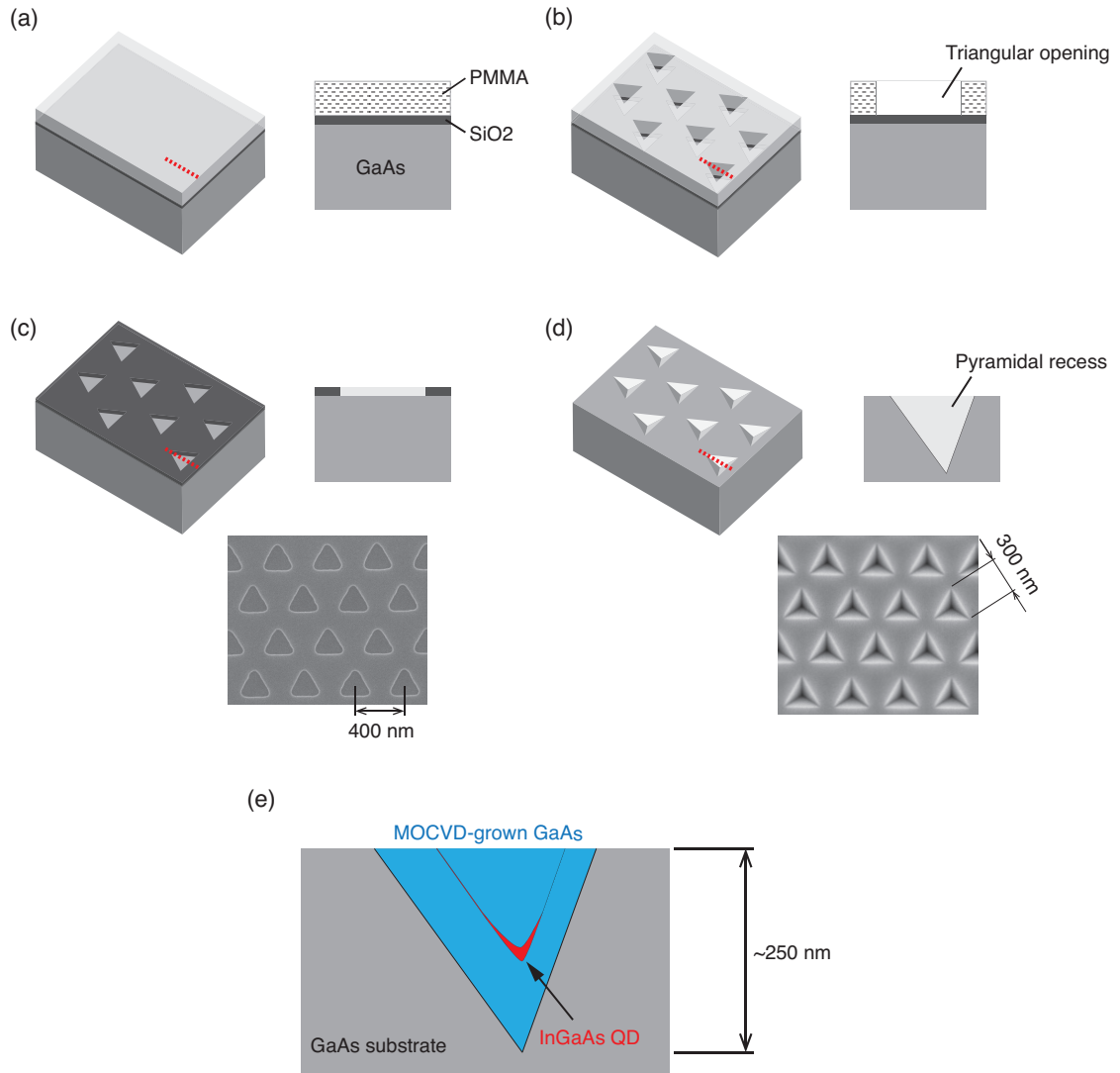


Figure 2.1: Overview of fabrication steps for pyramidal QDs. The red dashed line indicates the plane of the cross-sections shown next to the 3D schematic illustrations. (a) Substrate coated with SiO₂ and PMMA. (b) After EBL and PMMA development. (c) After RIE etching and PMMA removal. The SEM image shows a section of an actual sample in top view at this fabrication stage. (d) After wet chemical etching and SiO₂ mask removal. (e) Schematic cross-section of a pyramid after MOVPE growth.

2.1.2 Growth mechanisms

In view of interpreting the characteristics of pyramidal QDs in the cavity QED experiments described in the following chapters, it is important to understand how a QD is formed within the pyramid during MOVPE growth. The study of MOVPE growth within such pyramids has been the subject of investigation in a series of publications [38, 42, 124, 127, 128, 128–132].

As mentioned above, QDs self-form in the pyramids through the combined action of several processes, namely growth rate anisotropy, capillarity-assisted adatom diffusion and entropy of mixing. First, precursors arriving on the substrate predominantly decompose within the pyramids due to the exposure of $\{111\}A$ surfaces, while precursor decomposition on the $(111)B$ surface is suppressed [130, 131]. For this reason, the precursor decomposition rate depends on the ratio of the total area of the exposed $\{111\}A$ facets to the total $(111)B$ area. This anisotropy in the precursor decomposition rate is related to the chemical differences between the gallium-terminated $\{111\}A$ facets and the arsenic-terminated $(111)B$ plane [133]. Then, there is an intrinsic growth rate anisotropy between the different crystal facets, causing a faster growth rate on the $\{111\}A$ facets than on the $\{111\}B$ surface where growth is almost negligible [125, 126, 133].

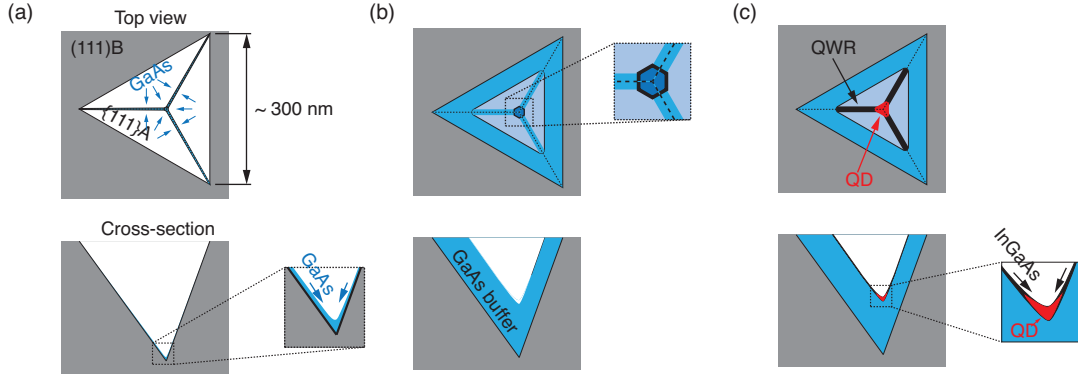


Figure 2.2: Evolution of growth within a single pyramid illustrated in top and cross-section view. (a) Initial stage of GaAs buffer layer growth. The blue arrows indicate the capillarity-driven surface fluxes of the adatoms. (b) Completed GaAs buffer layer. (c) InGaAs deposition and formation of the QD and the QWRs.

When the adatoms are released subsequent to precursor decomposition, they can undergo surface diffusion processes characterized by a diffusion length of $\sim 200 - 300$ nm [124, 131]. Due to capillarity, the adatoms tend to accumulate on the concave wedges and the apex of a pyramid, resulting in an increased thickness of the deposited material at those locations (Fig. 2.2(a) and (b)). However, the capillarity-induced

thickening of the grown layers is more pronounced at the sharp pyramid apex as compared to the wedges and sidewalls. Compositional non-uniformity within the pyramid is established by entropy of mixing: local variations in the alloy composition are counteracted by the buildup of a gradient in the chemical potential [125, 134].

Owing to the high structural symmetry of the pyramid and the nature of the growth mechanisms, the GaAs buffer forms a symmetric groove with a hexagonal surface pattern at its bottom (Fig. 2.2(b)) [135, 136]. Thus, when subsequently a very thin layer (0.2 – 0.5 nm nominal thickness) of InGaAs is grown on the substrate, capillarity guides the adatoms into the groove bottom and to the 3 wedges to form a highly symmetric single InGaAs QD at the center and 3 lateral InGaAs quantum wires (QWRs) (Fig. 2.2(c)). The high symmetry of pyramidal QDs is manifested in the linear polarization dependence of their PL emission, which is fully isotropic [137, 138].

The seeded growth approach of pyramidal QDs offers further desirable features:

- *Deterministic QD nucleation:* The growth process is inherently deterministic, such that a single QD (per layer) is formed within each pyramid. The nucleation of QDs at other locations on the substrate, or of multiple QDs within a specific pyramid, is suppressed.
- *Positioning control:* The growth sites of the QDs are determined by the positions of the pyramids on the substrate, which can be controlled with an accuracy down to ~ 5 nm by means of EBL. This is an essential advantage for device integration, particularly in view of the targeted placement of a QD at a desired position within an optical microcavity.
- *Scalability:* In view of the realization of complex nanophotonic devices and cavity QED experiments, the availability of a scalable QD technology is a prerequisite. Pyramidal QDs are ideal candidates in this respect, since they can readily be fabricated in arrays to cover large areas of several mm^2 [38].
- *Spectral uniformity and reproducibility:* Due to the great uniformity of MOVPE growth in pyramid arrays, the pyramidal QD system yields high reproducibility of the QD spectral features [39, 40] and tight control over their emission energies. The regularly attainable inhomogeneous broadening is ~ 10 meV, although a record value of ~ 1 meV has recently been demonstrated [38].
- *Tunable emission energy:* The QD exciton transition energies can be engineered either by choosing different material compositions for the QD heterostructure, by modifying the nominal layer thicknesses in MOVPE growth, by varying the

pitch of the pyramid arrays [131], and through controlling the size of the pyramids [124].

- *No wetting layer*: In contrast to SKQDs, pyramidal QDs do not grow on top of a 2D wetting layer. The only carrier-confining nanostructures in the vicinity of pyramidal QDs are the lateral 1D QWRs [124]. Our findings from experiments with pyramidal QDs in PhC cavities (see Chapter 4 and 5) suggest that the QWRs play a far less important role in perturbing the QD states than the wetting layer in the case of SKQDs. As a consequence, the multiexcitonic transitions that contaminate the cavity emission in the case of SKQDs appear to be absent in the case of pyramidal QDs [64].

2.2 Fabrication tools

2.2.1 Metal-organic chemical vapor deposition

Metal-organic chemical vapor deposition (MOVPE) is an epitaxial growth technique for fabricating multilayer crystalline structures based on, e.g., III-V and II-VI compound semiconductor materials. It is widely used in research institutions for experimental purposes, as is one of the leading technologies in the industry for the production of optoelectronic and electronic devices such as light emitting diodes (LEDs), solar cells, lasers and transistors. In MOVPE, vaporized metalorganic precursors are transported with the aid of a carrier gas (usually nitrogen or hydrogen) into the growth reactor, where the precursor molecules thermally decompose into their constituents and result in the epitaxial growth of crystalline layers of the desired semiconductor material on the substrate surface (Fig. 2.3(a)). The main strengths of MOCVD include its flexibility for heteroepitaxial growth of a wide range of materials, the possibility to produce atomically sharp interfaces, monolayer precision over large surface areas, very low defect density of the grown layers, and scalability from laboratory to production systems.

MOVPE allows to finely adjust the growth conditions depending on the specific application. The main parameters to control the epitaxy are the substrate temperature, the total reactor pressure, and the gas composition. Our group uses a commercial Aixtron 200 MOVPE facility (Fig. 2.3(b)), which contains 2 reactors capable of supporting 2 inch wafers. The carrier gas in this system is N_2 , and the precursor materials for the deposition of $Al_xGa_{1-x}As$ and $In_xGa_{1-x}As$ layers are trimethylaluminium ($Al_2(CH_3)_6$), trimethylgallium ($Ga(CH_3)_3$), trimethylindium ($In(CH_3)_3$) and arsine (AsH_3). These gases are introduced horizontally into the reaction chamber, where the sample is

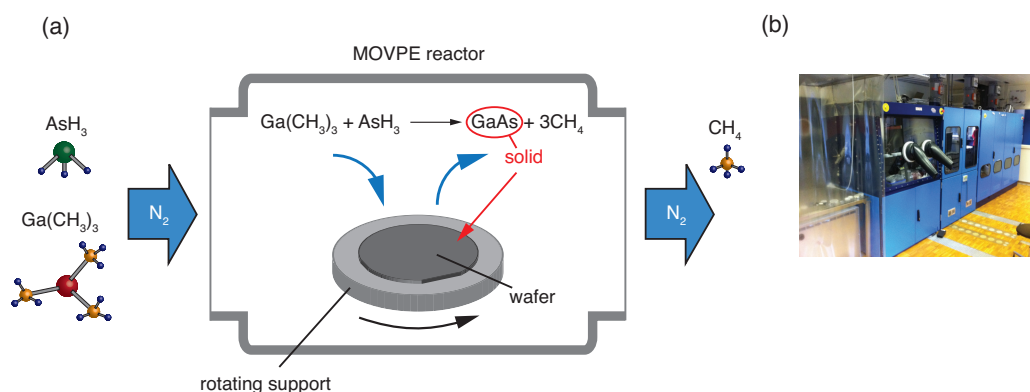


Figure 2.3: (a) Working principle of GaAs epitaxy in MOVPE. (b) Photograph of the Aixtron 200 MOVPE system used in this thesis work.

placed on susceptor plate that is slowly rotating during epitaxy in order to increase growth uniformity. The gas fluxes are regulated by means of electronic mass flow controllers. Tubular quartz lamps are employed to control the sample temperature. Growth is typically performed at temperatures between 550°C and 700°C and at a pressure of 20 mbar.

The working principle of the MOVPE is illustrated in Fig. 2.3 for the case of GaAs. In a simplified picture, the precursors flowing through the reactor begin to undergo a thermally activated decomposition process already in the gas phase as soon as they approach the heated wafer surface. Precursor molecules reaching the wafer then may diffuse across the surface until they further decompose into adatoms of the growth species (e.g. Ga or As) and methyl radicals. The radicals eventually desorb and are transported out of the reactor, while the adatoms can migrate over the surface between different adsorption sites. The surface diffusion and sequential adsorption/desorption processes of the adatoms are strongly affected by the presence of vacancy defects such as at atomic step edges, since the adatoms preferentially incorporate at those sites. In fact, slightly (up to a few degrees) misoriented substrates are intentionally used for MOVPE growth due to the higher growth rates and better quality films that can be obtained through the step flow growth mode. Finally, epitaxial layers that match the crystalline structure of the substrate are formed as a result of these chemical reactions.

2.2.2 Scanning electron microscopy

The wavelength of propagating electrons depends on their momentum through the de-Broglie relationship and is by orders of magnitude smaller than the wavelength of light. A scanning electron microscope (SEM) is a device that exploits this property

by illuminating specimens with an electron beam to produce microscopic images of the surface topography [139]. The electron beam is generated by an electron gun that can either be a thermionic or a field emission source, and then passes through a set of magnetic lenses that collimate and focus the electrons onto the sample surface (Fig. 2.4(a)). When the electrons impinge on the specimen, they can either be backscattered or undergo a cascade of scattering events, upon which they may eject secondary electrons (Fig. 2.4(b)). These signals are detected by specialized detectors, through which topographic and chemical information can be obtained. A microscopic image is then acquired by using the deflector coils to scan the electron probe across a spatial region of interest.

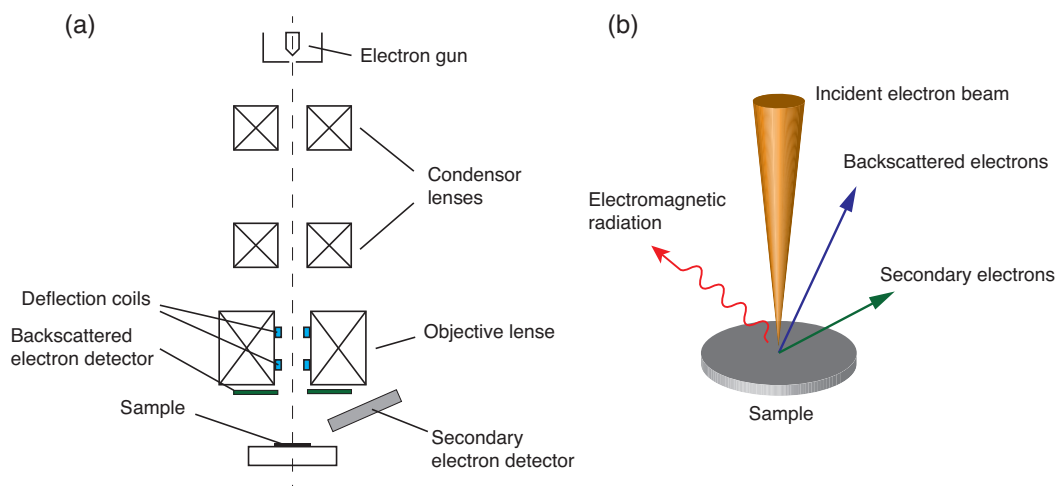


Figure 2.4: (a) Schematic cross-section through a SEM, depicting its essential components. (b) Illustration of the signals created by the electron beam.

The maximum attainable resolution of an SEM depends on several factors, such as the minimum spot size to which the electron beam can be focused and the contrast that can be achieved with the type of materials that are investigated. Nowadays commercial SEM systems can resolve details of 1 nm in size or less. The acceleration voltage of an SEM is variable and typically ranges from ~ 1 kV to 30 kV. Images giving information about the surface morphology and topography are generated by measuring the secondary electrons, while the backscattered electrons come from deeper below the surface and are sensitive to the chemical composition. The SEM system that we employed for SEM imaging was a JEOL (JSM-6701F), which had a resolution of 1 nm at 15 kV acceleration voltage.

2.2.3 Atomic force microscopy

Atomic force microscopy (AFM) is a method to acquire 3D surface images of conductive and non-conductive materials with atomic resolution, by sensing atomic forces with a sharp tip [140]. The tip, which is typically made of Si or Si_3N_4 , is attached at the end of a flexible cantilever and is brought in close proximity to the sample. As the cantilever is deflected due to the forces acting between individual atoms of the AFM tip and of the sample surface, the vertical cantilever displacement is monitored by measuring the position of a reflected laser beam with a photodetector (Fig. 2.5(a)). The sample is mounted on an XY-stage that allows for raster-scanning large areas, and the vertical cantilever position is fixed with a piezoelectric actuator that is controlled by the feedback signal coming from the laser position measurement.

In general, the intermolecular forces that are involved in the sample-tip interaction include electrostatic, magnetic and van-der-Waals forces. A simple model (applicable for non-magnetic materials) that approximates the forces experienced by the AFM tip is given by the Lennard-Jones potential (Fig. 2.5(b)). When the sample-tip distance is very small (few Å), Pauli repulsion due to overlapping electron orbitals overwhelms and the tip is bent upwards. These forces have a magnitude of only $\sim 1 - 10$ nN, such that the spring constant of the cantilever has to be sufficiently small to enable their detection. At slightly larger sample-tip distances (few tens to hundreds of Å), repulsive forces become negligible and the dominant van-der-Waals forces pull the tip downwards.

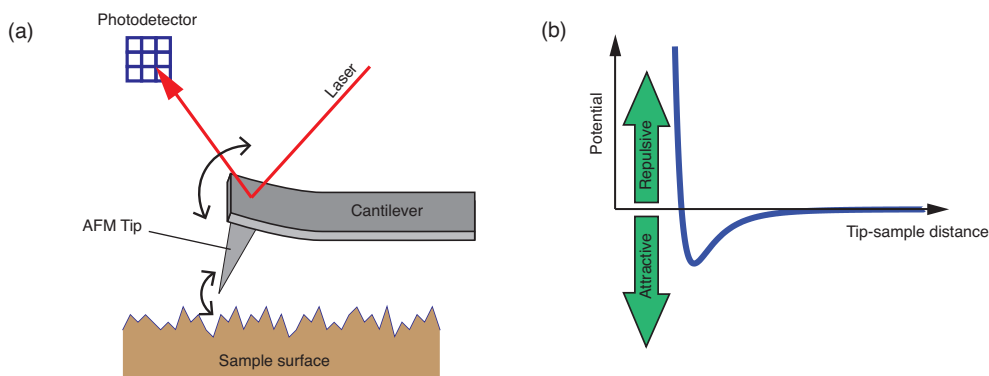


Figure 2.5: (a) Schematic of an AFM instrument. (b) Illustration of the potential sensed by the AFM tip.

There are basically three different AFM imaging modes which are referred to as contact mode, non-contact mode and tapping mode. In the contact mode, the sample topography is probed by keeping the repulsive force acting on the AFM tip constant through a feedback loop. If it is required to keep the degradation of

the sample and the tip at a minimum, the non-contact imaging mode is beneficial where the cantilever is kept at relatively large distances. In this operation mode, the cantilever is driven to oscillate at high resonance frequency and the surface profile is measured by detecting the amplitude and phase changes that are induced. The tapping mode is very similar to the non-contact mode, however the distance to the sample is kept shorter such that an intermittent contact is established. The AFM instrument that was used in the course of this thesis was a commercial PSIA XE-100 AFM. It was operated in tapping mode to record images from (1 1 1)B GaAs substrates.

2.2.4 Electron beam lithography

Electron beam lithography (EBL) is a nanofabrication tool that uses a focused electron beam to write structures with features in the nanometer size range onto a resist-coated substrate [141]. The working principle of an EBL system is very similar to that of an SEM: electrons are accelerated to energies of up to 100 keV and are focused on the target surface by means of electric and magnetic lenses. However, EBL systems are not intended for microscopic imaging, but dedicated to exposing user-defined patterns that will eventually be transferred to the sample.

The electron wavelength at typical operation conditions is 10 pm or less, and the electron beam spot size is of the order of 5 nm. In comparison to conventional photolithography techniques, EBL offers advantages such as superior resolution and versatile pattern formation; the main disadvantage of EBL is that it is a serial process, because only 1 pixel of the whole pattern can be exposed at a time.

EBL resists usually consist of high-molecular weight polymers dissolved in a liquid solvent. One of the most commonly used resists for semiconductor processing is PMMA. When high-energy electrons impinge on PMMA, the polymer chains are split and the molecular weight is locally reduced. Using a solvent developer (MIBK), the exposed parts of the PMMA resist can selectively be washed away. The remaining pattern can then be transferred to the substrate either through a lift-off process, or to a hard mask layer (such as SiO₂) covering the substrate via RIE etching.

The resolution of EBL is not limited by diffraction, but mainly by what is referred to as the proximity effect: electron scattering interactions with the resist material and the substrate cause additional resist exposure in the region adjacent to the electron beam spot. To some extent, the proximity effect can be corrected by deliberate pattern design and by systematic modifications of the electron beam dose, in order to adapt the overall exposure to the specific writing pattern. However, the resolution also depends on the type of resist material used. In case of PMMA, the minimum feature

size that can be regularly attained is between 10 and 20 nm.

We used two different commercially purchased EBL systems in the course of this thesis work:

- *JEOL JSM 6400*: Originally a SEM, this machine (manufactured in the 1990s) was upgraded to have EBL capabilities and can therefore be used both for imaging and beam writing. Its acceleration voltage is set to 40 kV, the maximum writing speed is 5 MHz and the maximum attainable writing resolution is 30 nm. The alignment procedure has to be performed manually by the user.
- *Vistec EPBG5000*: This is a state-of-the-art EBL tool that is highly automatized and capable of writing <10 nm features. It can be operated with a maximum acceleration voltage of 100 kV and writing speeds of up to 50 MHz. Alignment is performed automatically by the machine, which finds the positions of the reference marks by means of a back-scattered electron detector.

2.2.5 Reactive ion etching

Reactive ion etching (RIE) is a versatile plasma etching technology commonly used in microfabrication. It has the ability to etch nanometer-sized structures and to achieve etch directionality, which is of great utility for transferring lithographically defined patterns into underlying layers. The main elements of a typical RIE setup include a vacuum chamber, two parallel electrodes connected to a radio-frequency (RF) generator, and a suitable feed gas (Fig. 2.6(a)). The substrate is placed on top of the lower electrode.

The plasma is created from the injected gas via a high-power RF electric field that is applied between the two electrodes. While the rapid variations of the electric field cause the plasma electrons to be accelerated very efficiently and to further ionize the gas, the movement of the ions remains almost unaffected, because they are too heavy to respond to the high frequency (typically 13.56 MHz) of the driving field. However, positively charged ions are pulled towards the lower electrode due to the build-up of a large negative bias between the electrode and the plasma. This so-called self-bias is generated by the accumulation of negative charge on the lower electrode, aided by the presence of a capacitor between the latter and the RF supply. The directed momentum of the accelerated ions assists the chemical reaction taking place on the substrate surface and causes the etching to be directional in the vertical axis.

The RIE system used for the fabrication purposes of this thesis was an Oxford Instruments Plasmalab 80 (Fig. 2.6(b)), configured for fluorine-based plasma etching.

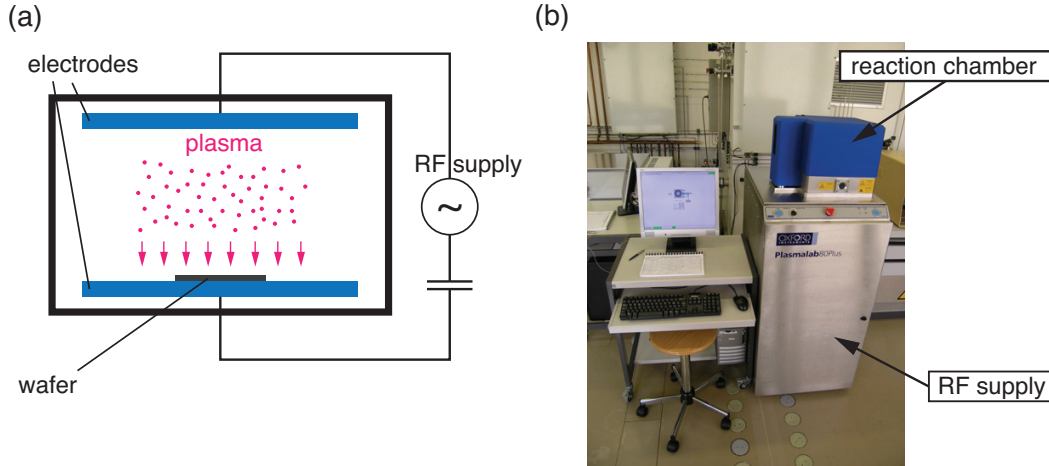


Figure 2.6: (a) Schematic of RIE. (b) Oxford Instruments Plasmalab 80.

Its RF generator provided a power of 600 W and a driving frequency of 13.56 MHz. This Oxford RIE system was employed both for pyramid and PhC processing in order to perform pattern transfer from the PMMA to SiO₂ layer, based on a gas mixture consisting of CHF₃ and Ar. The working recipe was adapted such as to achieve the best compromise between SiO₂-to-PMMA selectivity and etch rate [142].

2.2.6 Inductively coupled plasma etching

Inductively coupled plasma (ICP) etching is another etching technique applied in micro- and nanofabrication, with the ability to independently control the plasma density and the energy of ion impact on the substrate. In comparison to conventional RIE, ICP offers higher etch rates, better mask selectivity, and lower surface damage. Apart from that, good sidewall angle adjustment can be achieved owing to the superior control over the etching parameters, which is especially important for the etching of high aspect ratio structures such as PhCs [143].

The basic principle of operation of ICP etching is the same as for RIE: a plasma is generated by coupling the electromagnetic energy from an RF source to a feed gas. However, in contrast to RIE where the excitation is provided by capacitive coupling, ICP uses electromagnetic induction to power the plasma [144]. As illustrated in Fig. 2.7(a), the cylindrical reaction chamber is surrounded by a coil that is connected to the ICP power source. The latter drives the coils with an RF field, such that they produce a time-varying magnetic field inside the reactor. The changing magnetic field in turn induces a circular electric field $E(t)$ in the plane perpendicular to the coil axis, thereby accelerating the plasma electrons and causing more ions to be created by

collisions. By applying a RF bias voltage to the wafer holder, the energy of the ions bombarding the wafer can be adjusted.

For the purpose of etching alignment marks and PhCs with vertical sidewalls into GaAs substrates, we employed a Sentech Plasma Etcher SI 500 ICP system (Fig. 2.7(b)). This system is equipped with a 1200 W, 13.56 MHz ICP source, and a 600 W RF bias (also with 13.56 MHz driving frequency) is applied to the wafer holder. Gases available for processing include BCl_3 , N_2 , Cl_2 , Ar, H_2 , O_2 and SiCl_4 .

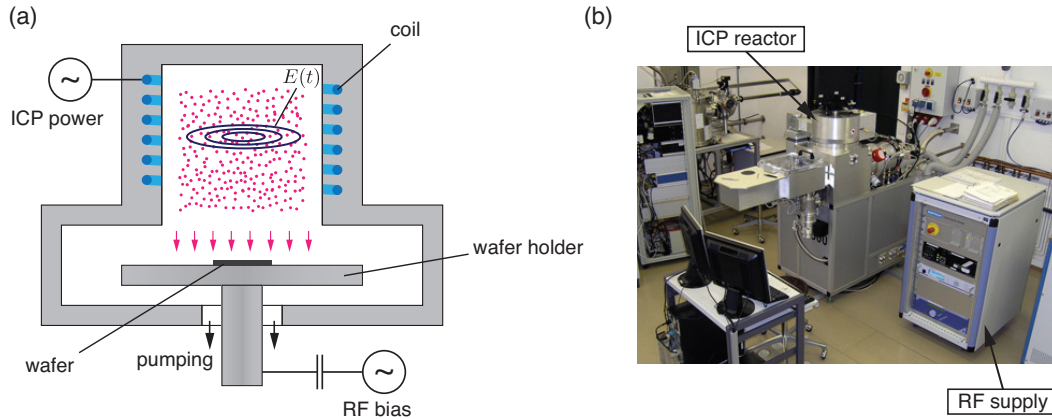


Figure 2.7: (a) Sketch of an ICP reactor with cylindrical geometry. (b) Sentech Plasma Etcher SI 500.

2.3 Optical characterization techniques

2.3.1 Micro-Photoluminescence spectroscopy

The process in which a substance emits photons upon excitation by means of a light source is called photoluminescence (PL). In semiconductor research, PL spectroscopy is a technique for measuring optical properties of materials and to gain insight into their electronic structure via their radiation spectrum [145]. In order to study the PL of micron- or submicron-sized objects, a conventional approach to achieve the necessary spatial resolution is to use a microscope objective that has the function of focusing the excitation beam onto the sample and of collecting the signal at the same time. The PL is then spectrally analyzed by means of an optical spectrometer. This method is referred to as micro-PL spectroscopy.

The micro-PL setup used for the low-temperature experiments of the present work is schematically depicted in Fig. 2.8. Light coming from a laser source is focused to a small spot ($\sim 1 - 2 \mu\text{m}$ diameter) on the sample surface by means of a microscope

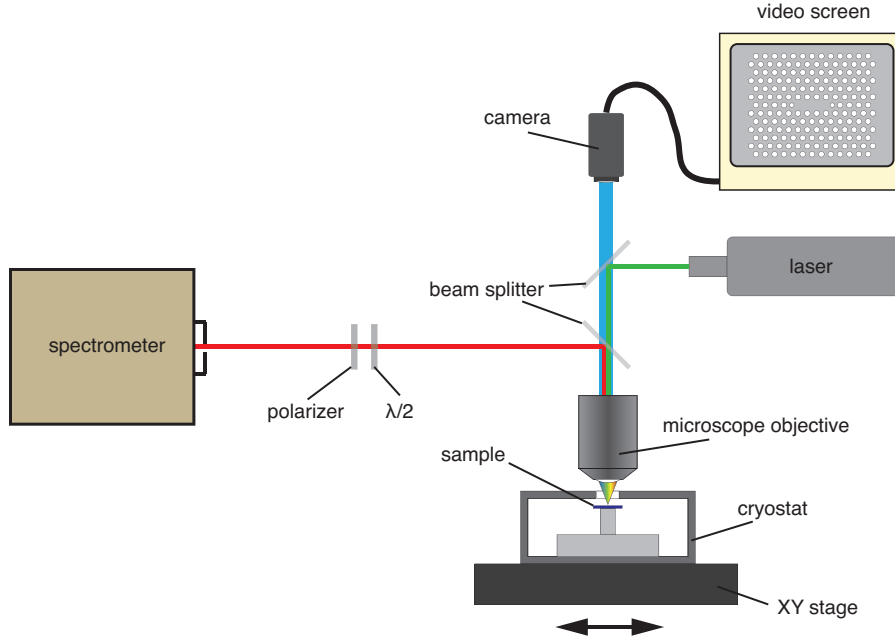


Figure 2.8: Schematic drawing of our micro-PL setup. The path for optical excitation is highlighted in green, while the detection line is depicted in red. The XY stage is used to move the laser spot across the sample, which is displayed in magnified view on a monitor.

objective (Zeiss, $50\times$ magnification, $NA = 0.55$, $f = 3.6$ mm), which also collects the PL signal. The laser unit consists of a Spectra Physics Tsunami Ti:sapphire laser (tunable within 700–1000 nm) that is optically pumped at 532 nm by a Spectra Physics Millennia Nd:YAG laser. The objective lens is part of an optical microscope system equipped with 2 beamsplitters and a camera, which allows monitoring the magnified image of the sample on a video screen. In order to position the excitation spot accurately at a desired location, an XY stage is employed can translate the continuous flow helium cryostat (Janis ST-500) holding the sample in the horizontal plane. The sample temperature is regulated by a Lakeshore 331 temperature controller. For detecting the PL signal, a Jobin Yvon Triax 550 spectrometer (55 cm focal length, 1200 grooves/mm grating, dispersion 1.55 nm/mm) equipped with a charge coupled device (CCD) detector is used. The liquid nitrogen-cooled CCD is a Jobin Yvon Spex Spectrum One, consisting of a 2048×512 pixel array of silicon photodetectors that respond to optical signals within the spectral range between 400 nm and 1050 nm. Optionally, a half wave plate combined with a linear polarizer can be inserted in the detection path in order to map the polarization features of the PL emission. The spatial resolution of the micro-PL setup is $\sim 2 \mu\text{m}$ and its spectral resolution is approximately $100 \mu\text{eV}$.

For studying QDs in conventional micro-PL, the excitation wavelength is cho-

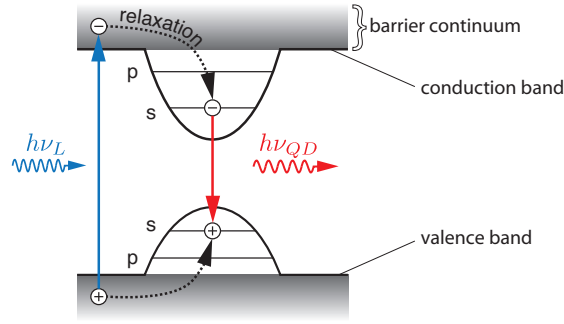


Figure 2.9: PL from a single QD (schematic). Free electrons and holes are created in the barriers by laser excitation at an energy $h\nu_L$. Carriers captured by the QD can recombine radiatively from different confined states ($h\nu_{QD}$), giving rise to the characteristic QD spectrum.

sen such that the energy $h\nu_L$ of the incident photons is greater than energy of the QD barriers (Fig. 2.9). The laser light is absorbed by the semiconductor material, injecting electrons and holes into extended barrier states. Interactions with phonons cause the carriers to relax very rapidly (within ~ 1 ps) to the band edge, where they either recombine radiatively or get captured by a QD. Within a QD, radiative carrier relaxation is slower (few tens of picoseconds [146]) than in the bulk. The reason for this is the mismatch between the energy gaps in the DOS of a QD and the available phonon energies that could induce radiative decay. QD-confined excitons can only couple to longitudinal-acoustic (LA) phonons with energies limited to few meV [77]. Longitudinal-optical (LO) phonons exhibit a nearly monochromatic dispersion and an energy of ~ 35 meV in the case of bulk GaAs, whereby they only provide a narrow energy window for the relaxation process. The slowdown of carrier-phonon interactions in QDs is known as the *phonon bottleneck* [146, 147] and still remains a controversial topic.

Photons emitted in the direction of the microscope objective are collimated into the detection path and measured with the spectrometer. In a sense, the PL spectrum is the fingerprint of the QD, since it contains essential information about its level structure and the nature of the confined excitonic species.

2.3.2 Photon correlation measurements

In quantum optics, a widely used method to study photon correlation statistics is to adopt the Hanbury Brown – Twiss (HBT) experiment (Fig. 2.10). Here a 50 : 50 beam splitter divides the incoming stream of photons equally between two output channels, each of which is equipped with a photodetector capable of counting single

photons. The correlation counter registers the time delay between photon detection events occurring on the two separate channels, i.e.: whenever a photon is detected on channel *A*, the correlation counter starts measuring the time that elapses until channel *B* reports a photon detection event. The results are accumulated in a correlation histogram that represents the number of correlation counts versus time delay.

We implemented the HBT arrangement as a part of our micro-PL setup by using two silicon avalanche photodiodes (APDs) for single photon detection. The APDs are single photon counting modules of Perkin Elmer (AQR series), which have a dark count rate of ~ 200 Hz. Their photon detection efficiency varies approximately linearly from 45% at 850 nm to 35% at 900 nm. One of the APDs is mounted on the Jobin Yvon Triax 550 (see description of our micro-PL setup above) and the other one on a Jobin Yvon Triax 320 spectrometer (32 cm focal length, 1200 grooves/mm grating, dispersion 2.64 nm/mm). The APD outputs are both connected to a modulation domain analyzer (Hewlett Packard 53310A), which acts as a correlation counter and produces a cumulative correlation histogram. In total, the timing resolution of our HBT setup is about 1 ns, and the spectral resolution amounts 100 μeV .

The HBT arrangement provides a method to measure photon correlation statistics and to verify whether a given light emitter exhibits classical or quantum character [18], since the correlation histogram obtained from the experiment is proportional to the second-order correlation function $g^{(2)}(\tau)$:

$$g^{(2)}(\tau) = \frac{\langle I_A(t) I_B(t + \tau) \rangle}{\langle I_A(t) \rangle \langle I_B(t + \tau) \rangle} = \frac{\langle n_A(t) n_B(t + \tau) \rangle}{\langle n_A(t) \rangle \langle n_B(t + \tau) \rangle}. \quad (2.1)$$

I_A and I_B are the time-varying intensities measured on detector *A* and *B*, which are directly proportional to the respective number of photon counts n_A and n_B . The function $g^{(2)}(\tau)$ quantifies the conditional probability of detecting a photon at a time

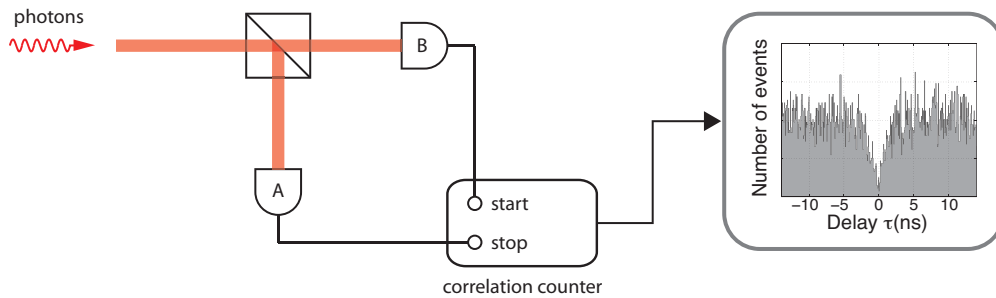


Figure 2.10: Hanbury Brown – Twiss setup for photon correlation measurements. The presented example histogram corresponds to an autocorrelation measurement performed on a single QD exciton, which shows evidence of antibunching.

$t + \tau$ on detector B , provided that a photon detection event was registered at time t on detector A .

For large values of τ , $g^{(2)}(\tau)$ is expected to be equal to 1 for any kind of photon stream. At short delay times, however, $g^{(2)}(\tau)$ is predicted to give different results depending on the nature of the investigated light field and the associated photon statistics. For example, a perfectly coherent and monochromatic beam of light with constant intensity is characterized by $g^{(2)}(\tau) = 1$ for all values of τ (Fig. 2.11(c)); this is a manifestation of the underlying Poissonian statistics of temporally uncorrelated photons. The Poisson distribution (Fig. 2.11(a)) gives the probability of detecting n photons within a given time interval as

$$P(n) = \frac{\bar{n}^n}{n!} e^{-\bar{n}}, \quad (2.2)$$

where \bar{n} denotes the average number of photons. A specific feature of this distribution is its standard deviation Δn around the mean value \bar{n} :

$$\Delta n = \sqrt{\bar{n}} \iff \text{Poissonian}. \quad (2.3)$$

This means that for a coherent light beam, the relative amount of photon number fluctuations decreases with increasing intensity (i.e. with larger \bar{n}). A photon stream with Poissonian characteristics can be approximately produced by a single mode laser. Partially coherent and thermal light emitters such as candles or a gas discharge lamps are characterized by an unstable intensity that originates from photon number fluctuations. These occur on a time scale determined by the coherence time τ_0 . The associated photon number distribution is broader than for Poissonian light (see comparison in Fig. 2.11(a)), thus $\Delta n > \sqrt{\bar{n}}$, which is why such light sources are classified as Super-Poissonian. In this case, the photons have the tendency to form bunches. This implies that when a photon is detected at $t = 0$, the probability of detecting another one immediately afterwards is higher than at long delay times. Bunched light is thus equivalent to the condition $g^{(2)}(\tau = 0) > 1$ (see Fig. 2.11(c)).

In fact, the observation of light with Poissonian and super-Poissonian characteristics can be explained by considering purely classical electromagnetic waves, without taking the quantum nature of light into account. The outcome of the HBT experiment is then interpreted in terms of classical intensity fluctuations. However, it is not possible to conceive any situation where $g^{(2)}(\tau = 0) < 1$ from a classical perspective. Nevertheless, it is experimentally well established that the emission from individual atoms, molecules and QDs exhibit the property $g^{(2)}(\tau = 0) < 1$, which is a quantum effect known as antibunching. This can be understood by considering a

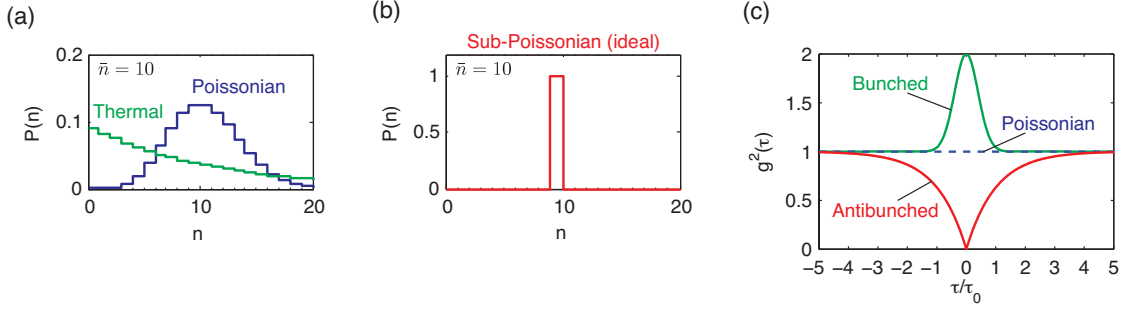


Figure 2.11: (a) Photon number distribution for a Poissonian and a thermal light source, illustrated for $\bar{n} = 10$. (b) Photon number distribution for light with ideal sub-Poissonian characteristics. (c) Second-order correlation function $g^{(2)}(\tau)$ for Poissonian, bunched and antibunched light. The time axis is normalized by the characteristic time period τ_0 of the emitting species (i.e. coherence time or lifetime).

single atom (or QD) that is continuously excited by a laser: once the atom is de-excited by spontaneously releasing a photon, it will take a certain amount of time before the atom can be re-excited again to emit the next photon. The rate at which this excitation-emission cycle takes place is mainly determined by the radiative lifetime of the atomic transition. Therefore, the radiation originating from the atom will consist of a stream of single photons with approximately regular time intervals between them, and the probability two simultaneous photon detection events is zero. This is why $g^{(2)}(\tau = 0) = 0$ for an ideal single photon source, and its photon number distribution is distinguished by a standard deviation of zero (Fig. 1.7(b) and (c)). In literature, the case where $\Delta n < \sqrt{\bar{n}}$ and $g^{(2)}(\tau = 0) < 1$ is usually referred to as antibunched or sub-Poissonian light.

2.4 Chapter summary

In this chapter, we summarized the patterning and growth procedures for fabricating arrays of site-controlled pyramidal QDs. We explained the MOVPE growth in pyramidal recesses and the mechanisms leading to deterministic QD formation. The different fabrication tools that were used in the fabrication process were briefly described. Finally, the principles of PL and photon correlation measurements were explained.

3 Integration of site-controlled quantum dots into photonic crystal cavities

In order to realize targeted experiments in cavity quantum electrodynamics, it is necessary to fulfill the stringent requirements for spatial, spectral and polarization matching between the quantum emitters and the cavity. The majority of research groups that currently conduct research on QDs in cavities employ randomly distributed self-assembled SKQDs for their experiments, which poses several problems. Although there has been remarkable progress in making site-controlled SKQDs, none of these approaches are currently technically mature enough to implement a large-scale integration of devices on a single substrate and to obtain cavities with two or more coupled QDs.

In 2008, Gallo *et al.* reported the first successful attempt to integrate a single site-controlled pyramidal QD made of InGaAs/GaAs within a PhC nanocavity, which paved the way for establishing a well-controlled and scalable platform for experiments [43]. This served as a starting point for the present thesis, in the course of which we were able to achieve the large-scale and deterministic integration of single QDs and pairs of QDs into PhC nanocavities. In this chapter, we report how we combined pyramidal QDs with the 2D PhC platform to obtain $L3$ -type nanocavities containing single and pairs of QDs. We describe how our method is able to guarantee high yield of effectively coupled QD-PhC structures on a single substrate. This chapter begins with a review of currently existing fabrication technologies for integrating QDs into cavity structures.

3.1 State of the art

From a technological point of view, the realization of QD-cavity systems is a highly challenging task. The majority of research groups in the field of solid-state cavity QED utilize self-assembled In(Ga)As SKQDs, which were described in Sec. 1.2.3. These grow at random sites on (001)-oriented GaAs substrates (Fig. 3.1(a)) and exhibit an

Chapter 3. Integration of site-controlled quantum dots into photonic crystal cavities

inhomogeneous broadening of typically 30-50 meV (Fig. 3.1(b)). SKQDs emit strongly linearly polarized photons due to the in-plane asymmetry of their geometric shapes, which has to be taken into account in designing microcavities in order to avoid a polarization mismatch between the resonant optical modes and the QD emission [31]. A common practice for obtaining a single QD that spectrally and spatially coincides with a cavity mode is to fabricate a large number of cavity structures in an area of the substrate where the QD density is low ($\sim 0 - 100$ QDs per μm^2) [71, 113, 114, 148, 149]. These cavities are then sequentially characterized in lengthy PL measurements, with the hope of finding a structure that shows signatures of coupling between a single QD and the cavity mode. It is evident that this procedure is as cumbersome as searching for a needle in a haystack; the results from such experiments are indeed ambiguous because the exact location of the presumed single QD inside the cavity is not known and the presence of "parasitic" QDs in the vicinity cannot be excluded.

More sophisticated approaches rely on the active positioning of the cavity structures around pre-selected QDs [110, 116, 151, 152]. Here the precise locations of isolated QDs are determined prior to fabricating the cavities, by performing either SEM [110], AFM [116, 151] or micro-PL scans [152] in order to obtain the coordinates of the QDs with respect to alignment marks on the substrate. The cavity structures are subsequently defined around these target QDs (see example in Fig. 3.1(c)). Owing to these techniques, it was possible to achieve an average positioning accuracy of 30 nm [110, 116, 151] or even below 10 nm [152], while maintaining sharp excitonic transitions and high Q factors. In fact, it was demonstrated that such active positioning methods allowed to drastically increase the likelihood for reaching the strong coupling regime, which was an important step forward in the fabrication technology of QD-cavity devices. However, the major obstacle that remained was the infeasibility to target any experimental design involving more than a single QD at desired locations within a cavity. Apart from that, the spectral matching between an actively positioned QD and a cavity mode is still difficult to realize because of fabrication imperfections.

To avoid the complications arising from the randomness of the QD positions and to facilitate scalable implementations into cavity devices, efforts were undertaken to control the nucleation points of the QDs. One of the site-controlled methods that was developed in this endeavor consists in using (1 0 0) GaAs substrates patterned with shallow nanoholes as growth templates for MBE [33–36]. The strain-induced nucleation of the QDs then only occurs at the locations of the nanoholes with near certainty and is suppressed elsewhere (Fig. 3.1(d), left). As far as the accuracy is concerned in terms of the placement of the QD at their target positions, the average alignment precision amounts to 50 nm [33, 34]. This is sufficient for the deterministic positioning of single QDs within micropillar (see Fig. 3.1(d), right) and PhC cavities,

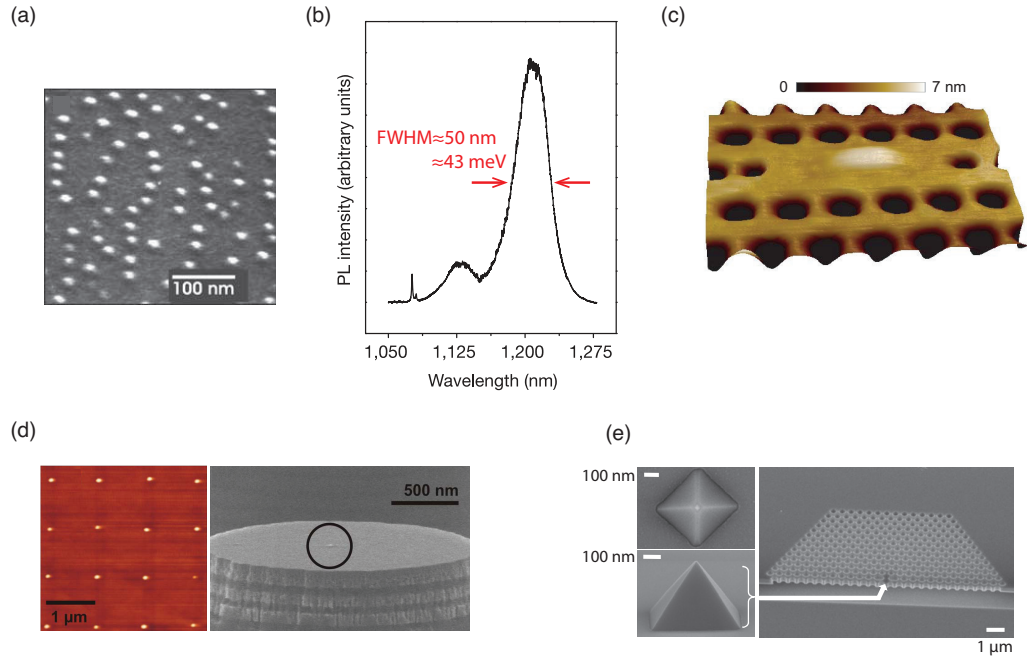


Figure 3.1: (a) SEM picture of self-assembled InGaAs/GaAs SKQDs that are customarily used for cavity QED purposes. Reprinted by permission from Macmillan Publishers Ltd: [Nature](#) [113]. Copyright 2004. (b) PL spectrum at high excitation power of an ensemble of InAs/GaAs SKQDs. Reprinted by permission from Macmillan Publishers Ltd: [Nature](#) [28]. Copyright 2004. (c) AFM image of a single SKQD that was placed at the center of a PhC cavity using an active positioning technique (see text). Reprinted by permission from Macmillan Publishers Ltd: [Nature](#) [116]. Copyright 2007. (d) Left: AFM micrograph of site-controlled SKQDs obtained by performing MBE growth on an array of predefined nanoholes. Right: SEM image of the lower half of a micropillar cavity, showing a site-controlled SKQDs aligned at its center. Reprinted with permission from [35]. Copyright 2009, AIP Publishing LLC. (e) Left: SEM pictures of a site-controlled InP pyramid, at the apex of which a single InAs QD nucleates. Right: Oblique view on a single-defect PhC cavity. Reproduced from [150]. Copyright 2010 by the American Physical Society.

as it was successfully demonstrated [35, 36]. However, the major issue that is yet to be solved is the large inhomogeneous broadening of these QDs, which is comparable to that of randomly grown QDs [36]. Aside from that, further optimizations are needed to improve the poor optical quality of these QDs.

Another promising technology employs position-controlled nanopillars defined on (001) InP substrates as templates for selective-area epitaxy of InAs/InP QDs at pre-determined locations [153, 154]. The positions of the upright-standing, square-based nanopillars are defined through a combination of EBL and wet etching. Provided that a pyramid is sufficiently small, only a single QD would nucleate at its

Chapter 3. Integration of site-controlled quantum dots into photonic crystal cavities

apex during the chemical beam epitaxy process [153]. The typical exciton linewidths for such InAs/InP QDs amounts 50 μeV and the optical transitions are centered at around 850 meV, which is close to the telecom wavelength of 1.55 μm . Recently, the successful integration of these QDs within single-defect PhC cavities was reported (see SEM images shown in Fig. 3.1(e)), and observations of Purcell enhancement were shown [150]. The precision of alignment between the QDs and the PhC cavities noted in the latter article amounted to 50 nm.

Despite the progress achieved in controlling the QD nucleation sites, it has so far not been feasible to yield coupled QD-cavity systems involving two or more QDs in a targeted fashion. The still unresolved problem in all of the methods mentioned above is the vanishingly small probability of finding QDs that coincide spectrally. Another drawback of SKQDs and site-controlled versions thereof is the presence of the 2D WL, which introduces complex multi-excitonic effects that screen the two-level system behavior of the QD states (described in Sec. 4.1).

3.2 Combining site-controlled pyramidal quantum dots with photonic crystals

3.2.1 Design of our experiments

Our choice of using planar PhCs as a platform for designing cavities was based on their versatility and our previously gained knowledge from integrating quantum wires and QDs into PhC cavities [43, 155]. Central to our experiments was the three-hole defect *L3* cavity in a triangular lattice PhC [156], which has been used in many studies of QD-cavity coupling. Most prominently, strong coupling effects have been reported from studies of single QDs integrated in *L3* cavities, where the achieved *Q* factors ranged from ~ 10000 to ~ 30000 [28, 71, 116, 148, 149].

The main advantages of the *L3* cavity design are its superior quality factor *Q* and its simultaneously ultrasmall mode volume *V*. The *Q/V*-ratio is the most important figure of merit for implementing QD-cavity structures and should be as large as possible, since the *Q*-factor is proportional to the photon confinement time and because the coupling strength *g* of the QD-cavity interaction scales with $V^{-1/2}$. The *L3* structure confines light to a volume of $V \sim (\lambda/n)^3 < 0.1 \mu\text{m}^3$ [28], where *n* is the effective refractive index and λ is the vacuum wavelength of the resonant cavity mode.

The basic semiconductor material that we used for producing suspended PhC membranes were 2 inch wafers that contained a GaAs/AlGaAs/GaAs heterostructure

3.2. Combining site-controlled pyramidal quantum dots with photonic crystals

grown by MBE. These "membrane substrates" were provided to us by Dr. Giorgio Biasiol from the TASC laboratory in Trieste (Italy) [157]. Fig. 3.2(a) shows an example image of the surface of a membrane substrate, which is characterized by a roughness of 2 nm here. As illustrated in Fig. 3.2(b), the top GaAs layer is 265 nm thick and is separated from the blank (1 1 1)B-oriented GaAs substrate by a 1 μm spacer of AlGaAs. The AlGaAs layer is later selectively removed underneath the PhCs in the final step of the fabrication process (Fig. 3.2(c)).

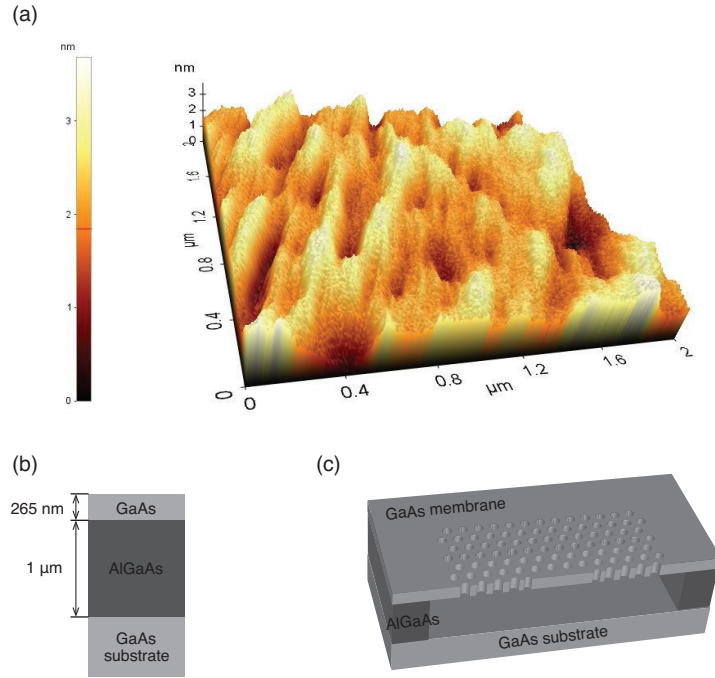


Figure 3.2: (a) AFM image of the surface of a membrane substrate. (b) Layer structure of the basic semiconductor material. (c) Schematic cross-section through a suspended PhC.

To model the PhC cavity structures, we performed both 3D FDTD simulations and 2D finite-difference calculations [142]. The pattern of the total electric field inside an $L3$ cavity is shown in Fig. 3.3(a). The parameters of this particular PhC structure were $r = 0.3 \cdot a$ for the hole diameters and $d = 1.325 \cdot a$ for the slab thickness, with a being the PhC lattice constant. Since the membrane thickness was fixed at $d = 265$ nm, the corresponding real values of the remaining parameters were $a = 200$ nm and $r = 60$ nm. To optimize the Q factor, the holes at either end of the cavity were laterally shifted outwards by $0.15 \cdot a$ and shrunk by 15% [156, 158, 159]. According to our FDTD calculations, the Q factor for such an optimized $L3$ cavity is ~ 30000 , which is lower than values reported in literature because of the relatively large membrane thickness in the present case.

Chapter 3. Integration of site-controlled quantum dots into photonic crystal cavities

From inspection of Fig. 3.3(a), one can see that the stationary electromagnetic field has 3 pronounced maxima inside the cavity, with the central peak being the highest. These 3 peaks are separated from each other by $0.875 \cdot a$, which translates to roughly one fifth of the resonance wavelength or ~ 175 nm for $a = 200$ nm. Therefore it is apparent that the targeted placement of QDs inside an $L3$ cavity requires nanometer accuracy in order to achieve sufficient overlap with either of the field maxima. To illustrate these stringent requirements for spatial alignment, we plotted the cross-sections of the cavity field along the dashed lines labeled A , B and C in Fig. 3.3(b). There one can see more clearly that the field strength varies sensitively as a function of position, and that a QD alignment accuracy of better than 50 nm is needed to achieve an overlap greater than 50 % of the field maximum. A misalignment larger than 50 nm could result in placing a QD at a field node or completely off its targeted position inside the cavity.

An important feature to notice about the 3 maxima of the cavity mode field distribution is that they coincide with the maxima of the E_y field component (see Fig. 3.3(c)). Simultaneously, the E_x field component exhibits nodes at those locations (Fig. 3.3(d)). Therefore one can expect an efficient coupling of the y -polarized emission from a QD that is positioned at a field maximum, while x -polarized emission should be suppressed.

In principle, each of the 3 cavity field maxima is well suited for placing a QD at its respective position. For a single QD experiment, it is of course favorable to target for the strongest field maximum at the cavity center. To integrate a pair of QDs inside the cavity, it is reasonable to place one QD at each secondary field maximum such as to ensure equal coupling strengths for both QDs. However, in reality the presence of disorder in fabricated PhCs may cause the field distribution to become more localized towards one side of the $L3$ cavity, which will inevitably lead to slightly different coupling strengths. One could basically also place 3 QDs inside an $L3$ cavity, one at each field maximum, but in the case of our samples we could not accommodate more than 2 pyramidal QDs due to the spatial restriction given by the PhC membrane thickness.

3.2.2 Meeting the spatial and spectral matching requirements

The 265 nm thickness of our PhC membranes was specifically chosen to accommodate the InGaAs/GaAs pyramidal QDs, for which the pyramid base length was $L_b = 300$ nm (height ≈ 245 nm). The MOVPE growth parameters had been adjusted specifically for pyramid arrays with a pitch of 400 nm, and the lower GaAs buffer thickness was adapted such as to ensure the vertical positioning (i.e. in the growth direction) of the

3.2. Combining site-controlled pyramidal quantum dots with photonic crystals

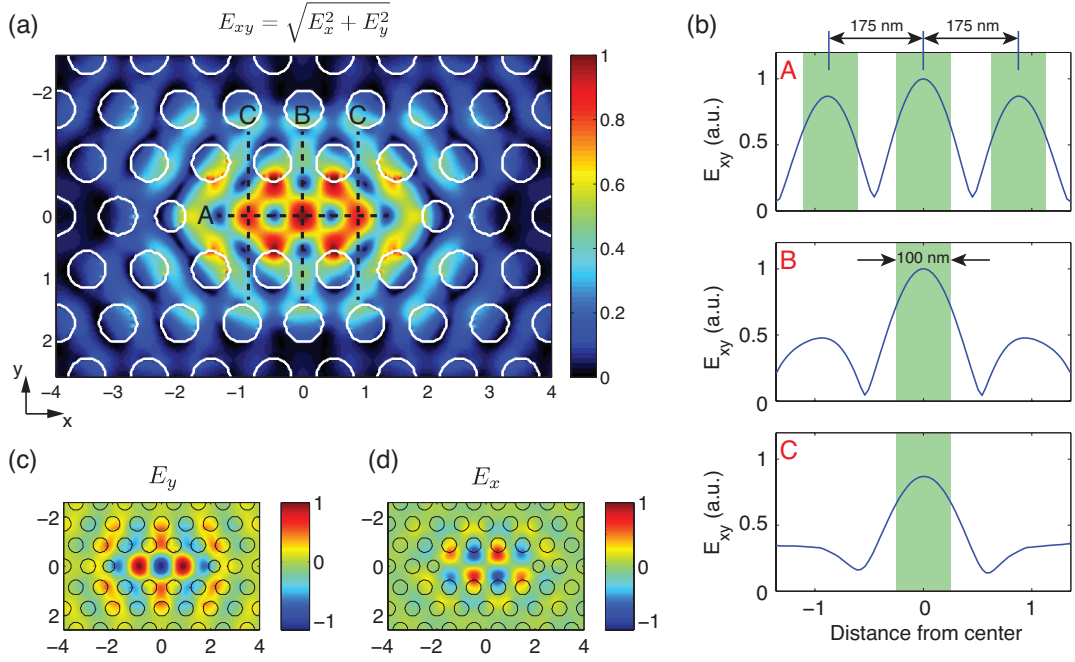


Figure 3.3: Calculation of the electric field distribution of the fundamental cavity mode at the center of the membrane. The spatial distances in the presented calculations have been normalized by the PhC lattice constant a . (a) Modulus of the total electric field $E_{xy} = \sqrt{E_x^2 + E_y^2}$. The field values were normalized with respect to the central field maximum. (b) Cross-sections of E_{xy} along the dashed black lines shown in (a), labeled A, B and C, respectively. The ranges highlighted in green illustrate the spatial overlap achieved with a QD alignment accuracy of ± 50 nm for $a = 200$ nm. (c) and (d): Electric field components E_x and E_y of the fundamental cavity mode.

QDs to coincide with the center of the PhC membrane. To integrate a single pyramidal QD at the center of a PhC cavity as targeted by the design shown in Fig. 3.4(a), we employed an approach that is based on isolating the target QD out of a QD array as illustrated in Fig. 3.4(b) and (c). Once the QD growth was performed in the pyramid array seen in Fig. 3.4(b), an $L3$ PhC structure with a lattice parameter $a = 200$ nm was lithographically defined on top of the buried QDs (Fig. 3.4(c)). In the following PhC etching step, all QDs except for the one in the cavity center were eliminated. The same approach was applied to incorporate a pair of QDs into an $L3$ PhC cavity, as depicted in Fig. 3.4(d)-(e). Here the QDs were intended to be positioned at the secondary maxima of the intracavity field (see Fig. 3.3(a)).

One of the greatest challenges in the process of developing the fabrication technology for our QD-PhC structures was to make sure that the PhCs were aligned with the QD pattern. For this purpose, we made use of mutual alignment marks to

Chapter 3. Integration of site-controlled quantum dots into photonic crystal cavities

lithographically define both the pyramid patterns and the PhCs in EBL. The details about our fabrication method will be explained further below.

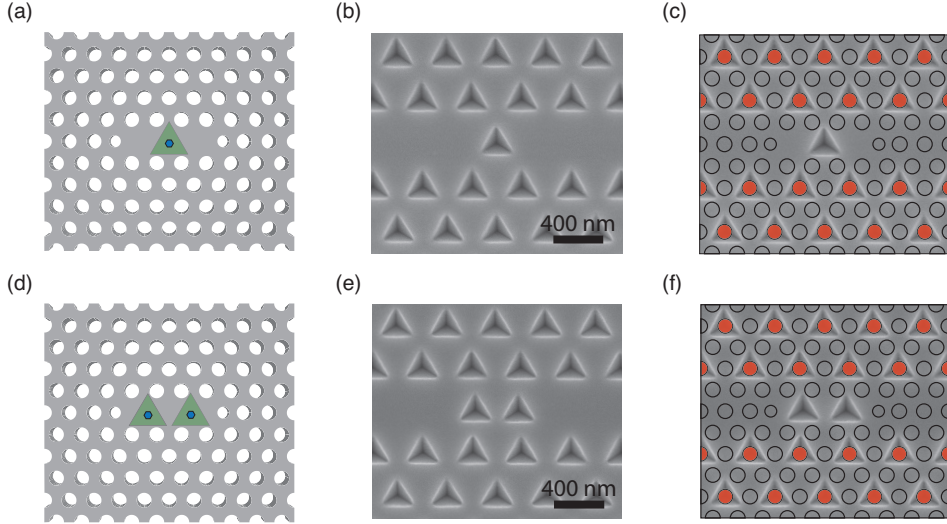


Figure 3.4: (a) Sketch of the design for coupling a single QD to an $L3$ PhC cavity. (b) SEM image of an array of etched pyramids that was used as a template for QD growth. (c) Subsequent to MOVPE growth, the PhC pattern is overlayed with the QD pattern as illustrated here. All QDs situated below the holes highlighted here in red are eliminated in the PhC etching process, thus yielding an isolated single QD at the cavity center as intended in the design. (d)-(e) Equivalent to (a)-(c), but with a pair of QDs.

Our motivation for using pyramid arrays instead of isolated pyramids for the integration into PhCs was to take advantage of the excellent optical properties of pyramidal QDs that can only be obtained with array patterns. In fact, it is technically difficult to fabricate a QD in an isolated single pyramid that is only surrounded by the $(1\ 1\ 1)B$ surface plane, because in that case a large number of metalorganic precursors migrate from the $(111)B$ surface towards the $1\ 1\ 1A$ facets of the pyramid and the growth rate becomes excessively high. One way to circumvent this problem would be to utilize a pyramid pattern that consists of a large dense array (size $\approx 300 \times 300\ \mu\text{m}^2$) with an empty area of $\sim 10^2 - 10^3\ \mu\text{m}^2$ size at its center [124]. Here the empty region provides the space to define single isolated pyramids. Using such a modified pattern for MOVPE growth allows for obtaining isolated QDs, which can in principle be integrated into PhC cavities. However, the quality of such QDs might not be as good as individual QDs from dense QD arrays, which are characterized by a remarkably high uniformity with a typical inhomogeneous broadening of $\sim 10\ \text{meV}$ and by sharp ground state transitions with linewidths around $100\ \mu\text{eV}$ [40]. This is why we eventually adopted a technique where the auxiliary QDs are removed from the array in the PhC etching process.

3.2. Combining site-controlled pyramidal quantum dots with photonic crystals

A good uniformity of the QDs is of great importance to conform to the spectral matching requirement for realizing coupling. This is because the spectral separation between a QD and the cavity should not be larger than 5 meV in order to ensure either direct coupling or dephasing-assisted coupling (see next chapter). To estimate the probability for fulfilling this spectral matching condition, we assume that the QD exciton transition energy is normally distributed around a certain mean value with a full-width at half maximum (FWHM) of 10 meV, corresponding to the typical inhomogeneous distribution attainable with a pyramid array pattern¹. If it were possible to deterministically fabricate a PhC cavity that has a resonance exactly centered at the mean QD energy, then there would be a $\sim 76\%$ chance that an individual QD would lie within the ± 5 meV coupling interval.

However, in reality there are statistical variations in the spectral position of the cavity resonance for nominally equal PhCs due to fabrication imperfections, which resulted in an uncertainty in the resonance position equivalent to ~ 10 meV width around a center mean value in our experiments. Thus we have to consider the conditional probability of having both the QD transition and the cavity resonance within a 2.5 meV interval around a target value, in order to ensure that the maximum QD-cavity detuning does not exceed 5 meV as given by the spectral matching condition. Using the multiplication rule of probability theory, we estimate this probability as $\sim 20\%$. However, this yield would only be attainable in the case where one could produce PhCs with a resonance energy that is distributed around the exact same value as the central energy of the QD emission pattern. Such a precision cannot be implemented due to the insufficient control over the effective PhC hole sizes. Our workaround for this issue was to fabricate several series of PhCs with different nominal hole sizes on the same substrate, such that ideally at least one of the series would spectrally coincide with the central QD emission energy.

The spectral matching condition is even more challenging to fulfill for a QD pair, because in that case both QDs must simultaneously be close enough in energy to the cavity resonance. These considerations lead us to the conclusion that in order to obtain a sample which contains a sufficient number of useful structures (i.e. showing signatures of coupling) for conducting systematic studies, it is necessary to produce a large number of well-aligned QD-PhC structures on a single substrate.

¹It should be noted at this point that we are ignoring the existence of other QD states such as the biexciton or charged excitons in the present considerations, which actually add to the probability of realizing an overlap with the cavity mode.

3.2.3 Growth optimization

The membrane substrates are more expensive to produce than comparable GaAs substrates and were therefore used only after careful calibrations of all fabrication steps were carried out. We thus first optimized all processing steps (RIE, ICP, pyramid etching, etc.) and MOVPE growth on regular (1 1 1)B GaAs substrates. Regarding growth, the goal was to achieve QD ensembles with narrow spectral distributions and sharp excitonic features. To this end, we prepared "dummy" substrates consisting of the target pyramid patterns on regular (1 1 1)B GaAs, prior to using membrane substrates.

We performed a series of growth iterations with dummy substrates before converging to the optimum growth conditions and parameters. The optimum growth sequence begins with a thermal deoxidation of the substrate at 570° C, followed by the deposition of a GaAs layer with nominal thickness² 1.3 nm during which the temperature is gradually ramped up from 570° C to 590° C. The temperature ramp ensures that the material deposited within the pyramids retains a self-limited profile [126]. Afterwards the temperature is left constant at 590° C during the rest of the growth process, and a GaAs/InGaAs/GaAs layer structure with 3 nm, 0.2 nm, 2.5 nm respective (nominal) thicknesses is deposited.

After each MOVPE growth iteration, the respective dummy sample was characterized with PL spectroscopy to check the center wavelength of the QD ensemble emission and to assess the quality of the QDs, which is essentially represented by the inhomogeneous broadening (=width of the Gaussian-shaped spectral distribution) and the linewidths of individual excitonic features within the spectra. An example PL spectrum of a QD ensemble grown on a dummy substrate is displayed in Fig. 3.5(a). It should be noted that this spectrum is composed of different excitonic features (i.e. mainly the neutral exciton, biexciton, negatively charged exciton) from different QDs. The inhomogeneous broadening of 16 meV therefore does not reflect the fluctuations of only the exciton energy, but of the different excitonic species combined. By zooming into the ensemble spectrum (see Fig. 3.5(b)), one can see that the individual excitonic transitions have linewidths close to the resolution limit of the used spectrometer ($RL \approx 80 \mu\text{eV}$).

The exact same processing steps and growth parameters that were applied for dummy substrates were later used for the membrane substrates. Fig. 3.5(c)) shows the PL spectrum a QD ensemble that was grown on a membrane substrate. The inhomogeneous broadening amounted to 12 meV in this case, and the excitonic

²"Nominal thickness" to reference thickness values that were obtained by growing planar layers on GaAs (1 0 0) substrates.

3.2. Combining site-controlled pyramidal quantum dots with photonic crystals

lines (see enlarged view in Fig. 3.5(d)) were as sharp as observed on dummy samples. This demonstrates that the whole QD fabrication procedure could be transferred from dummy substrates to membrane substrates without problems or any need for adaptation.

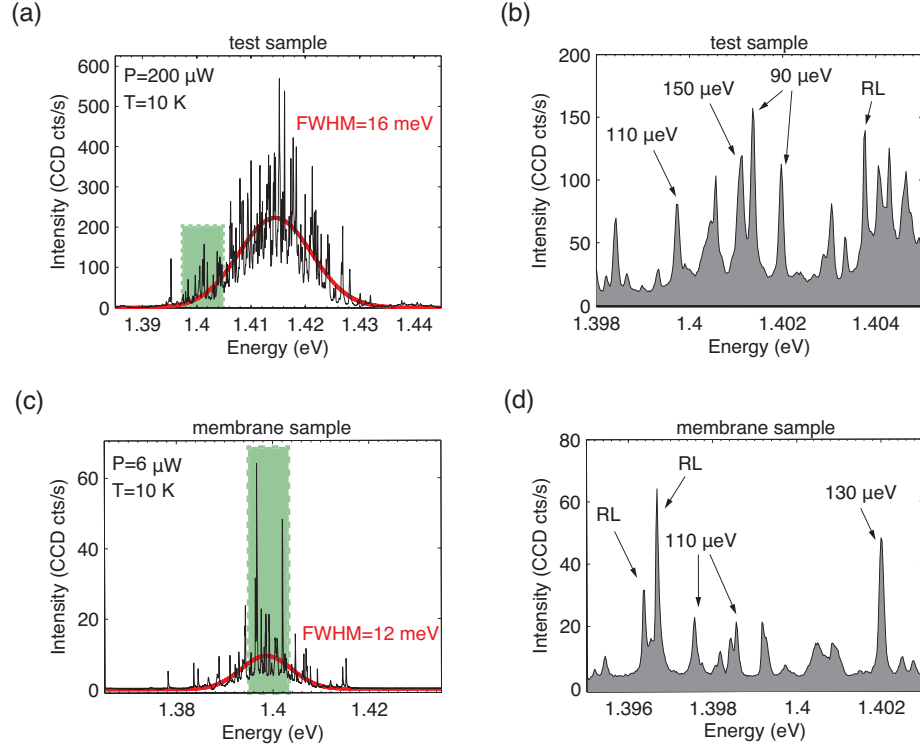


Figure 3.5: (a) PL spectrum measured from an ensemble of InGaAs/GaAs pyramidal QDs grown on a (1 1 1)B GaAs "dummy" substrate. The box highlighted in green is shown in magnified view in (b), where the linewidths of representative excitonic peaks are denoted. "RL" stands for resolution-limited. (c) and (d) show the QD ensemble emission measured from equivalent QD patterns grown on a (1 1 1)B GaAs membrane substrate. Note that the excitation power in (c) was more than 10 times lower than in (a), such that less excitonic species contributed to the overall emission.

3.2.4 Description of the fabrication procedure

We designed the layout of our integrated QD-PhC devices on a full 2" wafer scale, as schematically shown in Fig. 3.6(a). The wafer is subdivided into 12 pieces that are later separated from each other through cleaving during the fabrication process. Each piece constitutes an individual growth substrate and contains a set of square-shaped alignment marks together with a $2.5 \times 4.5 \text{ mm}^2$ -sized area that consists of a few dozen of separate zones. An example of such a zone is shown in Fig. 3.6(b).

Chapter 3. Integration of site-controlled quantum dots into photonic crystal cavities

The checkerboard pattern that one can see there is made up of 120 PhCs that each have a size of $12 \times 12 \mu\text{m}^2$ and contain an $L3$ -type defect cavity at the center. What is not visible in the image is that the whole central area of the zone is covered with a $300 \times 300 \mu\text{m}^2$ array of pyramids that have a base length of $\sim 300 \text{ nm}$ and are positioned on a triangular array with a pitch of 400 nm . Isolated single QDs and pairs of QDs are obtained from the QD arrays through the selective elimination of the sacrificial QD, as shown previously in Fig. 3.4. Each zone is framed by a set of larger pyramids (Fig. 3.6(c)) that serve as auxiliary structures for determining the mutual alignment accuracy between the pyramid array and the PhC patterns within the zone.

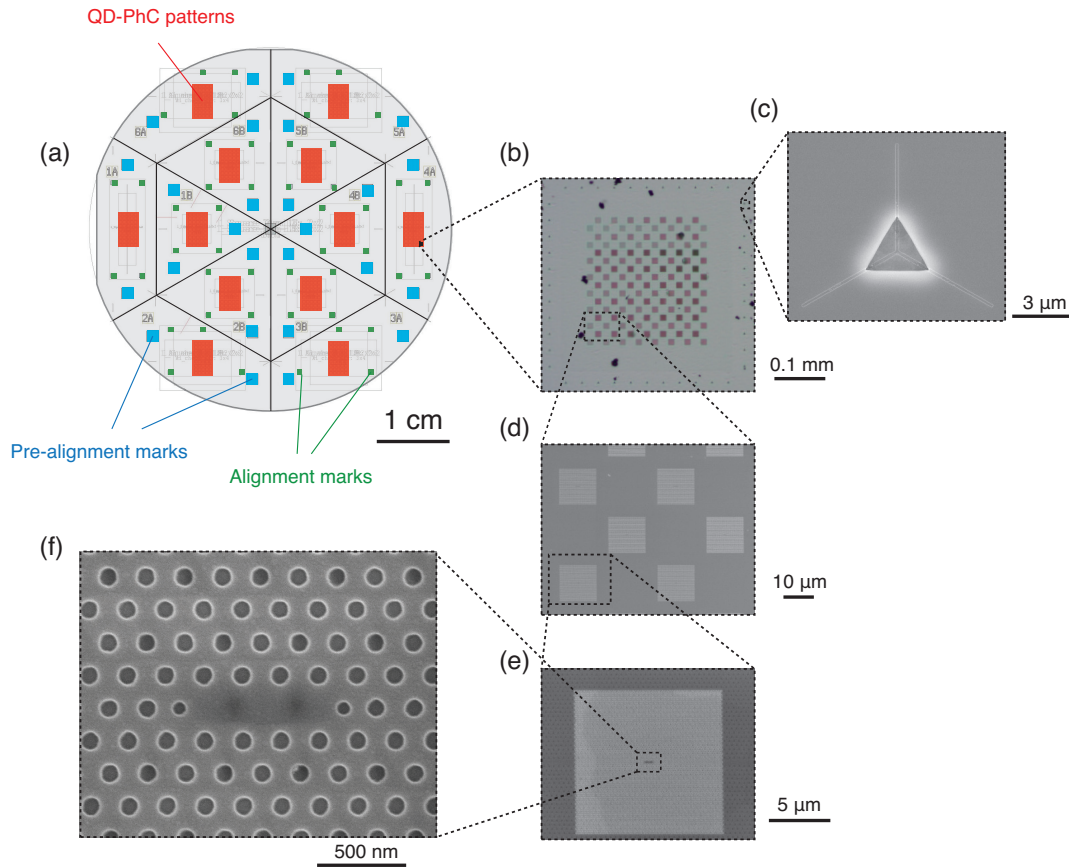


Figure 3.6: (a) Full wafer design for fabricating integrated QD-PhC structures. The 2" wafer is cleaved into 12 smaller pieces (delimited by black lines here) during the fabrication process. The (pre-)alignment marks (green and blue squares) are used as references in the EBL step to accurately position the QD-PhC patterns (red rectangles). (b) Optical microscope image of a single zone, showing the finalized structures. This zone contains a $300 \times 300 \mu\text{m}^2$ large array of pyramidal QDs, at the center of which the PhCs have been arranged in a checkerboard pattern. (c) Structure for alignment verification. (d)-(f): SEM images of $L3$ PhC patterns with increasing magnification. In (f), the two shaded spots inside the cavity indicate the positions of the pyramids buried below the surface.

3.2. Combining site-controlled pyramidal quantum dots with photonic crystals

The 120 PhCs of a single zone are grouped into series of 15 PhCs (2 consecutive rows from the checkerboard) where the nominal hole radius is varied in steps of 1 nm from one PhC to another. A single zone thus contains 8 such PhC series. Using our EBL-based positioning technique for both the QDs and the PhCs, we were able to achieve an alignment accuracy of 39 ± 15 nm averaged over all zones of a single substrate, which in total contained > 4000 integrated QD-PhC structures. The accuracy of the positioning was verified by SEM observations of the auxiliary pyramids (Fig. 3.6(c)) as well as of the integrated QD-PhC structures themselves (Fig. 3.6(f)).

Our fabrication scheme begins with a bare membrane-type wafer (see Fig. 3.2) that is processed with the following sequence of steps:

1. **Lithography and etching of the alignment marks:** The first step in the fabrication is to produce alignment marks that are later used as references by the EBL system during the writing of the pyramids and the PhCs. These marks are obtained through a combination of EBL and ICP etching, using PMMA resist and a SiO_2 mask. Each individual alignment mark is a $20 \times 20 \mu\text{m}^2$ square with $\sim 1 \mu\text{m}$ depth, and each substrate (i.e. $1/12$ th piece of the wafer) contains 4 areas with 4 alignment marks in each area. The 4 alignment mark areas are highlighted in green in Fig. 3.6(a).
2. **Lithography and etching of the pyramid patterns:** Here the pyramid patterns are lithographically defined within each zone. The pyramids are obtained via EBL and wet etching, as described in Sec. 2.1.1. To accurately place the pyramids at their target positions, the EBL system uses the previously defined alignment marks. The resulting positioning accuracy for a QD array relative to the alignment marks is ~ 25 nm. However, the offset of individual pyramids with respect to the gridpoints of the triangular array does not exceed 5 nm.

Note that prior to the wet etching step of the pyramidal recesses, the wafer is cleaved into 12 approximately equal-sized pieces (see in Fig. 3.6(a); cleaving lines are indicated in black). Each piece is then processed separately in the subsequent fabrication steps. The reason for cleaving the wafer into smaller pieces was to reduce the material waste that could incur due to faults in the subsequent fabrication steps.

3. **QD growth:** Once a single substrate has been patterned with exposed pyramids, it is introduced into the MOVPE reactor to grow the GaAs/InGaAs/GaAs layer structure that yields deterministic QD nucleation at the exact site of each pyramid. For details about the QD growth mechanisms, see Sec. 2.1.2. The substrate is intentionally not completely planarized such as to facilitate the

Chapter 3. Integration of site-controlled quantum dots into photonic crystal cavities

verification of the pyramid positions at the PhC fabrication stage by means of SEM observation.

4. **PL characterization of the QDs:** After MOVPE growth, the QDs are optically characterized in a micro-PL setup in order to assess their quality and their spectral emission distribution. A typical spectrum from a QD ensemble measured at this stage is shown in Fig. 3.7(a). As one can see there, the QD ensemble has a Gaussian-shaped spectrum that is centered in this case at ~ 1.40 eV and is characterized by a FWHM of 12 meV. However, the center of this emission distribution can vary from one zone to another by a few meV due to differences in the average pyramid size and also due to inhomogeneities related to the MOVPE growth process.
5. **Adapting the design of the PhCs for spectral matching:** The layout and the parameters of the PhC patterns are defined in a design file that is later used by the EBL system. Following the PL characterization of the QD ensembles, the range of hole sizes of the PhCs is adapted to match the cavity resonance energy to the spectral distribution of the QDs (Fig. 3.7(b))

The total energy range covered by the 15 PhCs of one series amounts to ~ 80 meV, large to ensure spectral overlap with the QDs. The minimum step size between two consecutive PhC hole radii values that we can attain with our EBL system is 1 nm (nominal), which corresponds to a step of roughly 5 meV in the cavity resonance energy. However, fabrication-related disorder introduces variations in the actual resonance energy for nominally equal PhCs, corresponding to deviations of approximately ~ 4 meV from the mean values (see next section).

6. **Lithography of the PhCs and alignment verification:** The substrate is then coated with SiO_2 and PMMA resist prior to performing the EBL of the PhC patterns. After the electron beam exposure and the subsequent PMMA development, we conduct SEM observations to check whether the PhCs are accurately aligned in each zone. Here we sample the alignment directly on the PhC structures (Fig. 3.6(f)) as well as on the auxiliary pyramids (Fig. 3.6(c)) of each zone. By examining Fig. 3.6(c) carefully, one can see 3 diagonal lines; these are written at the same time with the PhCs. Any offset between these lines and the auxiliary pyramid would indicate a misalignment between the PhCs and the pyramid ensembles.
7. **PhC pattern transfer:** The pattern transfer of the PhCs to the substrate is carried out in two steps. First, we apply RIE to imprint the PhC patterns through the PMMA into the SiO_2 mask. After PMMA removal, we use ICP to etch the PhC

3.2. Combining site-controlled pyramidal quantum dots with photonic crystals

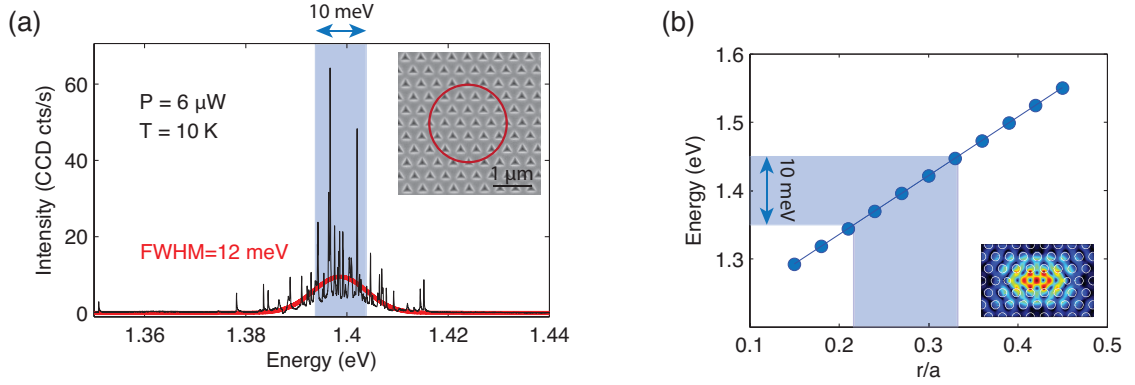


Figure 3.7: (a) Spectrum of a QD ensemble grown on a membrane substrate at low excitation power, where only neutral and charged excitonic species are excited. Inset: SEM image of a pyramid pattern. The red circle depicts the approximate size of the laser excitation spot. (b) Dispersion of the cavity mode resonance energy as a function of the normalized PhC hole size r/a , computed by 3D FDTD. The blue-shaded area indicates the range of radii that have to be implemented to cover a spectral range of 10 meV around 1.40 eV, which approximately corresponds to the QD emission spectrum.

holes ~ 300 nm deep into the substrate³.

To obtain PhC holes with straight vertical profiles by means of ICP, we utilize a BCl_3/N_2 gas mixture where the adjustment of the N_2 content allows to maintain good PhC hole verticality throughout the etching process [143]. We optimize the ICP etching step by means of a series of tests performed on GaAs dummy substrates as well as on membrane substrates, where we probe the profiles of the PhC holes via cleaving and cross-sectional SEM observations. Example images of PhC membrane cross-sections are shown in Fig. 3.8(a) and (b).

8. **Membrane release:** The final step in the fabrication process is the selective removal of the sacrificial AlGaAs below the PhCs, which is called "membrane release". Here we insert the substrate into a 4% $\text{HF} : \text{H}_2\text{O}$ solution that is pre-heated slightly above room temperature in order to avoid the building of cracks in the PhCs [142]. After the membrane release, we verify the quality of the result and the extent of the undercut in observations under the optical microscope (Fig. 3.8(c) and (d)).

The most time-consuming parts in the fabrication method described here are the test runs for optimizing the EBL, the MOVPE growth of the QDs, the ICP etching of the PhCs and the final alignment verification, respectively. Due to the complexity of

³More information about RIE and ICP is given in Sections 2.2.5 and 2.2.6.

Chapter 3. Integration of site-controlled quantum dots into photonic crystal cavities

the overall procedure, it is necessary to keep track of the different fabrication stages separately for each substrate in the form of detailed documentation. The flowchart in Fig. 3.9 summarizes the main steps of the whole fabrication process once again.

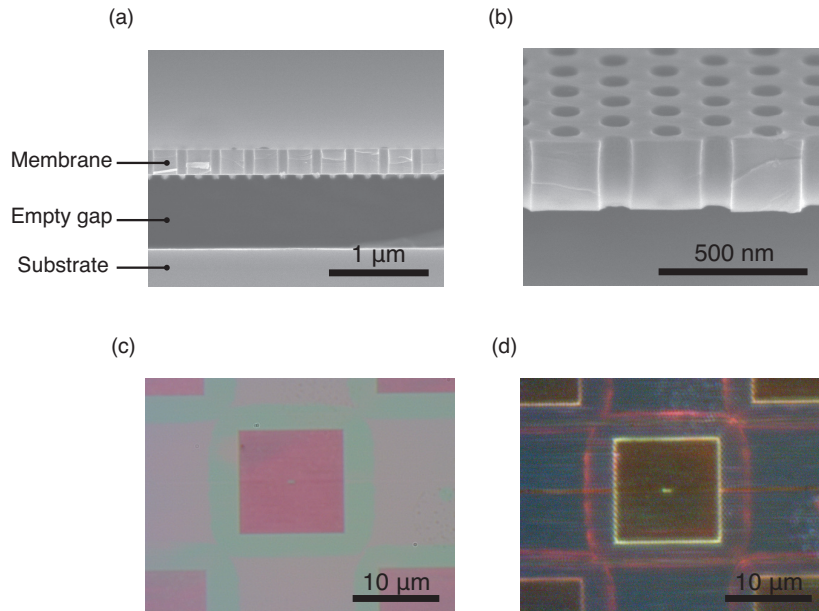


Figure 3.8: (a) Cross-section of a PhC membrane structure after releasing the sacrificial AlGaAs layer. (b) Tilted perspective of a released PhC membrane. (c) and (d): Bright and dark field optical images of a released QD-PhC structure. Notice that the $L3$ cavity is visible at the center of the PhC.

3.2. Combining site-controlled pyramidal quantum dots with photonic crystals

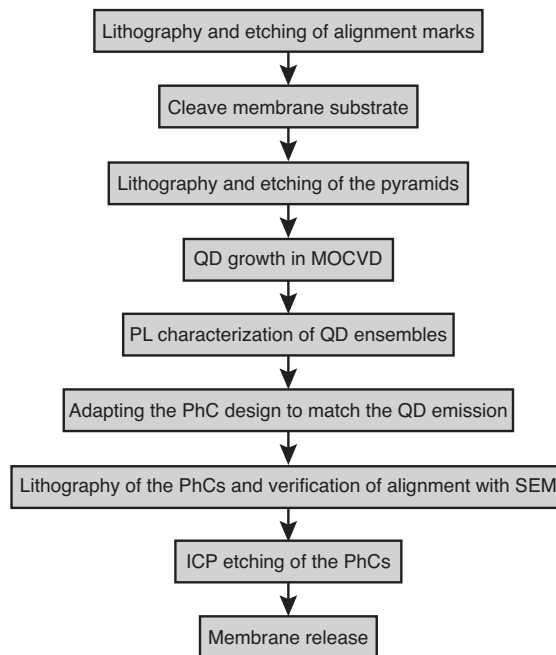


Figure 3.9: Flowchart of the essential fabrication steps for integrating pyramidal QDs into PhC structures.

3.2.5 Control over the cavity resonance position

The spectral position of the $L3$ cavity resonance can be controlled by varying the PhC hole sizes, which in turn are defined lithographically and are subject to fabrication-related non-uniformities. As mentioned in the previous section, our approach to ensuring a sufficient yield of coupled QD-cavity structures was to implement many repetitions of so-called "PhC series" on the same sample. Each series consisted of 15 PhCs placed side by side (as it can be seen in Fig. 3.6(b) and (c)), for which the nominal hole sizes were increased by 1 nm from one PhC to the next. Using 3D FDTD simulations with dispersion-corrected refractive index, we adapted the range of hole sizes in the PhC designs to match the cavity resonances with the central wavelength of the QD ensemble emission that we obtained from PL measurements. The adapted design was subsequently used in EBL to write the PhC patterns.

In order to examine the validity of our simulations and the accuracy by which the PhC designs had been transferred to the real sample, we spectroscopically measured the finalized QD-PhC structures at 10 K and determined the experimental cavity resonance positions. A comparison between experimental data and simulation results is displayed in Fig. 3.10(a). The simulation results (red diamonds) are plotted as a function of the expected PhC hole radius, i.e. after ICP etching. The experimental data were extracted from 2 different PhC series (green triangles and blue circles in the graph) that incorporated QD pairs in $L3$ cavities. Both PhC series are plotted as a function of the nominal PhC hole size in the graph.

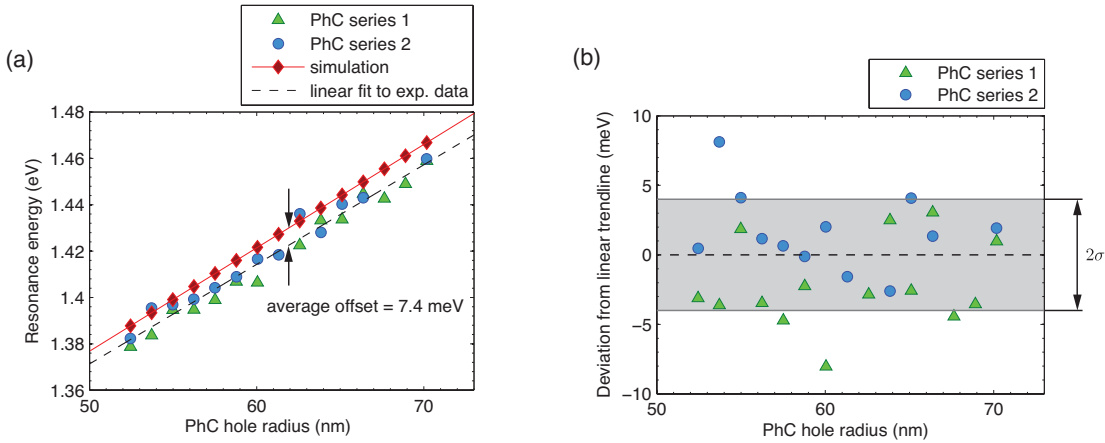


Figure 3.10: (a) Variation of the $L3$ cavity resonance energy as a function of the nominal PhC hole radius. The red diamonds correspond to simulation results from 3D FDTD, while the circles and triangles are experimental datapoints obtained from 2 equivalent series of $L3$ cavities which contained QD pairs. (b) Deviation of the experimental datapoints from their linear trendline. The standard deviation is $\sigma = 4.06$ meV.

3.2. Combining site-controlled pyramidal quantum dots with photonic crystals

As one can see, the experimental datapoints are in close agreement with the simulations. In addition, the comparison between PhC series 1 and 2 demonstrates that the r/a variation was well reproduced. The simulation predicted cavity resonances that are systematically shifted to higher energies (on average by ~ 7 meV) than in reality, which might be explained by PhC hole sizes that were effectively smaller than the targeted values. There are different factors that may have contributed to this offset, including PhC hole sizes that were effectively smaller from their design values and a deviation of the real refractive index from their numerical values used in our FDTD simulations. Indeed, SEM investigations showed that the PhC hole sizes were 10 nm smaller on the actual sample, which should induce a redshift in the cavity resonances. On the other hand, cross-sectional images of other membrane substrates revealed that the slab thickness was 10 to 20 nm smaller than the target value of 265 nm, which should lead to a blue-shift of the cavity resonances. It is therefore not straightforward to determine the cause of the systematic offset between the design values for the cavity resonances and the actual ones.

To quantify the fluctuations in the cavity resonance position due to fabrication-related disorder, we subtracted a linear trendline from the experimental datapoints in Fig. 3.10(a). The result is shown in Fig. 3.10(b). The calculation of the standard deviation gave 4.06 meV. This is an important figure of merit, which allowed us to estimate the cavity resonance positions in PL experiments in situations when the mode was not visible in the spectrum (such as in off-resonant $L3$ cavities with single QDs, see Chapter 4).

Another parameter to consider is the step in the cavity resonance energy that is induced by an increase of 1 nm in PhC hole radius, because this gives the resolution by which the QD spectra can be scanned through PhC hole size variation. By calculating the mean energy difference between consecutive PhCs, we obtained an energy step of 5.4 meV. This is almost equal to the simulation result, from which we obtained an average step size of 5.6 meV.

The results in Fig. 3.10 prove that our fabrication method allows to yield cavities that correspond well to their intended designs and that it is possible to systematically scan the cavity resonances through a wide energy range of ~ 80 meV, which validates our r/a tuning approach. On the other hand, it is also clear that one needs to introduce many copies of nominally equal PhC structures in order to account for the statistical fluctuations of the cavity resonance.

3.2.6 Optical properties of non-resonant single and pairs of quantum dots

In the context of cavity QED and quantum information processing, an ideal material for applications would consist of an ensemble of identical two-level systems [51, 160, 161]. However, in contrast to their atomic counterparts, QDs are in general never absolutely identical. There are variations in size, shape, material composition, strain and other factors that contribute to differences in the energy level structure of QDs, and therefore their emission spectra cannot be equal in every detail. In fact, one of the greatest challenges with currently existing QD fabrication approaches is to improve the spectral uniformity, which is particularly difficult with self-assembled QDs.

In this regard, the spectral uniformity and reproducibility of the pyramidal QDs evidenced in Fig. 3.11 demonstrates their great potential. The spectra shown there were measured for QDs that were embedded in non-resonant $L3$ PhC cavities. As it can be seen in Fig. 3.11(a) and (b), the single QDs are characterized by remarkable similarities in their optical response. The first striking feature is that the PL spectra consist of 3 distinct peaks. Excitation power dependence measurements and photon correlation spectroscopy allowed us to identify that the lowest-energy peak corresponds to the negatively charged exciton X^- , followed by the neutral exciton X at ~ 5 meV distance and the biexciton $2X$ [40] (Fig. 3.11(a),(b)). The X^- feature was present in almost all QDs that we measured, which can be ascribed to residual background doping in the material and consequent charging of the QDs by extra single electrons.

By conducting a statistical analysis on 83 pyramidal QDs, we found that the X^- binding energy was strikingly reproducible with a value of 4.9 ± 0.3 meV. Interestingly, the $2X$ binding energy varied from +1 meV to -4 meV, and we were able to establish that some of the QDs of our study exhibited spectrally coincident X and $2X$ features [40]. The average sublevel spacing between the s - and p -shells was 20 meV, and the linewidths of these excitonic features typically amounted ~ 100 μ eV, which is well represented by the example in Fig. 3.11(b).

Fig. 3.11(a) also illustrates the energy distribution of the QDs and the likelihood of finding two different QDs that are spectrally sufficiently close to each other such as to obtain a mutual coupling to a cavity mode. As we elaborated in Sec. 3.2.2, in that case the detunings between the individual QDs and the cavity resonance should not exceed 5 meV. Indeed, the example spectra in Fig. 3.11(a) demonstrate that this condition can indeed be fulfilled for a good fraction of the QDs.

The relevance of the great similarities between the QD spectra becomes apparent when we regard the example spectrum of a pair of pyramidal QDs in Fig. 3.11(c).

3.2. Combining site-controlled pyramidal quantum dots with photonic crystals

By comparing this spectrum to the characteristic optical "fingerprint" of a single pyramidal QD (Fig. 3.11(b)), one can already make a good guess about the identity of the excitonic features. In the particular case of Fig. 3.11(c), we carried out excitation power dependence and photon correlation measurements to identify the peaks.

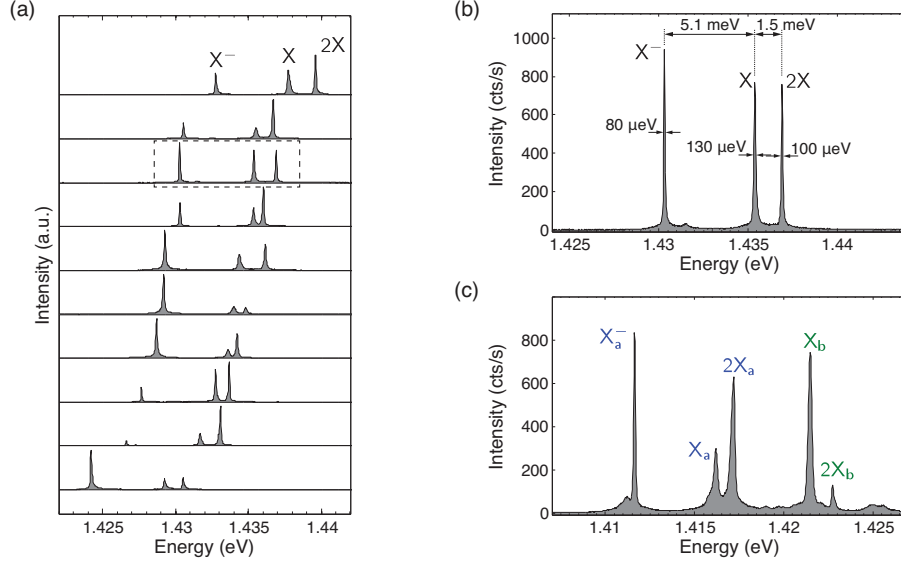


Figure 3.11: Example spectra of pyramidal QDs in non-resonant $L3$ PhC cavities, measured at 10 K. (a) Spectra of 10 different single QDs. (b) Enlarged view of the single QD spectrum highlighted in (a) with a dashed square. (c) Example spectrum of a pair of QDs. The indices a and b are used to distinguish the 2 QDs. Here the X_b^- feature was presumably overlapping with the $2X_a$.

It should be emphasized at this point that the similarities of the PL spectra in Fig. 3.11 and the knowledge about the respective excitonic transitions (i.e. the X^- , X and $2X$) are of great utility for the interpretation of experimental data measured from resonant QD-cavity structures. We will show in Chapter 4 that it is possible to investigate the Purcell effect for each excitonic feature separately in the case of a single pyramidal QD. In Chapter 5, we will rely on the knowledge obtained from our studies of non-resonant single QDs to demonstrate the mutual coupling of a QD pair to an $L3$ cavity.

3.2.7 Comparison with other fabrication approaches

To our knowledge, our method is currently the only one available that provides the possibility of large-scale integration of single and multiple QDs into PhCs with an average alignment accuracy of better than 50 nm. At the same time, no other existing

Chapter 3. Integration of site-controlled quantum dots into photonic crystal cavities

QD technology offers an inhomogeneous broadening as low as 10 meV and a similar reproducibility of the distinctive optical transitions as it is the case with pyramidal QDs. These are highly valuable features in view of realizing deterministic coupling between one or more QDs with the same cavity, and are indispensable for facilitating systematic studies on a set of equivalent devices. As we pointed out in our review in Sec. 3.1, the lack of scalability and the poor spectral control are major issues with current QD systems that have so far hindered further progress in the implementation of more advanced QD-cavity configurations. In view of this, pyramidal QDs validate the potential of solid state cavity QED for exploring scalable quantum information processing schemes [51, 160, 162].

However, there are two important issues with our fabrication technique that need to be improved. One of the problems encountered in the course of the present thesis is that the average Q factor of the $L3$ cavities was around 2000, which is on the one hand sufficient for studying the Purcell regime of cavity QED, but on the other hand not enough to reach strong coupling. In those cases where Vacuum Rabi splitting was observed for single SKQDs integrated in $L3$ cavities, the Q factors were greater than 10000 [28, 71, 116, 148, 149]. The other problem is spectral diffusion, which broadens the linewidths of the excitonic transitions in pyramidal QDs to typically $\sim 100 \mu\text{eV}$. We suspect carbon-related impurities incorporated in the material during the MOVPE growth process to be responsible for the presence of fluctuating charge traps near the pyramidal QDs [163]. In addition, the proximity of the QDs to the etched interfaces of the pyramidal recesses presumably adds a contribution to spectral diffusion due to surface states.

The origin of the rather low Q of our PhC nanocavities is most probably due to a combination of fabrication imperfections, intrinsic material absorption related to impurities and disorder-induced Urbach tails [164], and due to the large thickness of the membrane. To obtain high- Q cavities, the membrane thickness d has to be small because of its inverse correlation with the size of the photonic bandgap [165]. Currently the thickness of our PhC membranes is 265 nm, which corresponds to $1.325 \cdot a$. In comparison, in the case of $L3$ PhC cavities for which Q factors greater than 10000 were achieved in GaAs, the membrane thickness was $d = 0.9 \cdot a$ or less [28, 116, 149]. Therefore one way of increasing the Q factors of our PhC nanocavities would be to reduce d and thereby increase the bandgap. In order to accommodate the pyramids into a thinner membrane, their size has to be reduced below their current base length of $L_b = 300$ nm. With the latest successes in the fabrication and growth of QDs in pyramids with $L_b < 200$ nm by Surrente *et al.* and their integration into PhCs [42, 46], the development of our fabrication technology towards thinner-membrane PhCs appears to be promising route for improving the Q factors.

Another possibility for increasing the Q factor would be to redshift the operation wavelength of the QD-cavity devices, because material absorption is lower at longer wavelengths [164]. For this purpose, the QD growth parameters have to be modified and optimized in order to maintain their high-quality features.

3.3 Chapter summary

In this chapter, we described our newly developed method for integrating pyramidal QDs into PhC nanocavities in a deterministic and scalable fashion, which provided the foundation for conducting systematic studies of cavity QED effects on single and pairs of QDs in the course of this thesis. To our knowledge, there is no other fabrication approach that can yield QD-PhC structures with comparable site- and spectral control as reported here. This technological progress can be regarded as a significant step towards scalable quantum information processing schemes.

4 Coupling characteristics of single pyramidal quantum dots

The two most prominent phenomena of cavity QED are the Purcell-enhancement of spontaneous emission in the weak coupling regime and vacuum Rabi splitting in the strong coupling regime, which were both first observed with atoms [95–97]. It was later demonstrated that these effects could also be observed with QDs in microcavities [14, 113], which opened the path for exploring cavity QED in the solid state. However, a series of studies with single SKQDs – which are used by the large majority of research groups - revealed peculiar effects that were contradictory with the artificial atom picture. One striking feature is the presence of intense photon emission at the cavity frequency in a situation where its mode resonance is spectrally far detuned from the QD transitions [110, 113, 115, 116, 166–171]. Furthermore, photon correlation measurements performed on single SKQDs in PhC cavities showed that the photon streams emitted at the QD exciton frequency and from the far-off-resonant cavity were anticorrelated at the level of single quanta [116, 167, 171], thus proving that the cavity was "fed" by the QD. This non-resonant excitation transfer from the QD to the cavity contradicted atomistic models and therefore presented the need for more refined experimental studies and theoretical analyses.

With this background, it was important to verify whether far-off-resonance cavity feeding is a universal feature, exhibited by all different types of QDs. To investigate this matter, among other issues, we integrated pyramidal QDs into *L3*-type cavities (Fig. 4.1(a)) according to the procedure described in Chapter 3. Our site-controlled fabrication technique enabled us to ensure that the QD was deterministically placed at the cavity field antinode and that no unwanted "parasitic" QDs could exist in the vicinity. Furthermore, our pyramidal QDs were made of the widely used InGaAs/GaAs material combination, such that direct comparison of the results with those obtained with SKQDs was facilitated. Since pyramidal QDs do not have a 2D wetting layer, in contrast to SKQDs, our experiments would also allow to evaluate whether and how the different barrier environment of a QD influences its coupling characteristics in a

photonic cavity.

Fig. 4.1(b) shows an SEM image of an actual single-QD-PhC structure, where one can infer the position of the single QD from the dark spot at the approximate center of the cavity. Note that the sample was tilted for this image by 20° with respect to the horizontal plane to obtain better contrast. The dark spot indicates the presence of a small indentation at the surface and stems from the pyramid buried underneath, which is not fully planarized. As one can see in Fig. 4.1(c), the QD is slightly offset (~ 50 nm) from the targeted central maximum of the cavity field profile, but the QD-field overlap is still sufficient to expect efficient coupling. The measured r/a ratio of the PhC in *S1* was 0.332, corresponding to an average hole radius of ~ 66 nm.

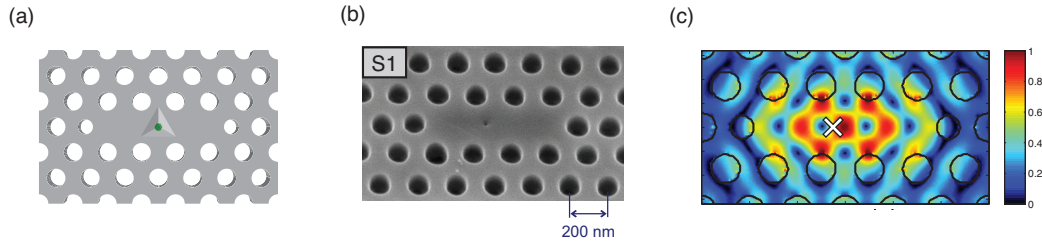


Figure 4.1: (a) Design of the single-QD-cavity structure. (b) SEM image of an example QD-cavity device (named *S1*). The position of the QD can be inferred from the black spot approximately in the center of the cavity. (c) Simulated electric field amplitude distribution in the central plane of the cavity. The white cross indicates the actual QD position for *S1*.

In the present chapter, we summarize our findings for a single pyramidal QD in a PhC nanocavity. We present PL studies and photon correlation measurements which show that the phenomenon of far-off-resonance cavity feeding is absent (or at least negligible) in the case of pyramidal QDs. The rich polarization features associated with the Purcell effect in an $L3$ PhC cavity are examined in detail, providing complementary information about the coupling characteristics and the photonic environment of the QDs. Furthermore, we analyze and discuss the role of exciton-phonon interactions and spectral diffusion on QD-cavity coupling. This chapter begins with a review of the phenomena that are known to influence the spontaneous emission properties of single QDs in a solid state environment.

Several of the findings presented in this chapter were published in Physical Review Letters [64].

4.1 Review of the coupling phenomena observed with single quantum dots

4.1.1 Introduction

As mentioned earlier, the far-off resonance cavity feeding of SKQDs [110, 113, 115, 116, 166–171] seemed very odd at first, since excitation transfer should only be possible when a quantum emitter is in spectral overlap with the cavity mode. Apart from that, the cavity emission itself exhibited Poissonian or even bunched photon statistics [116, 169], which meant that the cavity was emitting multiple photons at the same time. Another phenomenon that challenged the artificial atom model of a QD was the observation of a triplet (instead of the vacuum Rabi splitting doublet) in the optical spectrum at the anticrossing point of a strongly coupled single-QD-cavity system [116, 117, 172]. While the two outer peaks corresponding to the QD exciton and the cavity exhibited the anticrossing trend specific to the strong coupling regime, the central peak was not predicted by theory and has not been observed in cavity QED experiments with single atoms [96, 97]. Since the middle peak preserved the same polarization, wavelength and linewidth as the bare cavity mode, it was concluded that it was attributed to the bare cavity state [116, 117, 172, 173].

These unexpected experimental findings triggered a (still ongoing) series of theoretical and experimental investigations that have aimed at shedding light on the mechanisms behind the observed phenomena. In essence, it was found that the environment of a QD plays a crucial role in the coupling characteristics of a QD in a cavity. The decoherence processes governing the eigenstate evolutions are much more complex in the solid state than in atomic systems, and as it has been highlighted by a growing number of publications, their influence in cavity QED experiments can be dramatic. Understanding how environment-induced dephasing processes affect the characteristics of QD-cavity systems is important because of their implications for solid-state cavity QED in general, as well as for applications such as lasing and quantum information processing [51, 53, 160, 166].

4.1.2 Cavity-enhanced continuum transitions associated with the quantum dot barriers

One of the main reasons for the confusions associated with the observation of non-resonant cavity emission was the misconception that the energy level spectrum of a QD consists only of 3D-confined states. However, excitons bound by the confinement

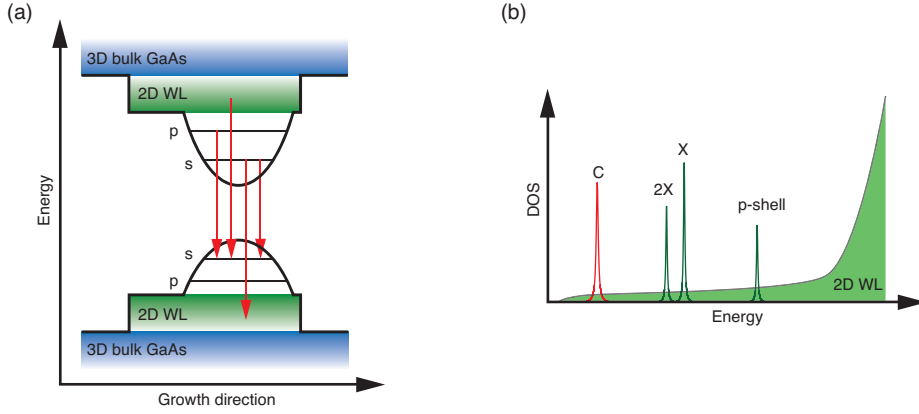


Figure 4.2: Schematic energy level diagram of a SKQD. Red arrows indicate examples of possible optical transitions. (b) Illustration of the DOS of a SKQD and far-off resonance cavity luminescence. The continuum overlapping with the bound QD states is mainly associated with crossed QD-WL transitions.

potential may interact with delocalized charges in their barriers to form a broadband continuum of hybridized states, which is superimposed with the discrete energy levels of the QD [174]. This is known to be a dominant process in SKQDs, where strong optical transitions were discovered to take place between the 0D confined states and extended 2D WL states in photoluminescence excitation (PLE) studies [175–178] (see Fig. 4.2(a)). In addition, it was proposed by Winger *et al.* [169] that a variety of multi-excitonic configurations exists in QDs involving carriers in higher excited states, which sum up to a quasi-continuum in the electronic density of states (DOS).

Given that a cavity enhances optical transitions overlapping with its mode via the Purcell effect, the phenomenon of far-off-resonance coupling should thus not seem surprising anymore: when the cavity mode is not resonant with any of the bound QD states, its emission can still be sustained by the QD-WL continuum (Fig. 4.2(b)). This accounts for the far-off-resonance cavity luminescence that has been reported in experiments with SKQDs incorporated in PhC cavities [116, 166–171] micropillars [113, 115] and microdisks [114]. As a result, the photon stream emitted by the cavity is not antibunched in this case as one would expect from a single photon light source, but bunched or Poissonian instead due to cascaded optical transitions that feed the cavity [169]. The QD-WL continuum also contributes to cavity emission at zero detuning and is responsible for the appearance of the central peak of the spectral triplet in strongly coupled QD-cavity systems [116, 167, 171].

The spurious background is evidently an intrinsic feature of SKQDs and is correlated with the presence of charges in their adjacent WL. In order to diminish it,

4.1. Review of the coupling phenomena observed with single quantum dots

resonant pumping schemes have to be adopted where the QD is excited uniquely through its p- or s-shell [60, 68, 179]. By this means, it is avoided that WL states get populated as in the case of above-bandgap pumping. Alternatively, an electric field bias can be applied to the QD-cavity structure to sweep away charges from the WL region [168].

The existence of a continuum in the DOS of a QD has far-reaching implications for QD-based cavity QED. From a theoretical viewpoint, it greatly complicates the realistic modeling of QD-cavity systems, because one has to include a multitude of interactions and exciton configurations to explain experimental data [169]. In view of using QD-cavity systems as a light-matter interface in quantum information processing where isolated quantum states with 0D nature are required [160], the mixing of bound QD states with a delocalized continuum is clearly detrimental. On the other hand, it has been demonstrated that the continuum of intermixed QD-WL states inherent to SKQDs facilitates lasing for single- and few-QD-cavity devices [149, 166, 180].

In this setting, it is important to ask whether the continuum of crossed QD-barrier transitions is a universal feature of all QD systems. As we will elaborate later in Section 4.2, the answer to this question is negative; the DOS of pyramidal QDs indeed contains discrete excitonic transitions that are well-isolated from the barrier continua, as it is manifested in their background-free coupling characteristics in cavity QED experiments [64]. The explanation for this striking difference between pyramidal QD and SKQDs lies in their different barrier environments: while SKQDs have 2D barriers due to the WL in their proximity (Fig. 4.2(a)), pyramidal QDs do not have a 2D WL but are connected to 1D quantum wires instead (as described in Sec. 2.1.2). It appears that the presence of the quantum wires plays a negligible role in perturbing the discrete QD states.

4.1.3 Influence of pure dephasing

Physical processes that disrupt the wavefunction of a quantum system without leading to population relaxation are gathered under the term *pure dephasing*. In the case of QDs, the main mechanisms that cause pure dephasing and thereby spectral broadening are carrier-phonon interactions and spectral diffusion. Recent theoretical and experimental studies have pointed out that these processes have a considerable impact on the coupling characteristics of QD-cavity systems.

A simple and widely used approach for modeling pure dephasing is to adopt the Markovian approximation, which consists in introducing an additional damping

term in the description of the quantum dynamics [56, 62, 69, 70]. Such models are based on the assumption that the phase fluctuations lead to a modulation of the instantaneous transition frequency via $\omega_0(t) = \omega_0 + \dot{\phi}(t)$, where ω_0 is the transition frequency of the QD and $\dot{\phi}(t)$ is the time derivative of the phase with an average value $\langle \dot{\phi}(t) \rangle \equiv 0$ [70]. As a result, the spectral lineshape of the two-level system becomes symmetrically broadened. The linewidth of the Lorentzian emission profile then equals $\hbar\gamma = \hbar\gamma_0 + \hbar\gamma_p$, where γ_0 is the intrinsic radiative decay rate and γ_p represents the Markovian pure dephasing rate.

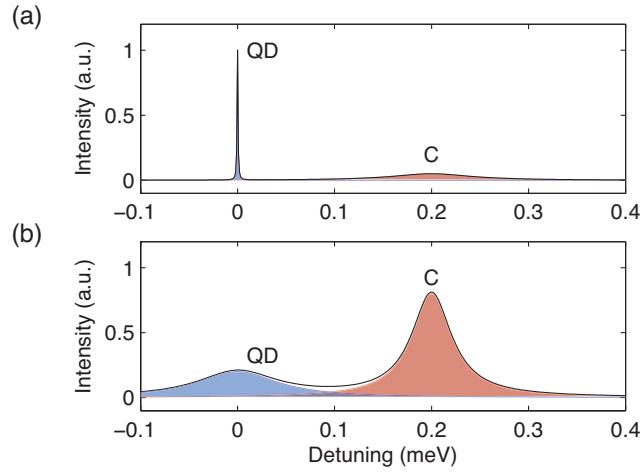


Figure 4.3: Schematic illustration of the intensity shifting effect induced by Markovian pure dephasing at non-zero detuning: (a) $\gamma_p = 0$, (b) $\gamma_p \sim 50 \cdot \gamma_0$.

The effect of pure dephasing is to smear out the coherent Rabi oscillations of strongly coupled systems at resonance, whereby the polariton peaks of the emission spectrum become blurred [70]. In addition, when the QD and the cavity are spectrally detuned, pure dephasing causes the intensity to be shifted from the QD towards the cavity peak [56, 62, 69]. This phenomenon is illustrated schematically in Fig. 4.3 for non-zero detuning: without pure dephasing, the QD is the dominant peak in the spectrum and only a fraction of the intensity is emitted at the cavity frequency. However, if pure dephasing is included, then the spectral overlap between the QD and the cavity is improved and a large fraction of the QD emission is channeled into the cavity mode. This implies that the pure dephasing processes actually *assist* QD-cavity coupling at moderate detunings.

While Markovian theories are applicable to model scattering of the QD states due to a fluctuating environment to a first approximation, they fail to reproduce the pronounced spectral asymmetries observed in the coupling characteristics of single QDs in nanocavities [69]. In particular, time-resolved measurements of the radiative

4.1. Review of the coupling phenomena observed with single quantum dots

decay curves revealed that the QD generally decays faster at positive detunings as compared to negative detunings [59]. Furthermore, the emission intensity detected at the cavity mode frequency is larger when the detuning is positive in comparison to the case where the detuning is negative [59, 69, 181, 182].

The origin of the discrepancies between Markovian theories and experimental findings lies in the fact that phonon-induced dephasing processes introduce memory effects into the quantum dynamics of QD-cavity systems [65, 69, 103, 182, 183]. Due to interactions between the QD excitons and the phonon reservoir of the semiconductor crystal, the QD transitions are *asymmetrically* broadened by phonon sidebands (see Section 1.2.5). This is due the presence of the phonon reservoir that introduces additional paths for a QD exciton to decay radiatively, which involve either the absorption or the emission of a phonon. When a phonon is released in the radiative decay process, then the photon is emitted at a lower energy compared to an unperturbed exciton. On the other hand, when a phonon is absorbed by the QD, then the additional energy is transferred to a photon which is emitted at a higher energy as compared to an unperturbed exciton. The reason why the phonon sidebands of a QD are asymmetric is because the phonon emission and absorption events occur with different probabilities, especially at low temperatures ($T < 60$ K) when the phonon bath is sparsely populated [75, 103].

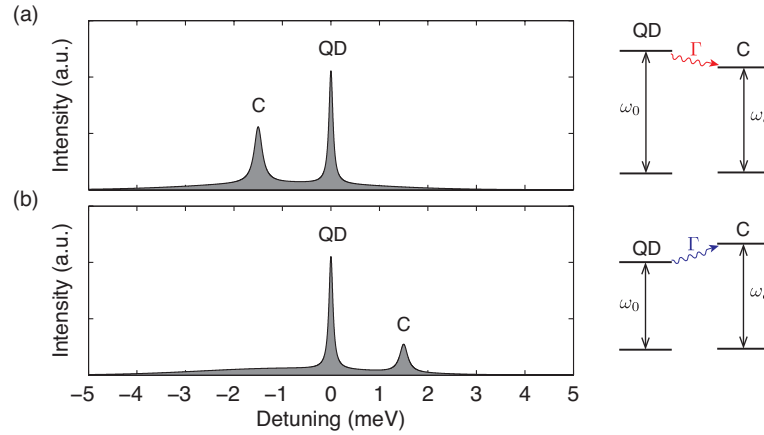


Figure 4.4: Schematic illustration of phonon-assisted QD-cavity coupling at positive (a) and negative (b) detuning. It is assumed that the temperature is low (< 80 K) and kept constant.

Given that phonon-induced dephasing processes participate in the QD decay dynamics, it is natural to expect that they will increase the spectral bandwidth over which the QD can couple to the cavity mode. If the cavity is detuned to the low energy side of the zero phonon line (ZPL), it Purcell-enhances the radiative transitions of the QD exciton involving the emission of a phonon Γ (Fig. 4.4(a)). Thus, the phonon inter-

actions assist the QD to emit a photon into the cavity mode. Equivalently, if the cavity is energetically above the QD ZPL, the optical transitions associated with phonon absorption events will couple to the mode (Fig. 4.4 (b)). Since at low temperatures phonon absorption is less probable than phonon emission, the cavity peak is more intense at positive detunings than at negative detunings (compare Fig. 4.4 (a) and (b)). This difference has been observed experimentally [59, 182] and reflects the underlying asymmetry of the effective phonon density of states that contributes to the radiative decay of the QD [103, 184].

According to current knowledge, the dominant mechanism behind QD-phonon interactions is coupling of longitudinal-acoustic phonons with the deformation potential of the confined electron and hole states [77, 78, 80]. The energy range over which phonon-assisted QD-cavity coupling can occur is determined by the extent of the phonon sidebands [64, 65, 103, 181], which is inversely related to the localization length of the confinement and adds approximately **3-5 meV** long spectral tails to the ZPLs of QD transitions [75, 77]. In the present chapter, we demonstrate that the coupling characteristics of pyramidal QDs can be explained by taking into account phonon interactions.

4.1.4 Modification of spontaneous emission in a 2D photonic crystal

Spontaneous emission is not an intrinsic property of a quantum emitter alone, but it is a joint property of the emitter and the "empty" radiation field, i.e. the vacuum. In fact, quantum electrodynamics explains spontaneous emission as a process that is stimulated by random fluctuations of the vacuum field [18, 99]. The magnitude of the vacuum fluctuations depends on the density of electromagnetic modes that are spectrally and spatially overlapping with the emitter. Therefore, the spontaneous emission rate Γ of an emitter depends on the *local density of optical states* (LDOS). In the weak coupling regime, Γ can be calculated via Fermi's golden rule [14, 18, 99]:

$$\Gamma = \frac{2\pi}{\hbar} |M|^2 \rho(\vec{r}_0, \omega). \quad (4.1)$$

Here $M = -\vec{\mu} \cdot \vec{E}(\vec{r}_0)$ is the transition matrix element quantifying the overlap between the radiation field \vec{E} and the emitter's dipole moment μ , and $\rho(\vec{r}_0, \omega)$ is the LDOS at the position \vec{r}_0 and at the frequency ω . The parameters M and ρ can in general be different for each polarization. In a homogeneous 3D medium, the LDOS is independent of position and polarization and increases quadratically with the optical frequency

4.1. Review of the coupling phenomena observed with single quantum dots

[18, 99, 185]:

$$\rho_0(\omega) = \frac{n\omega^2}{\pi^2 c^3}, \quad (4.2)$$

and the quantum emitter radiates isotropically in all spatial directions with a spontaneous emission rate

$$\Gamma_0 = \frac{n\mu^2\omega^3}{3\pi\epsilon_0\hbar c^3}. \quad (4.3)$$

However, PhCs and other photon-confining structures allow to engineer the LDOS both spatially and spectrally by suppressing the propagation of a range of electromagnetic modes and by strongly localizing a discrete set of modes to a wavelength-sized spatial region. As a result, the radiative lifetime of a quantum light source embedded in a PhC cavity can either be strongly increased or reduced with respect to the situation in a bulk semiconductor material. The modification of spontaneous emission through a tailored LDOS is the physical origin of the Purcell effect and provides a basic concept for designing PhC devices [85].

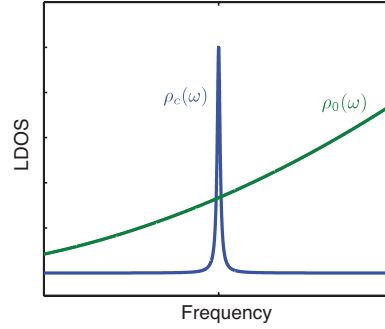


Figure 4.5: Schematic comparison of the LDOS of a homogeneous medium ($\rho_0(\omega)$) and of a single-mode cavity ($\rho_c(\omega)$).

If we consider a cavity that only has a single mode with a frequency ω_c and a linewidth κ , then the LDOS in this case can be described by the Lorentzian-shaped function:

$$\rho_c(\omega) = \frac{2Q}{\pi\omega} \frac{\kappa^2}{4(\omega - \omega_c)^2 + \kappa^2}, \quad (4.4)$$

with Q being the quality factor $Q = \omega_c / \Delta\omega_c$. As it is sketched in Fig. 4.5, in this case the LDOS can be larger as compared to bulk near the cavity resonance and smaller under

Chapter 4. Coupling characteristics of single pyramidal quantum dots

detuned conditions. The spontaneous emission rate inside the cavity becomes [18]

$$\Gamma_c = \frac{2Q\mu^2}{\hbar\epsilon_0 V_m} \zeta^2 \frac{\kappa^2}{4(\omega - \omega_c)^2 + \kappa^2}, \quad (4.5)$$

where V_m is the mode volume and the term

$$\zeta = \frac{\vec{\mu} \cdot \vec{E}(\vec{r}_0)}{|\vec{\mu}| |\vec{E}_{max}|} \quad (4.6)$$

quantifies the spatial overlap and polarization matching between the field and the emitter's dipole. The parameter \vec{E}_{max} stands for the maximum field amplitude of the cavity mode. By taking the ratio between Γ_c and Γ_0 , one obtains an equation that describes the Purcell enhancement of spontaneous emission induced by the cavity [18, 111, 112, 185]:

$$\frac{\Gamma_c}{\Gamma_0} \equiv F_c(\omega) = \frac{3}{4\pi^2} \left(\frac{\lambda}{n} \right)^3 \frac{Q}{V_m} \zeta^2 \frac{\kappa^2}{4(\omega - \omega_c)^2 + \kappa^2}. \quad (4.7)$$

The factor F_c essentially quantifies by how much the cavity accelerates or slows down spontaneous emission relative to the bulk. If $F_c > 1$, then the cavity enhances the emission rate through an intensified interaction of the QD with the vacuum field, while $F_c < 1$ means that emission is inhibited. Due to the Lorentzian-shaped LDOS of the cavity mode, F_c sensitively depends on the detuning $\omega - \omega_c$. At exact resonance and with the dipole being parallel to the field ($\zeta = 1$), Eq. (4.7) becomes equal to the *Purcell factor*

$$F_c(\omega = \omega_c) = F_{Purcell} = \frac{3}{4\pi^2} \left(\frac{\lambda_c}{n} \right)^3 \frac{Q}{V_m}, \quad (4.8)$$

which is a figure of merit that characterizes the capacity of a cavity to increase an emitter's radiative decay rate. An increase is only possible if $F_{Purcell} > 1$, which requires that the Q factor of the cavity is sufficiently large and its mode volume V_m is sufficiently small. This is precisely the reason why PhC nanocavities provide higher Purcell factors as compared to micropillars and microdisks [20]. For example, an L3-type PhC cavity has a mode volume comparable to the cubic wavelength ($V_m \sim (\lambda_c/n)^3$); assuming an intermediate Q factor of 3000, the estimated Purcell factor in this case would be $F_{Purcell} \sim 230$. However, reported experimental values for the lifetime shortening of weakly coupled SKQDs in PhC nanocavities with $Q \sim 3000$ are between 5 and 10 [110–112, 186]. The reasons for these modest enhancement values are presumably 1.) a spatial misalignment between the QDs and the cavity field maxima, 2.) a mismatch between the orientations of the QD dipole and the cavity

4.1. Review of the coupling phenomena observed with single quantum dots

field ($\zeta \ll 1$) and 3.) a reduction of the effective Q factor due to pure dephasing [62].

Although eq. (4.7) formulates the effect of a confined cavity mode on spontaneous emission, it ignores the fact that in reality the LDOS of a nanocavity has a complex structure that cannot be simply described by a single Lorentzian as in eq. (4.4). This is because real nano- and microcavities (except for ideal 3D PhCs [187]) do not possess completely empty PBGs where all frequencies except for the resonant modes are suppressed. In particular, the resonant modes of point-defect nanocavities implemented in 2D PhCs are not spectrally isolated, but coexist together with a continuum of modes.

Indeed, triangular-lattice PhCs exhibit a PBG only in the TE polarization (electric field oriented parallel to the PhC slab plane), but not in the TM polarization (electric field oriented orthogonal to the PhC slab plane) [165, 186, 188]; hence the cavity resonances are positioned within the TE bandgap and simultaneously overlap with delocalized Bloch modes from the TM band [186]. To illustrate this point, we performed band structure calculations based on a 2D PWE method, using the parameters $r = 0.325 \cdot a$ for the PhC hole radii and a slab thickness of $d = 1.325 \cdot a$. It is evident from the results shown in Fig. 4.6 that the PhC slab supports a continuum of guided modes with TM polarization within the spectral range where the PBG is present in the TE polarization. In addition, it is well known that the modes of a planar PhC structure cannot be rigorously categorized as TE or TM polarized as in ideal 2D systems, because the waveguide confinement of the modes introduces mixing effects between the two polarizations [189]. Consequently, a QD that is off-resonant with respect to a cavity resonance can radiatively decay into a continuum that consists of mixed TE-TM states, or through residual TE modes that exist in the PBG due to the finite size of the PhC [190].

Based on these considerations, it is appropriate to separate the emission from a QD in a nanocavity into two contributions: one that contains the Purcell enhancement exerted by the localized cavity mode, and one that represents coupling to a continuum of modes that contribute to the LDOS. The total radiative decay rate from the QD can then be written as [111, 112, 186]

$$\Gamma_{tot}(\omega, \alpha) = \Gamma_c(\omega, \alpha) + \Gamma_{cont}(\omega, \alpha), \quad (4.9)$$

where Γ_c is given by eq. 4.5 and Γ_{cont} is the emission rate into the continuum. Both Γ_c and Γ_{cont} have a distinct frequency dependence. The variable α designates the polarization state to indicate that Γ_c and Γ_{cont} can generally have a different dependence on the frequency ω for two orthogonal polarization states. Within the PBG of a PhC, Γ_{cont} can be strongly reduced relative to the bulk emission rate Γ_0 .

Chapter 4. Coupling characteristics of single pyramidal quantum dots

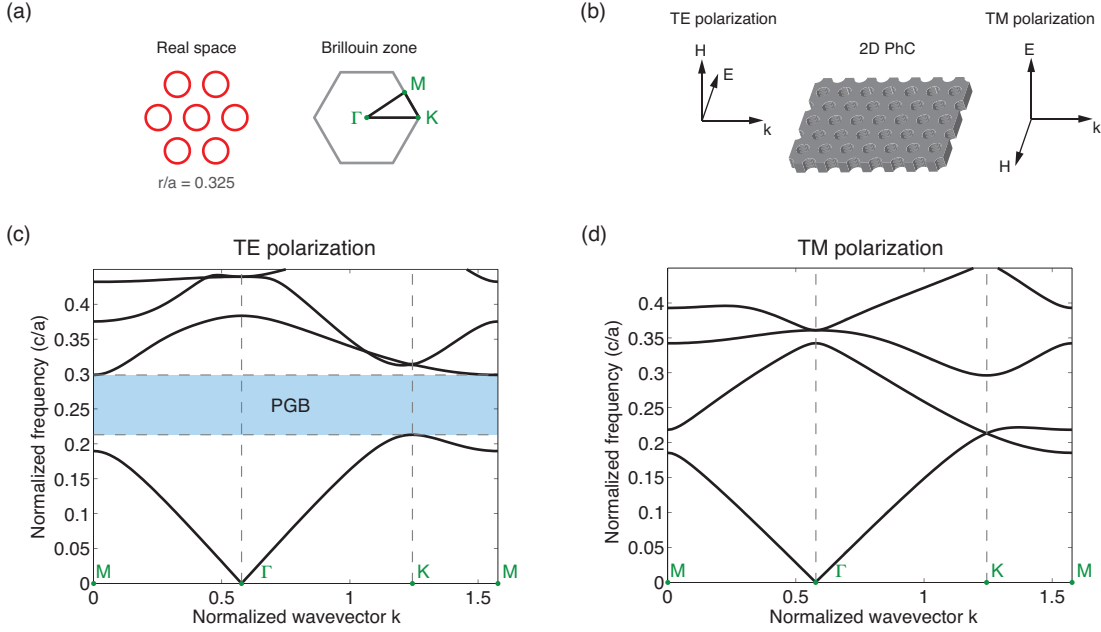


Figure 4.6: (a) Sketch of the triangular PhC lattice and its Brillouin zone with the symmetry points Γ , K and M . (b) Illustration of the TE and TM polarizations. (c) and (d): TE and TM band diagrams, respectively, for a PhC slab with $r = 0.325 \cdot a$ and $d = 1.325 \cdot a$. The band structures were calculated using a PWE toolbox developed by V. Zabelin [191].

Equivalently, the LDOS of a cavity can also be expressed as a sum of the Lorentzian mode function ρ_c (eq. (4.4)) and a term ρ_{cont} for the continuum:

$$\rho_{tot}(\omega, \alpha) = \rho_c(\omega, \alpha) + \rho_{cont}(\omega, \alpha). \quad (4.10)$$

These functions also depend on the respective polarization state α . Indeed, recent experiments performed by Wang *et al.* demonstrated that ρ_{cont} can be determined for two orthogonal in-plane polarizations of a PhC by means of time-resolved PL measurements of embedded SKQDs [192].

Eq. 4.10 implies that when a QD transition is detuned from the cavity (i.e. from ρ_c), it can only relax radiatively by coupling to the continuum of states (i.e. via ρ_{cont}). However, within the bandgap of a PhC, ρ_{cont} can be strongly reduced relative to the LDOS ρ_0 of the bulk. The radiative decay into continuum states also has to be taken into account for evaluating the effective enhancement (or inhibition) of spontaneous emission:

$$\frac{\Gamma_{tot}}{\Gamma_0} \equiv F_{eff}(\omega) = F_c(\omega) + F_{cont}(\omega). \quad (4.11)$$

The factor $F_c(\omega)$ is defined by eq. (4.7). The second factor, $F_{cont}(\omega) = \Gamma_{cont}/\Gamma_0$, is responsible for the inhibition of spontaneous emission in a PhC. Inhibition occurs when $F_{eff}(\omega) < 1$, which is the case for a QD that is detuned from the cavity mode and emits within the PBG [116, 192].

4.2 Investigation of the Purcell effect with a single quantum dot

4.2.1 Polarization-resolved photoluminescence

It is well known from FDTD calculations and from experiments [166, 193] that the fundamental mode of an $L3$ cavity intrinsically exhibits a characteristic polarization dependence, as illustrated in Fig. 4.7(a): the fraction of light that escapes into the light cone is strongly polarized along the perpendicular direction V . The polarization of the mode reflects the symmetry of the electric field profile inside the cavity, and it can be very useful for its spectral identification.

On the contrary, the light emission of bare pyramidal QDs towards the top (away from the substrate) is distinguished by a polarization dependence that does not possess any preferential direction, as sketched in Fig. 4.7(b) [137, 138]. The isotropic polarization dependence of a pyramidal QD is a signature of its high structural symmetry (see Sec. 2.1.2), as a result of which the in-plane orientation of the exciton dipole moment remains statistically random [137]. In contrast, conventional SKQDs produce light with a preferential polarization axis due to their anisotropic in-plane shape and strain effects [30, 105, 194].

By keeping in mind that the coupling of the QD to the cavity depends on detuning and on polarization, it is intuitively straightforward to expect that the intrinsic polarization of the cavity mode will affect any spectrally overlapping QD transition through the Purcell effect (see Eq. (4.5) and (4.7)). Consequently, by measuring polarization-resolved PL, one can gain information about the coupling between a specific QD exciton line to the cavity [64, 195]. We exploited this principle to find and study spectrally matched QD-cavity structures on our samples, as it will be explained in the following.

In our micro-PL experiments, we used above-bandgap CW excitation at 700 nm and extracted the linear polarization component of the QD emission by passing the optical signal through a half-wave plate and a linear polarizer in the detection path of our micro-PL setup. In those cases where a cavity mode was spectrally overlapping

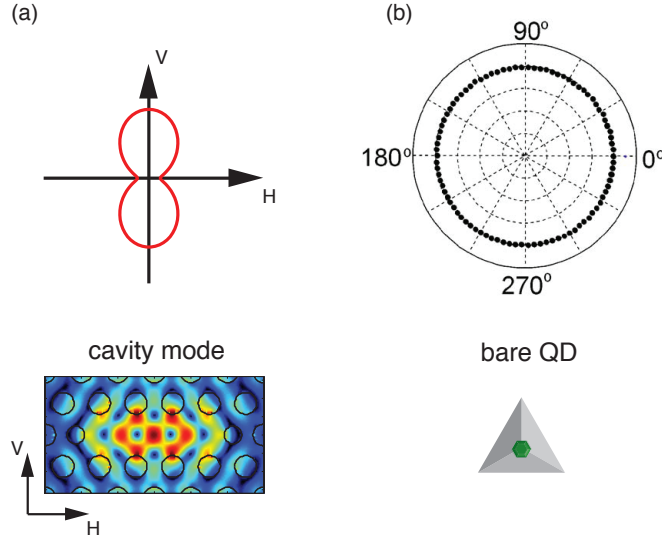


Figure 4.7: (a) Sketch of the in-plane linear polarization dependence of the optical emission associated with the fundamental mode of an $L3$ cavity. (b) Measured in-plane linear polarization dependence of a bare pyramidal QD (i.e. not integrated in a cavity structure). Reprinted with permission from [137]. Copyright 2006, AIP Publishing LLC.

with a QD transition, we could observe distinct polarization features in the spectra. In Fig. 4.8, we present the polarization-resolved spectra of two nominally equal structures $S1$ and $S2$, i.e. both QD-cavity devices were fabricated with the same design values for the PhC parameters and both had an alignment accuracy of ~ 50 nm for the positioning of the QD within the cavity.

Let us first discuss the properties of $S1$ (Fig. 4.8(a) and (c)). One can see that its lowest-energy peak is strongly polarized along the V direction, while the 3 other main peaks are H -polarized. As one might assume at this point, the strongly V -polarized peak labeled as C is the spectral signature of the fundamental cavity mode. We confirmed this by measuring the temperature dependence of $S1$, which will be presented in Sec. 4.2.2. The remaining emission peaks correspond to the negatively charged exciton X^- , the neutral exciton X and the neutral biexciton $2X$. Transitions from p-shell states are also present in the spectra, but they are only noticeable on a logarithmic scale (Fig. 4.8(c)). Note that the X^- and $2X$ binding energies (i.e. spectral separation from the X) amount to 4.6 meV and -1.5 meV, respectively; these are typical values for the InGaAs/GaAs QDs used in the experiments of the present work, as we reported in our statistical study of single QDs in Ref. [40].

The cavity peak of $S1$ is situated ~ 1.5 meV below X^- and has a linewidth of

4.2. Investigation of the Purcell effect with a single quantum dot

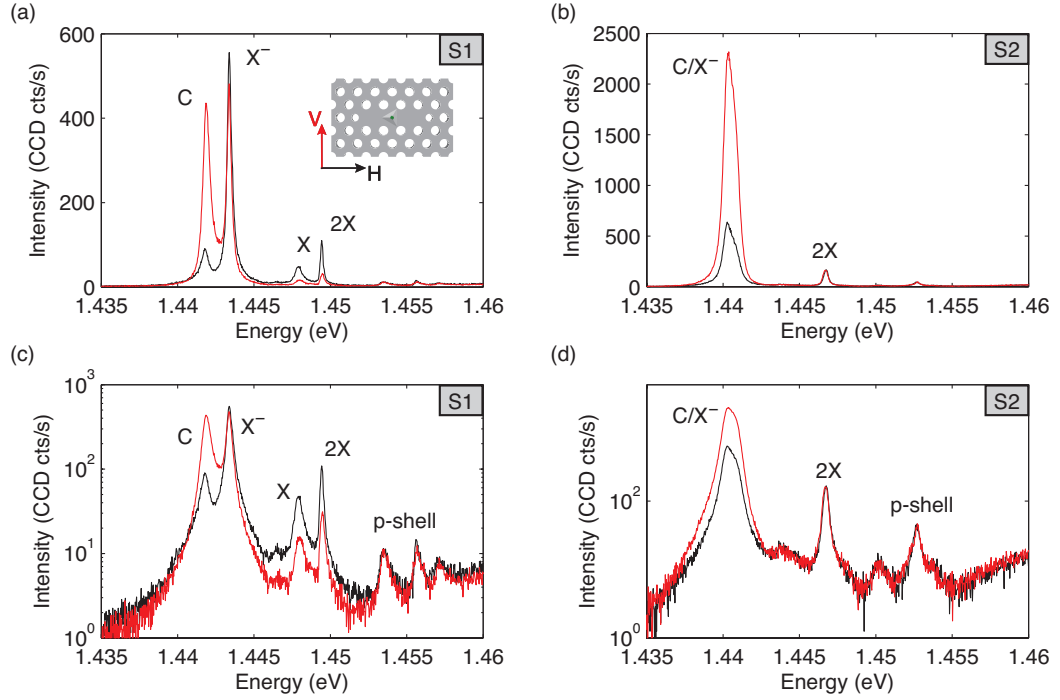


Figure 4.8: (a) Polarization-resolved PL spectrum of a single-QD-cavity structure, labeled *S1*. The red and black curves represent the linear polarization orientations V and H, respectively (see inset). (b) Polarization-resolved PL spectrum of a second single-QD-cavity structure, named *S2*. (c) and (d) are semilogarithmic plots of the same data as in (a) and (b). The spectra were measured at $T = 10$ K and $P = 200$ μ W.

$\hbar\gamma_C = 577$ μ eV, corresponding to a quality factor of $Q \sim 2500$. Due to this intermediate value of Q , the QD-cavity system is most likely in the weak coupling regime. The linewidths of the QD peaks X^- , X and $2X$ amount $\hbar\gamma_{X^-} = 385$ μ eV, $\hbar\gamma_X = 790$ μ eV and $\hbar\gamma_{2X} = 330$ μ eV, respectively. Such large values suggest that spectral diffusion is a dominant dephasing mechanism in our samples, causing the optical transitions to be broadened far beyond the lifetime limit (see Sec. 1.2.5). In the case of pyramidal QDs, the origins of spectral diffusion are most likely carbon-related impurities incorporated in the material during the MOVPE growth process and charges trapped at the pyramid interfaces.

In comparison to *S1*, the second QD-cavity device *S2* presented in Fig. 4.8(b) and (d) seemingly exhibits fewer emission lines. However, what appears to be a single peak at ~ 1.44 eV is actually the superposition of the cavity peak C with the X^- , which are separated by only $\Delta E \sim -0.47$ meV. Interestingly, they are both *co-polarized*; this is a striking difference to *S1*, where the two peaks were oppositely polarized. The linewidths were evaluated to be $\hbar\gamma_C = 590$ μ eV ($Q \sim 2440$) and $\hbar\gamma_{X^-} = 581$ μ eV.

Chapter 4. Coupling characteristics of single pyramidal quantum dots

Although the neutral exciton transition X is not seen in Fig. 4.8(b) and (d), it emerged at higher temperatures as the X^- was detuned from C (not shown here).

At this point, the striking similarities between the two devices $S1$ and $S2$ should be emphasized. Apart from small differences in the respective excitonic binding energies and QD-cavity detunings, both systems are almost like duplicates of each other. This evidences the great reproducibility of our QD-cavity systems, which is highly valuable for realizing systematic studies. Another remarkable property is the simplicity of the QD spectra, which only contain of 3 ground state transitions. In comparison, SKQDs normally have complex spectra with many spectral lines attributed to charged states [169] (and possibly to other "parasitic" QDs), which makes it difficult to avoid ambiguities in the results from cavity QED experiments.

An inspection of the spectra in Fig. 4.8 suggests that the polarization state of each QD transition depends on its detuning with respect to the cavity mode frequency, as expected from direct Purcell enhancement. All QD peaks that are energetically above C are either H -polarized or unpolarized; however, when a QD peak is sufficiently close to C (i.e. when the detuning is comparable to the cavity linewidth), its polarization becomes cavity-like. To visualize this effect, we present full polarization dependence measurements for both QD-cavity systems $S1$ and $S2$ in Fig. 4.9.

In Fig. 4.9(a)-(d), one can examine the polarization-resolved spectra of $S1$ at different temperatures (and therefore at different detunings). Interestingly, the X^- (marked in green) and also the other QD transitions are substantially H -polarized, which is precisely the opposite of the V -polarized cavity. As the temperature is increased and the detuning becomes smaller, the X^- gradually becomes less H -polarized until it eventually switches to being V -polarized like the cavity in Fig. 4.9(d). This is a clear signature of the Purcell effect, whereby the QD adopts the polarization of the cavity mode when the detuning is comparable to the cavity linewidth or smaller. Note that only the X^- is V -polarized in Fig. 4.9(d), while the other QD transitions at higher energy remain H -polarized.

Before proceeding to present further results from our experiments, it is important to point out that we never observed a spectrally significant cavity peak at detunings greater than ~ 5 meV, even when the excitation power was large enough to saturate the QDs. In reports on similar experiments with single SKQDs, strong off-resonant emission from the cavity mode (i.e. with an intensity comparable or even larger than the excitonic lines) was observed to persist even at moderate excitation powers for detunings beyond 20 meV under above-bandgap excitation conditions [116, 169]. We will show further below that this departure of pyramidal QDs from the behavior of SKQDs is associated with fundamental differences in their coupling

4.2. Investigation of the Purcell effect with a single quantum dot

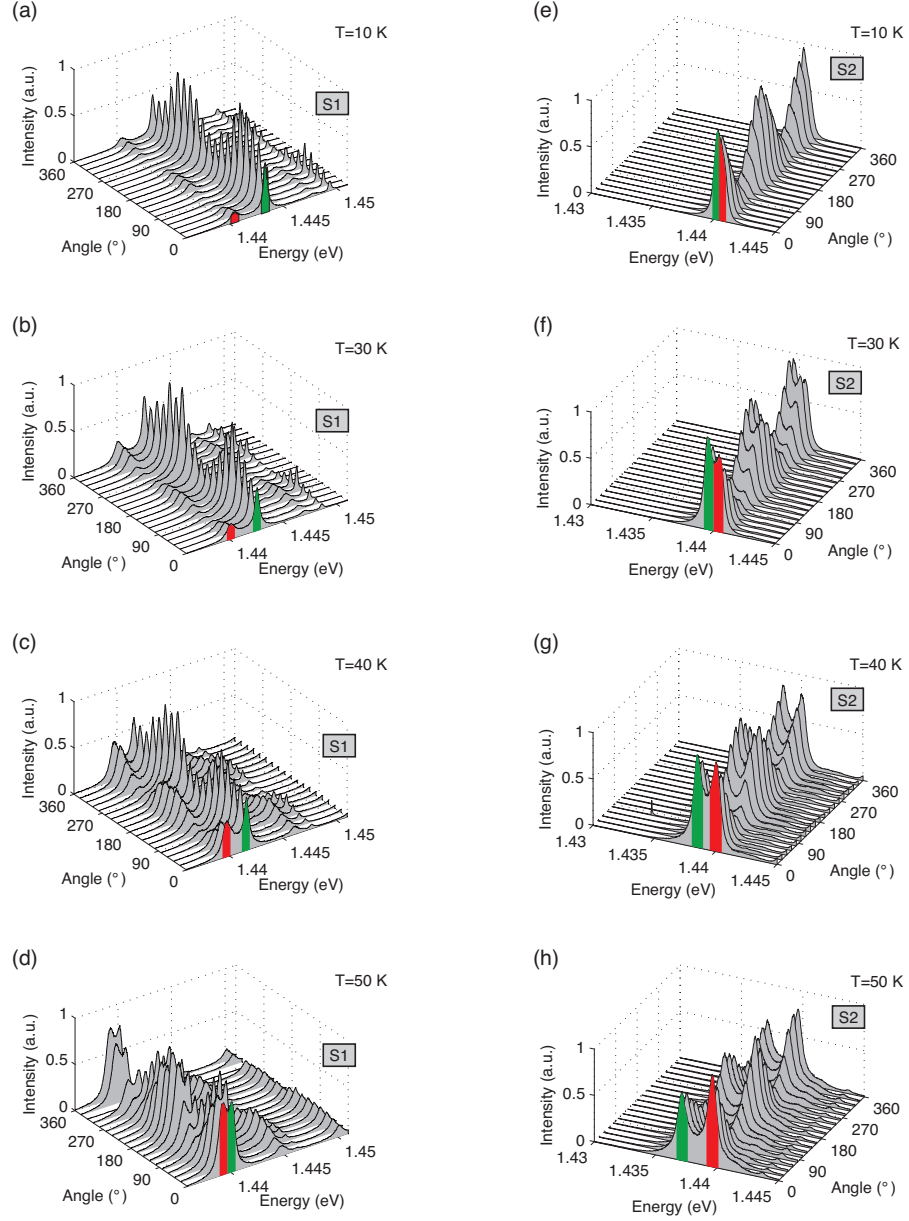


Figure 4.9: Full linear polarization dependence of two different, but nominally equal, single-QD-cavity structures at different temperatures. The graphs in (a)-(d) show the polarization-resolved spectra of the example structure S1 at 10 K, 30 K, 40 K and 50 K, respectively. The cavity peak is highlighted in red and the near-resonant X^- transition is marked in green. Equivalently, structure S2 is shown in (e)-(h) for the same temperatures. Both S1 and S2 were measured at $P = 200 \mu\text{W}$.

characteristics.

4.2.2 Temperature-tuning the quantum dot through resonance

To study the detuning-dependent properties of the QD-cavity systems, we measured their PL spectra as a function of temperature. While the QD transitions follow the trend of the GaAs bandgap upon temperature variation, the resonance frequency of the cavity mode shifts at a slower rate corresponding to the change of the refractive index of the material. This property is commonly exploited to tune a QD transition of interest through the cavity resonance, which allows to investigate signatures of the Purcell effect and of strong coupling [113, 196].

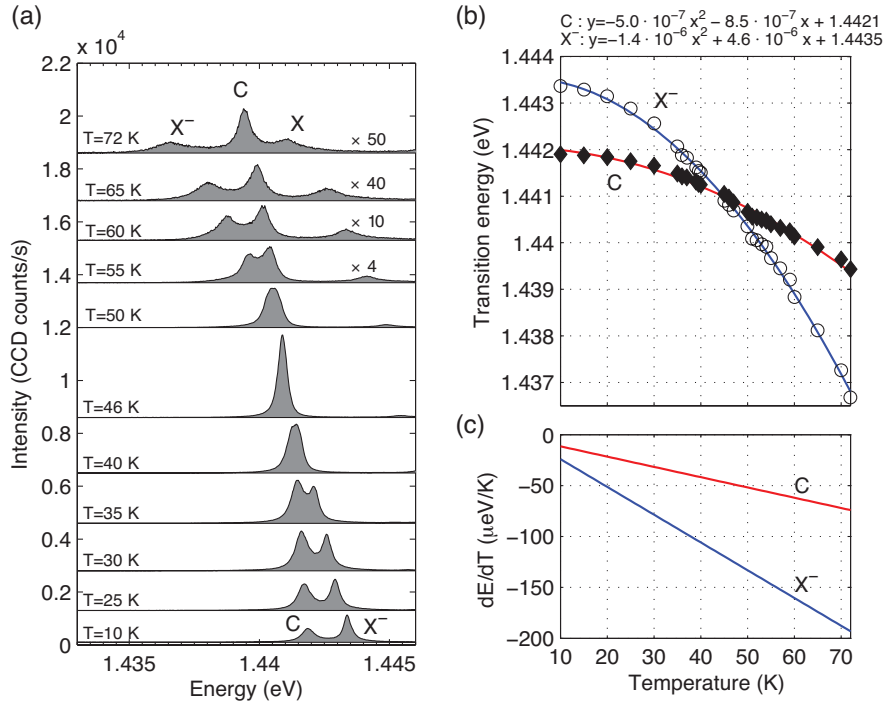


Figure 4.10: (a) PL spectra of *SI* for a set of temperatures. The curves have been vertically offset for clarity. For $T > 50$ K, the data was scaled by the indicated factors. (b) Temperature dependence of the X^- and *C* transition energies. The blue and red curves represent quadratic fits to the data, of which the parameters are displayed on top. (c) Derivative of the transition energies with respect to temperature.

Following this approach, we measured the PL of *SI* (already shown previously in Fig. 4.8) for a set of different temperatures. A subset of these spectra is presented in Fig. 4.10(a). Since the *Q* factor is not sufficiently high and the dephasing-induced broadening of the QD is too large, the QD peak crosses (rather than anti-crosses) with the cavity mode and the system is in the weak coupling regime. In Fig. 4.10(b), the energy shifts of the X^- and the *C* are traced as a function of temperature. Their trends were fitted with a quadratic polynomial, from which the slopes plotted in Fig. 4.10(c)

4.2. Investigation of the Purcell effect with a single quantum dot

were obtained.

As the temperature is raised from 10 K to 46 K in Fig. 4.10(a), the X^- is tuned into resonance with the cavity mode C . Here one observes that both X^- and C gradually gain in intensity, and that the C peak eventually becomes more intense than the X^- . Evidently, the Purcell effect must be responsible for the observed intensity enhancements. At temperatures around resonance (i.e. between 40 K and 50 K), both peaks merge to a single spectral feature. As the temperature is increased above 50 K, the X^- peak reappears and undergoes significant broadening due to thermally activated carrier-phonon interactions [74, 77, 79]. Note that for temperatures above 50 K, the spectra were magnified by multiplication with a constant factor (indicated in the figure) to counteract the drop of the overall intensity due to non-radiative recombination processes.

In order to gain information on the variations of the position, integrated intensity and the linewidth of each peak as a function of temperature, we analyzed the spectra by fitting each individual spectrum with a sum of Lorentzian curves. Examples of such fits are shown in Fig. 4.11. To avoid ambiguities, we did not include the spectra measured at exact resonance between X^- and C in our analysis, because in those cases it was not possible to separate the two peaks.

The very good agreement between the Lorentzian fits and the data in Fig. 4.11 might seem surprising at first sight, because non-Lorentzian asymmetries in the form of phonon sidebands are expected to appear in the optical spectra [75–77]. However, since here the QD peaks are significantly broadened by spectral diffusion, the phonon-induced asymmetries of the QD lineshapes are not visible in the spectra.

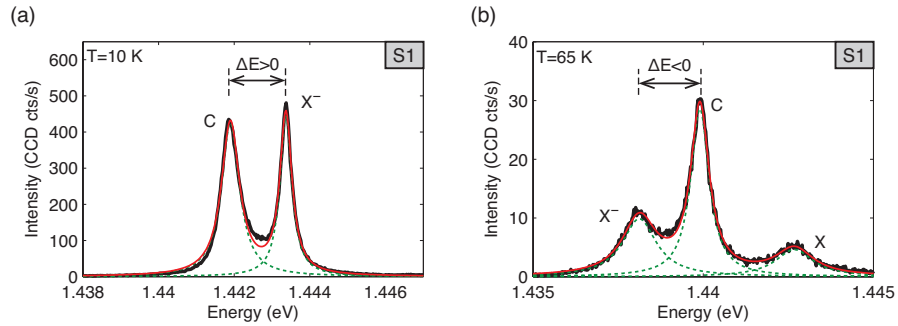


Figure 4.11: Examples of Lorentzian fits to the data at low (a) and high (b) temperature for structure S1. In (a), the detuning $\Delta E = \hbar\omega_{X^-} - \hbar\omega_C$ is positive, while in (b) it is negative. The data is displayed in black, while the fit is shown in red. Individual Lorentzians are plotted as green dashed lines.

For analysis purposes, it is insightful to plot the data as a function of detuning,

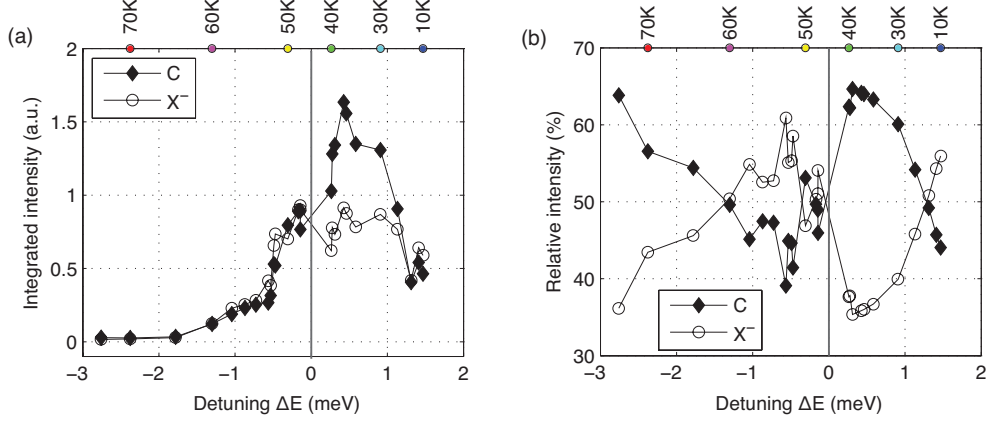


Figure 4.12: Absolute (a) and relative (b) intensities (see definition in Eq. (4.12)) of the X^- and C features versus detuning for sample $S1$. Temperatures corresponding to given detunings are indicated on the top axis of the graph.

which we define here as $\Delta E = \hbar\omega_{X^-} - \hbar\omega_C$. Here ω_{X^-} and ω_C are the frequencies corresponding to the X^- and C transitions, respectively. We speak of positive (negative) detuning when the cavity peak C is energetically below (above) the X^- feature (illustrated in Fig. 4.11). Let us first focus our attention on the variation of the integrated intensities of C and X^- versus detuning, presented in Fig. 4.12(a). Note that the temperature values increase from right to left, i.e. from positive detuning towards negative detuning (see markers on top of the graph). As the detuning is reduced from $\Delta E \sim 1.5$ meV to ~ 0.4 meV, the intensities of the X^- and the C peaks increase by a factor of ~ 1.6 and 3.5 , respectively. From $\Delta E \sim 0.4$ meV to -2.8 meV, both peaks gradually decrease towards small intensity values.

The drop in the intensities of both X^- and C for temperatures above 40 K (detunings below ~ 0.3 meV) is not related to QD-cavity coupling phenomena, but is caused by the increased rate of non-radiative recombination events that reduce the overall photon emission rate of the QD. In order to subtract this temperature-induced effect, we examine the relative intensities in Fig. 4.12(b), which we define by

$$I_{C,rel} = \frac{I_C}{I_C + I_{X^-}} \quad \text{and} \quad I_{X^-,rel} = \frac{I_{X^-}}{I_C + I_{X^-}}. \quad (4.12)$$

Here I_C and I_{X^-} are the integrated intensities, i.e. the peak areas of the fitted Lorentzians. It becomes evident in the graph that the cavity peak C is more intense at small positive detuning ($\Delta E \sim +0.5$ meV) as compared to small negative detuning ($\Delta E \sim -0.5$ meV). This asymmetry is a manifestation of the phonon-assisted Purcell enhancement of the QD decay [59, 64, 65, 69, 103, 182, 184], which has the property of being more efficient

at positive detunings than at negative detunings (as described in Sec. 4.1.3).

4.2.3 Detuning-dependent polarization features

In the previous section, we observed signatures of the Purcell effect in the detuning dependence of the integrated intensities. The question that we want to address now is how the polarization of the QD emission is affected as a function of detuning and temperature. For this purpose, we define a quantity which allows to analyze the polarization properties, namely the *degree of linear polarization* (DOLP):

$$DOLP = \frac{I_V - I_H}{I_V + I_H}. \quad (4.13)$$

This ratio quantifies the relative difference between the PL intensities I_V and I_H detected for the V and H polarizations, respectively. Unpolarized light is therefore characterized with $DOLP = 0$, and the maximum and minimum attainable values for the DOLP are 1 and -1 for completely V - or H -polarized light, respectively.

The polarization-resolved PL spectra of $S1$ are presented in Fig. 4.13(a) for a few selected temperatures between 10 K and 72 K. Evidently, the X^- peak is slightly H -polarized at 10 K, when it is spectrally detuned from the cavity C . As the temperature is increased up to 46 K where resonance occurs, the polarization of the X^- gradually switches from H to V : the X^- becomes co-polarized to the cavity. Then, when the temperature is further increased and the X^- is tuned further towards lower energies, it gradually returns to its virtually unpolarized state. The polarization of the X^- is thus strongly influenced within a small detuning range, which is another signature of the Purcell effect.

We proceed to analyze the polarization features in more depth in Fig. 4.13(b), where the DOLP is plotted. Let us first focus our attention to the situation at 10 K. There one can notice several interesting details:

- The DOLP reaches a maximum of $\sim 70\%$ at the resonance frequency of the cavity, and the nearby spectrum is V -polarized over a range of 2.5 meV (emission range A , highlighted in red in the figure). For means of comparison, note that the linewidth of the cavity peak C at 10 K is ~ 0.6 meV.
- At energies above the V -polarized region around the cavity resonance, a range of 9 meV of the spectrum is H -polarized (emission range B , highlighted in green in the figure). Remarkably, the 2 distinct minima that can be seen in this range correspond to the positions of the X and the $2X$ (compare with the spectra in

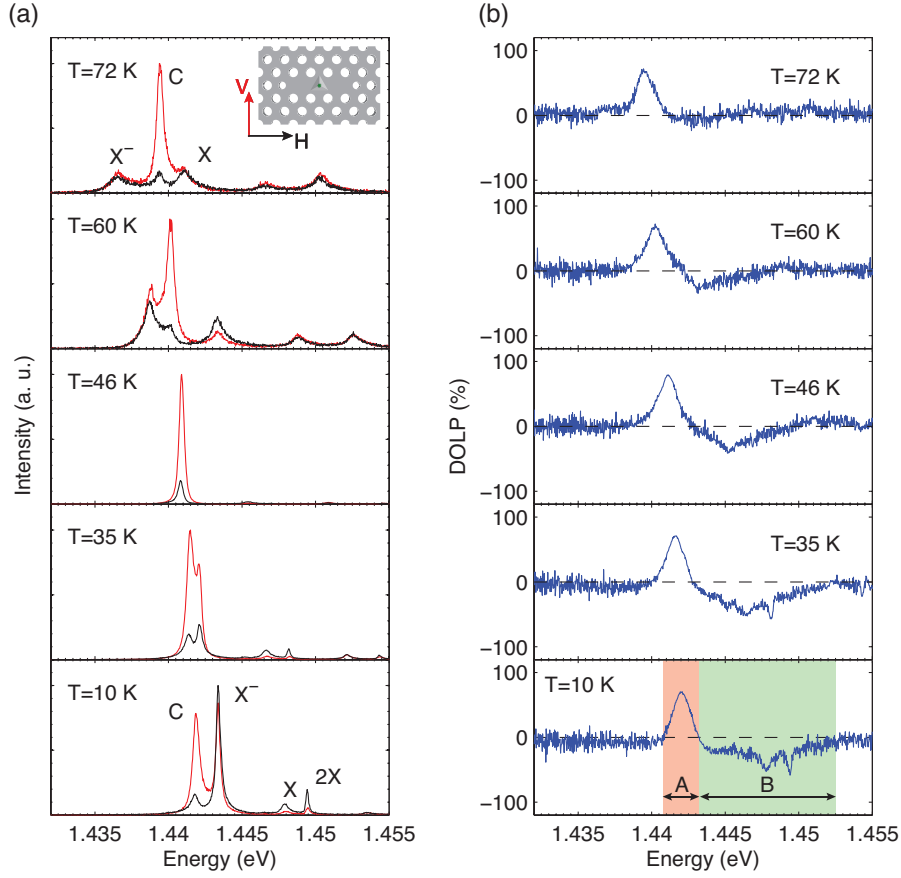


Figure 4.13: (a) Polarization-resolved PL spectra of *S1* as a function of temperature. The excitation power was held constant at $P = 200 \mu W$. (b) DOLP extracted from the spectra in (a).

Fig. 4.13(a)).

By examining the DOLP evaluated at different temperatures in Fig. 4.13(b), one can deduce that the extent and the shape of region *A* do not vary significantly, while the emission in region *B* becomes less polarized with increasing temperature. Before interpreting these rich polarization features, it is important to remember that the Purcell enhancement directly exerted by the cavity is described by a Lorentzian function (see Eq. (4.7)), and furthermore that the QD simultaneously has the possibility to relax into a continuum of mixed TE-TM modes of the PhC [189], as well as residual TE modes within the PBG [190] (see discussion in Sec. 4.1.4). This means that we expect the polarization a QD transition to become cavity-like only within a small detuning range, corresponding approximately to the extent of the Lorentzian cavity profile. Outside of this range, the only electromagnetic modes available are given by the complex continuum of other modes (i.e. TE-TM bands + residual modes). Following this logic, we

4.2. Investigation of the Purcell effect with a single quantum dot

can infer from the plots of the DOLP that region *A* reflects direct Purcell enhancement (Eq. (4.7)), while region *B* must be related to the continuous term in the LDOS of the PhC (Eq. (4.10)). This interpretation is consistent with the experiments recently performed by Wang *et al.*, who demonstrated that QDs act as probes of the LDOS inside PhCs [192].

One might also speculate that the negative DOLP of the emission range *B* is a phonon-mediated depletion effect. More precisely, one could argue that the *X* and *2X* become *H*-polarized as a result of phonon-assisted coupling to the cavity mode. If we apply this hypothesis to the situation at 10 K in Fig. 4.13, then it would mean that the *X* and *2X* transitions were coupled to the mode to the cavity mode despite an energy mismatch of 6 meV and 7.6 meV, respectively. However, this scenario is incompatible with the knowledge that phonon-assisted coupling is only efficient up to a maximum detuning of ± 5 meV [64, 65, 103, 181]. This line of reasoning leads us to the conclusion that the polarization of the emission range *B* cannot be related to phonon-assisted Purcell enhancement.

In order to investigate how a single transition is influenced in its polarization as a function of detuning, we evaluate its DOLP according to Eq. (4.13) by using the integrated intensities projected along *V* and *H*, as extracted from the Lorentzian profile fits of the corresponding emission peak. Using this approach, Fig. 4.14 summarizes how the polarizations of the *X*⁻ and *C* peaks vary as a function of detuning. From this graph it is apparent that the polarization of the *X*⁻ is greatly influenced by the cavity: its DOLP varies steeply from $\Delta E = 1.5$ meV towards resonance and decreases towards zero as the sign of the detuning is reversed. The maximum DOLP value that the *X*⁻ reaches $\sim 80\%$, which matches with the average DOLP of the cavity. One can also notice here that the spectral range within which the polarization of the *X*⁻ becomes cavity-like is limited to $\sim 2 - 3$ meV, which corresponds to the width of the emission range *A* identified in Fig. 4.13(b). The strong variation of the polarization for the *X*⁻ near resonance is an evidence of direct Purcell enhancement.

4.2.4 Linewidth narrowing at resonance

When a QD transition is tuned into resonance with a cavity mode in the weak coupling regime, it is experimentally observed that its photon emission rate is enhanced as a result of Purcell-shortening of the exciton lifetime [111, 112, 186]. If we translate this to an expected behavior of the optical linewidth, it means that the spectral line of the QD should be broader at resonance than when it is detuned from the cavity [20]. However, this only applies in the limit where the spectral width of the QD line is lifetime-limited.

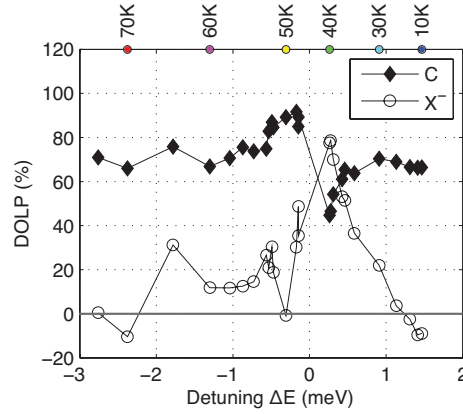


Figure 4.14: (a) Polarization-resolved PL spectra of *S1* as a function of temperature. The excitation power was held constant at $P = 200 \mu W$. (b) DOLP extracted from the spectra in (a).

The results from our experiments demonstrate linewidth behavior that is opposite to this simple picture. In Fig. 4.15(a), we have summarized the variations of the X^- and C linewidths as a function of detuning. Following the QD peak X^- from positive towards negative detunings (i.e. from 10 K to higher temperatures), we see that its linewidth significantly narrows down at resonance. Note that the large broadening of the QD line at higher temperatures (50-70 K) is caused by thermally activated carrier-phonon interactions [74, 77, 79].

Even more strikingly, the linewidth of the cavity peak C also becomes reduced towards zero detuning. Another interesting aspect about the trend of the cavity linewidth is that it appears to have a quadratic dependence on detuning, as shown by the quadratic fits in red. If we analyze the characteristics of the cavity in terms of its quality factor, we find that Q is 1.5 to 2 times larger close to resonance than at an intermediate detuning of ± 1.5 meV. The fact that the cavity linewidth varies as a function of detuning demonstrates that the cavity actually depends on the emitter's emission dynamics, which is a remarkable result.

To the best of our knowledge, such linewidth characteristics have neither been theoretically predicted nor reported from experimental investigations. Incidentally, it has been observed that the QD and the cavity exchange their linewidths when the strong coupling regime is reached, i.e. the cavity line gets narrower while the QD line becomes broader [113, 173]. This differs from the behavior found in Fig. 4.15(a), where *the QD and the cavity both undergo linewidth narrowing*, and apart from that, the sample *S1* investigated here was well within the weak coupling regime. We observed such linewidth narrowing also on other samples (from a separate fabrication run) that contained single QDs in *L3* cavities, which confirmed that this is a reproducible effect.

4.2. Investigation of the Purcell effect with a single quantum dot

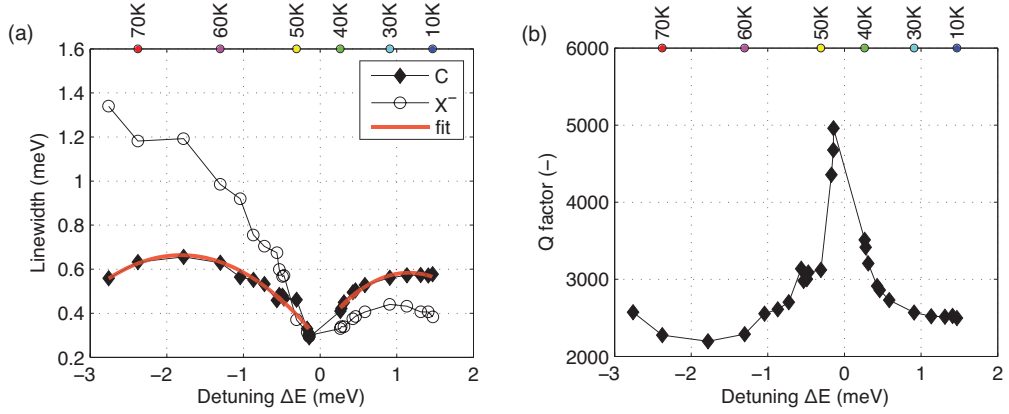


Figure 4.15: (a) Detuning dependence of the X^- and C linewidths and (b) of the quality factor Q , as evaluated for sample S1. The power was held constant at $P = 200 \mu W$. The red curves in (a) are quadratic fits to the data.

Let us first attempt to interpret the linewidth characteristics for the QD within a more refined model that takes into account the non-Markovian dynamics of phonon-assisted QD decay. Following the formalism of Kaer *et al.* [103], we write the total QD decay rate as a sum of 3 contributions:

$$\Gamma_{tot}(\Delta) = \Gamma_{cont}(\Delta) + \Gamma_{Purcell}(\Delta) + \Gamma_{phonon}(\Delta), \quad (4.14)$$

where $\Delta = \omega_{QD} - \omega_c$ is the QD-cavity detuning, Γ_{cont} is the background decay rate which includes emission into a continuum of radiation modes and non-radiative recombination, $\Gamma_{Purcell}$ is the direct Purcell-enhanced rate into the cavity mode, as described by Eq. (4.7) and Γ_{phonon} is the phonon-assisted Purcell enhancement rate. The term Γ_{phonon} is proportional to the *effective phonon density of states*, which is an asymmetric and temperature-dependent function that contains the information about the phonon modes that interact with the QD at a given detuning (see Fig. 6 in Kaer *et al.*, Ref. [103]). At zero detuning, Γ_{phonon} is reduced due to the absence of phonon modes, and the direct Purcell term $\Gamma_{Purcell}$ is dominant. Therefore the total QD decay rate Γ_{tot} is distinctively larger at resonance than for non-zero detunings, i.e. $\Gamma_{tot}(\Delta = 0) \gg \Gamma_{tot}(|\Delta| > 0)$. Again, this would mean that the QD linewidth $\gamma = \Gamma_{tot}$ must broaden at resonance, which contradicts our experimental observations.

The fallacy in our argumentation so far lies in ignoring the effect of the rapidly fluctuating charge environment on the QD [79,81]. An assessment of the X^- linewidth at 10 K in Fig. 4.15(a), which amounts almost $400 \mu eV$, makes it clear that the QD emission line is broadened far beyond the lifetime limit, and entails the conclusion that spectral diffusion has a major influence on the radiative decay dynamics of the

pyramidal QD. Hence, the linewidth γ of the QD must contain an additional pure dephasing term γ_s that specifically takes into account the broadening induced by spectral diffusion:

$$\gamma(\Delta) = \Gamma_{tot}(\Delta) + \gamma_s(\Delta). \quad (4.15)$$

Here we postulate that γ_s is a detuning-dependent function with a minimum at resonance, which we justify by the following arguments:

- The linewidth narrowing effect observed for the X^- in Fig. 4.15(a) can be explained by considering that the QD lifetime $\tau(\Delta) = 1/\Gamma_{tot}(\Delta)$ decreases for $\Delta \rightarrow 0$ due to the Purcell effect. At $\Delta = 0$, the QD exciton is exposed to the fluctuating charge environment for a shorter duration than for $\Delta > 0$. Logically, the total number of pure dephasing events associated with spectral diffusion is reduced for $\Delta \rightarrow 0$, whereby the QD line becomes narrower. To reproduce these characteristics with a theoretical model, it is necessary to introduce a dephasing variable $\gamma_s(\Delta)$.
- According to the experimental results of Berthelot *et al.* [79], the environmental charge fluctuations in InAs/GaAs SKQDs at low temperature take place on a timescale of ~ 10 ps, which is roughly 2 orders of magnitude smaller than the lifetime of a QD in a homogeneous medium (~ 1 ns). If one considers that the reported QD lifetime from experiments comparable to ours [111, 112, 186] became as short as 50-200 ps at $\Delta = 0$, it becomes reasonable to expect that the impact of dephasing due to spectral diffusion must be considerably diminished at resonance. With increasing detuning, the QD lifetime becomes longer and thus the influence of spectral diffusion on dephasing should rise.

To conclude, the linewidth narrowing of the X^- in Fig. 4.15(a) is most likely associated with the reduction of environment-induced decoherence due to of the Purcell effect. However, we have disregarded the linewidth characteristics of the cavity peak so far, which is observed to depend on the QD emission dynamics. In this context, the theoretical analysis of Auffeves *et al.* in Ref. [62] might provide an explanation. We use the approach of Ref. [62] and replace the standard expression for the Q factor of the cavity by

$$\frac{1}{Q_{eff}} = \frac{1}{Q_c} + \frac{1}{Q_d}, \quad (4.16)$$

where $Q_c = \omega_c/\kappa$ is the quality factor of the bare cavity and $Q_d = \omega_d/\gamma$ is the quality factor of the QD. The parameter κ represents the intrinsic photon loss rate of the

cavity, while $\gamma = \Gamma_{tot} + \gamma_s$ is the linewidth of the QD.

According to Eq. (4.16), the effective quality factor Q_{eff} of the cavity is indeed modified as a result of coupling to the QD. If this expression holds true, then a reduction in pure dephasing γ_s of the QD should lead to an increase of Q_{eff} and therefore to a narrowing of the cavity linewidth. Likewise, it follows from Eq. (4.16) that Q_{eff} will be limited if the cavity is coupled to a strongly dephased QD emitter. In contrast to Ref. [62] where the dephasing γ_s was assumed to be a constant parameter, we propose here that γ_s is actually a variable that is also influenced by coupling and depends on detuning, as described earlier. This would explain our observation of linewidth narrowing and the increase in the Q factor in Fig. 4.15.

On the other hand, it cannot be completely excluded that the linewidth narrowing effect could be connected with a polariton-like behavior of the system. Although the characteristic anticrossing behavior of strong coupling was absent in our samples, it is conceivable that the mutual linewidth narrowing of both the QD and the cavity is associated with an intermediate cavity QED regime at the boundary between weak and strong coupling [62, 71, 102, 197]. In this regime, the anticrossing is blurred due to dephasing even though the system exhibits polariton characteristics, and the linewidths of the QD and the cavity become interdependent [197].

In conclusion, the mutual linewidth narrowing of our QD-cavity systems is an intriguing effect that has not been reported before. Further investigations will be necessary to understand its underlying physics. We are planning to report our observations of the linewidth narrowing effect soon.

4.2.5 Photon statistics of the quantum-dot-cavity system

An excited QD that is situated inside a weakly coupled cavity basically has two pathways to deexcite radiatively: it can either pass a photon to the localized cavity mode, or emit a photon directly into a continuum of leaky modes. Provided that the Q factor is large enough, then the cavity can store the captured photon for a finite amount of time before it irreversibly escapes into the environment. For example: if the Q factor amounts to 3000, then the photon storage time $\tau_c = \hbar Q / E_c$ is roughly 10 ps, which is much shorter than the QD exciton lifetime. Thus, the cavity photon will be lost before the QD has had the chance to recapture an electron-hole pair and emit the next photon.

If we translate these considerations to a gedankenexperiment where we measure the photon statistics (see Sec. 2.3.2) of such a QD-cavity system, then we would expect

in the above-mentioned scenario to see antibunching in the $g^2(\tau)$ -histograms for the QD peak as well as for the cavity peak, respectively. The reason for this outcome is that the QD is a single photon emitter, for which the characteristic signature is $g^2(\tau = 0) < 1$ [39, 40, 198]. The same should hold true for the cavity, since it only acts as a funnel for the QD emission. In consequence, the cross-correlation between the QD and the cavity should also exhibit antibunching, since under the described circumstances the photon is either emitted directly by the QD or through the cavity channel.

As it turns out, these expectations comply with the coupling characteristics of pyramidal QDs in PhC cavities. We performed photon correlation experiments for sample *S1* at 10 K where the X^- and the cavity peak were separated by 1.5 meV (Fig. 4.16(a)). The auto- and cross-correlation histograms in Fig. 4.16(b) show an antibunching dip at zero time delay proves that the coupling between the QD and the cavity is regulated at the level of single quanta [64]. This behavior is unique among all QD-cavity systems reported so far. In similar experiments with SKQDs where above-bandgap excitation was employed, the emission from the cavity was observed to be Poissonian or even bunched [116, 169], but never antibunched unless resonant excitation was employed [60, 179]. It was proposed by Winger *et al.* that these unusual photon correlation signatures were a universal feature of QDs in nanocavities and could be explained by cascaded photon emission events stemming from transitions between excited multiexcitonic states [169]. However, our experimental results in Fig. 4.16 unequivocally demonstrate that the latter hypothesis does not apply to pyramidal QDs, and thus not to QD systems in general.

The differences in the photon statistics of SKQDs and pyramidal QDs are most likely related to the differing potential barriers and the resulting electronic DOS, as explained in Sec. 4.1.2. While the lowest-energy barriers of SKQDs are given by the vicinal 2D wetting layer, in pyramidal QDs the lowest-energy barrier structures are the three lateral 1D quantum wires (see Sec. 2.1.2). It is known from PLE and magneto-PL studies that the presence of the 2D WL in the vicinity of SKQDs gives rise to hybridization between bound exciton states and extended WL states [175, 177], such that a continuum of intermixed 0D-2D states is created. The cascaded photon emission from the cavity is a direct consequence of the existence of this continuum [169]. On the other hand, the fact that the cavity emission in Fig. 4.16(b) is antibunched strongly suggests that excitons confined in pyramidal QDs are well isolated from hybridization effects involving delocalized barrier states.

Although the correlation histograms in Fig. 4.16(b) reveal the quantum nature of the light emission characteristics, the rather large value of $g^2(\tau)$ at $\tau = 0$ indicates

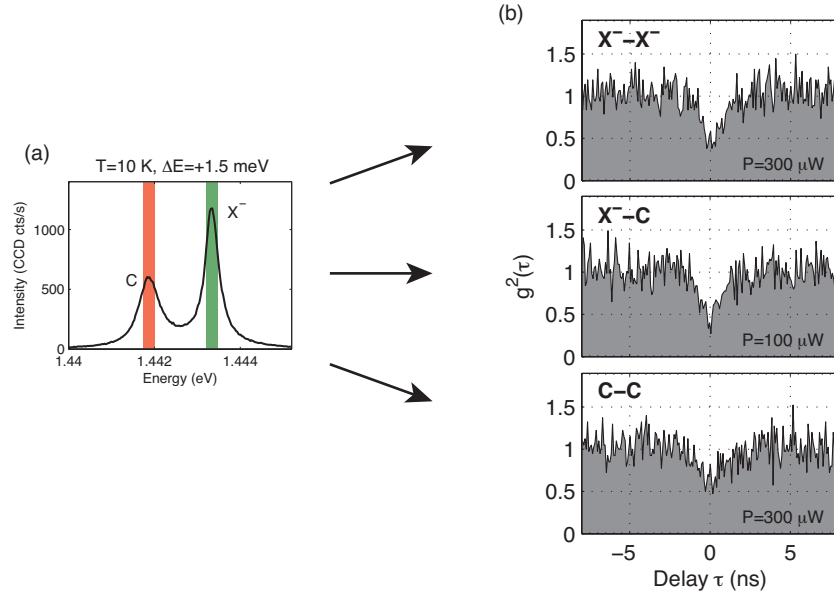


Figure 4.16: (a) Spectrum of SI recorded at 10 K ($\Delta E = 1.5$ meV) and $100 \mu\text{W}$ excitation power. The QD and cavity signals (highlighted in red and green, respectively) were collected from $\sim 100 \mu\text{eV}$ -wide spectral ranges centered on each line. (b) Photon correlation histograms: (top) autocorrelation of the X^- , (middle) $X^- - C$ cross-correlation and (bottom) autocorrelation of the cavity peak C . The sample was excited above-bandgap in CW mode at 700 nm with power levels that are indicated within the graphs.

that uncorrelated photons are admixed to the single photon emission of the QD and the cavity. The origin of this background is partly related to the instrumental response of our measurement setup [39]. An additional contribution to the background is presumably associated with the non-negligible spectral overlap of the X^- and the C peaks in Fig. 4.16(a).

4.2.6 Excitation power dependence

As we argued earlier, the observation of sub-Poissonian emission from the cavity indicates that it is exclusively coupled to a single bound QD state. This statement implies that the cavity should replicate the power dependence of the coupled QD transition, which includes saturation at high powers. If the cavity intensity would instead continue to grow beyond the saturation level of the QD as a function of excitation power, then it would mean that the cavity mode is receiving photons from other transitions, possibly multiexcitonic ones that might involve delocalized charges from the QD barriers [169].

In this context, the power dependence measurements from sample *S1* presented in Fig. 4.17 provide further verification that the cavity is not coupled to any other transitions except for the QD transition in its spectral vicinity [64]. The analysis of the data shown in Fig. 4.17(b) demonstrates that the cavity *C* follows almost precisely the trend of the spectrally close-by X^- , starting from a near-linear increase up to saturation. Clearly, the variation of the cavity intensity does not resemble any of the other QD peaks. This result for pyramidal QDs stands in striking contrast to the behavior of SKQDs incorporated in cavities. In the case of SKQDs, it was observed that the cavity continued to grow in a superlinear fashion far above the saturation levels of the s-shell states, mimicking the behavior of the p-shell states [169–171].

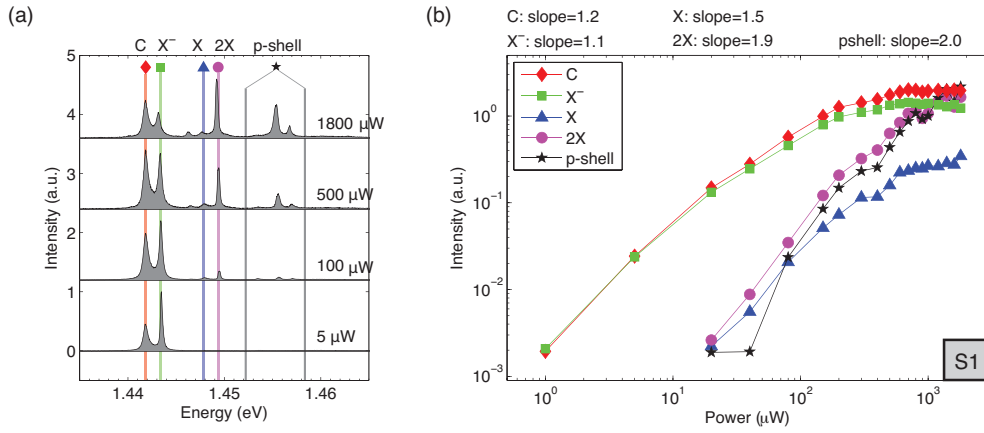


Figure 4.17: Excitation power dependence of *S1* at $T = 10$ K ($\Delta E = 1.6$ meV). (a) Examples of the spectra, showing the cavity *C* and the different QD states. (b) Variation of the intensities as a function of power. The p-shell transition intensities were integrated over the spectral range indicated in (a). Linear fits to the curves yielded the slopes that are specified on top of the graph.

In Ref. [169], where cavity QED experiments with SKQDs are discussed, it was argued that the bunched photon emission characteristics and the superlinear power dependence of the cavity intensity was consistent with the theory that the cavity enhances transitions from higher excitation manifolds of the QD, and that these effects were intrinsic features of QD-cavity systems in general. However, the results of our experiments presented here clearly evidence that such effects are either absent or strongly suppressed in the case of pyramidal QDs. We also mentioned earlier that we did not observe emission from the cavity in a situation where its resonance was far detuned (> 5 meV) from the QD transitions. This also supports the absence of a multiexcitonic background in pyramidal QDs, which would allow the cavity to emit light for detunings larger than the phonon sidebands. As described in the previous section, we suspect that the differences in the coupling characteristics of SKQDs

versus pyramidal QDs are related to their different barrier environments.

4.3 Theoretical analysis

4.3.1 Mode structure of an $L3$ cavity

The results of this thesis are centered on the coupling of QDs to an $L3$ -type PhC cavity, which has been used as a prototype for many cavity QED studies with QDs due to its exceptionally high Q/V ratio with Q factors above 10000. Although we exclusively targeted for the fundamental mode of the $L3$ cavity in our experiments, an understanding of the overall mode structure was important to allow a correct interpretation of the PL spectra. For this purpose we performed both 2D finite-difference calculations as well as 3D FDTD simulations using Matlab codes that were programmed by Dr. K. E. Karlsson (who is currently working at Linköping University). The latter is useful to extract the theoretical Q factor for ideal cavity structures and also to obtain realistic values for the spectral positions of the resonances, but the disadvantage is that these 3D simulations were lengthy and required extensive computational resources. Our 2D modeling is based on an effective index method [199] and is by orders of magnitude faster; it is basically a frequency domain eigenvalue solver that could be applied to obtain the full mode structure and the field distributions in a single run. However, the 2D model is not suitable to get a correct numerical value for the Q factor.

Our calculations of the mode structure for an optimized $L3$ cavity are summarized in Fig. 4.18 and Fig. 4.19. In order to reduce radiation losses and thereby to improve the Q factor, the lateral holes of this cavity were shifted outwards by $0.15 \cdot a$ and shrunk by 15% [156, 158, 159]. Each of the 6 confined modes of the $L3$ cavity is distinguished by a characteristic electromagnetic field distribution and a different resonance wavelength. In Fig. 4.18, the electric field components E_x and E_y as well as the total amplitude $E_{xy} = \sqrt{E_x^2 + E_y^2}$ are plotted for all occurring resonances of the $L3$ structure. The field distributions in Fig. 4.19 were obtained from our 2D model, for which we used the parameters $r/a = 0.3$ and an effective index of $n_{eff} = 3.255$ to account for the vertical confinement of the modes within a slab of finite thickness [199] (in this case $d = 1.325 \cdot a \equiv 265$ nm).

The localized modes are labeled as $M0, \dots, M5$ and are ordered from low to high resonance energy. They can be categorized as "TE-like" modes that belong to the TE polarization of the PhC where a bandgap exists (see Fig. 4.6). Confinement to a patterned slab waveguide structure has the effect of mixing the TE and TM polarization, whereby the guided and localized modes cannot be strictly divided into

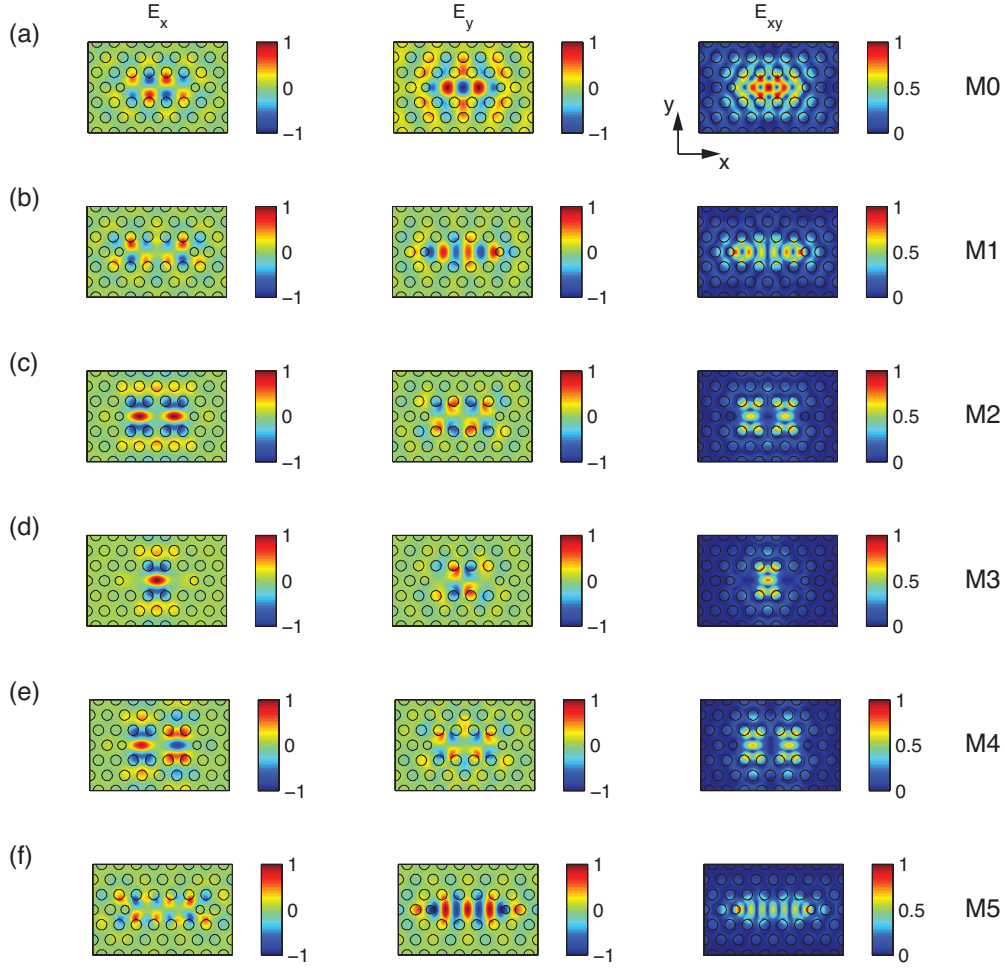


Figure 4.18: Field distributions of the 6 confined modes of an $L3$ cavity, computed by 2D finite differences. The E_x , E_y and $E_{xy} = \sqrt{E_x^2 + E_y^2}$ are shown for the six confined modes labeled $M0 - M5$ in (a)-(f).

TE and TM as in an ideal 2D system [189]. Fig. 4.19(a) shows the results of a 2D calculation of all TE modes within a limited energy range, where one can see that the localized modes $M0, \dots, M5$ are situated within a bandgap between delocalized modes from the so-called dielectric and air bands [92]. The corresponding resonance energies and the magnitudes of the spectral separations are listed in the tables in Fig. 4.19(b) and Fig. 4.19(c), respectively.

Experimentally the modes can be identified in two ways: 1) by comparing the absolute and relative positions of the occurring resonances with theoretical predictions and 2) by measuring the polarization of each mode. According to calculations by Chalcraft *et al.* [159], the $M0$ and $M1$ should be predominantly y -polarized, while

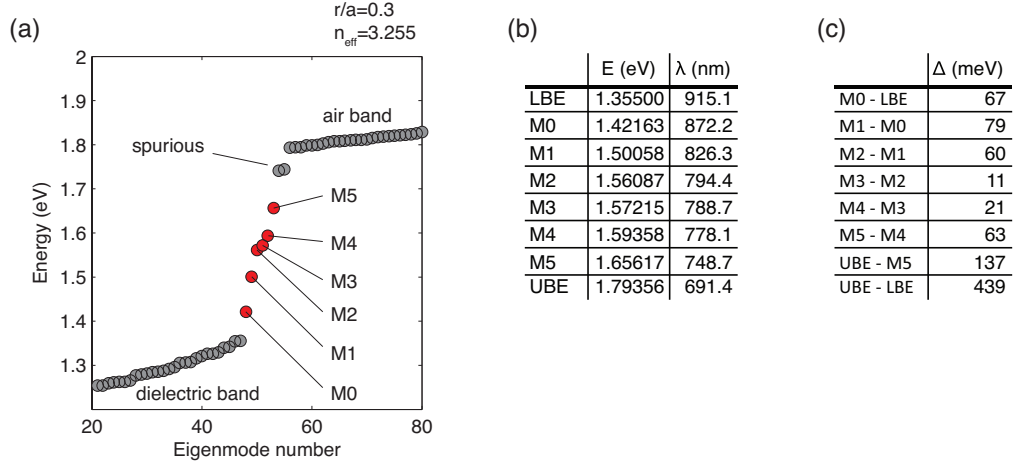


Figure 4.19: (a) TE modes of an $L3$ cavity, calculated by means of 2D finite differences. (b) Energy and wavelength values for the cavity resonances $M0 - M5$, as well as of the lower band-edge (LBE) and the upper band-edge (UBE). (c) Energy difference Δ between the relevant modes.

$M2$, $M3$ and $M5$ are expected to be x -polarized. However, not all modes were simultaneously visible in our experiments, particularly when only a single pyramidal QD was integrated as an internal light source.

4.3.2 Modeling of phonon-assisted Purcell enhancement

One of the main conclusions that can be drawn from our results is that in order to avoid spurious emission in cavity QED experiments with QDs, the QD must be isolated from other low-dimensional confinement structures in its vicinity. This condition appears to be well fulfilled in the case of pyramidal QDs, since we observed that the characteristic features of crossed barrier-QD transitions characteristic of SKQDs were absent in our PL studies. The optical properties of pyramidal QDs are therefore in accordance with the artificial atom picture of "ideal" QDs and ensure that the quantum effects are not masked by spurious phenomena. This is of crucial importance regarding applications of QDs in quantum information processing and opens the way to investigate the influence of inherent decoherence phenomena arising due to the semiconductor crystal environment.

As pointed out in a series of publications from recent years, the existence of quantized lattice vibrations modifies the spectral response of QD-cavity systems and enlarges the bandwidth over which coupling can take place [59, 60, 64–66, 69, 103, 181]. We employed the formalism by Tarel and Savona [181] to evaluate whether the PL

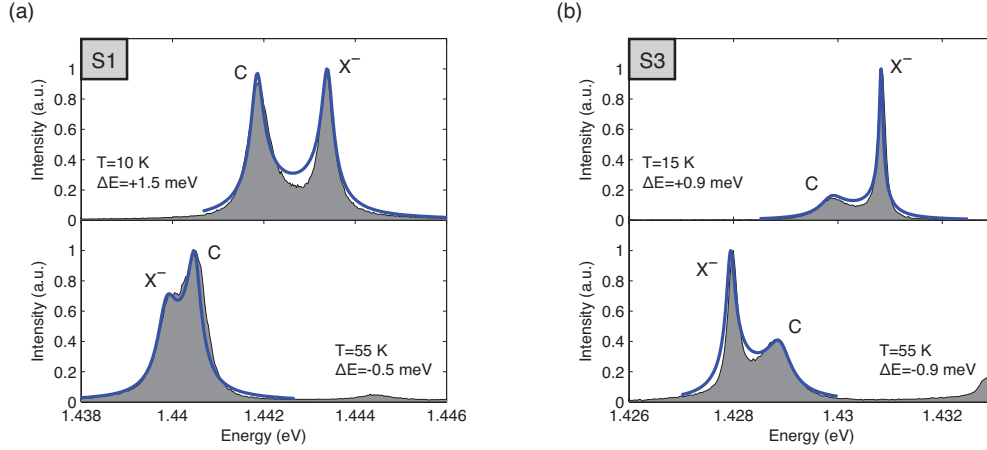


Figure 4.20: Modeling of the measured PL spectra of a single pyramidal QD in an $L3$ cavity, including phonon-assisted coupling processes. The experimental data is presented in gray and the calculated fits in blue, respectively. (a) Spectra of sample $S1$. Used parameters: $g = 150 \mu\text{eV}$, $\gamma = 200 \mu\text{eV}$, $\kappa = 250 \mu\text{eV}$. (b) Spectra of sample $S3$. Used parameters: $g = 200 \mu\text{eV}$, $\gamma = 100 \mu\text{eV}$, $\kappa = 250 \mu\text{eV}$.

spectra that we measured for pyramidal QDs in PhC cavities could be adequately described with phonon-induced pure dephasing. The semiclassical theory in Ref. [181] models the interaction between the QD and the acoustic phonon reservoir by means of a Greens-function approach. In the mentioned article, Tarel and Savona derived an analytic formula for calculating the total emission spectrum $S(\omega)$ of a QD-cavity system:

$$S(\omega) = \left| \frac{\sqrt{4g^2 - \frac{(\gamma - \kappa)^2}{4}} \left(\omega_c - \omega - i\frac{\kappa}{2} \right)}{\left(\omega_0 - \omega - i\frac{\gamma}{2} + \Sigma(\omega) \right) \left(\omega_c - \omega - i\frac{\kappa}{2} \right) - g^2} \right|^2 \quad (4.17)$$

Here g , γ and κ represent the coupling strength, the exciton free decay rate and the cavity loss rate, respectively. In this expression, the imaginary part of the exciton-phonon self-energy $\Sigma(\omega)$ contributes to the QD lineshape. Using this approach, we performed fits to the emission spectra for two different, but nominally equal, QD-cavity structures $S1$ and $S3$ measured at different temperatures. As can be verified in Fig. 4.20, the theoretical modeling nicely reproduces the measured lineshapes in both cases. Other pure dephasing mechanisms such as spectral diffusion were taken into account phenomenologically as a constant factor in the modeling, by setting γ to match the observed lineshape in the PL spectrum.

The good agreement between our experimental data and the fits shows that the signatures of phonon-induced dephasing are visible in the spectra presented in Fig. 4.20. In addition, it can be ruled out that an additional background feeds the cavity emission, because in that case there would be a pronounced discrepancy between the model and the data. In order to produce more accurate fits, it will most likely be necessary to develop a model that also includes the effects of spectral diffusion in a more realistic way.

4.3.3 Effect of pure dephasing at resonance

It appears from the temperature dependence in Fig. 4.10(a) that the QD-cavity system *S1* is in the weak coupling regime, since the characteristic anticrossing behavior of strong coupling is not observed. At temperatures between 40 K and 50 K where resonance occurs, only a single peak is seen in the spectra instead of a polariton doublet. However, there also exists an intermediate cavity QED regime where Vacuum Rabi splitting is actually present, but cannot be resolved in the spectral domain due to dephasing mechanisms [62, 71, 102]. The existence of such an intermediate coupling regime was experimentally confirmed by Laucht *et al.*, who showed that the polariton doublet is reduced to a singlet as the dephasing rate is increased. One should therefore be cautious not to classify a QD-cavity system prematurely as being weakly coupled.

In order to establish a better judgement of the coupling regime probed in our experiments, we first investigate the coupling between the emitter and the cavity theoretically. Here we apply the analytical expressions for the side emission spectrum derived by Cui and Raymer [70] to calculate the temporal evolution of the state populations and the emission spectra for different sets of parameters. The derivations in Ref. [70] are based on the Weisskopf-Wigner approximation of spontaneous emission and also treat the influence of Markovian pure dephasing to the coupling process. Although the model does not capture the complexities of dephasing interactions happening at the microscopic level (such as carrier-phonon scatterings), it is still a very useful tool for developing an understanding of how emitter-cavity coupling is affected by these processes.

Let us first consider the resonant situation, i.e. at zero QD-cavity detuning, in the absence of pure dephasing. The QD and the cavity are both described as coupled two-level systems that weakly interact with continuous reservoir fields of the environment. The population decay rates of the QD and the cavity are given by γ and κ , respectively, and the QD-cavity coupling strength is designated by g_0 . As a first step, we will investigate how the QD-cavity dynamics is affected by varying κ .

Since we are completely ignoring pure dephasing for the moment, the QD decay rate should in principle only be limited by the intrinsic exciton lifetime τ_0 . For our InGaAs QDs, τ_0 amounts approximately to 1 ns [200], which corresponds to a linewidth of $\sim 1 \mu\text{eV}$. We therefore assume that $\hbar\gamma = \hbar\gamma_0 = 1 \mu\text{eV}$, where γ_0 stands for the intrinsic decay rate of the QD. We choose to set the coupling strength to $\hbar g_0 = 150 \mu\text{eV}$, which is based on results obtained from numerical modeling of our data [64]. It should be noted that this number is possibly overestimated, because it is about twice as large as the values reported from similar experiments with strongly coupled SKQD-cavity systems [28, 71, 116, 118, 120, 121, 149].

The results of our calculations for 3 different, realistic values of κ are shown in Fig. 4.21. With $\hbar\kappa = 100 \mu\text{eV}$ ($Q \sim 14000$), the QD-cavity system is in the strong coupling regime, as damped Rabi oscillations are seen in the state population dynamics in Fig. 4.21(a). Here we assumed an excited QD and an empty cavity as the initial state. A quantum of energy is exchanged between the QD and the cavity every ~ 87 ps, corresponding to a Rabi frequency of $\Omega_R \sim 2g_0 \sim 72.54$ GHz. In the spectral domain, the coherent quantum dynamics are manifested by the presence of two non-Lorentzian polariton peaks split by $\hbar\Omega_R \sim 300 \mu\text{eV}$. When the cavity losses are doubled to $\hbar\kappa = 200 \mu\text{eV}$ ($Q \sim 7000$), the period shortens over which Rabi oscillations take place and the two polariton peaks broaden (Fig. 4.21(c) and (d)). Finally, using $\hbar\kappa = 500 \mu\text{eV}$ ($Q \sim 3000$) which is comparable to our experimental values, Fig. 4.21(e) shows that the losses overwhelm the coherent QD-cavity interaction, such that reversible energy exchange cannot persist. As a result, the emission spectrum becomes single-peaked and the QD-cavity system is in the weak coupling regime.

We now proceed to investigate the influence of the QD environment by introducing pure dephasing with a rate γ_d , while keeping the other parameters fixed at $\hbar g_0 = 150 \mu\text{eV}$, $\hbar\gamma_0 = 1 \mu\text{eV}$ and $\hbar\kappa = 100 \mu\text{eV}$. The results presented in Fig. 4.22 for 3 different values of γ_d visualize the effect of pure dephasing: its presence causes the Rabi oscillations to be smeared out towards an exponentially decaying curve in the temporal dynamics of the QD and the cavity state populations. In consequence, the polariton peaks of the emission spectrum become broadened and eventually merge to a single peak when the rate of phase fluctuations becomes too large.

Based on this analysis, one would tend to conclude that the QD-cavity investigated experimentally in this thesis were most likely in the weak coupling regime. First of all, it is possible that $\hbar g_0 = 150 \mu\text{eV}$ is overestimated, so the Rabi splitting is likely to be smaller in reality than what we obtained in the calculations above. Second, the Q factors of our systems were not larger than 3000, which is not sufficient for achieving strong coupling even if we believe that $\hbar g_0 = 150 \mu\text{eV}$ and disregard pure dephasing

(Fig. 4.21(e) and (f)). Finally, if we do take into account pure dephasing as well - which often contributes to $\sim 100 \mu\text{eV}$ or more in our QD systems - , then the prospects of reaching the strong coupling regime become even slimmer. We therefore interpreted the experiments presented in this chapter within the weak coupling picture. However, the boundary between weak and strong coupling is not sharply defined, and it is possible that effects such as the linewidth narrowing (see Sec. 4.2.4) are associated with the physics of an intermediate cavity QED regime [62, 71, 102, 197].

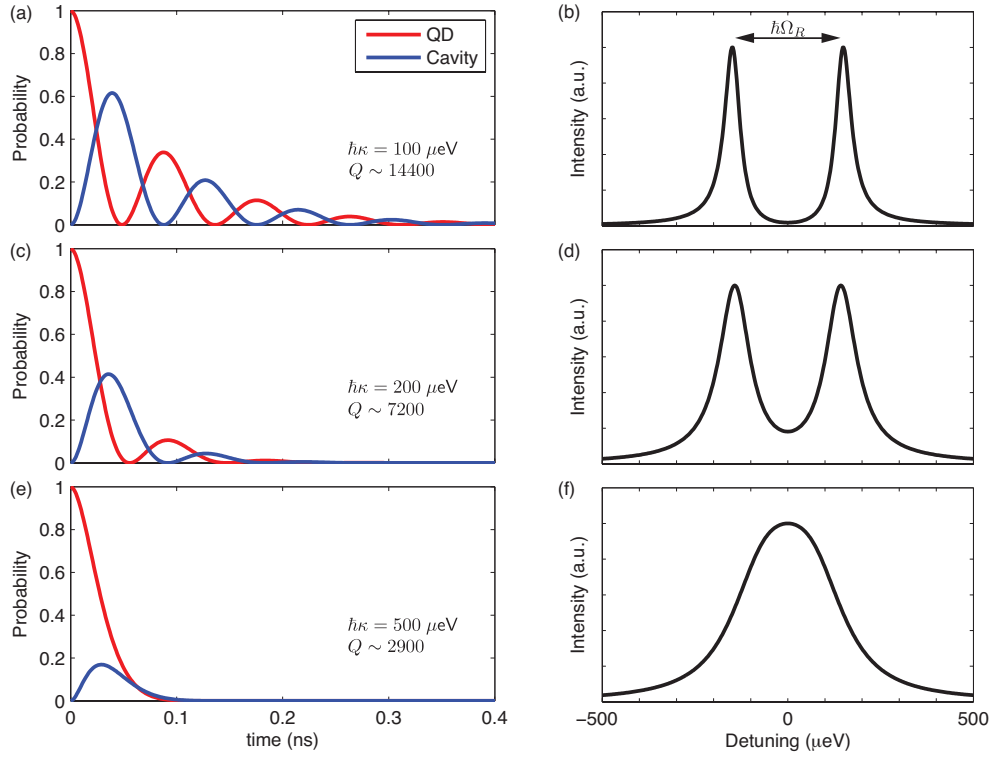


Figure 4.21: Calculated population dynamics (left column) and side emission spectra (right column) of a QD-cavity system at resonance and in the absence of pure dephasing. The only parameter that was varied here was the cavity loss rate κ , as indicated in the graphs. The remaining parameters were fixed at $\hbar g_0 = 150 \mu\text{eV}$ and $\hbar\gamma = 1 \mu\text{eV}$.

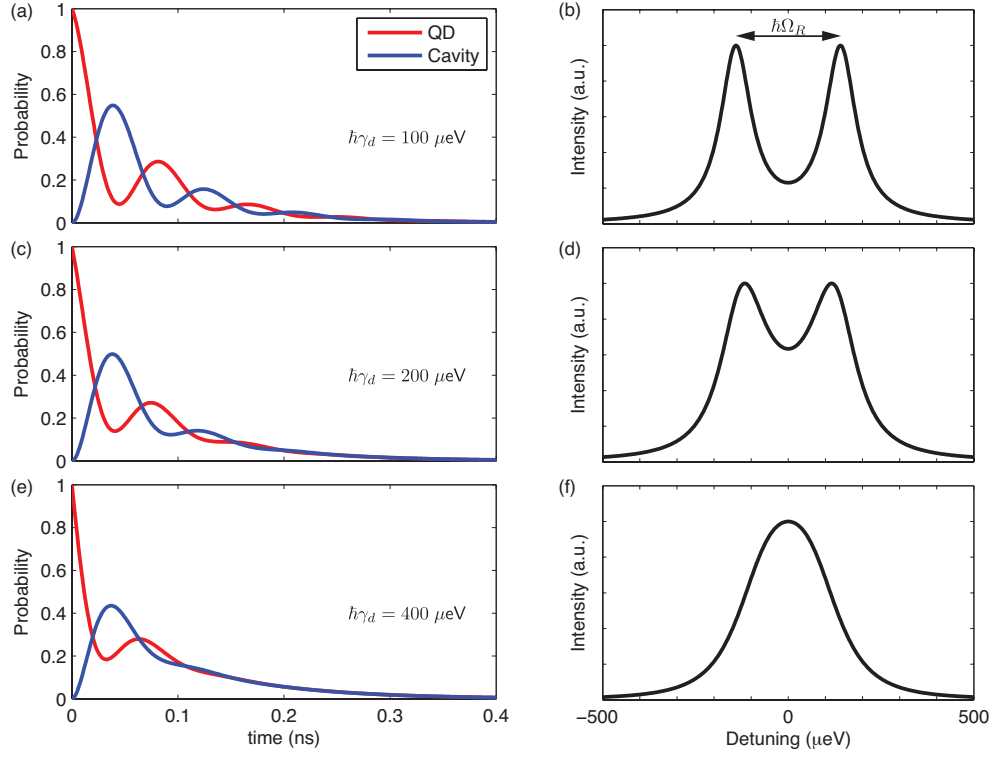


Figure 4.22: Calculated population dynamics (left column) and side emission spectra (right column) of a QD-cavity system at resonance, this time in the presence of pure dephasing. Only the pure dephasing rate γ_d was varied here, as indicated in the graphs. The remaining parameters were fixed at $\hbar g_0 = 150 \mu\text{eV}$, $\hbar \gamma_0 = 1 \mu\text{eV}$ and $\hbar \kappa = 100 \mu\text{eV}$ ($Q \sim 14000$).

4.4 Chapter summary

In summary, in this chapter we presented polarization-resolved PL studies and photon correlation measurements of single pyramidal QDs in $L3$ PhC cavities. Our findings, which we partly published in [64], showed that the coupling characteristics of single pyramidal QDs in PhC nanocavities is very close to the model of an "artificial atom" in a solid state matrix. More specifically, we demonstrated that the photon emission from the cavity mode is antibunched and correlated only with a single excitonic transition of the pyramidal QD. Our measurements of the excitation power dependence showed that the cavity mode saturates simultaneously with the near-resonant excitonic transition. We also found that the optical polarization of a QD exciton sensitively depends on detuning, such that close to resonance the QD transition switches from being oppositely polarized to co-polarized with the cavity mode. By means of a theoretical model of phonon-assisted Purcell enhancement, we were able to fit the optical spectra with good agreement. Taking these results together, we conclude that the behavior of a pyramidal QD in a cavity is in accordance with the picture of an artificial atom with well isolated, discrete 0D states that interact with the solid state environment.

This conclusion is a priori not obvious, since in experiments performed by a number of research groups working with more conventional self-assembled SKQDs revealed that the coupling features of these systems were contradictory with the artificial atom model. It was observed that the cavity mode emission was contaminated with uncorrelated photons, which could also "feed" the cavity in a far-off resonance situation. Another aspect of this spurious cavity feeding phenomenon with SKQDs is that in power dependence measurements the cavity emission does not saturate together with the s-shell states. A candidate explanation for the negligible influence of cavity feeding in the case of pyramidal QDs is that their barrier environment does not contain a 2D wetting layer like SKQDs, thus favoring better isolation of confined excitons. The lowest-energy barriers of pyramidal QDs are the lateral 1D quantum wires, which do not seem to perturb the quantized states of the QD. However, the reason for this negligible influence of the quantum wires on the QD states has not been theoretically analyzed yet; a modeling of Auger processes involving 1D barrier transitions could provide valuable insights [201].

Last but not least, we reported a previously unnoticed linewidth narrowing phenomenon that occurs when a pyramidal QD is spectrally tuned through resonance with the cavity mode. This brought up the question about whether effects related to spectral diffusion might explain the results. To date, there exists no microscopic description of spectral diffusion that could be included in theoretical cavity QED models.

5 Two spatially separated quantum dots in a photonic crystal cavity

The great interest in QDs has largely been driven by their potential of being used as tailor-made quantum light sources for chip-scale realizations of novel nanophotonic devices as well as fundamental experiments in quantum optics [51, 105, 162]. Several proof-of-principle experimental works in recent years (e.g. Refs. [100, 107, 118, 122]) have shown that single QDs could be combined with photonic cavities to build elementary components of quantum networks and quantum communication systems [51, 53, 160, 162, 202]. One of the pivotal questions to be addressed for future developments in this area is whether QD-based cavity QED systems can be scaled such that two or more QDs can be mutually coupled to the same mode of the electromagnetic field. In particular, the cavity-mediated radiative coupling of distant QDs is not only highly interesting for exploring multi-particle entanglement [203] and collective behavior of interacting quantum systems [204, 205], but is also a prerequisite for constructing efficient QD nanolasers [206] and for performing logic gate operations on multi-qubit systems [207].

However, the targeted and controlled scaling of the number of QD emitters effectively coupled to a microcavity had so far been obstructed due to the lack of spatial alignment methods and the large inhomogeneous broadenings of the conventionally used self-assembled QDs [34]. Although the signatures of cavity-mediated coupling between QDs were the subject of several recent publications [195, 208–213], they all relied on SKQDs that were randomly distributed in the spatial region of the cavity and only coincidentally happened to overlap spectrally and spatially with its resonant optical mode. Apart from being fabricated in a nondeterministic fashion, the reported experiments had the following flaws in common: 1) The precise locations of the QDs were unknown. 2) SKQDs exhibit a background continuum related to intermixed QD-WL states, which also couple to the cavity and thereby introduce spurious photons (the so-called "cavity feeding" phenomenon, see Sec. 4.1.2). 3) The presence of additional "parasitic" QDs in the cavity region cannot be excluded [115].

Chapter 5. Two spatially separated quantum dots in a photonic crystal cavity

In the previous two chapters, we demonstrated that pyramidal QDs do not suffer from these drawbacks. Their site-controlled fabrication approach leads to deterministic nucleation of QDs at precisely defined sites, and the number of QDs can be scaled in a targeted fashion. In the present chapter, we summarize our experimental studies performed on $L3$ -type PhC cavities with two embedded pyramidal QDs. The QDs were spatially separated from each other by a subwavelength distance of ~ 350 nm and were individually positioned at the secondary antinodes of the fundamental cavity mode (Fig. 5.1(b) and (c)). Owing to the precise spatial and spectral alignment features of the pyramidal QDs and their scalable fabrication method (see Chapter 3), we were able to integrate many such devices on a single chip and systematically investigate their PL characteristics.

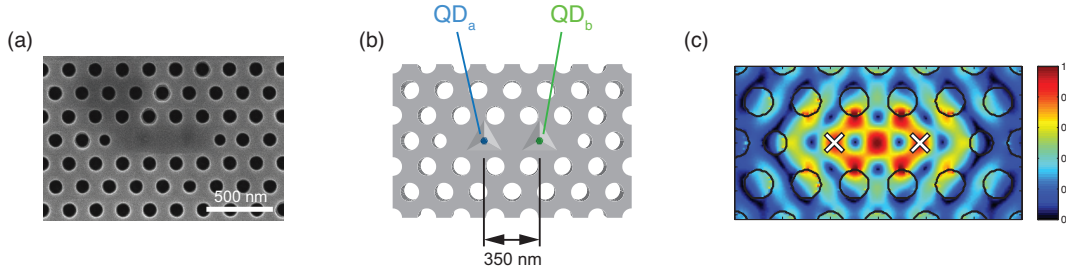


Figure 5.1: (a) Image of a fabricated structure consisting of 2 pyramidal QDs embedded in an $L3$ PhC cavity. The locations of the pyramids are visible in this picture in the form of slightly darker spots. (b) Schematic of the design. (c) Electric field distribution of the fundamental cavity mode, computed by a 2D finite differences method. The white crosses designate the target positions of the QDs.

The outline of this chapter is as follows: In Sec. 5.1, we introduce the reader to the Dicke model which describes the mutual interaction of $N \geq 2$ quantum emitters with the quantized field of a cavity. Furthermore, we briefly discuss physical realizations with atoms, superconducting qubits and QDs.

In Sec. 5.2, we discuss the general behavior of 2 pyramidal QDs in an $L3$ cavity. We show spectra from polarization-resolved PL studies that demonstrate the systematic r/a -tuning of the cavity resonances and reveal characteristic polarization features that we reproducibly measured in many different devices. Interestingly, we found that even non-resonant cavities are capable of emitting a significant amount of light at the cavity mode resonance frequency, which is in stark contrast to the coupling characteristics that we observed with single pyramidal QDs. However, as our results from power dependence measurements suggest, the off-resonant cavity emission from pairs of pyramidal QDs is not related to excited QD states from the p-shells as in the case of SKQDs [169], but comes from the ground state transitions from the s-shells.

In Sec. 5.3, we show evidence of mutual coupling of a QD pair with a resonant $L3$ cavity mode. This finding represents the first successful demonstration of coupling two site-controlled QDs to a PhC cavity. We present results from the power dependence of the coupled system, which exhibits a markedly different behavior compared to a single QD in a cavity. In particular, the cavity mode emission does not saturate together with the spectrally adjacent QD transitions, but at much higher powers. Remarkably, at high powers the emission peaks of both QDs gradually disappear from the spectrum, leaving the cavity mode as the only dominant emission channel. These observations might be an indication of collective behavior, possibly induced by radiative coupling [214–217].

5.1 Two quantum emitters in a cavity: An Introduction

5.1.1 Theory

The Dicke model

Prior to discussing the experimental results of this chapter, it is instructive to address the following central question: What is to be expected when two or more quantum emitters are encapsulated within a microcavity such that they can only interact with a single quantized mode of the radiation field (Fig. 5.2(a))?

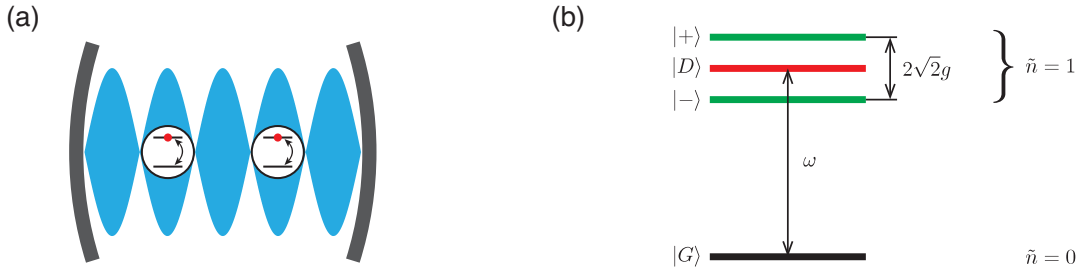


Figure 5.2: (a) Illustration of 2 emitters interacting with a single mode (depicted in blue) of the quantized radiation field within a cavity. (b) Corresponding energy level structure at resonance for the $\tilde{n} = 0, 1$ manifolds. $|G\rangle$ is the ground state of the system, $|+\rangle$ and $|-\rangle$ are two bright dressed states and $|D\rangle$ is the dark state.

Apart from the possibility of generating entanglement among the constituent members of the qubit ensemble [218] and facilitating lasing [219], the interaction with a distinct photonic mode can induce collective spontaneous emission, a phenomenon known as *superradiance* that was first predicted in the seminal paper by Dicke in 1954 [220]. In his theoretical analysis, Dicke considered a cloud of inverted atoms

densely packed within a volume that is much smaller than the wavelength of the radiation. He suggested that in this case the N emitters could no longer be treated as being independent. The mutual interaction of the atomic dipoles with a common radiation field synchronizes their phase relationships and makes them relax their energy in a very short, intense burst of light. This *superradiant* pulse has a duration which is N times shorter than the exponential decay time of N independent emitters, and its intensity scales with N^2 [204, 220]. Another consequence from Dicke's model is the emergence of *subradiant* states, for which the dipoles interfere destructively and spontaneous emission is suppressed. In general, the radiative dynamics of an N -emitter system is determined by an interplay between the collective super- and subradiant states [214, 219, 221].

While Dicke's original model was dedicated to emission in free space and required the atoms to be very close to each other, the presence of a cavity permits the observation of cooperative emission for much larger dipole-dipole separations [204, 205]. The most common theoretical approach to investigating the properties and the dynamics of multiple quantum emitters in a cavity is to adopt the Tavis-Cummings Hamiltonian [209, 211, 212, 216, 220, 222–227]

$$\hat{H} = \hbar\omega_c \hat{a}^\dagger \hat{a} + \sum_{i=1}^N \left(\frac{\hbar\omega_i}{2} \hat{\sigma}_i^z + \hbar g_i (\hat{a}^\dagger \hat{\sigma}_i^- + \hat{\sigma}_i^+ \hat{a}) \right). \quad (5.1)$$

This equation implies that the cavity acts as a "quantum bus" which coherently distributes quantum information among the N qubits by using photons as information carriers [207, 227]. Here ω_c is the resonance frequency of the cavity, \hat{a}^\dagger and \hat{a} are the photon creation and annihilation operators, N is the number of qubits interacting with the cavity, ω_i is the transition frequency of the i th qubit, $\hat{\sigma}_i^z = \frac{1}{2}(|g_i\rangle\langle e_i| - |e_i\rangle\langle g_i|)$ is a Pauli operator with $|g_i\rangle$ and $|e_i\rangle$ being the ground and excited states of the qubit, g_i is the light-matter coupling strength, and $\hat{\sigma}_i^+ = |e_i\rangle\langle g_i|$ and $\hat{\sigma}_i^- = (\hat{\sigma}_i^+)^\dagger$ are raising and lowering operators. In the model discussed here, it is assumed that the inter-qubit distance is large enough so that direct wavefunction overlap (tunneling) and electrostatic dipole-dipole interactions can be neglected. The total number of excitations in the system described by the Hamiltonian in Eq. (5.1) is $\tilde{n} = \hat{a}^\dagger \hat{a} + \sum_{i=1}^N |e_i\rangle\langle e_i|$ (which is not the same as the number of photons $n = \hat{a}^\dagger \hat{a}$).

The case of 2 emitters

Let us now restrict ourselves to the simple case where $N = 2$ identical quantum emitters are at exact resonance with a cavity ($\omega_1 = \omega_2 = \omega_c \equiv \omega$) and further assume

5.1. Two quantum emitters in a cavity: An Introduction

equal coupling strengths ($g_1 = g_2 \equiv g$). In this case, the Hamiltonian becomes

$$\hat{H} = \hbar\omega\hat{a}^\dagger\hat{a} + \hbar\omega\hat{\sigma}^z + 2\hbar g(\hat{a}^\dagger\hat{\sigma}^- + \hat{\sigma}^+\hat{a}), \quad (5.2)$$

where the first two terms represent the energies of the bare photonic mode and of the quantum emitters, respectively, and the third term describes their mutual interaction in the rotating wave approximation. The $2 \otimes 2 \otimes \infty$ Hilbert space of this tripartite quantum system is spanned by the basis $|j, j\rangle \otimes |n\rangle$, where $|j, j\rangle$ with $j = e, g$ denotes the eigenstates of the free quantum emitters and $|n\rangle$ with $n = 0, 1, 2, \dots$ is a Fock state of the cavity [223, 227].

When there is only a single excitation present in the coupled system, then the collective eigenstates of the Hamiltonian are

$$|+\rangle = \frac{1}{\sqrt{2}}|g, g\rangle \otimes |1\rangle + \frac{1}{2}(|e, g\rangle + |g, e\rangle) \otimes |0\rangle \quad (5.3)$$

$$|-\rangle = \frac{1}{\sqrt{2}}|g, g\rangle \otimes |1\rangle - \frac{1}{2}(|e, g\rangle + |g, e\rangle) \otimes |0\rangle \quad (5.4)$$

$$|D\rangle = \frac{1}{\sqrt{2}}(|e, g\rangle - |g, e\rangle) \otimes |0\rangle \quad (5.5)$$

and the corresponding eigenfrequencies are $\omega_{\pm} = \omega \pm \sqrt{2}g$ and $\omega_D = \omega$. An energy level diagram of the system is depicted in Fig. 5.2(b). The two states $|+\rangle$ and $|-\rangle$ are optically bright states, because they can be excited from and decay to the ground state $|G\rangle = |g, g\rangle \otimes |0\rangle$. Their splitting amounts to $2\sqrt{2}g$, which is exactly $\sqrt{2}$ times larger compared to the Vacuum Rabi splitting of a single emitter coupled to a single cavity mode in the Jaynes-Cummings model. The antisymmetric third state of the triplet, $|D\rangle$, does not couple to the radiation field and is therefore referred to as the subradiant (dark) state. Higher excitation manifolds ($\tilde{n} = 2, 3, \dots$) of the two-emitter system also consist of such triplets, where the energy spacing between the two bright states scales with $\sqrt{4\tilde{n} - 2}$ with increasing excitation number \tilde{n} [226].

Increasing the number of resonant emitters N beyond 2 does not introduce new energy levels to the triplet structure of the first excitation manifold. Instead, the system acquires $N - 1$ dark eigenstates that are degenerate, and the energy separation between the two Rabi-split bright states amounts $2\sqrt{N}g$ [221, 224]. The \sqrt{N} scaling of the normal mode splitting is indicative for collective behavior and has indeed been observed in experiments with cesium atoms and superconducting qubits [96, 224], but not yet with QDs.

Collective behavior in open emitter-cavity systems

We have so far only discussed the ideal situation where we have identical emitters in a perfect cavity, with equal coupling strengths and no interactions with the environment. But in real systems, dephasing processes and imperfections can reduce or even break the cooperativity. In the case of QD excitons, additional complications occur because of intrinsic differences in their optical transition energies (i.e. inhomogeneous broadening) and due to many-body interactions with the environment.

Nevertheless, Temnov and Woggon showed in their theoretical analysis [214] that even an ensemble of non-monochromatic emitters in a low- Q cavity could experience superradiant and subradiant emission dynamics, which would be manifested in a bi-exponential energy decay. The same authors later postulated [228] that the cooperative evolution of $N < 10$ continuously pumped emitters via collective states would be distinguished by photon bunching, thus permitting experimental verification by means of photon correlation spectroscopy. Perhaps unexpectedly, the bunching amplitude in the second order correlation function $g^{(2)}(\tau)$ was predicted to be larger for $N = 2$ emitters than for $N > 2$ [216, 228].

Temnov and Woggon further found that pure dephasing and inhomogeneous broadening would couple the bright and dark collective states, leading to a reduction and eventual disappearance of the bunching peak in $g^{(2)}(\tau)$ [228]. These conclusions were shared by Auffèves *et al.* [216], who also went further and examined the impact of the cavity loss rate κ on the temporal correlations of the emitted photons. The calculations of these authors showed that cooperative bunched emission is favored at intermediate κ (as compared to the coupling strength g), while $\kappa \ll g$ would induce lasing and for $\kappa \gg g$ the emitters would lose their collective behavior.

5.1.2 Physical realizations

Atoms

Atoms might naturally appear as a first choice to experimentally study the Dicke model, since they are truly identical and because they constitute the simplest two-level systems that one can controllably manipulate in a laboratory. However, isolating single atoms in vacuum and localizing them within high-finesse cavities requires very sophisticated methods and expensive equipment. The first successful attempt to investigate a small number of atoms ($N \leq 10$) in an optical cavity was reported by Thompson *et al.* in 1992, for which they used an atomic beam apparatus where cesium atoms were passed through a cavity formed by two mirrors [96]. The authors

5.1. Two quantum emitters in a cavity: An Introduction

measured the transmission spectrum for $N = 1$ to 10 atoms and found a Rabi doublet for which the splitting scaled with \sqrt{N} , indicating collective coupling (as discussed above). However, the drawbacks of this experiment were the number fluctuations of the atoms and their undetermined positions. In order to eliminate these uncertainties, efforts were undertaken to keep the atom positions fixed within a cavity. This was achieved by Ye *et al.* in 1999 by means of laser cooling and trapping techniques to trap a single cesium atom [229], and later by Keller *et al.* in 2004 using an ion trap arrangement to localize a single calcium ion [230]. Nonetheless, these elaborate methods have so far not been extended to allow the trapping of two or more atoms.

Superconducting qubits

Among the candidates for exploring controlled collective interactions between few emitters and a cavity, superconducting circuits [231] are currently one of the most promising and advanced platforms. In 2009, Fink *et al.* investigated a millimeter-sized circuit structure that contained 3 superconducting qubits embedded in a microwave resonator [224]. The flux-controlled qubits were deterministically positioned at the field antinodes of the cavity mode and could be tuned independently in and out of resonance, which made it possible to selectively probe the eigenvalue spectrum of $N = 1, 2$ and 3 strongly coupled quantum emitters for a continuous range of detunings. The measured transmission spectra were in excellent agreement with the Tavis-Cummings model, demonstrating the \sqrt{N} nonlinearity of the Rabi splitting and the coexistence of both bright and dark collective states. These results underline the advantages of a solid-state approach to studying multiple emitters in a cavity, where the coupling can be precisely controlled. On the other hand, the milli-Kelvin operation temperatures and the lack of efficient detectors at gigahertz frequencies [205] pose limitations to the use of superconducting qubits for practical applications in cavity QED devices.

Quantum dots

The advantages of QDs over superconducting qubits are their operation at elevated temperatures (up to $\sim 70 - 80$ K for GaAs-based materials), their 100 times larger coupling strengths (up to $\sim 100 \mu\text{eV}$ for QDs [116, 120, 149] compared to $\sim 1 \mu\text{eV}$ for superconducting qubits [207, 224, 232]) and their potential telecom-wavelength emission. An initial report of cavity-mediated coupling of 2 QDs was published by Reitzenstein *et al.* in 2006, where the authors studied a micropillar system with InGaAs QDs and observed an anticrossing of 2 spectrally close excitonic lines with the cavity mode [208]. They observed a spectral triplet at resonance; however, according to the Dicke model and experimental observations with two superconducting qubits in

a cavity [224], in a cooperative system there should only be a doublet at resonance consisting of the two Rabi-split bright states. Four years later, Laucht *et al.* examined the PL from 2 InGaAs QDs as they were tuned into resonance with an $L3$ -type PhC cavity by means of applying a voltage to the structure [209]. In that case, they observed a triplet-like spectral feature when two separate QDs were mutually tuned into resonance with the cavity mode. Also here the presence of cooperative effects could not be unambiguously concluded. Similar experiments with 2 QDs in a cavity were reported in Refs. [195, 210–212]. However, as already mentioned in the beginning of this chapter, the most problematic issue common to all these studies was that the QDs were randomly distributed in the cavity structures. As a consequence, the actual positions of the QDs within the cavity were unknown, and the presence of additional parasitic QDs could not be excluded. There are no reports to date that unambiguously demonstrated the *deterministic* coupling of exactly two QDs to a cavity.

5.2 Two pyramidal quantum dots in a photonic crystal cavity: General observations

5.2.1 r/a -tuning of the cavity resonances

As described in Sec. 3.2.4, our samples contained many repetitions of so-called "PhC series", where each series consisted of 15 collocated PhCs for which the nominal hole sizes were increased by 1 nm from one PhC to the next. The purpose of the r/a -tuning within one PhC series was to scan the $M0$ resonance of the $L3$ cavity across the QD spectra and to probe the PL emission at different detunings.

Our procedure for identifying the position of the cavity resonance within a PL spectrum was based on polarization-resolved measurements of the light emission, which already proved to be a reliable method in the case of single QDs in $L3$ cavities (see previous chapter). The PL characterization of a representative PhC series with QD pairs is shown in Figs. 5.3-5.7. There one can see 15 polarization-resolved spectra of one PhC series together with the extracted DOLP. In the following discussion, we will ignore the details of the individual excitonic transitions and focus on the mode emission and the polarization features.

The most intriguing observation that is evident from this dataset is the reproducible presence of photon emission from the far-detuned cavity mode. Even when the $M0$ resonance is more than 10 meV below the QD transitions, the emission from the cavity peak does not vanish. In some cases one can directly notice the off-resonant cavity peak in the spectrum, in other cases it is only noticable in the DOLP. Let us

5.2. Two pyramidal quantum dots in a photonic crystal cavity: General observations

discuss the case of Fig. 5.3(b) as an example: there one can see a sharp and strongly polarized emission peak in the spectrum at ~ 1.384 eV, which is more than 30 meV below the QD transitions. It is certain that this peak corresponds to the $M0$ resonance, because it has the expected polarization and it can be clearly seen from the other spectra that the position of this peak is varied through r/a tuning. We also verified that the spectral position of the cavity mode was consistent with 3D FDTD calculations (see Fig. 3.10).

The appearance of non-resonant mode emission from $L3$ cavities with QD pairs was surprising to us since we had not seen it in our experiments with single QDs. The coupling range of single pyramidal QDs was limited to the phonon sidebands, which extended the spectral tails of the QD transitions by up to ~ 5 meV; for detunings ≥ 5 meV, we normally did not observe any emission from the cavity mode. If at all a detectable signal from the far-off resonant cavity was present in the single-QD systems, then it was vanishingly small compared to the QD transitions. As we will show in power dependence measurements further below, the phenomenology of this mechanism differs from the cavity feeding phenomenon of SKQDs.

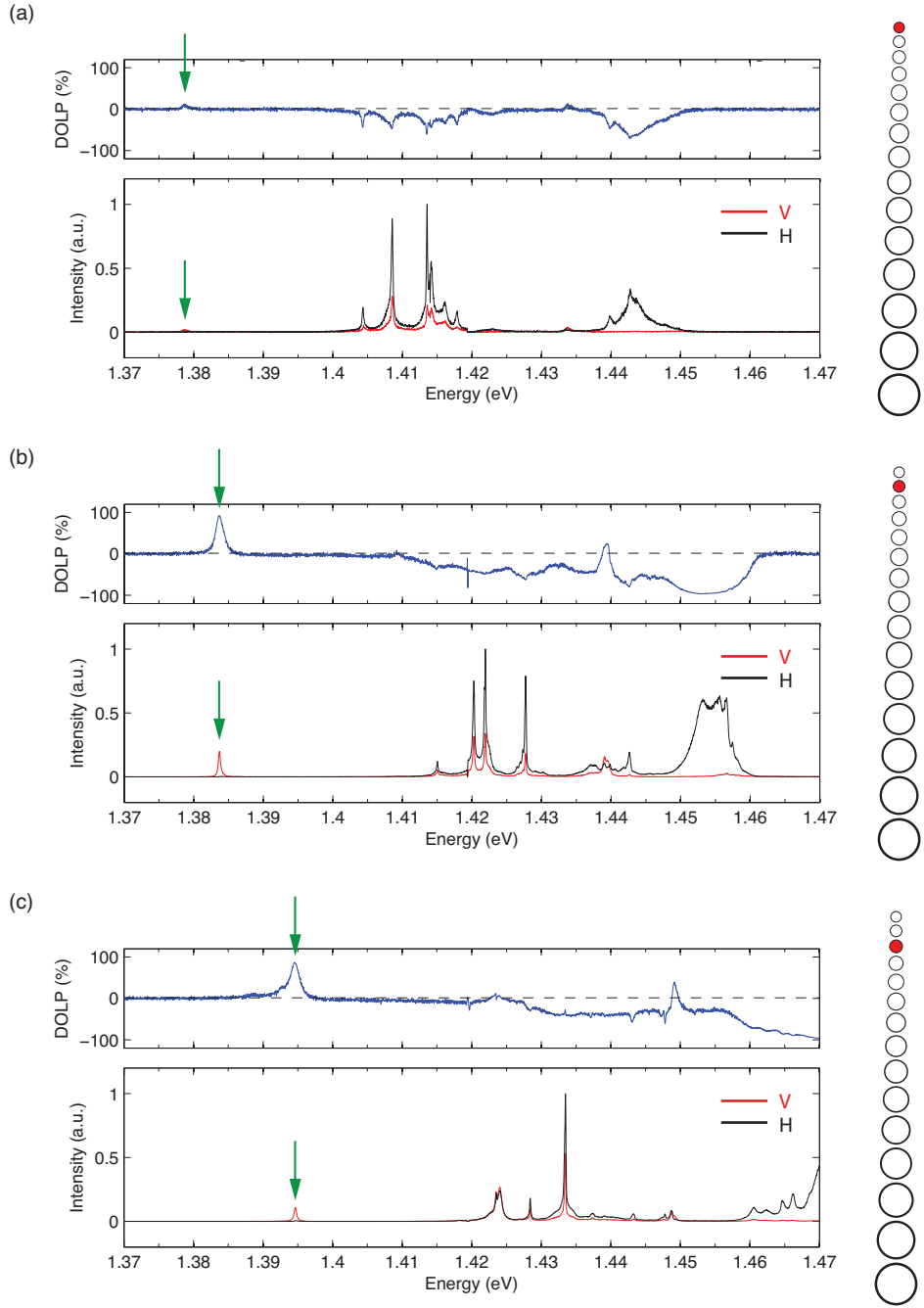


Figure 5.3: (a)-(c) Resonance scanning for 2 QDs in an $L3$ cavity through PhC hole size variation, with $T = 10$ K and $P = 100 \mu\text{W}$. The bottom part of each panel shows the polarization-resolved PL spectra, where the V- and H-polarized spectra are represented in red and black, respectively. The corresponding DOLP is displayed on top of each panel. The position of the $M0$ mode is marked with a green arrow as a guide to the eye. On the right side of each graph, the stepwise increase of the nominal PhC hole sizes is illustrated and the current PhC is highlighted in red.

5.2. Two pyramidal quantum dots in a photonic crystal cavity: General observations

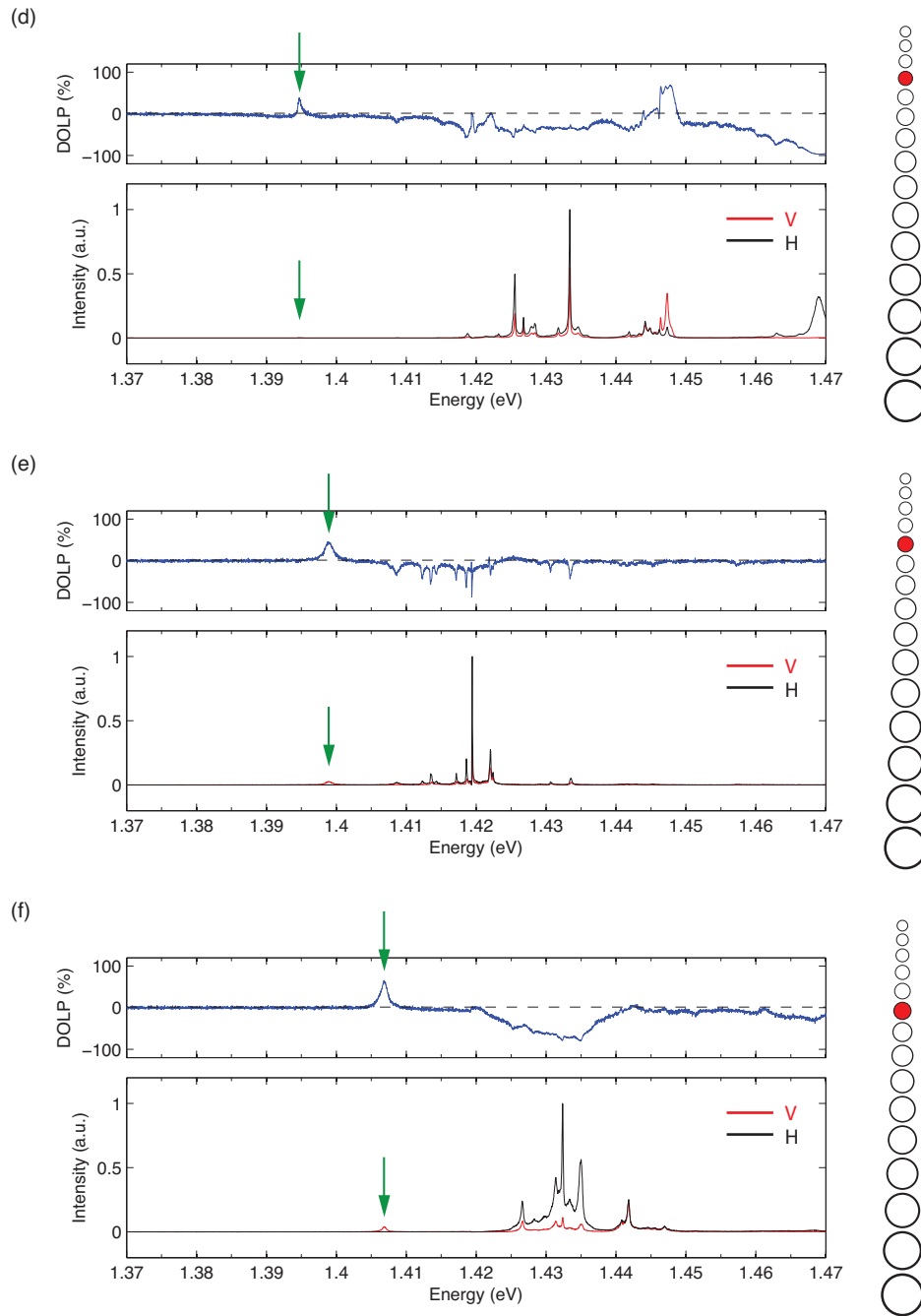


Figure 5.4: (d)-(f) Continuation of the previous figure.

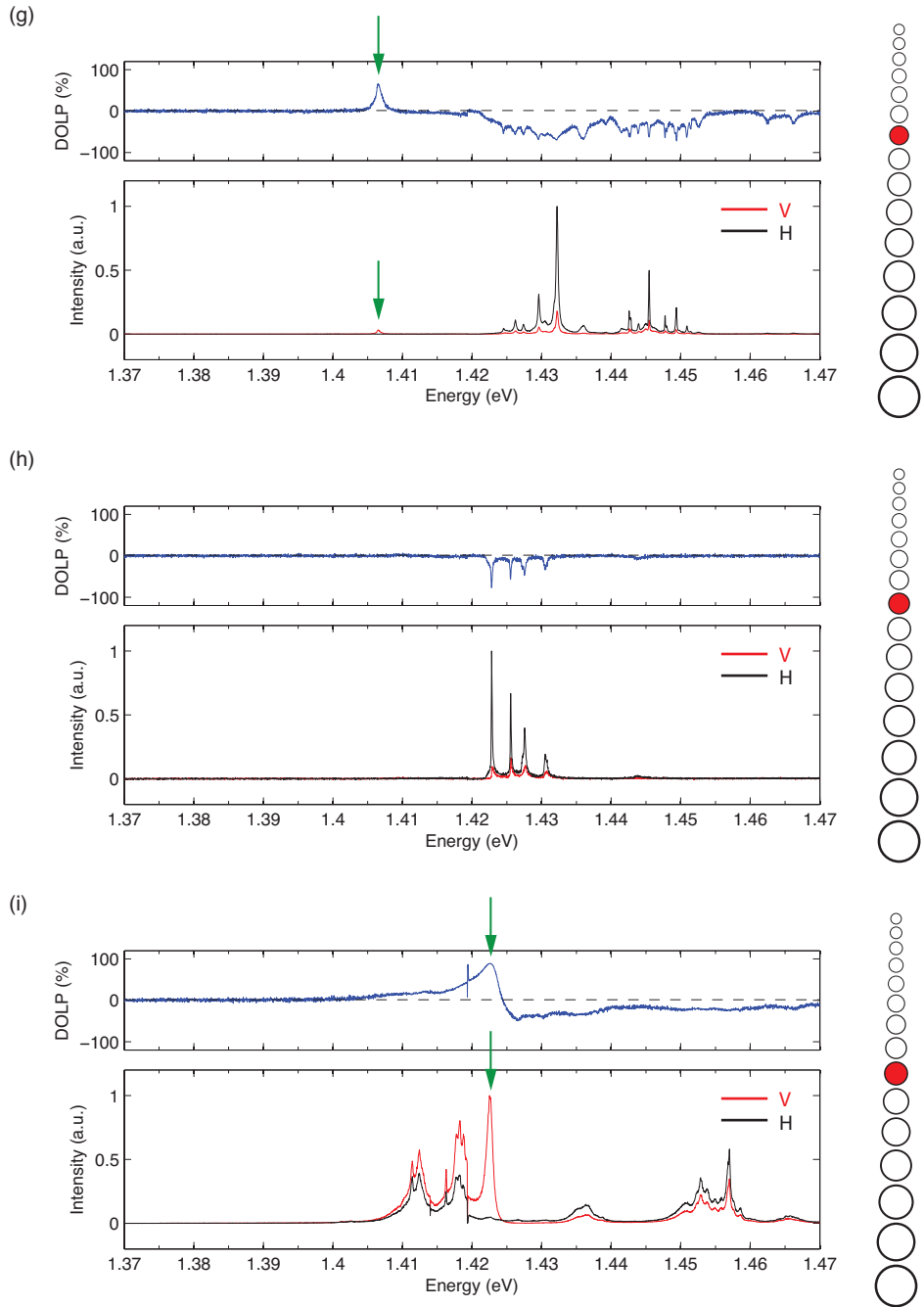


Figure 5.5: (g)-(i) Continuation of the previous figure. In (h), the $M0$ mode appears to be absent. Note the characteristic shape of the DOLP in the example of (i); we observed such profiles in many other structures.

5.2. Two pyramidal quantum dots in a photonic crystal cavity: General observations

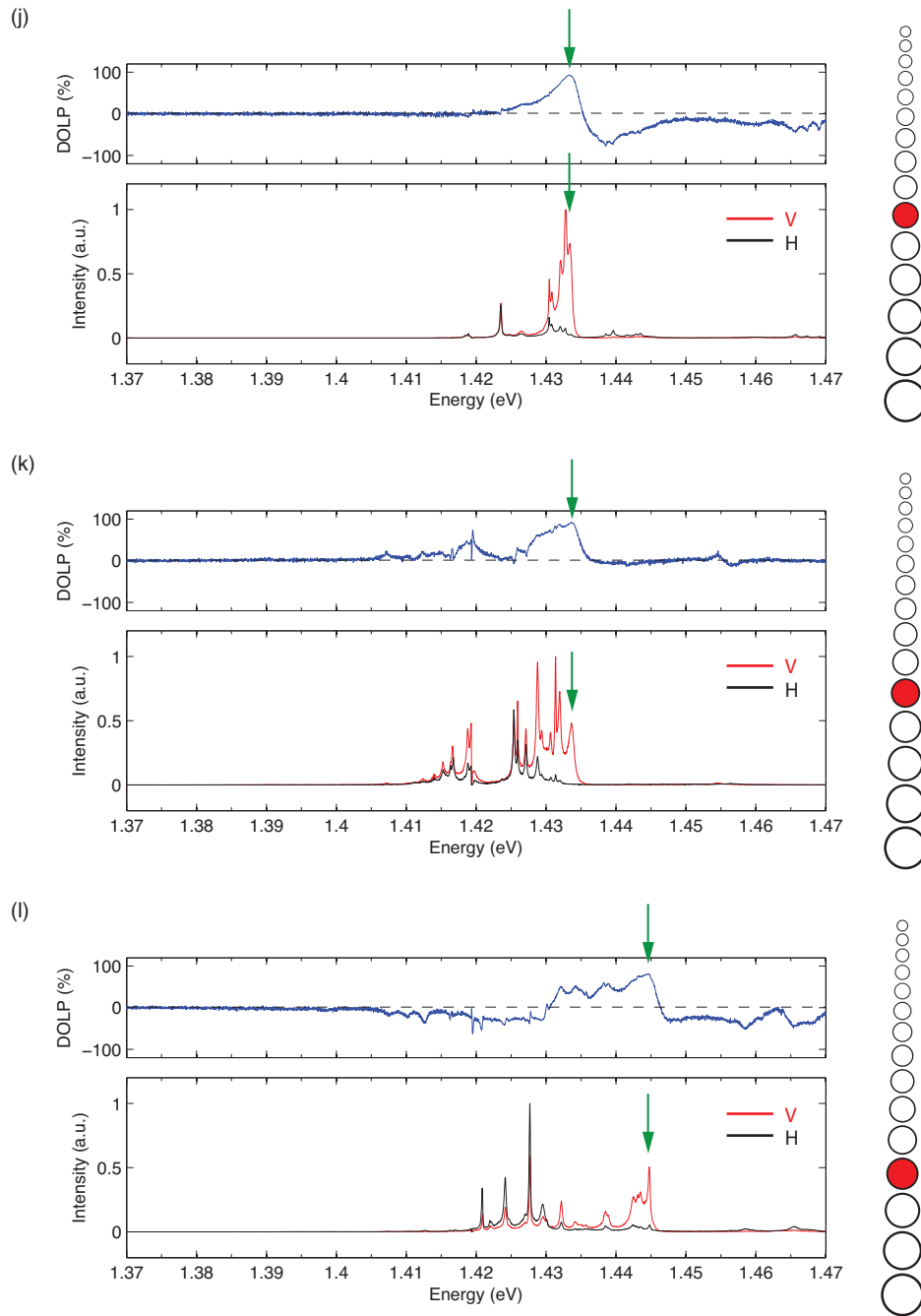


Figure 5.6: (j)-(l) Continuation of the previous figure. The QD-cavity structure in (j) is another example where the characteristic profile in the DOLP is revealed.

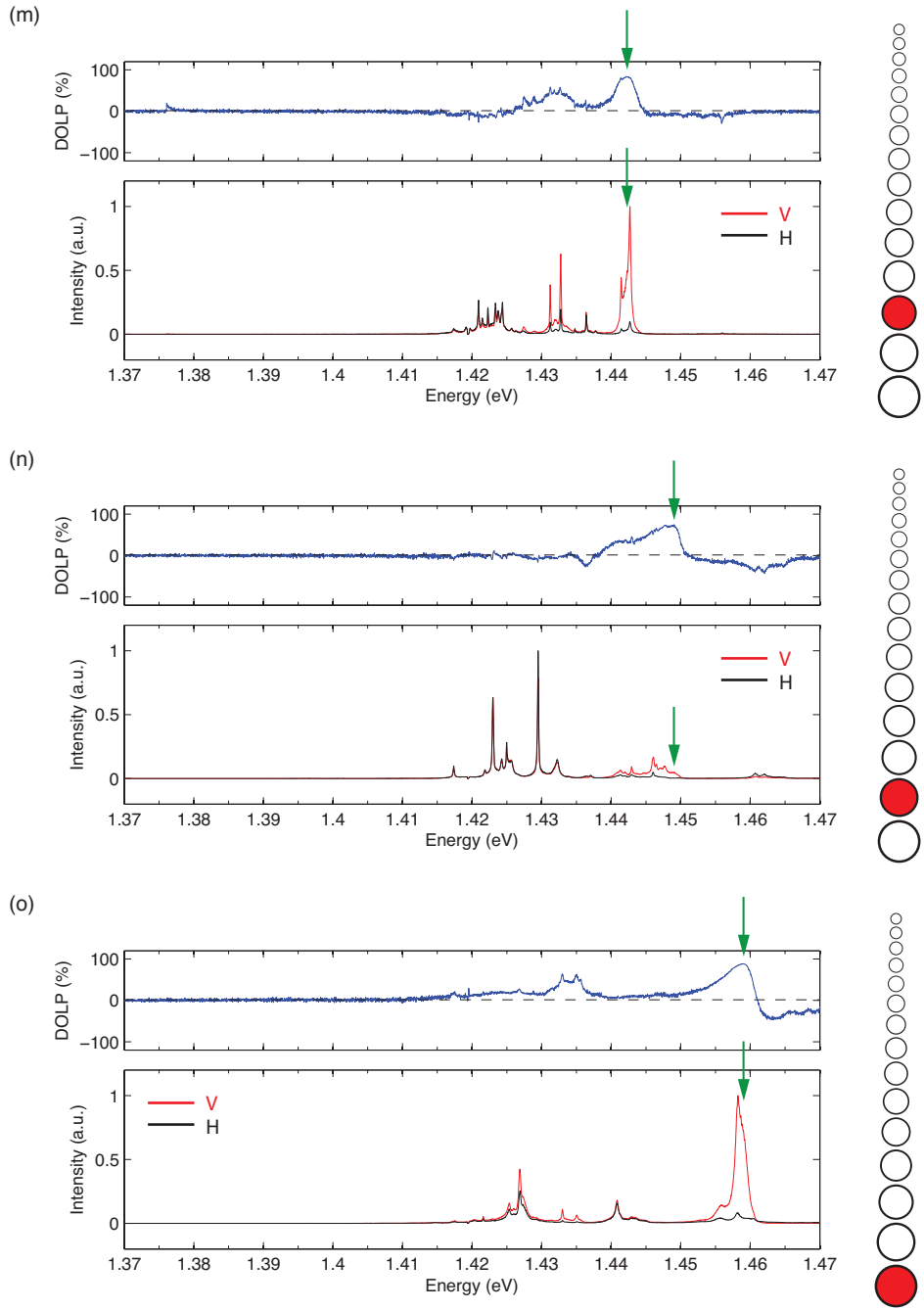


Figure 5.7: j)-(l) Continuation of the previous figure. The QD-cavity structure in (o) also exhibits the characteristic polarization profile seen before.

5.2.2 Cavity mode intensity and Q factor

In order to obtain quantitative information about the off-resonant cavity emission, we analyzed the data from 2 PhC series that were measured under the same conditions to extract the integrated intensity of the cavity mode by means of Lorentzian fits. The analysis is presented in Fig. 5.8(a), where each datapoint represents the cavity mode intensity measured from a different PhC structure. One can deduce from these results that the cavity mode emission is strongly enhanced when the mode spectrally overlaps with QD transitions, while in off-resonant situations the mode signal is several times weaker in comparison. Remarkably, the off-resonant mode intensities have very similar magnitudes, even though the data was measured for different QD-PhC devices that also exhibited different detunings.

A possible explanation for the latter observation is that pure dephasing mechanisms (i.e. carrier-phonon scattering and spectral diffusion) cause an excitation transfer from the QDs towards the off-resonant cavity mode [56–58, 69]. In fact, Naesby *et al.* predicted that pure dephasing should lead to off-resonant emission from the cavity mode that remains practically constant at large detunings [56]. Apart from that, Yamaguchi *et al.* suggested that the off-resonant cavity emission could be understood as a "summation" of all detuned QD states that couple to the cavity indirectly via pure dephasing [58, 69]. Therefore it would be reasonable to expect more intense emission from the off-resonant mode when the cavity contains two QDs as compared to the situation with a single QD, because there would be twice more QD states that can couple via the pure dephasing mechanism.

We further evaluated the Q factors of the $M0$ cavity mode from our fitting analysis, as shown in Fig. 5.8(b). The graph shows that the Q factors ranged between 1000 and 4000 in the investigated devices, and evidently the Q factor decreases towards higher energies (shorter wavelengths). This trend is consistent with the findings of Michael *et al.* [164], who measured the wavelength dependence of the Q factor in GaAs and AlGaAs microdisks. Michael *et al.* concluded from their analysis that the larger losses at shorter wavelengths are mainly related to residual absorption from bulk impurities and from surface states.

In view of the future goal of reaching strong coupling in our devices, it is important to take the wavelength dependence of the Q factor into account in the sample design. The analysis in Fig. 5.8(b) suggests that it is favorable to target longer wavelengths, which means that the central emission wavelength of the QDs has to be shifted away from currently ~ 870 nm (~ 1.425 meV) towards wavelengths above 900 nm.

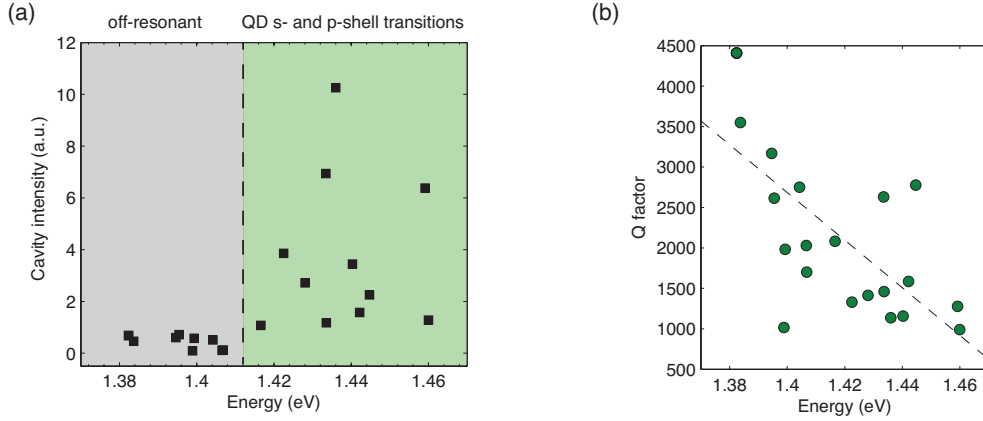


Figure 5.8: (a) Analysis of the cavity intensity for different detunings, as extracted from a set of QD-cavity structures with different PhC hole sizes. The data was extracted from 2 PhC series that were measured with $T = 10$ K and $P = 100 \mu\text{W}$. The approximate energy ranges where the cavity overlaps with the QD s- and p-shells are highlighted. (b) Variation of the Q factor of the $M0$ mode as a function of resonance energy. The dashed line represents a linear fit to the data.

5.2.3 Polarization features

By inspecting the spectra in Figs. 5.3-5.7, one can examine that the cavity mode strongly co-polarizes the spectrally overlapping excitonic transitions in addition to enhancing their intensities, see e.g. Fig. 5.5(i). This behavior is the expected signature of the Purcell effect. However, one may notice that the peculiar polarization features of the resonant structure in Fig. 5.5(i) are quite different from the other examples in Figs. 5.3-5.7 when the cavity mode was detuned in energy below the QD s-shell transitions. This is clearly visible in the "s-shaped" profile of the DOLP in Fig. 5.5(i): the QD spectrum is V -polarized starting from the cavity resonance towards lower energies, while at energies above the cavity resonance the whole spectrum is H -polarized over a broad range. We had previously observed similar DOLP profiles with single QDs (see for example Fig. 4.13), but they were not as pronounced as in the case of QD pairs.

We consistently (with few exceptions) observed such s-shaped DOLP profiles in different cavities that contained QD pairs in $L3$ cavities. For example, the PhC cavities in Fig. 5.6(j) and Fig. 5.7(o) also exhibit an s-shaped DOLP profile. The s-shaped DOLP therefore appears to be independent of detuning and on the particular configuration of the QD states, which suggests that the characteristic polarization features in the PL spectra manifest the photonic environment of the cavity, i.e. the LDOS of the $L3$ PhC cavity (see discussion in Sec. 4.1.4 and Sec. 4.2.3). Naively, one might expect that the DOLP of the $M0$ mode should be Lorentzian-shaped, but our results indicate that the LDOS of the PhC cavity deviates from this simple notion.

5.2. Two pyramidal quantum dots in a photonic crystal cavity: General observations

We also performed temperature-dependence measurements (not shown here) where we observed that the DOLP profile remained unchanged, apart from being shifted in energy by the same amount as the cavity mode itself. However, if the s-shaped DOLP profile is an inherent property of the $L3$ cavity that does not depend on the detailed structure of the QD emission spectra, then why is it not observed in all devices in Figs. 5.3-5.7? The answer to this question can be deduced from Fig. 5.9, where one can see the spectra together with the DOLP for a QD pair in an $L3$ cavity at low and high excitation power (i.e. below and above saturation of the s-shell states), respectively.

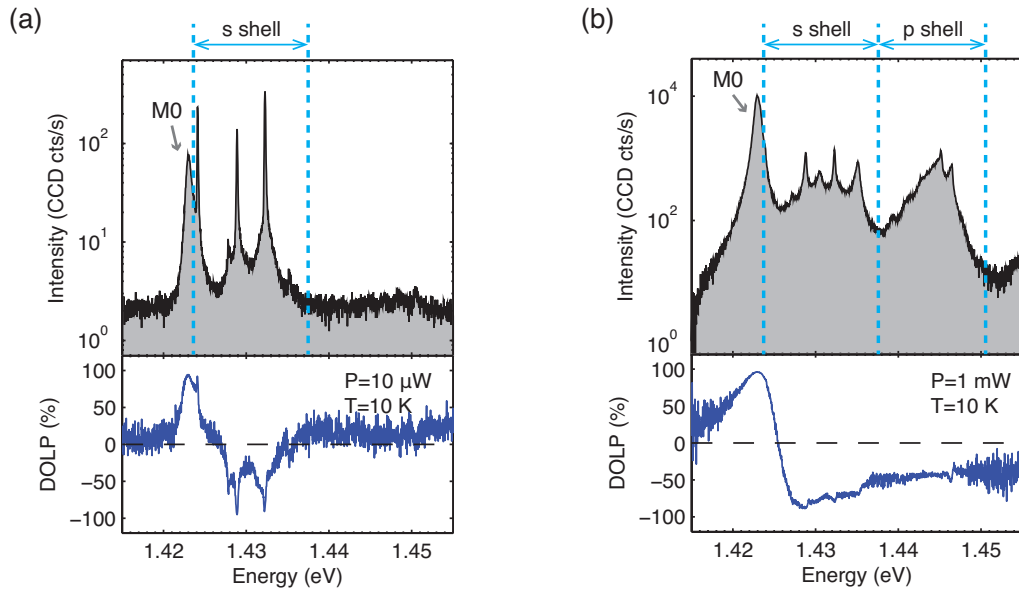


Figure 5.9: (a) Top panel: Semilogarithmic plot of the PL spectrum measured from a resonant QD pair at 10 K and with an excitation power of $P = 10 \mu\text{W}$. Bottom: Corresponding spectral DOLP. (b) Same QD pair as in (a), but at high excitation power ($P = 1 \text{ mW}$).

At low excitation power ($P = 10 \mu\text{W}$ in Fig. 5.9(a)), only the neutral and charged excitonic species X and X^- from the s-shells of both QDs are optically active. The spectrum shows that the $M0$ mode is spectrally overlapping with the lowest-energy QD peak, which is most likely an X^- of one of the QDs. The DOLP shows that a narrow spectral range ($\sim 3 \text{ meV}$ wide) surrounding the cavity mode is strongly V -polarized as expected, but the QD transitions that are energetically a few meV above are strongly H -polarized. The profile of the DOLP is not smooth, but it has sharp features at the positions of the QD peaks; furthermore, it is spectrally limited to the energy range that is "illuminated" by the QDs. On the contrary, when the excitation power is large enough to populate the excited QD states of the p-shell ($P = 1 \text{ mW}$ in Fig. 5.9(b)), then the characteristic s-shaped profile of the DOLP becomes visible. Here the polarization

profile is smooth, there are no more sharp features left in the polarization profile.

This comparison makes it apparent that the visibility of the characteristic polarization profile associated with the $M0$ mode of an $L3$ cavity depends on whether the whole spectral range of interest is fully covered by QD transitions. Therefore it is understandable why the s-shaped profile of the DOLP does not show appear in the PhC devices where the cavity mode is far detuned below the QD transitions: it is simply because the cavity spectrum surrounding the $M0$ mode is not illuminated. For the same reason, the characteristic DOLP profile was much less visible in $L3$ cavities with single QDs: there were much fewer excitonic states, so that the cavity spectrum was not fully covered in its extent by optically active states.

As far as we are aware, there are no publications where similar findings related to the characteristic spectral polarization features of an $L3$ cavity has been reported. Our results suggest that the s-shaped DOLP profile it is an intrinsic photonic property of the $L3$ cavity, which is determined by its specific LDOS. To verify this interpretation, one would need to perform a 3D computation for the LDOS of an $L3$ cavity. From this, one should in principle be able to extract the spectral polarization profile, by examining how the emitted light couples to the light cone (and thereby the microscope objective).

5.2.4 Power dependence of the emission spectra

The observation of significant far-off resonance cavity emission with QD pairs is puzzling, because this behavior was absent with single pyramidal QDs. Furthermore, it has not been predicted by theory that there would be such an anomaly in multi-QD systems starting from 2 QDs. Our experimental results for single-QD structures (see Chapter 4 and Ref. [64]) lead us to the conclusion that pyramidal QDs do not exhibit a broad multiexcitonic background as SKQDs, and that their coupling range is limited by the phonon sidebands. Is it possible that we made a premature judgement regarding the absence of a multiexcitonic background in the case of single pyramidal QDs?

One way to answer this question is to investigate the power dependence of the PL spectra. Experiments with single SKQDs in PhC cavities demonstrated that in those systems the cavity mode followed the trend of the QD p-shells, which was regarded as a proof for the excited-state nature of the the cavity feeding process [169–171]. Consequently, if the non-resonant cavity mode emission in the case of pyramidal QD pairs would have the same origin as for SKQDs, then the power dependence of the cavity mode intensity should mimic the trend of the p-shell states.

5.2. Two pyramidal quantum dots in a photonic crystal cavity: General observations

In order to investigate this issue, we selected a device for which the fundamental cavity mode $M0$ was ~ 30 meV lower in energy relative to the ground state transitions of the QD pair. A subset of the spectra from the power dependence measurements is shown in Fig. 5.10 and Fig. 5.11. The QD transitions are labeled as X , X^- , $2X$ and Xh , which designate the neutral exciton, negatively charged exciton, biexciton and excited hole state, respectively. The indices a and b signify the association of the transitions with each QD from the pair. An overview of the binding energies of the respective excitonic features is given in Fig. 5.12.

Our identification of the individual excitonic transitions and their association relied on the statistical study of single pyramidal QDs by Jarlov *et al.* [40]. In the latter study, it was found that a typical spectrum of a single pyramidal QD contained only three ground state transitions at low excitation power, namely the X , X^- and $2X$ (see also Sec. 3.2.6 and Fig 3.11). The spectral separation between the X and the X^- was statistically highly reproducible and amounted 4.9 ± 0.3 meV. The $2X$ binding energy exhibited more statistical fluctuations and varied from +1 meV to -4 meV, such that some of the examined single QDs had $2X$ transitions with zero binding energy [40].

Coincidentally, one of the two QDs in Fig. 5.10 and Fig. 5.11 appears to have a $2X$ transition with zero binding energy. The corresponding peak is labeled as $X_b + 2X_b$. This identification is concluded from the inspection and analysis of the present spectra as well as on the study of Jarlov *et al.* [40]. One can notice in Fig. 5.10(a) that the $X_b + 2X_b$ -peak is several times more intense than the other QD transitions.

In the semilogarithmic plot in Fig. 5.10(a), a very weak signal from the $M0$ mode can be seen to be already present with, even though the excitation power is so low ($P = 5 \mu\text{W}$) that only the neutral and charged excitons X and X^- are significantly populated. With increasing power, the first-order mode $M1$ is also observed to emerge. The $M1$ mode is only ~ 5 meV below X_a^- , such that it seems to overlap with the end of a phonon tail.

Evidently, both the $M0$ and the $M1$ grow at a very slow rate as a function of power. Even when the excitation power is so high that the QD emissions are saturated (Fig. 5.11(f)), the intensities of $M0$ and the $M1$ remain low compared to the QD transitions. In stark contrast, experiments with single SKQDs showed that the off-resonant cavity mode grew at a superlinear rate as a function of excitation power and eventually became dominant in the optical spectrum at high powers [169].

Let us now study the detailed analysis of the power dependence in Fig. 5.13, where the integrated intensities of the individual peaks are plotted as a function of excitation power. For better clarity, we present the analysis in 3 graphs: the first one

(Fig. 5.13(a)) analyzes the trends of the excitonic features associated with "QD *a*", the second one (Fig. 5.13(b)) is for "QD *b*", and the third one (Fig. 5.13(c)) summarizes the integrated intensities from the s-shell and p-shell transitions.

The first graph (dedicated to "QD *a*"), Fig. 5.13(a), shows that the *M0* mode does not follow the trends of any of the excitonic transitions associated with "QD *a*". In the second graph (dedicated to "QD *b*"), Fig. 5.13(b), one can see that the *M0* mode has a similar slope as $X_b + 2X_b$; however, at powers above 100 μW the trends begin to deviate from each other. In the third graph, Fig. 5.13(c), we look at the overall integrated intensities emitted from the s-shell and p-shell transitions. Here it becomes apparent that the *M0* mode directly mimics the power dependence of the s-shells, and that the p-shells do not seem to have an influence on the trend of *M0*. Also the *M1* mode which is spectrally much closer to the QD transitions follows almost precisely the same trend as the *M0*. Our observation of an s-shell-like power dependence of the *M0* mode strongly deviates from the characteristics of SKQDs in PhC cavities, where the *M0* mode was observed to follow the trend of the p-shell transitions [169–171].

These results prove that the mechanism leading to off-resonant cavity mode emission in the case of pyramidal QD pairs is distinct from the cavity feeding process that is known from studies with SKQDs [169–171]. Fig. 5.13(c) demonstrates that the off-resonant cavity emission from a pyramidal QD pair is directly related to s-shell transitions and clearly does not exhibit an excited-state nature as in cavity feeding with SKQDs. However, we have not performed a theoretical modeling to investigate how the off-resonant cavity emission from QD pairs is generated.

A possible explanation might be that the excitation transfer is assisted by pure dephasing processes (i.e. carrier-phonon scattering and spectral diffusion) [56–58, 69]. In fact, according to the theoretical analysis on the impact of pure dephasing on off-resonant coupling by Yamaguchi *et al.* [58], the light emission from the off-resonant cavity should scale with the number of detuned excitonic states. Therefore, it can be expected that the off-resonant cavity mode should emit more light when there are 2 QDs in the cavity as compared to 1 QD. This would explain our observation that the off-resonant cavity was either absent or vanishingly small in the spectra of single QDs, while it was much more noticeable with 2 QDs.

5.2. Two pyramidal quantum dots in a photonic crystal cavity: General observations

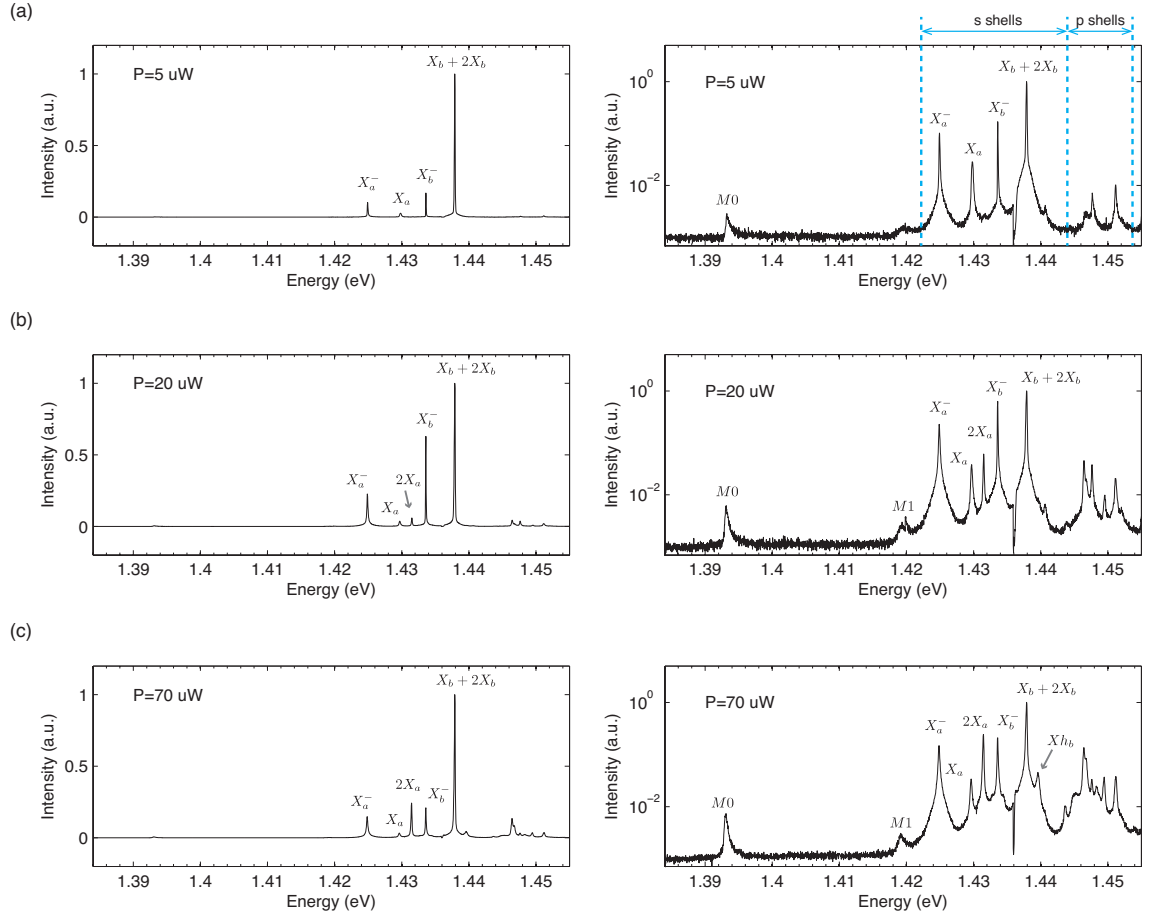


Figure 5.10: (a)-(c) PL spectra for an $L3$ cavity containing a far-off resonant QD pair, measured at different excitation powers. The QD pair is ~ 30 meV detuned from the fundamental cavity resonance $M0$, which has a Q factor of 2400. The panels on the left show linear plots, while the panels on the right display the same data in semilogarithmic form. The QD peaks are labeled with indices a and b to distinguish which transitions belong to which QD. In (b) and (c), one can recognize the appearance of the first order cavity mode $M1$.

Chapter 5. Two spatially separated quantum dots in a photonic crystal cavity

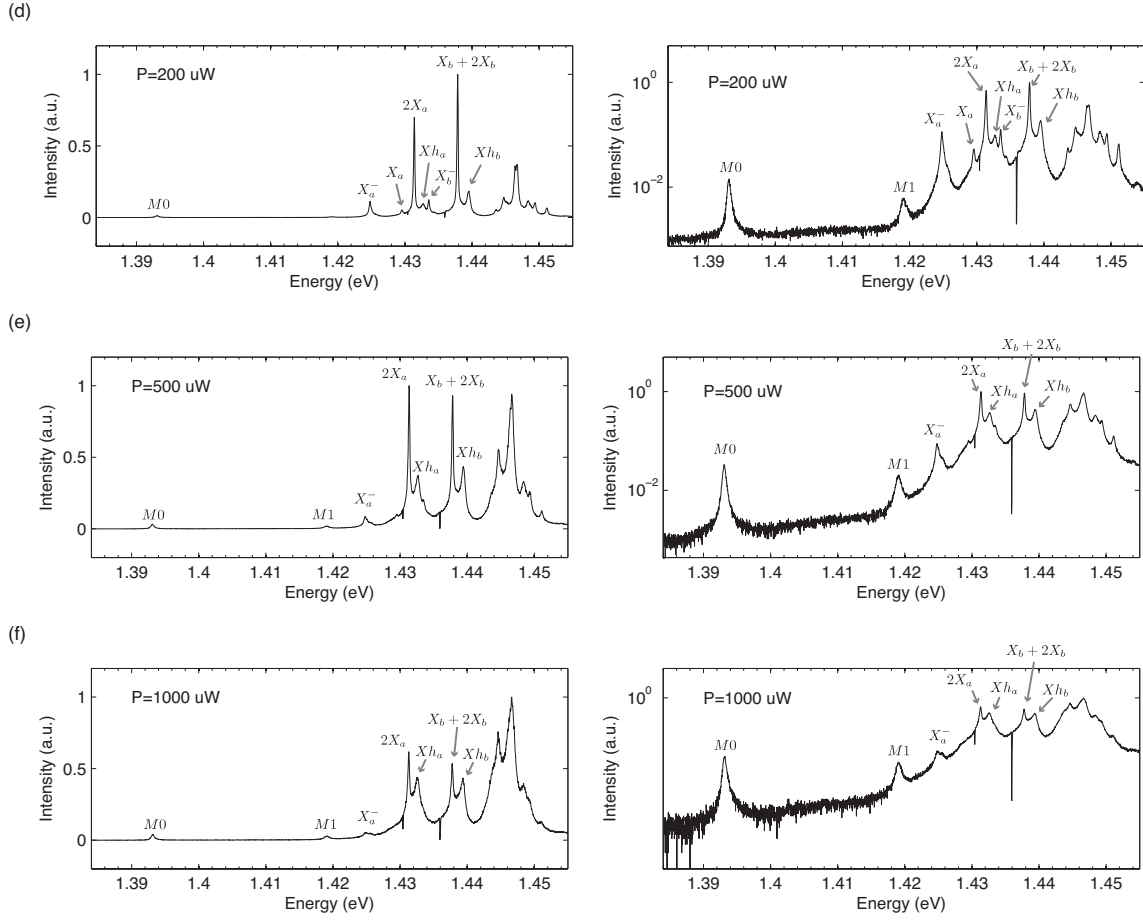


Figure 5.11: (d)-(e) Continuation of the previous figure. Notice the background tail that extends from the QD transitions to the $M0$ mode.

Quantum dot #1		Quantum dot #2	
Peak name	E_b (meV)	Peak name	E_b (meV)
X_a^-	-4.8	X_b^-	-4.3
$2X_a$	1.8	$2X_b$	0.0
Xh_a	3.0	Xh_b	1.5

Figure 5.12: Overview of the binding energies E_b (i.e. spectral distance with respect to the neutral exciton X) for the excitonic features of the two QDs in Figs. 5.10 and 5.11.

5.2. Two pyramidal quantum dots in a photonic crystal cavity: General observations

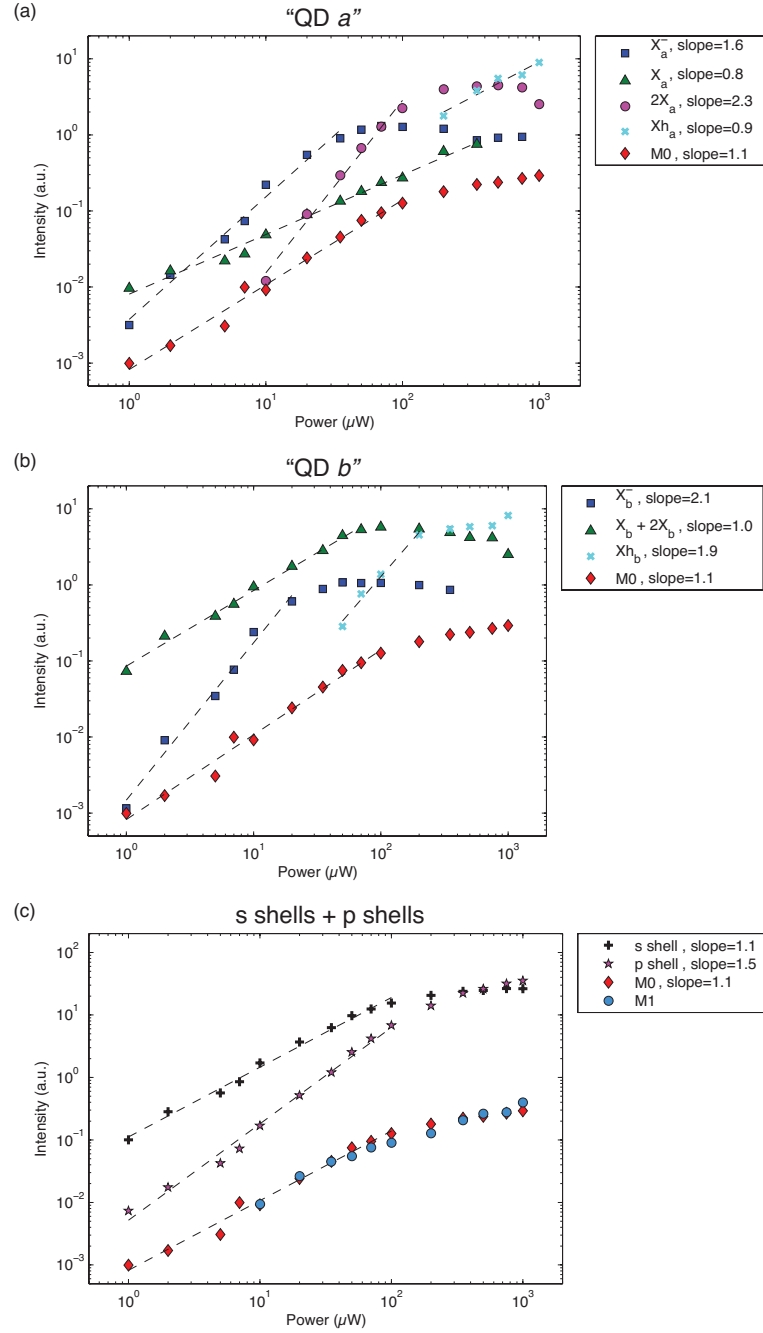


Figure 5.13: Analysis of the power dependence of the off-resonant QD pair structure. (a) and (b): Power dependence of the integrated intensities belonging to the corresponding excitonic transitions of the "QD a" and "QD b", respectively. The intensities for the $M0$ mode is plotted in all graphs for comparison. The dashed lines designate linear fits to the data; the slopes are indicated in the graph legend. (c) Dependence of the integrated intensities of the s and p shells on excitation power. Here the higher-order mode $M1$ is also shown.

5.3 A mutually coupled quantum dot pair

5.3.1 Purcell-enhancement of the intensities

In this section, we present an experimental study of the mutual interaction between a QD pair and the fundamental mode of a weakly coupled $L3$ cavity. The PL spectrum of this system at 40 K is displayed in Fig. 5.14(a) and (b). As in Sec. 5.2.4, the identification of the individual QD transitions here was based on previous studies of single QD spectra. An inspection of this spectrum makes it clear why this system is highly interesting: the spectra of the individual QDs partially overlap with each other, and in addition the cavity mode $M0$ with $Q \sim 2300$ is placed right in between the X_a transition of one QD and the X_b^- transition of the other QD. The spectral separation between X_a and X_b^- amounts to only ~ 1.9 meV, such that both transitions equally overlap with the cavity mode at their center. This system is therefore a suitable candidate to examine whether it exhibits collective behavior as predicted by the Dicke model.

First, we have to establish whether both QDs are mutually coupled to the cavity mode. To investigate this point, we conducted temperature dependence measurements of the PL spectra to tune the QD transitions accross the cavity mode (see Fig. 5.14(c)). From the dependence of the integrated intensities of the QD peaks versus detuning, we will be able to evaluate whether both QDs are subject to Purcell enhancement. In the following, we summarize the results of our analysis that we obtained from applying Lorentzian fits to the optical spectra.

As can be seen from the temperature dependence of the transition energies in Fig. 5.15(a), the temperature variation of the PL spectra from 10 K to 70 K allowed us to probe a few-meV range of detunings. Going from low to high temperature, the first QD peak that crosses the cavity mode is X_b^- at 30 K, followed by X_a at ~ 52 K. If the X_a and X_b^- transitions belonging to the separate QDs are both coupled to the cavity mode, then we should expect a Purcell enhancement of their intensities for both of them with a maximum at their respective crossing points. Indeed, this is precisely what we observe in Fig. 5.15(b). In addition, the graph also reveals that the cavity mode intensity decreases just before the two crossing points and recovers right afterwards. This effect is probably related to the interplay between direct Purcell enhancement and indirect Purcell enhancement mediated by pure dephasing mechanisms [56, 57, 183] (i.e. phonon scattering + spectral diffusion): at detunings larger than the cavity linewidth, indirect Purcell enhancement causes a stronger emission at the cavity frequency as compared to emission from the nearby QD transition, while at detunings smaller than the cavity linewidth the direct Purcell enhancement becomes dominant such that more photons are emitted from the QD transition than from the cavity mode.

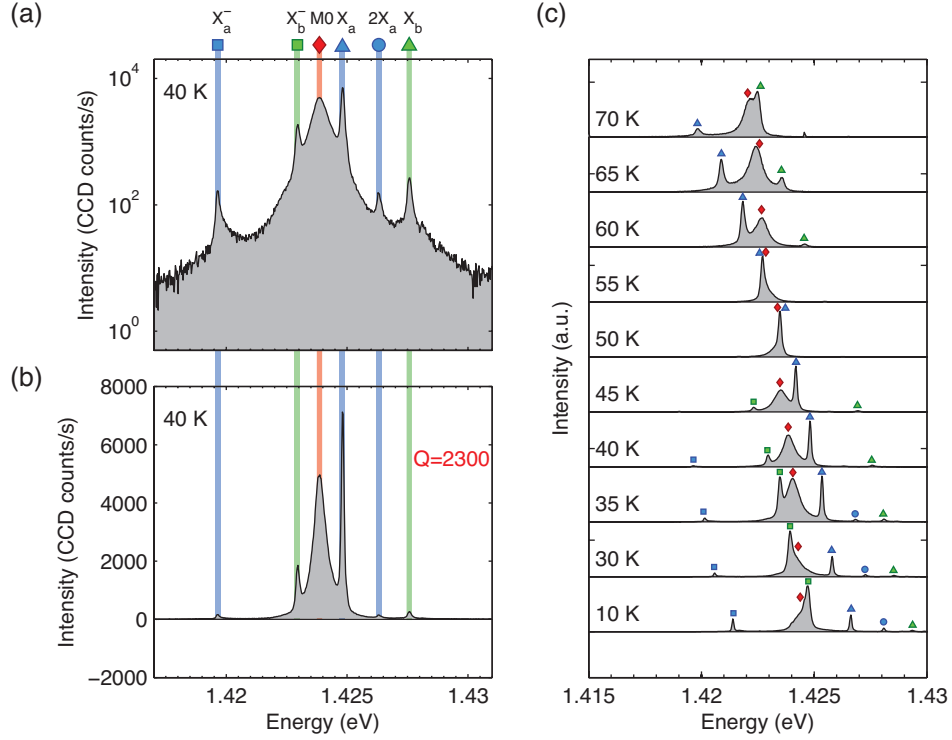


Figure 5.14: (a) and (b): Semilogarithmic and linear plot of the PL spectrum measured for the resonant two-QD-cavity system at 40 K and 100 μ W excitation power. Transitions belonging to the same QD are highlighted in blue and green, respectively, and labeled with the subscripts a and b to indicate their association. (c) Temperature dependence of the PL emission. The spectra were normalized by the maximum intensity value. The colored symbols identify the peaks the same way as in (a).

Note that the intensity values in Fig. 5.15(b) were normalized by the overall integrated intensity of the spectrum to account for the non-radiative losses that increase with temperature.

Evidently, the cavity mode intensity has a maximum when the sample temperature is 40 K (see Fig. 5.14 and Fig. 5.15). This is exactly the point where the $M0$ mode meets the center between the X_a and X_b^- , suggesting that both transitions are mutually emitting photons into the cavity mode. We therefore conducted photon correlation measurements at 40 K in order to examine whether we could find evidence of cooperative spontaneous emission in the form of bunched photon emission from the cavity mode, as predicted from theory [216, 228]. However, our measurements of $g^2(\tau)$ at different pump powers (not shown here) did not show any signs of bunching; the flat correlation histograms corresponded to Poissonian light emission. The absence of bunching from the cavity mode can be interpreted in two opposite ways: 1) The

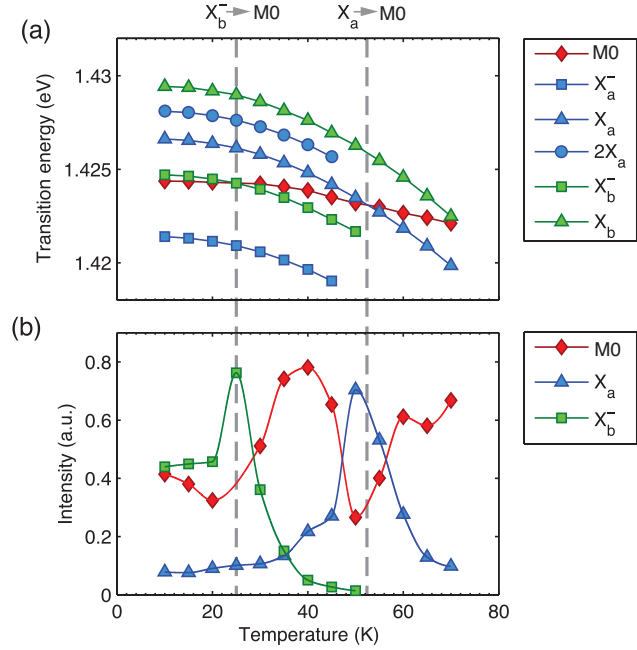


Figure 5.15: (a) Temperature dependence of the transition energies of the two-QD-cavity system of Fig. 5.14. (b) Variation of the integrated intensities of the X_b^- , X_a and $M0$ peaks as a function of temperature. The excitation power was $100 \mu\text{W}$.

system is not in the cooperative regime, such that the two QDs independently emit photons in to the cavity mode. 2) The system is actually in the cooperative regime, but the presence of a joint carrier reservoir causes a mixing of sub- and superradiant states, thereby suppressing multiphoton emission events [217]. Therefore we cannot draw a clear conclusion from our photon correlation measurements in favor or against the existence of cooperative effects.

In Fig. 5.15(b), we examine the intensities of the optical transitions as a function of temperature. However, the essential parameter that is modified through temperature variation is the respective detuning of the QD peaks relative to the cavity mode. We therefore investigated the intensities as a function of detuning in Fig. 5.16, and this time we include all 5 QD transitions. The result presented in Fig. 5.16 is rather astounding: the X_a^- and X_a peaks belonging to the first QD appear to trace a nearly Lorentzian-shaped curve with approximately 1 meV width, whereas the X_b^- and X_b peaks belonging to the second QD carve out a narrower Lorentzian (~ 0.6 meV). The only exception in these Lorentzian trends is the $2X_a$ feature, which is probably related to its conditional dynamics with X_a that is in turn enhanced by the cavity mode. Again, the intensity values in Fig. 5.16 were normalized by the overall integrated intensity of the spectrum, as in Fig. 5.15(b).

While one would expect a Lorentzian-shaped trend of the QD intensities as a function of detuning (see Purcell formula in Eq. (4.7), Sec. 4.1.4), it is yet surprising to find that the QD transitions associated with the neutral and charged exciton, X and X^- , seem to be influenced in the same way as a result of the Purcell effect. This seems to be the case for both QDs in Fig. 5.16. A likely reason for this observation is that the X and X^- have very similar coupling strengths with the cavity mode. Moreover, it is interesting that the association of the excitonic features to the individual QDs becomes obvious from Fig. 5.16, since they can be distinguished from their respective Lorentzian detuning dependence. The observation that the two Lorentzians traced out by the individual QDs do not have the same widths might be associated with different individual coupling strengths.

To conclude, in this section we studied the detuning dependence of two spatially separated pyramidal QDs in a resonant $L3$ PhC cavity and found evidence that both QDs are subject to Purcell enhancement. To our knowledge, this is the first successful report of achieving deterministic coupling with a pair of QDs.

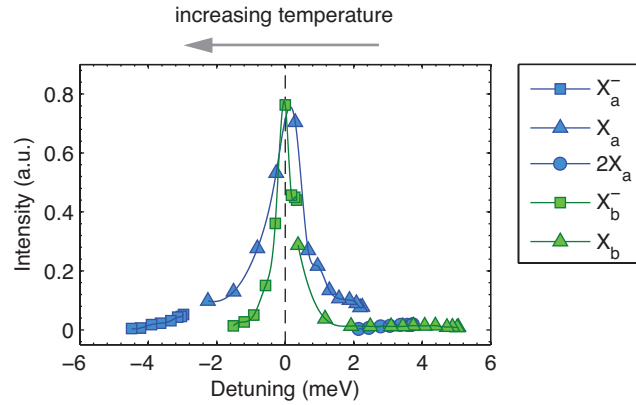


Figure 5.16: Integrated intensities of the QD peaks versus detuning with respect to the cavity peak $M0$. The data points were extracted from the temperature dependence shown in Fig. 5.14(c) by means of Lorentzian fits of each spectral line. Note that for any particular excitonic feature, each data point represents a different temperature; the rightmost datapoint corresponds to 10 K in each case, and the temperature increases from the right towards the left as indicated by the arrow.

5.3.2 Detuning dependence of the polarization features

We elaborated in the previous chapter that the detailed analysis of the polarization features in the PL emission can give additional insights into the coupling of a QD to a cavity. In this section, we will establish the connection between the spectral DOLP and the polarization of individual QD transitions in a two-QD-cavity structure.

Let us now take examine the temperature dependent spectra of the same QD pair that we studied in the previous section, but this time resolved in linear polarization. A subset of the spectra is shown in Fig. 5.17(a), together with the corresponding DOLP spectra in Fig. 5.17(b). It is evident from these results that the excitonic transitions belonging to separate QDs become co-polarized with the cavity mode as they are tuned through resonance. This behavior is consistent with our observations for single QDs, see Sec. 4.2.3. However, one may notice that the V -polarized spectral range (Fig. 5.17(b), bottom graph) is about 9 meV wide, which is roughly 3 times broader than for a single QD in a cavity (compare with Fig. 4.13 in Chapter 4).

In order to evaluate the detuning dependence of the polarization for each individual QD peak, we conducted Lorentzian fits to the polarization-resolved spectra at each temperature to extract the DOLP according to Eq. (4.13). The result is displayed in Fig. 5.18. This graph gives complementary information to the intensity data which we previously presented in Fig. 5.16. One can see in Fig. 5.18 that the excitonic transitions belonging to separate QDs appear to follow the same peculiar trace as a function of detuning. When we saw this polarization trace for the first time, we were struck by its resemblance to the s-shaped polarization profile that we had previously systematically observed in the DOLP of $L3$ cavities (see Sec. 5.2.1 and Sec. 5.2.3). Therefore we also plotted the spectral DOLP of this particular $L3$ cavity in Fig. 5.18 (black curve), which was extracted from its PL spectra at 40 K and at high excitation power ($P = 5$ mW). The excellent agreement between the spectral DOLP and the polarization of individual QD peaks is striking. Clearly, the detuning dependence of the optical polarization is determined by the s-shaped polarization profile for each individual excitonic feature, and this applies the same way for both QDs.

The result of Fig. 5.18 further confirms our claim from Sec. 5.2.3 that the s-shaped polarization profile is a manifestation of the characteristic LDOS of an $L3$ cavity. Since the QDs act as local probes of the photonic environment within the cavity, the polarization of their spontaneous emission is imposed by the LDOS. The analysis of the polarization features from QD-cavity systems thus gives important insight in the coupling characteristics as well as in the intrinsic polarization properties of the cavity.

5.3. A mutually coupled quantum dot pair

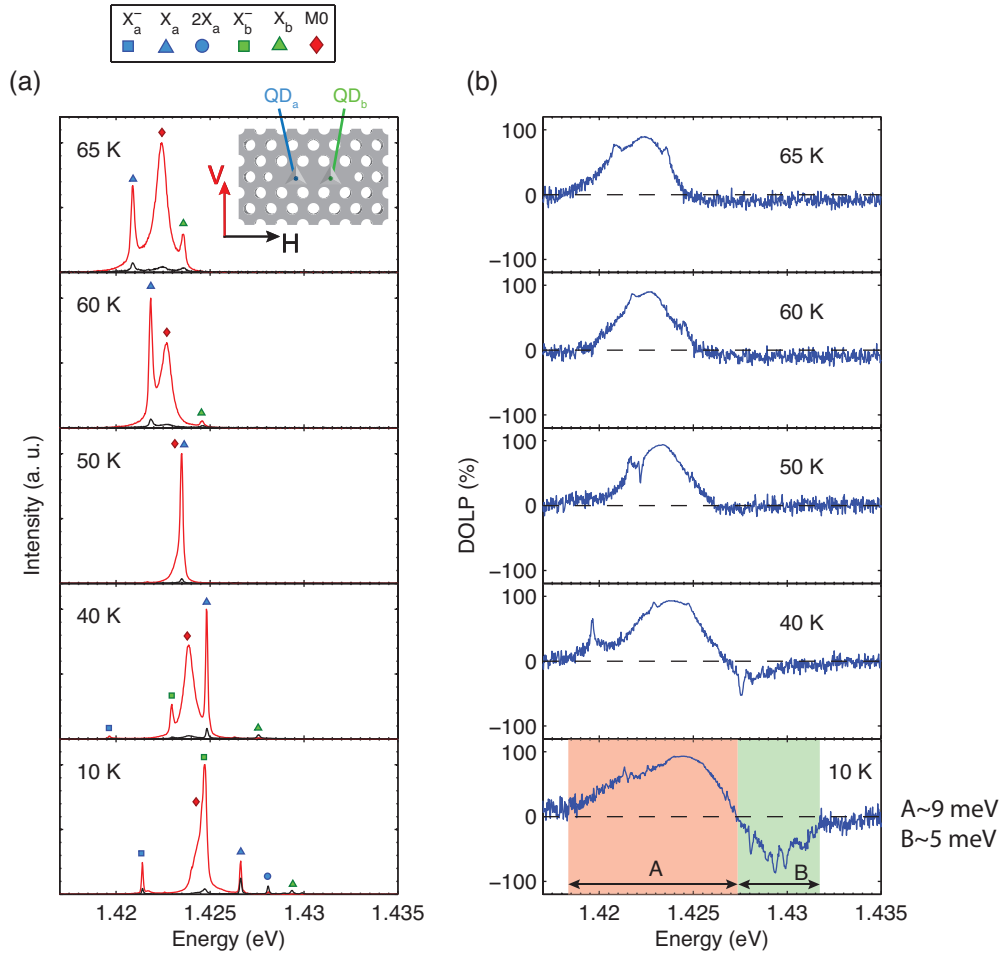


Figure 5.17: (a) Polarization-resolved spectra of the two-QD-cavity structure of Fig. 5.14 for a set of different temperatures, measured with 100 μW excitation power. (b) Corresponding DOLP of the spectra in (a).

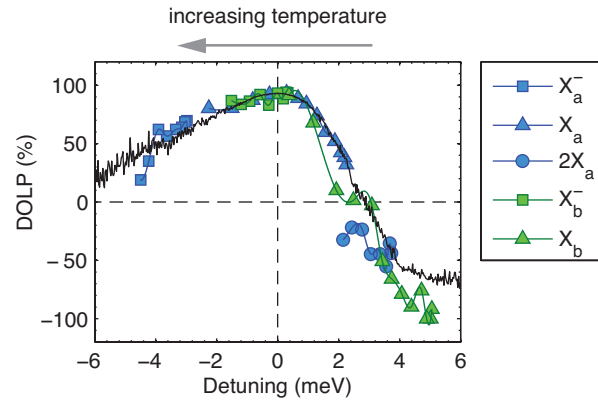


Figure 5.18: DOLP of the individual QD peaks versus detuning for the two-QD-cavity structure of Fig. 5.14, as obtained from the temperature dependent PL spectra. The black curve in the background represents the spectral DOLP, which was determined from PL spectra measured at 40 K and 5 mW power where the system was strongly excited.

5.3.3 Power dependent spectra of a resonant quantum dot pair

Up to this point, our analysis and the discussion was concentrated on establishing that we are dealing with a system where two separate pyramidal QDs are mutually coupled to the fundamental mode of an $L3$ cavity. Now we will proceed to investigate the consequences of the mutual interaction in the power dependence of the PL spectra. We chose to measure the power dependence in the situation where the cavity mode is spectrally in the center between the two QDs, i.e. at 40 K where $M0$ is between X_a and X_b^- (see Fig. 5.14(a),(b)).

A subset of the power-dependent PL spectra is shown in Fig. 5.19 and in Fig. 5.20. When the excitation power is lowest ($P = 5 \mu\text{W}$, Fig. 5.19(a)), the only peaks visible in the spectrum are the mode $M0$ and the neutral excitons of the two separate QDs, X_a and X_b . At $50 \mu\text{W}$ (Fig. 5.19(b)), the charged excitons X_a^- and X_b^- appear. By further increasing the power to $100 \mu\text{W}$ (Fig. 5.19(c)) and then to $400 \mu\text{W}$ (Fig. 5.20(d)), we observe the biexcitons $2X_a$ and $2X_b$ emerge. An overview of the binding energies of the respective excitonic features is given in Fig. 5.21. However, when the excitation power reaches levels of $1000 \mu\text{W}$ and beyond (Fig. 5.20(e),(f)), something peculiar happens: the formerly distinct QD transitions "melt" into the background, and the spectrum is eventually strongly dominated by the cavity mode emission. The latter finding is an intriguing new phenomenon that is specific to the mutually coupled QD pair. We never measured similar characteristic from resonant single QDs or from QD pairs that were off-resonant. The striking differences between the behavior of a resonant QD pair and a non-resonant system can be witnessed by comparing the spectra in Fig. 5.19 and Fig. 5.20 with Fig. 5.10 and Fig. 5.11.

In Fig. 5.22, we present an analysis of the power dependence of the individual peaks from the separate QDs as well as the combined s- and p-shell transitions. Let us first discuss the characteristics of the first QD in Fig. 5.22(a). The X_a transition of the first QD, which spectrally overlaps with the $M0$ mode, is observed to saturate at $\sim 200 \mu\text{W}$ and to attenuate at higher powers, until it eventually vanishes at $1000 \mu\text{W}$. The cavity mode, on the other hand, always has a larger intensity than the QD features and continues to grow in intensity up to $\sim 1000 \mu\text{W}$. Likewise, the near-resonant X_b^- peak of the second QD (Fig. 5.22(b)) also saturates at $\sim 200 \mu\text{W}$ and disappears at $1000 \mu\text{W}$ pump power. Finally, the behavior of all s-shell and p-shell transitions in the power dependence in Fig. 5.22(c) shows that the cavity mode follows the same trend as the s-shell transitions up to a power of $\sim 200 \mu\text{W}$. Note that this s-shell-like power dependence of the cavity mode is consistent with the behavior of the far-off resonant QD pair that we analyzed in Sec. 5.2.4. However, the characteristics of the resonant QD pair (Fig. 5.22(c)) deviates from the off-resonant situation (Fig. 5.13(c))

when the power is increased above the saturation point of the s-shells. In the case of the resonant QD pair in Fig. 5.22(c), the cavity mode intensity adopts a dependence on excitation power which is different from the s-shell states and also from the p shells. In contrast, in the case of the off-resonant QD pair in Fig. 5.13(c), we saw that the cavity mode entirely mimicked the power dependence of the s-shells, including the saturation trend.

One might suspect that the characteristics of this resonant QD pair could be associated with stimulated emission and lasing. In systems based on SKQDs in PhC nanocavities, lasing has indeed been evidenced in a threshold behavior of the light output together with a linewidth narrowing [166]. However, in that case lasing was assisted by transitions from the wetting layer. We do not observe a lasing threshold in the power dependence of the cavity mode intensity. In addition, the linewidth behavior of the resonant QD pair (Fig. 5.23(a)) shows non-trivial characteristics. To give complementary information, we also plotted the corresponding Q factor variation in Fig. 5.23(b). Although the mode linewidth does initially narrow down when the power is increased from $25\ \mu\text{W}$ to $200\ \mu\text{W}$ in Fig. 5.23(a), it then reaches a plateau. Interestingly, the plateau starts right at the point of saturation of the s-shell states, which suggests that the linewidth stops broadening due to absorption saturation [155]. After the plateau in the cavity linewidth, i.e. from $800\ \mu\text{W}$ onwards towards higher powers, the linewidth broadens back to a value that is close to the initial point at $25\ \mu\text{W}$. This is an indication for increased absorption and/or phase noise due to refractive index variations.

Therefore, it seems unlikely that the dynamics of the resonant QD pair were influenced by laser oscillation. We can only speculate at this point about the interpretation of the data, because we currently do not have a theoretical model to explain the phenomena. One possibility is that superradiance and subradiance effects contribute to the spontaneous emission characteristics, such that the pronounced cavity mode intensity and its dominance at high powers could be a signature of cooperative spontaneous emission of the two QDs. In fact, according to theoretical studies of few quantum emitters in a weakly coupled cavity, cooperative spontaneous emission should indeed take place [214–217, 228]. Another possible scenario is that at high powers the cavity mode begins to capture photons from higher-energy states, i.e. from the p-shells and possibly also from the quantum wires surrounding the QDs. This would explain the linewidth broadening at high powers.

5.3. A mutually coupled quantum dot pair

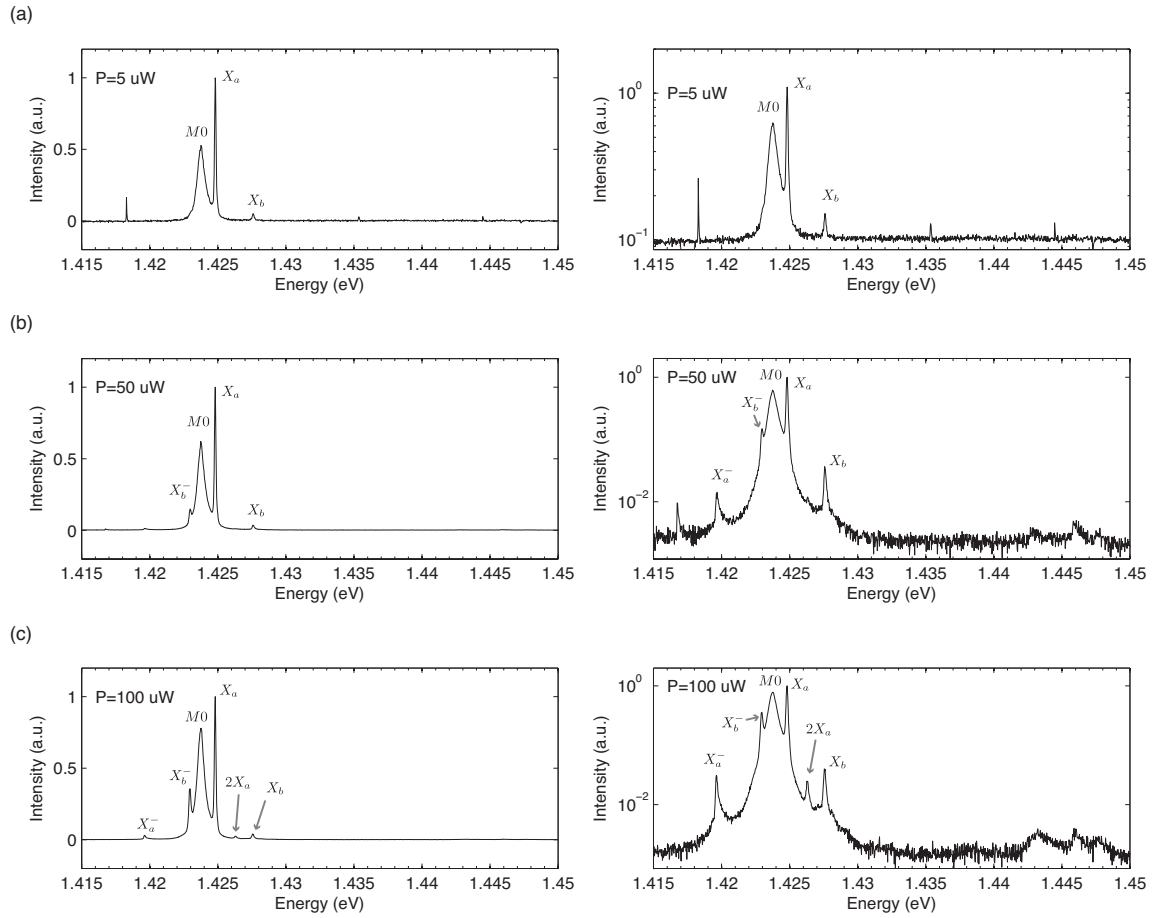


Figure 5.19: PL spectra from a resonant $L3$ cavity containing a QD pair, measured at different excitation powers. The panels on the left show linear plots, whereas the panels on the right display the same data in semilogarithmic form.

Chapter 5. Two spatially separated quantum dots in a photonic crystal cavity

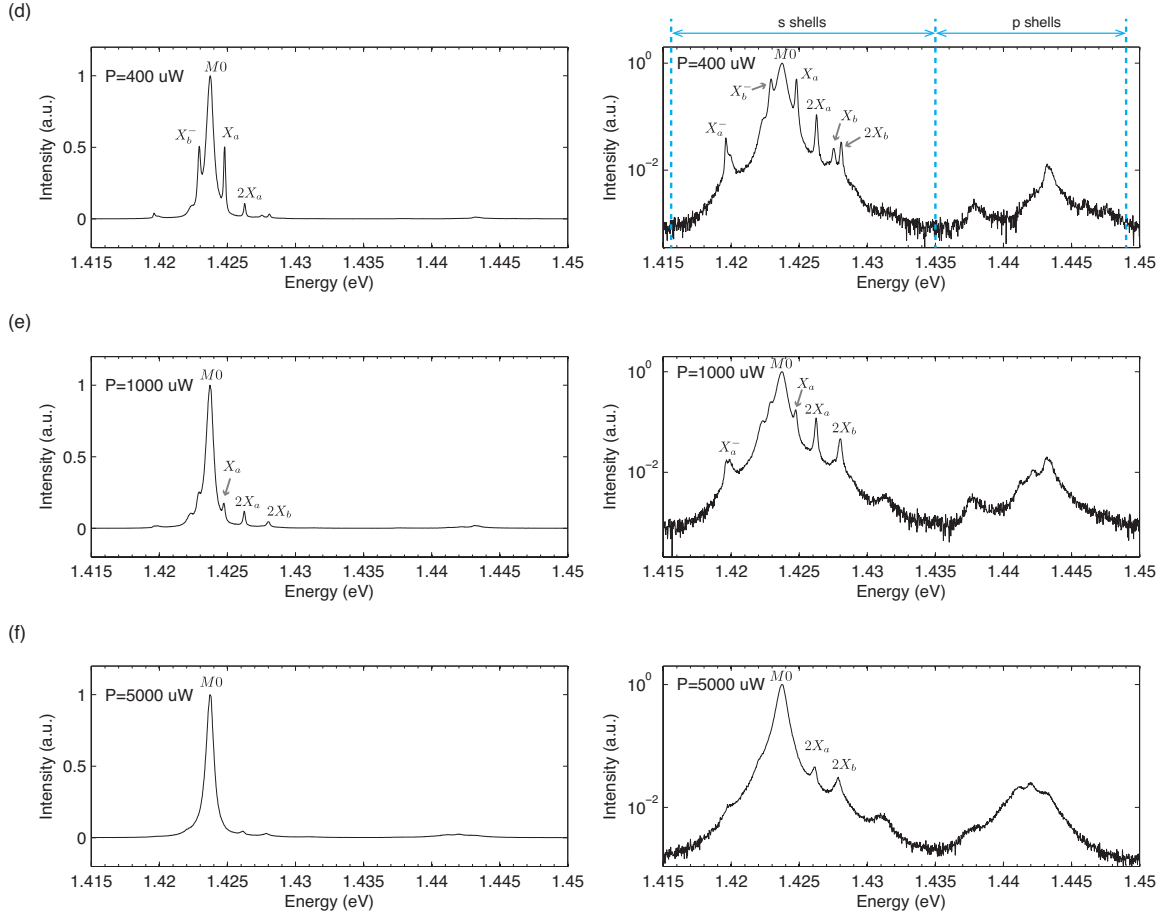


Figure 5.20: Continuation of the previous figure. Notice how the ground state transitions of the QD pair virtually disappear at high power.

Quantum dot #1		Quantum dot #2	
Peak name	E_b (meV)	Peak name	E_b (meV)
X_a^-	-4.9	X_b^-	-4.6
$2X_a$	1.5	$2X_b$	0.5

Figure 5.21: Overview of the binding energies E_b (i.e. spectral distance with respect to the neutral exciton X) for the excitonic features of the two QDs in Figs. 5.19 and 5.20.

5.3. A mutually coupled quantum dot pair

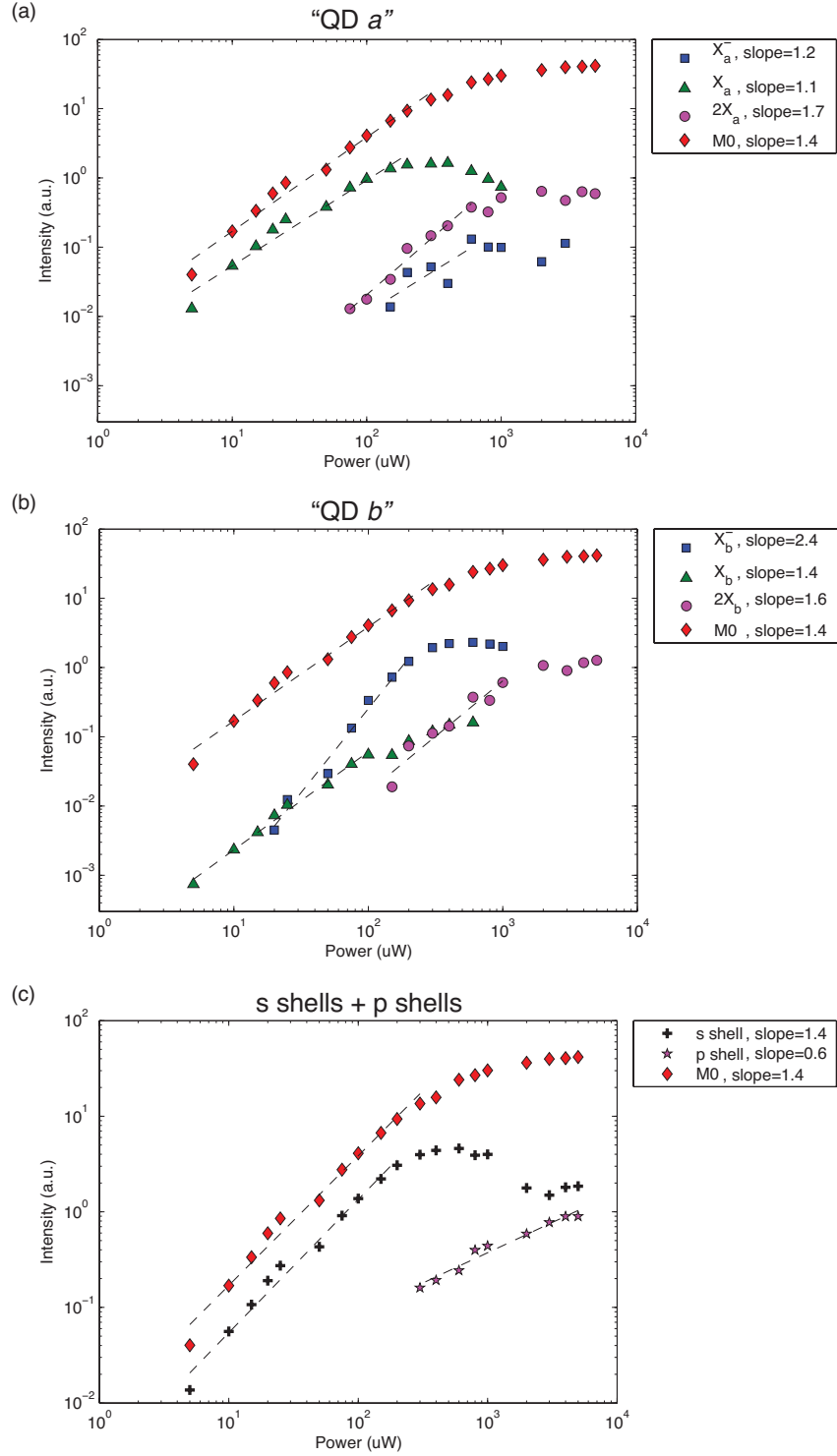


Figure 5.22: Analysis of the power dependence of a resonant QD pair, see previous figure. (a) and (b): Power dependence of the integrated intensities belonging to the corresponding excitonic transitions of "QD a" and "QD b", respectively. The mode $M0$ is plotted in all graphs for comparison. The dashed lines designate linear fits to the data; the slopes are indicated in the graph legend. (c) Dependence of the integrated intensities of the s and p shells on excitation power. The intensity of the cavity mode $M0$ was subtracted from the total intensity of the s shell transitions.

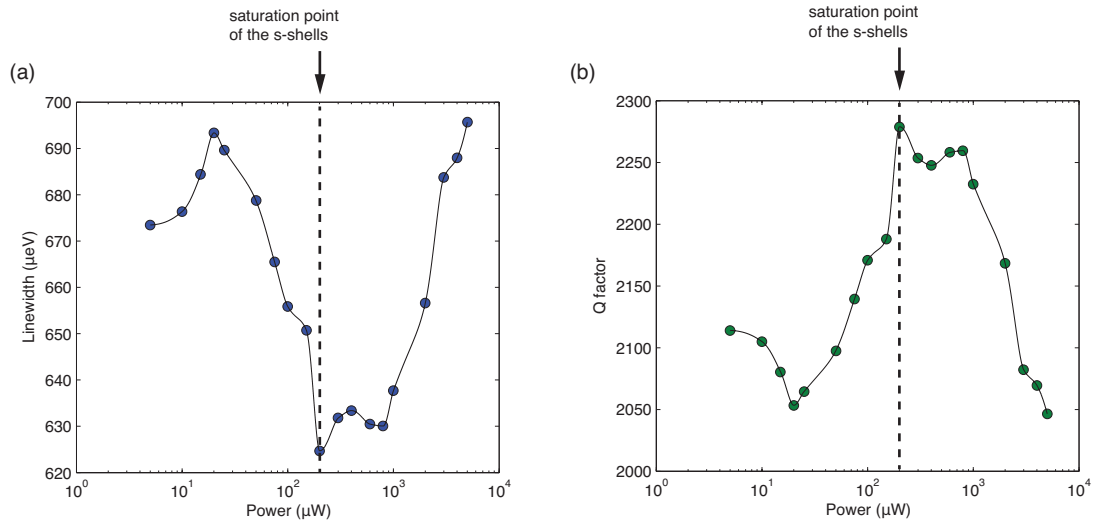


Figure 5.23: Variation of the cavity mode linewidth (a) and the Q factor (b) as a function of excitation power. The dashed line indicates the approximate power value at which the integrated intensity of the s-shells saturates.

5.4 Chapter summary

In this chapter, we studied the emission characteristics of two separate pyramidal QDs embedded in an $L3$ PhC cavity. We showed polarization-resolved spectra which evidenced the controlled r/a -tuning of the cavity resonance accross the QD spectra. The spectra also revealed that there exists off-resonant emission when the cavity mode is far detuned from the QD transitions. According to our analysis from power dependence measurements, the off-resonant emission from the cavity mode is associated with the sum of all s-shell states from both QDs.

Furthermore, we found that the polarization of the PL emission from an $L3$ cavity has a characteristic spectral profile surrounding its fundamental mode ("s-shaped DOLP"), which we assigned to the photonic density of states that is formed in the $L3$ PhC structure. In order to verify this point, a 3D computation for the LDOS of an $L3$ cavity should be performed.

Finally, we studied a mutually coupled QD pair and demonstrated that both QDs are simultaneously subject to the Purcell effect. Our analysis of the integrated intensities showed that the individual QD peaks traced nearly Lorentzian-shaped curves as a function of detuning. The polarization features of the individual QD peaks were found to precisely follow the s-shaped polarization profile of the cavity mode as a function of detuning.

The measurements furthermore revealed that at high excitation powers the discrete QD lines disappeared from the spectrum, leaving the cavity mode as the dominant emission channel of the system. The latter observation indicates the existence of a phenomenon that has previously not been reported for QDs in cavities so far. A candidate explanation for these emission characteristics could be the existence of collective effects (e.g. super- and subradiance [214–217, 228]). However, in order to be able to give a clearer assessment of the situation, further experimental and theoretical investigations will be necessary.

6 Conclusions and outlook

In the course of this thesis, we developed a novel nanofabrication technique for integrating single and pairs of site-controlled pyramidal QDs into PhC nanocavities. By taking advantage of the high-precision capabilities of electron-beam lithography for the definition and the alignment of the nanostructures, we were able to realize a scalable and deterministic method for yielding many effectively coupled QD-cavity devices on the same substrate. From a technical standpoint, this represents a major progress beyond state-of-the-art techniques which still mostly rely on randomly distributed self-assembled QDs. The average alignment accuracy of the QDs with respect to their target positions within the PhC cavities amounted 50 nm, the inhomogeneous broadening of the QDs was as low as 10 meV, and the individual excitonic linewidths were of the order of $\sim 100 \mu\text{eV}$. In addition, the reproducibility of the single QDs was outstanding, as evidenced in the recurring pattern of three distinct ground state transitions in the majority of the optical spectra [40]. However, the average Q factor of the PhC cavities was approximately 3000. Although this was sufficient to probe clear signatures of the Purcell effect, it was not enough to evidence strong light-matter coupling. Possible ways of increasing the average Q factors of the cavities are through improvements in the structural quality of the PhCs and through shifting the operation wavelength to above 900 nm in order to minimize material absorption losses (see Fig. 5.8(b)). Another issue that should be addressed in future works is the rather large broadening of the QD linewidths, which is mostly caused by spectral diffusion. Efforts should therefore be undertaken in order to minimize the incorporation of impurities during the substrate preparation and MOVPE growth.

Our studies on single pyramidal QDs in PhC nanocavities shed light on some detailed aspects of light-matter coupling in a solid state environment. The analysis of the experimental data unraveled the detail-rich polarization features that arise due to the interaction of a QD with the local photonic environment of the cavity. Polarization-resolved PL measurements are thus very useful for capturing the cou-

pling characteristics of QD-cavity systems. This allowed us to attest that the optical polarization of a QD exciton sensitively depends on detuning, such that close to resonance the QD transition switches from being oppositely polarized to co-polarized with the cavity mode [64]. In addition to the polarization switching, we also observed an enhancement of the QD intensity and a linewidth narrowing upon crossing the cavity resonance. These variations are all manifestations of the Purcell effect. Our observation of the linewidth narrowing effect brought up the question about how one can distinguish between the influence of phonons from that of the fluctuating charge environment (spectral diffusion). To better understand the role of spectral diffusion in QD-cavity coupling, a microscopic model should be developed.

Probably the most important result from our experiments with single pyramidal QDs in cavities is the finding that their coupling behavior in PhC cavities is in accordance with the picture of an artificial atom with well isolated, discrete 0D states that interacts with the phonon reservoir of the solid state environment [64, 181]. The relevance of this finding is emphasized by the series of publications where the origin of the cavity feeding phenomenon has been debated [56–61, 65, 69, 115, 116, 150, 166–172]. Our results from photon correlation and power dependence measurements proved that only the near-resonant QD exciton emits photons into the cavity mode, such that the presence of the spurious emission background responsible for cavity feeding can be ruled out [169]. In contrast, previous experimental studies with systems based on SKQDs had all consistently evidenced the cavity feeding mechanism, which led to the belief that this was a universal phenomenon [169]. Our results therefore provided substantial proof that the latter hypothesis does not apply to QD systems in general. The seemingly near-ideal behavior of pyramidal QDs in cavity QED experiments might be due to their specific barrier structure; in particular, they do not possess a 2D wetting layer like SKQDs. However, further experimental and theoretical investigations will be necessary in order to analyze the role of the barriers on the electronic density of states in the case of pyramidal QDs. On the experimental side, one could gain important information about the electronic density of states by conducting photoluminescence excitation (PLE) measurements on single pyramidal QDs [175, 177]. On the theoretical side, it could be very insightful to compare the differences between the situation where a QD is coupled to a 2D wetting layer reservoir [201] and the situation where the QD only interacts with 1D quantum wires, which exist in the barrier environment of pyramidal QDs.

Regarding our experiments with two separate pyramidal QDs in a PhC nanocavity, it should first be pointed out that prior to this thesis work there were no systematic studies reported for similar systems (i.e. two QDs in a cavity). The reason for this is that none of the other currently existing QD fabrication methods was (and still is)

advanced enough to systematically measure and compare the emission properties from many nominally equal two-QD-cavity systems. The site-controlled technology of pyramidal QDs was therefore of crucial importance for conducting the systematic investigations reported in this thesis.

One of our main findings from two separate pyramidal QDs in a PhC nanocavity is the observation of a weak emission signal from the far-off resonance cavity mode. The far-off resonance emission from the cavity mode persisted for detunings of up to 30 meV, which indicates a yet unidentified excitation transfer mechanism. This phenomenon was specific to cavities that contained two QDs; in the case of single QDs, we never observed a significant emission from the cavity mode when it was detuned by more than 5 meV. Our power dependence measurements from QD pairs showed that the off-resonant cavity mode exhibits a trend that mimics the sum of all s-shell states, indicating that the latter somehow couple to the cavity mode in a combined fashion. It is not understood at this point what causes this interaction. It might be related to a radiative interaction between the two QDs, or possibly to a pure dephasing mechanism.

Another interesting discovery that came out from our systematic PL measurements of QD pairs in a cavity was that the polarization of the emitted light exhibited a characteristic "s-shaped" spectral profile, which was centered at the cavity mode frequency. We concluded that this polarization profile is the "footprint" of the local photonic environment inside the *L3* nanocavity. However, this point should be theoretically examined by performing a calculation of the local optical density of states and investigating the consequences on the Purcell enhancement.

Finally, the highlight from our experiments with pairs of QDs was the demonstration of mutual Purcell enhancement by the cavity. We found that the emission intensities of QDs traced Lorentzian-shaped curves as a function of detuning. The polarizations of the individual QD peaks were observed to follow the intrinsic s-shaped polarization profile of the *L3* cavity. Probably the most striking observation from this particular system was that when the excitation power was increased to high levels, the discrete peaks from both QDs gradually disappeared from the spectrum and left the cavity mode as the dominant emission channel. This might be an aspect of cavity-mediated radiative coupling [214–217, 228]. In order to further investigate effects of cooperative emission in future works, one interesting possibility would be to systematically scale the number of emitters within a cavity [216].

In conclusion, the present thesis consolidates the potential of site-controlled QD technology as a scalable platform for realizing advanced cavity quantum electrodynamics schemes. The developed nanofabrication technique can readily be

extended to implement more complex architectures, such as multiple QDs in a cavity [46], coupled-cavity structures [93, 233] (Fig. 6.1) and waveguide-coupled distant cavities [234].

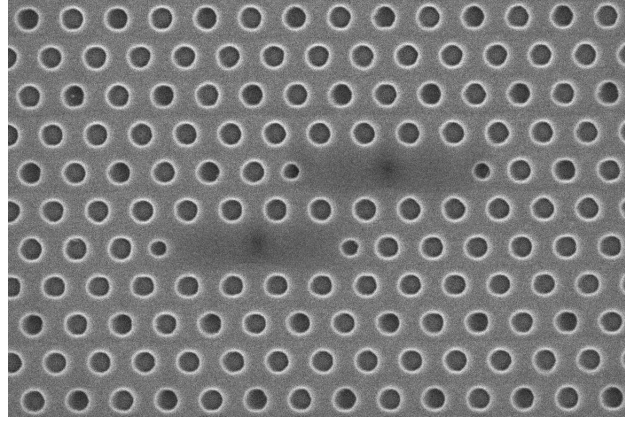


Figure 6.1: SEM image of a coupled-cavity structure that was fabricated towards the end of this thesis, consisting of two diagonally coupled $L3$ cavities [233] that each contain a single pyramidal QD at their centers (visible as dark spots). This picture was taken before the PhC holes were transferred from the SiO_2 mask to the underlying GaAs membrane.

A List of publications and conferences

Journal publications

- C. Jarlov, P. Gallo, M. Calic, B. Dwir, A. Rudra, and E. Kapon, “Bound and antibound biexciton in site-controlled pyramidal GaInAs/GaAs quantum dots”, *Applied Physics Letters* **101**, 191101 (2012).
- M. Calic, P. Gallo, M. Felici, K. A. Atlasov, B. Dwir, A. Rudra, G. Biasiol, L. Sorba, G. Tarel, V. Savona, and E. Kapon, “Phonon-mediated coupling of InGaAs/GaAs quantum-dot excitons to photonic crystal cavities” ,*Physical Review Letters* **106**, 227402 (2011).
- K. A. Atlasov, M. Calic, K. F. Karlsson, P. Gallo, A. Rudra, B. Dwir, and E. Kapon, “Photonic-crystal microcavity laser with site-controlled quantum-wire active medium”, *Optics Express* **17**, 18178 (2009).

Conference presentations

- M. Calic, P. Gallo, C. Jarlov, L. Ferrier, B. Dwir, A. Rudra, G. Biasiol and E. Kapon, “Coupling of two separate site-controlled quantum dots to a common photonic crystal cavity mode”, *31st International Conference on the Physics of Semiconductors (ICPS 2012)*, Zurich, Switzerland, July 29 – August 3, 2012. Contributed oral presentation.
- M. Calic, P. Gallo, C. Jarlov, L. Ferrier, B. Dwir, A. Rudra, G. Biasiol and E. Kapon, “Coupling of two separate site-controlled quantum dots to a common photonic crystal cavity mode”, *International Conference on Quantum Dots (QD 2012)*, Santa Fe, New Mexico, USA, May 13-18, 2012. Contributed oral presentation.
- M. Calic, P. Gallo, M. Felici, K. A. Atlasov, B. Dwir, A. Rudra, G. Biasiol, L. Sorba,

Appendix A. List of publications and conferences

and E. Kapon, "Phonon-mediated exciton-photon coupling in site-controlled quantum-dot-nanocavity systems", *Conference on Lasers and Electro-Optics 2011 (CLEO:2011)*, Baltimore, Maryland, USA, May 1-6, 2011. Contributed oral presentation.

- M. Calic, P. Gallo, M. Felici, K. A. Atlasov, B. Dwir, A. Rudra, G. Biasiol, L. Sorba, and E. Kapon, "Phonon-mediated exciton-photon coupling in site-controlled quantum-dot-nanocavity systems", *11th International conference on Physics of Light-Matter coupling in Nanostructures (PLMCN11)*, Berlin, Germany, April 4-8, 2011. Contributed oral presentation.
- M. Calic, P. Gallo, M. Felici, K. A. Atlasov, B. Dwir, A. Rudra, G. Biasiol, L. Sorba, and E. Kapon, "Evidence for the absence of non-resonant coupling in site-controlled pyramidal quantum dots integrated with photonic crystal cavities", *30th International Conference on the Physics of Semiconductors (ICPS 2010)*, Seoul, Korea, July 25-30, 2010 (Contributed, Oral).



Bibliography

- [1] B. Saleh and M. Teich, *Fundamentals of Photonics* (Wiley, 2007).
- [2] <http://www.rp-photonics.com>. RP Photonics Encyclopedia.
- [3] <http://www.photonics21.org>. "Photonics - Our vision for a key enabling technology for Europe", Brochure from the European Technology Platform Photonics 21.
- [4] http://researcher.ibm.com/researcher/view_project.php?id=2757. "Silicon Integrated Nanophotonics Technology: from the Lab to the Fab", Online article from IBM.
- [5] <http://www.intel.com/content/www/us/en/research/intel-labs-silicon-photonics-research.html>. "Intel silicon photonics technology", Online article by Intel.
- [6] C. M. Soukoulis and M. Wegener, "Past achievements and future challenges in the development of three-dimensional photonic metamaterials," *Nature Photonics* **5**, 523 (2011).
- [7] D. Schurig, J. J. Mock, B. J. Justice, S. A. Cummer, J. B. Pendry, A. F. Starr, and D. R. Smith, "Metamaterial electromagnetic cloak at microwave frequencies," *Science* **314**, 977 (2006).
- [8] S. A. Maier and H. A. Atwater, "Plasmonics: Localization and guiding of electromagnetic energy in metal/dielectric structures," *Journal of Applied Physics* **98**, 011101 (2005).
- [9] M. Kauranen and A. V. Zayats, "Nonlinear plasmonics," *Nature Photonics* **6**, 737 (2012).
- [10] D. Prather, *Photonic Crystals, Theory, Applications and Fabrication* (Wiley, 2009).
- [11] J. D. Joannopoulos, P. R. Villeneuve, and S. H. Fan, "Photonic crystals: Putting a new twist on light," *Nature* **386**, 143 (1997).

Bibliography

- [12] E. Kapon, *Semiconductor Lasers I: Fundamentals* (Elsevier Science, 1999).
- [13] K. J. Vahala, "Optical microcavities," *Nature* **424**, 839 (2003).
- [14] J. M. Gerard, B. Sermage, B. Gayral, B. Legrand, E. Costard, and V. Thierry-Mieg, "Enhanced spontaneous emission by quantum boxes in a monolithic optical microcavity," *Physical Review Letters* **81**, 1110 (1998).
- [15] D. K. Armani, T. J. Kippenberg, S. M. Spillane, and K. J. Vahala, "Ultra-high-q toroid microcavity on a chip," *Nature* **421**, 925 (2003).
- [16] K. Srinivasan and O. Painter, "Linear and nonlinear optical spectroscopy of a strongly coupled microdisk-quantum dot system," *Nature* **450**, 862 (2007).
- [17] O. Painter, R. K. Lee, A. Scherer, A. Yariv, J. D. O'Brien, P. D. Dapkus, and I. Kim, "Two-dimensional photonic band-gap defect mode laser," *Science* **284**, 1819 (1999).
- [18] A. M. Fox, *Quantum Optics: An Introduction*, Oxford Master Series in Physics (Oxford University Press, 2006).
- [19] A. Faraon, I. Fushman, D. Englund, N. Stoltz, P. Petroff, and J. Vuckovic, "Coherent generation of non-classical light on a chip via photon-induced tunnelling and blockade," *Nature Physics* **4**, 859 (2008).
- [20] G. Khitrova, H. M. Gibbs, M. Kira, S. W. Koch, and A. Scherer, "Vacuum rabi splitting in semiconductors," *Nature Physics* **2**, 81 (2006).
- [21] N. Ashcroft and N. Mermin, *Solid state physics* (Saunders College, 1976).
- [22] P. Michler, *Single Quantum Dots: Fundamentals, Applications and New Concepts* (Springer, 2003).
- [23] G. D. Scholes and G. Rumbles, "Excitons in nanoscale systems," *Nature Materials* **5**, 683 (2006).
- [24] S. Kiravittaya, A. Rastelli, and O. G. Schmidt, "Advanced quantum dot configurations," *Reports on Progress in Physics* **72**, 046502 (2009).
- [25] C. A. Foell, E. Schelew, H. J. Qiao, K. A. Abel, S. Hughes, F. C. J. M. van Veggel, and J. F. Young, "Saturation behaviour of colloidal pbse quantum dot exciton emission coupled into silicon photonic circuits," *Optics Express* **20**, 10453 (2012).
- [26] A. Zrenner, "A close look on single quantum dots," *Journal of Chemical Physics* **112**, 7790 (2000).

-
- [27] J. Marquez, L. Geelhaar, and K. Jacobi, "Atomically resolved structure of inas quantum dots," *Applied Physics Letters* **78**, 2309 (2001).
 - [28] T. Yoshie, A. Scherer, J. Hendrickson, G. Khitrova, H. M. Gibbs, G. Rupper, C. Ell, O. B. Shchekin, and D. G. Deppe, "Vacuum rabi splitting with a single quantum dot in a photonic crystal nanocavity," *Nature* **432**, 200 (2004).
 - [29] A. Badolato, M. Winger, K. J. Hennessy, E. L. Hu, and A. Imamoglu, "Cavity qed effects with single quantum dots," *Comptes Rendus Physique* **9**, 850 (2008).
 - [30] R. M. Stevenson, R. M. Thompson, A. J. Shields, I. Farrer, B. E. Kardynal, D. A. Ritchie, and M. Pepper, "Quantum dots as a photon source for passive quantum key encoding," *Physical Review B* **66**, 081302 (2002).
 - [31] D. C. Unitt, A. J. Bennett, P. Atkinson, D. A. Ritchie, and A. J. Shields, "Polarization control of quantum dot single-photon sources via a dipole-dependent purcell effect," *Physical Review B* **72**, 033318 (2005).
 - [32] R. M. Stevenson, R. J. Young, P. Atkinson, K. Cooper, D. A. Ritchie, and A. J. Shields, "A semiconductor source of triggered entangled photon pairs," *Nature* **439**, 179 (2006).
 - [33] C. Schneider, M. Strauss, T. Sunner, A. Huggenberger, D. Wiener, S. Reitzenstein, M. Kamp, S. Hofling, and A. Forchel, "Lithographic alignment to site-controlled quantum dots for device integration," *Applied Physics Letters* **92**, 183101 (2008).
 - [34] C. Schneider, A. Huggenberger, T. Sunner, T. Heindel, M. Strauss, S. Gopfert, P. Weinmann, S. Reitzenstein, L. Worschech, M. Kamp, S. Hofling, and A. Forchel, "Single site-controlled In(Ga)As/GaAs quantum dots: growth, properties and device integration," *Nanotechnology* **20**, 9 (2009).
 - [35] C. Schneider, T. Heindel, A. Huggenberger, P. Weinmann, C. Kistner, M. Kamp, S. Reitzenstein, S. Hofling, and A. Forchel, "Single photon emission from a site-controlled quantum dot-micropillar cavity system," *Applied Physics Letters* **94**, 111111 (2009).
 - [36] T. Sunner, C. Schneider, M. Strauss, A. Huggenberger, D. Wiener, S. Hofling, M. Kamp, and A. Forchel, "Scalable fabrication of optical resonators with embedded site-controlled quantum dots," *Optics Letters* **33**, 1759 (2008).
 - [37] E. Kapon, E. Pelucchi, S. Watanabe, A. Malko, M. H. Baier, K. Leifer, B. Dwir, F. Michelini, and M. A. Dupertuis, "Site- and energy-controlled pyramidal quantum dot heterostructures," *Physica E-Low-Dimensional Systems & Nanostructures* **25**, 288 (2004).

- [38] A. Mohan, P. Gallo, M. Felici, B. Dwir, A. Rudra, J. Faist, and E. Kapon, "Record-low inhomogeneous broadening of site-controlled quantum dots for nanophotonics," *Small* **6**, 1268 (2010).
- [39] M. H. Baier, E. Pelucchi, E. Kapon, S. Varoutsis, M. Gallart, I. Robert-Philip, and I. Abram, "Single photon emission from site-controlled pyramidal quantum dots," *Applied Physics Letters* **84**, 648 (2004).
- [40] C. Jarlov, P. Gallo, M. Calic, B. Dwir, A. Rudra, and E. Kapon, "Bound and anti-bound biexciton in site-controlled pyramidal GaInAs/GaAs quantum dots," *Applied Physics Letters* **101**, 191101 (2012).
- [41] A. Hartmann, Y. Ducommun, E. Kapon, U. Hohenester, and E. Molinari, "Few-particle effects in semiconductor quantum dots: Observation of multicharged excitons," *Physical Review Letters* **84**, 5648 (2000).
- [42] A. Surrente, P. Gallo, M. Felici, B. Dwir, A. Rudra, and E. Kapon, "Dense arrays of ordered pyramidal quantum dots with narrow linewidth photoluminescence spectra," *Nanotechnology* **20**, 415205 (2009).
- [43] P. Gallo, M. Felici, B. Dwir, K. A. Atlasov, K. F. Karlsson, A. Rudra, A. Mohan, G. Biasiol, L. Sorba, and E. Kapon, "Integration of site-controlled pyramidal quantum dots and photonic crystal membrane cavities," *Applied Physics Letters* **92**, 263101 (2008).
- [44] Q. Zhu, K. F. Karlsson, M. Byszewski, A. Rudra, E. Pelucchi, Z. B. He, and E. Kapon, "Hybridization of electron and hole states in semiconductor quantum-dot molecules," *Small* **5**, 329 (2009).
- [45] R. Carron, P. Gallo, B. Dwir, A. Rudra, and E. Kapon, "Dilute-nitride GaInAs-N/GaAs site-controlled pyramidal quantum dots," *Applied Physics Letters* **99**, 181113 (2011).
- [46] A. Surrente, M. Felici, P. Gallo, B. Dwir, A. Rudra, G. Biasiol, L. Sorba, and E. Kapon, "Ordered systems of site-controlled pyramidal quantum dots incorporated in photonic crystal cavities," *Nanotechnology* **22**, 465203 (2011).
- [47] E. Poem, Y. Kodriano, C. Tradonsky, N. H. Lindner, B. D. Gerardot, P. M. Petroff, and D. Gershoni, "Accessing the dark exciton with light," *Nature Physics* **6**, 993–997 (2010).
- [48] D. Gammon and D. G. Steel, "Optical studies of single quantum dots," *Physics Today* **55**, 36 (2002).

-
- [49] Z. L. Yuan, B. E. Kardynal, R. M. Stevenson, A. J. Shields, C. J. Lobo, K. Cooper, N. S. Beattie, D. A. Ritchie, and M. Pepper, “Electrically driven single-photon source,” *Science* **295**, 102–105 (2002).
- [50] C. L. Salter, R. M. Stevenson, I. Farrer, C. A. Nicoll, D. A. Ritchie, and A. J. Shields, “An entangled-light-emitting diode,” *Nature* **465**, 594 (2010).
- [51] J. L. O’Brien, A. Furusawa, and J. Vuckovic, “Photonic quantum technologies,” *Nature Photonics* **3**, 687 (2009).
- [52] D. Press, T. D. Ladd, B. Y. Zhang, and Y. Yamamoto, “Complete quantum control of a single quantum dot spin using ultrafast optical pulses,” *Nature* **456**, 218–221 (2008).
- [53] J. I. Cirac, P. Zoller, H. J. Kimble, and H. Mabuchi, “Quantum state transfer and entanglement distribution among distant nodes in a quantum network,” *Physical Review Letters* **78**, 3221 (1997).
- [54] K. De Greve, L. Yu, P. L. McMahon, J. S. Pelc, C. M. Natarajan, N. Y. Kim, E. Abe, S. Maier, C. Schneider, M. Kamp, S. Hofling, R. H. Hadfield, A. Forchel, M. M. Fejer, and Y. Yamamoto, “Quantum-dot spin-photon entanglement via frequency downconversion to telecom wavelength,” *Nature* **491**, 421 (2012).
- [55] K. De Greve, P. L. McMahon, L. Yu, J. S. Pelc, C. Jones, C. M. Natarajan, N. Y. Kim, E. Abe, S. Maier, C. Schneider, M. Kamp, S. Hofling, R. H. Hadfield, A. Forchel, M. M. Fejer, and Y. Yamamoto, “Complete tomography of a high-fidelity solid-state entangled spin-photon qubit pair,” *Nature Communications* **4** (2013).
- [56] A. Naesby, T. Suhr, P. T. Kristensen, and J. Mork, “Influence of pure dephasing on emission spectra from single photon sources,” *Physical Review A* **78**, 045802 (2008).
- [57] A. Auffeves, J. M. Gerard, and J. P. Poizat, “Pure emitter dephasing: A resource for advanced solid-state single-photon sources,” *Physical Review A* **79**, 053838 (2009).
- [58] M. Yamaguchi, T. Asano, K. Kojima, and S. Noda, “Quantum electrodynamics of a nanocavity coupled with exciton complexes in a quantum dot,” *Physical Review B* **80**, 155326 (2009).
- [59] U. Hohenester, A. Laucht, M. Kaniber, N. Hauke, A. Neumann, A. Mohtashami, M. Seliger, M. Bichler, and J. J. Finley, “Phonon-assisted transitions from quantum dot excitons to cavity photons,” *Physical Review B* **80**, 201311 (2009).

- [60] S. Ates, S. M. Ulrich, A. Ulhaq, S. Reitzenstein, A. Löffler, S. Hofling, A. Forchel, and P. Michler, “Non-resonant dot-cavity coupling and its potential for resonant single-quantum-dot spectroscopy,” *Nature Photonics* **3**, 724 (2009).
- [61] J. Suffczynski, A. Dousse, K. Gauthron, A. Lemaitre, I. Sagnes, L. Lanco, J. Bloch, P. Voisin, and P. Senellart, “Origin of the optical emission within the cavity mode of coupled quantum dot-cavity systems,” *Physical Review Letters* **103**, 027401 (2009).
- [62] A. Auffeves, D. Gerace, J. M. Gerard, M. F. Santos, L. C. Andreani, and J. P. Poizat, “Controlling the dynamics of a coupled atom-cavity system by pure dephasing,” *Physical Review B* **81**, 245419 (2010).
- [63] A. Ulhaq, S. Ates, S. Weiler, S. M. Ulrich, S. Reitzenstein, A. Löffler, S. Hofling, L. Worschech, A. Forchel, and P. Michler, “Linewidth broadening and emission saturation of a resonantly excited quantum dot monitored via an off-resonant cavity mode,” *Physical Review B* **82**, 045307 (2010).
- [64] M. Calic, P. Gallo, M. Felici, K. A. Atlasov, B. Dwir, A. Rudra, G. Biasiol, L. Sorba, G. Tarel, V. Savona, and E. Kapon, “Phonon-Mediated Coupling of InGaAs/GaAs Quantum-Dot Excitons to Photonic Crystal Cavities,” *Physical Review Letters* **106**, 227402 (2011).
- [65] S. Hughes, P. Yao, F. Milde, A. Knorr, D. Dalacu, K. Mnaymneh, V. Sazonova, P. J. Poole, G. C. Aers, J. Lapointe, R. Cheriton, and R. L. Williams, “Influence of electron-acoustic phonon scattering on off-resonant cavity feeding within a strongly coupled quantum-dot cavity system,” *Physical Review B* **83**, 165313 (2011).
- [66] A. Majumdar, E. D. Kim, Y. Y. Gong, M. Bajcsy, and J. Vuckovic, “Phonon mediated off-resonant quantum dot-cavity coupling under resonant excitation of the quantum dot,” *Physical Review B* **84**, 085309 (2011).
- [67] S. M. Ulrich, S. Ates, S. Reitzenstein, A. Löffler, A. Forchel, and P. Michler, “Dephasing of Triplet-Sideband Optical Emission of a Resonantly Driven InAs/GaAs Quantum Dot inside a Microcavity,” *Physical Review Letters* **106**, 247402 (2011).
- [68] A. Majumdar, E. D. Kim, and J. Vuckovic, “Effect of photogenerated carriers on the spectral diffusion of a quantum dot coupled to a photonic crystal cavity,” *Physical Review B* **84**, 195304 (2011).
- [69] M. Yamaguchi, T. Asano, and S. Noda, “Third emission mechanism in solid-state nanocavity quantum electrodynamics,” *Reports on Progress in Physics* **75**, 096401 (2012).

-
- [70] G. Q. Cui and M. G. Raymer, "Emission spectra and quantum efficiency of single-photon sources in the cavity-qed strong-coupling regime," *Physical Review A* **73**, 053807 (2006).
- [71] A. Laucht, N. Hauke, J. M. Villas-Boas, F. Hofbauer, G. Böhm, M. Kaniber, and J. J. Finley, "Dephasing of Exciton Polaritons in Photoexcited InGaAs Quantum Dots in GaAs Nanocavities," *Physical Review Letters* **103**, 087405 (2009).
- [72] P. Borri, W. Langbein, S. Schneider, U. Woggon, R. L. Sellin, D. Ouyang, and D. Bimberg, "Ultralong dephasing time in InGaAs quantum dots," *Physical Review Letters* **87**, 157401 (2001).
- [73] A. Hoge, S. Seidl, M. Kroner, K. Karrai, R. J. Warburton, B. D. Gerardot, and P. M. Petroff, "Voltage-controlled optics of a quantum dot," *Physical Review Letters* **93**, 217401 (2004).
- [74] M. Bayer and A. Forchel, "Temperature dependence of the exciton homogeneous linewidth in In_{0.60}Ga_{0.40}As/GaAs self-assembled quantum dots," *Physical Review B* **65**, 041308 (2002).
- [75] E. Peter, J. Hours, P. Senellart, A. Vasanelli, A. Cavanna, J. Bloch, and J. M. Gerard, "Phonon sidebands in exciton and biexciton emission from single GaAs quantum dots," *Physical Review B* **69**, 041307 (2004).
- [76] B. Urbaszek, E. J. McGhee, M. Kruger, R. J. Warburton, K. Karrai, T. Amand, B. D. Gerardot, P. M. Petroff, and J. M. Garcia, "Temperature-dependent linewidth of charged excitons in semiconductor quantum dots: Strongly broadened ground state transitions due to acoustic phonon scattering," *Physical Review B* **69**, 035304 (2004).
- [77] L. Besombes, K. Kheng, L. Marsal, and H. Mariette, "Acoustic phonon broadening mechanism in single quantum dot emission," *Physical Review B* **63**, 5 (2001).
- [78] B. Krummheuer, V. M. Axt, and T. Kuhn, "Theory of pure dephasing and the resulting absorption line shape in semiconductor quantum dots," *Physical Review B* **65**, 195313 (2002).
- [79] A. Berthelot, I. Favero, G. Cassabo, C. Voisin, C. Delalande, P. Roussignol, R. Ferreira, and J. M. Gerard, "Unconventional motional narrowing in the optical spectrum of a semiconductor quantum dot," *Nature Physics* **2**, 759 (2006).
- [80] E. A. Muljarov and R. Zimmermann, "Dephasing in quantum dots: Quadratic coupling to acoustic phonons," *Physical Review Letters* **93**, 237401 (2004).

Bibliography

- [81] I. Favero, A. Berthelot, G. Cassabois, C. Voisin, C. Delalande, P. Roussignol, R. Ferreira, and J. M. Gerard, "Temperature dependence of the zero-phonon linewidth in quantum dots: An effect of the fluctuating environment," *Physical Review B* **75**, 073308 (2007).
- [82] M. J. Fernee, B. Littleton, T. Plakhotnik, H. Rubinsztein-Dunlop, D. E. Gomez, and P. Mulvaney, "Charge hopping revealed by jitter correlations in the photoluminescence spectra of single cdse nanocrystals," *Physical Review B* **81**, 155307 (2010).
- [83] P. Russell, "Photonic crystal fibers," *Science* **299**, 358–362 (2003).
- [84] H. G. Park, S. H. Kim, S. H. Kwon, Y. G. Ju, J. K. Yang, J. H. Baek, S. B. Kim, and Y. H. Lee, "Electrically driven single-cell photonic crystal laser," *Science* **305**, 1444–1447 (2004).
- [85] S. Noda, M. Fujita, and T. Asano, "Spontaneous-emission control by photonic crystals and nanocavities," *Nature Photonics* **1**, 449 (2007).
- [86] S. Y. Lin, J. G. Fleming, D. L. Hetherington, B. K. Smith, R. Biswas, K. M. Ho, M. M. Sigalas, W. Zubrzycki, S. R. Kurtz, and J. Bur, "A three-dimensional photonic crystal operating at infrared wavelengths," *Nature* **394**, 251 (1998).
- [87] M. Fujita, S. Takahashi, Y. Tanaka, T. Asano, and S. Noda, "Simultaneous inhibition and redistribution of spontaneous light emission in photonic crystals," *Science* **308**, 1296 (2005).
- [88] N. Volet, T. Czystanowski, J. Walczak, L. Mutter, B. Dwir, Z. Mickovic, P. Gallo, A. Caliman, A. Sirbu, A. Mereuta, V. Iakovlev, and E. Kapon, "Transverse mode discrimination in long-wavelength wafer-fused vertical-cavity surface-emitting lasers by intra-cavity patterning," submitted to *Optics Express* (2013).
- [89] E. Yablonovitch, "Inhibited spontaneous emission in solid-state physics and electronics," *Physical Review Letters* **58**, 2059 (1987).
- [90] S. John, "Strong localization of photons in certain disordered dielectric superlattices," *Physical Review Letters* **58**, 2486 (1987).
- [91] E. Yablonovitch, T. J. Gmitter, and K. M. Leung, "Photonic band-structure - the face-centered-cubic case employing nonspherical atoms," *Physical Review Letters* **67**, 2295 (1991).
- [92] J. Joannopoulos, R. Meade, and J. Winn, *Photonic Crystals: Molding the Flow of Light* (Princeton University Press, 1995).

-
- [93] K. A. Atlasov, K. F. Karlsson, A. Rudra, B. Dwir, and E. Kapon, "Wavelength and loss splitting in directly coupled photonic-crystal defect microcavities," *Optics Express* **16**, 16255 (2008).
- [94] J. M. Raimond, M. Brune, and S. Haroche, "Colloquium: Manipulating quantum entanglement with atoms and photons in a cavity," *Reviews of Modern Physics* **73**, 565 (2001).
- [95] P. Goy, J. M. Raimond, M. Gross, and S. Haroche, "Observation of cavity-enhanced single-atom spontaneous emission," *Physical Review Letters* **50**, 1903 (1983).
- [96] R. J. Thompson, G. Rempe, and H. J. Kimble, "Observation of normal-mode splitting for an atom in an optical cavity," *Physical Review Letters* **68**, 1132 (1992).
- [97] A. Boca, R. Miller, K. M. Birnbaum, A. D. Boozer, J. McKeever, and H. J. Kimble, "Observation of the vacuum rabi spectrum for one trapped atom," *Physical Review Letters* **93**, 233603 (2004).
- [98] E. T. Jaynes and F. W. Cummings, "Comparison of quantum and semiclassical radiation theories with application to the beam maser," *Proceedings of the IEEE* **51**, 89 (1963).
- [99] G. Grynberg, A. Aspect, C. Fabre, and C. Cohen-Tannoudji, *Introduction to Quantum Optics: From the Semi-classical Approach to Quantized Light* (Cambridge University Press, 2010).
- [100] T. Volz, A. Reinhard, M. Winger, A. Badolato, K. J. Hennessy, E. L. Hu, and A. Imamoglu, "Ultrafast all-optical switching by single photons," *Nature Photonics* **6**, 605 (2012).
- [101] F. P. Laussy, E. del Valle, and C. Tejedor, "Luminescence spectra of quantum dots in microcavities. i. bosons," *Physical Review B* **79**, 235325 (2009).
- [102] F. P. Laussy, E. del Valle, and C. Tejedor, "Strong coupling of quantum dots in microcavities," *Physical Review Letters* **101**, 083601 (2008).
- [103] P. Kaer, T. R. Nielsen, P. Lodahl, A. P. Jauho, and J. Mork, "Microscopic theory of phonon-induced effects on semiconductor quantum dot decay dynamics in cavity qed," *Physical Review B* **86**, 085302 (2012).
- [104] E. M. Purcell, "Spontaneous emission probabilities at radio frequencies," *Physical Review* **69**, 681 (1946).

Bibliography

- [105] A. J. Shields, "Semiconductor quantum light sources," *Nature Photonics* **1**, 215 (2007).
- [106] C. Santori, D. Fattal, J. Vuckovic, G. S. Solomon, and Y. Yamamoto, "Indistinguishable photons from a single-photon device," *Nature* **419**, 594 (2002).
- [107] A. Dousse, J. Suffczynski, A. Beveratos, O. Krebs, A. Lemaitre, I. Sagnes, J. Bloch, P. Voisin, and P. Senellart, "Ultrabright source of entangled photon pairs," *Nature* **466**, 217 (2010).
- [108] P. Michler, A. Kiraz, C. Becher, W. V. Schoenfeld, P. M. Petroff, L. D. Zhang, E. Hu, and A. Imamoglu, "A quantum dot single-photon turnstile device," *Science* **290**, 2282 (2000).
- [109] M. Pelton, C. Santori, J. Vuckovic, B. Y. Zhang, G. S. Solomon, J. Plant, and Y. Yamamoto, "Efficient source of single photons: A single quantum dot in a micropost microcavity," *Physical Review Letters* **89**, 233602 (2002).
- [110] A. Badolato, K. Hennessy, M. Atature, J. Dreiser, E. Hu, P. M. Petroff, and A. Imamoglu, "Deterministic coupling of single quantum dots to single nanocavity modes," *Science* **308**, 1158 (2005).
- [111] D. G. Gevaux, A. J. Bennett, R. M. Stevenson, A. J. Shields, P. Atkinson, J. Griffiths, D. Anderson, G. A. C. Jones, and D. A. Ritchie, "Enhancement and suppression of spontaneous emission by temperature tuning in quantum dots to photonic crystal cavities," *Applied Physics Letters* **88**, 131101 (2006).
- [112] D. Englund, D. Fattal, E. Waks, G. Solomon, B. Zhang, T. Nakaoka, Y. Arakawa, Y. Yamamoto, and J. Vuckovic, "Controlling the spontaneous emission rate of single quantum dots in a two-dimensional photonic crystal," *Physical Review Letters* **95**, 013904 (2005).
- [113] J. P. Reithmaier, G. Sek, A. Löffler, C. Hofmann, S. Kuhn, S. Reitzenstein, L. V. Keldysh, V. D. Kulakovskii, T. L. Reinecke, and A. Forchel, "Strong coupling in a single quantum dot-semiconductor microcavity system," *Nature* **432**, 197 (2004).
- [114] E. Peter, P. Senellart, D. Martrou, Lema, icirc, A. tre, J. Hours, eacute, J. M. rard, and J. Bloch, "Exciton-photon strong-coupling regime for a single quantum dot embedded in a microcavity," *Physical Review Letters* **95**, 067401 (2005).

-
- [115] D. Press, S. Gotzinger, S. Reitzenstein, C. Hofmann, A. Löffler, M. Kamp, A. Forchel, and Y. Yamamoto, “Photon antibunching from a single quantum-dot-microcavity system in the strong coupling regime,” *Physical Review Letters* **98**, 117402 (2007).
 - [116] K. Hennessy, A. Badolato, M. Winger, D. Gerace, M. Atatüre, S. Gulde, S. Falt, E. L. Hu, and A. Imamoglu, “Quantum nature of a strongly coupled single quantum dot-cavity system,” *Nature* **445**, 896 (2007).
 - [117] M. Winger, A. Badolato, K. J. Hennessy, E. L. Hu, and A. Imamoglu, “Quantum dot spectroscopy using cavity quantum electrodynamics,” *Physical Review Letters* **101**, 226808 (2008).
 - [118] I. Fushman, D. Englund, A. Faraon, N. Stoltz, P. Petroff, and J. Vuckovic, “Controlled phase shifts with a single quantum dot,” *Science* **320**, 769 (2008).
 - [119] J. Kasprzak, S. Reitzenstein, E. A. Muljarov, C. Kistner, C. Schneider, M. Strauss, S. Hofling, A. Forchel, and W. Langbein, “Up on the jaynes-cummings ladder of a quantum-dot/microcavity system,” *Nature Materials* **9**, 304 (2010).
 - [120] D. Englund, A. Majumdar, M. Bajcsy, A. Faraon, P. Petroff, and J. Vuckovic, “Ultrafast photon-photon interaction in a strongly coupled quantum dot-cavity system,” *Physical Review Letters* **108**, 093604 (2012).
 - [121] A. Reinhard, T. Volz, M. Winger, A. Badolato, K. J. Hennessy, E. L. Hu, and A. Imamoglu, “Strongly correlated photons on a chip,” *Nature Photonics* **6**, 93 (2012).
 - [122] H. Kim, R. Bose, T. C. Shen, G. S. Solomon, and E. Waks, “A quantum logic gate between a solid-state quantum bit and a photon,” *Nature Photonics* p. 373 (2013).
 - [123] J. L. Silverberg, M. Bierbaum, J. P. Sethna, and I. Cohen, “Collective motion of humans in mosh and circle pits at heavy metal concerts,” *Physical Review Letters* **110** (2013).
 - [124] M. Felici, P. Gallo, A. Mohan, B. Dwir, A. Rudra, and E. Kapon, “Site-Controlled InGaAs Quantum Dots with Tunable Emission Energy,” *Small* **5**, 938 (2009).
 - [125] G. Biasiol and E. Kapon, “Mechanisms of self-ordering of quantum nanostructures grown on nonplanar surfaces,” *Physical Review Letters* **81**, 2962 (1998).
 - [126] G. Biasiol, A. Gustafsson, K. Leifer, and E. Kapon, “Mechanisms of self-ordering in nonplanar epitaxy of semiconductor nanostructures,” *Physical Review B* **65**, 205306 (2002).

Bibliography

- [127] S. Watanabe, E. Pelucchi, B. Dwir, A. Baier, K. Leifer, and E. Kapon, "Growth and optical characterization of dense arrays of site-controlled quantum dots grown in inverted pyramids," *Physica E-Low-Dimensional Systems & Nanostructures* **21**, 193 (2004).
- [128] A. Hartmann, L. Loubies, F. Reinhardt, and E. Kapon, "Self-limiting growth of quantum dot heterostructures on nonplanar 111b substrates," *Applied Physics Letters* **71**, 1314 (1997).
- [129] S. Watanabe, E. Pelucchi, B. Dwir, M. H. Baier, K. Leifer, and E. Kapon, "Dense uniform arrays of site-controlled quantum dots grown in inverted pyramids," *Applied Physics Letters* **84**, 2907 (2004).
- [130] E. Pelucchi, S. Watanabe, K. Leifer, B. Dwir, and E. Kapon, "Site-controlled quantum dots grown in inverted pyramids for photonic crystal applications," *Physica E-Low-Dimensional Systems & Nanostructures* **23**, 476 (2004).
- [131] E. Pelucchi, S. Watanabe, K. Leifer, Q. Zhu, B. Dwir, P. De Los Rios, and E. Kapon, "Mechanisms of quantum dot energy engineering by metalorganic vapor phase epitaxy on patterned nonplanar substrates," *Nano Letters* **7**, 1282 (2007).
- [132] V. Dimastrodonato, E. Pelucchi, and D. D. Vvedensky, "Self-limiting evolution of seeded quantum wires and dots on patterned substrates," *Physical Review Letters* **108**, 256102 (2012).
- [133] F. Lelarge, G. Biasiol, A. Rudra, A. Condo, and E. Kapon, "Self-ordered nanostructures grown by organometallic chemical vapor deposition on v-grooved substrates: experiments and monte-carlo simulations," *Microelectronics Journal* **30**, 461 (1999).
- [134] G. Biasiol, "Formation mechanisms of low-dimensional semiconductor nanostructures grown by omcvd on nonplanar substrates," Ph.D. thesis (1998).
- [135] A. Surrente, "Epitaxial growth and optical properties of dense arrays of pyramidal quantum dots," Ph.D. thesis (2013).
- [136] R. Carron, "Dilute-nitride low-dimensional nanostructures formed on nonplanar substrates," Ph.D. thesis (2013).
- [137] K. F. Karlsson, V. Troncale, D. Y. Oberli, A. Malko, E. Pelucchi, A. Rudra, and E. Kapon, "Optical polarization anisotropy and hole states in pyramidal quantum dots," *Applied Physics Letters* **89**, 251113 (2006).

-
- [138] M. A. Dupertuis, K. F. Karlsson, D. Y. Oberli, E. Pelucchi, A. Rudra, P. O. Holtz, and E. Kapon, "Symmetries and the polarized optical spectra of exciton complexes in quantum dots," *Physical Review Letters* **107**, 127403 (2011).
- [139] J. Goldstein, D. Newbury, D. Joy, C. Lyman, P. Echlin, E. Lifshin, L. Sawyer, and J. Michael, *Scanning electron microscopy and X-ray microanalysis* (Springer, 2003).
- [140] G. Binnig, C. F. Quate, and C. Gerber, "Atomic force microscope," *Physical Review Letters* **56**, 930 (1986).
- [141] A. A. Tseng, K. Chen, C. D. Chen, and K. J. Ma, "Electron beam lithography in nanoscale fabrication: recent development," *Ieee Transactions on Electronics Packaging Manufacturing* **26**, 141 (2003).
- [142] K. A. Atlasov, "Light control and microcavity lasers based on quantum wires integrated in photonic-crystal cavities," Ph.D. thesis (2009).
- [143] K. A. Atlasov, P. Gallo, A. Rudra, B. Dwir, and E. Kapon, "Effect of sidewall passivation in BCl₃/N₂ inductively coupled plasma etching of two-dimensional GaAs photonic crystals," *Journal of Vacuum Science & Technology B* **27**, L21 (2009).
- [144] S. Jensen, "Inductively coupled plasma etching for microsystems," Ph.D. thesis (2004).
- [145] A. M. Fox, *Optical properties of solids*, Oxford Master Series in Physics (Oxford University Press, 2001).
- [146] E. A. Zibik, L. R. Wilson, R. P. Green, G. Bastard, R. Ferreira, P. J. Phillips, D. A. Carder, J. P. R. Wells, J. W. Cockburn, M. S. Skolnick, M. J. Steer, and M. Hopkinson, "Intraband relaxation via polaron decay in inas self-assembled quantum dots," *Physical Review B* **70**, 161305 (2004).
- [147] X. Q. Li, H. Nakayama, and Y. Arakawa, "Phonon bottleneck in quantum dots: Role of lifetime of the confined optical phonons," *Physical Review B* **59**, 5069 (1999).
- [148] D. Englund, A. Faraon, I. Fushman, N. Stoltz, P. Petroff, and J. Vuckovic, "Controlling cavity reflectivity with a single quantum dot," *Nature* **450**, 857 (2007).
- [149] M. Nomura, N. Kumagai, S. Iwamoto, Y. Ota, and Y. Arakawa, "Laser oscillation in a strongly coupled single-quantum-dot-nanocavity system," *Nature Physics* **6**, 279 (2010).

Bibliography

- [150] D. Dalacu, K. Mnaymneh, V. Sazonova, P. J. Poole, G. C. Aers, J. Lapointe, R. Chertton, A. J. SpringThorpe, and R. Williams, "Deterministic emitter-cavity coupling using a single-site controlled quantum dot," *Physical Review B* **82**, 4 (2010).
- [151] M. Winger, "Mesoscopic cavity qed with a single quantum dot," Ph.D. thesis (2009).
- [152] S. M. Thon, M. T. Rakher, H. Kim, J. Gudat, W. T. M. Irvine, P. M. Petroff, and D. Bouwmeester, "Strong coupling through optical positioning of a quantum dot in a photonic crystal cavity," *Applied Physics Letters* **94**, 111115 (2009).
- [153] D. Chithrani, R. L. Williams, J. Lefebvre, P. J. Poole, and G. C. Aers, "Optical spectroscopy of single, site-selected, inas/inp self-assembled quantum dots," *Applied Physics Letters* **84**, 978 (2004).
- [154] P. J. Poole, D. Dalacu, J. Lefebvre, and R. L. Williams, "Selective epitaxy of semiconductor nanopyrramids for nanophotonics," *Nanotechnology* **21**, 295302 (2010).
- [155] K. A. Atlasov, M. Calic, K. F. Karlsson, P. Gallo, A. Rudra, B. Dwir, and E. Kapon, "Photonic-crystal microcavity laser with site-controlled quantum-wire active medium," *Optics Express* **17**, 18178 (2009).
- [156] Y. Akahane, T. Asano, B. S. Song, and S. Noda, "High-q photonic nanocavity in a two-dimensional photonic crystal," *Nature* **425**, 944 (2003).
- [157] <http://www.tasc.infm.it/research/amd/staff/biasiol.htm>. Personal website of Giorgio Biasiol from TASC laboratory in Trieste (Italy).
- [158] S. L. Portalupi, M. Galli, C. Reardon, T. F. Krauss, L. O'Faolain, L. C. Andreani, and D. Gerace, "Planar photonic crystal cavities with far-field optimization for high coupling efficiency and quality factor," *Optics Express* **18**, 16064 (2010).
- [159] A. R. A. Chalcraft, S. Lam, D. O'Brien, T. F. Krauss, M. Sahin, D. Szymanski, D. Sanvitto, R. Oulton, M. S. Skolnick, A. M. Fox, D. M. Whittaker, H. Y. Liu, and M. Hopkinson, "Mode structure of the l3 photonic crystal cavity," *Applied Physics Letters* **90**, 241117 (2007).
- [160] A. Imamoglu, D. D. Awschalom, G. Burkard, D. P. DiVincenzo, D. Loss, M. Sherwin, and A. Small, "Quantum information processing using quantum dot spins and cavity qed," *Physical Review Letters* **83**, 4204 (1999).
- [161] H. Mabuchi and A. C. Doherty, "Cavity quantum electrodynamics: Coherence in context," *Science* **298**, 1372 (2002).

-
- [162] P. Lodahl and S. Stobbe, "Solid-state quantum optics with quantum dots in photonic nanostructures," *Nanophotonics* **2**, 39 (2013).
- [163] A. Hartmann, Y. Ducommun, E. Kapon, U. Hohenester, C. Simserides, and E. Molinari, "Optical spectra of single quantum dots: Influence of impurities and few-particle effects," *Physica Status Solidi a-Applied Research* **178**, 283 (2000).
- [164] C. P. Michael, K. Srinivasan, T. J. Johnson, O. Painter, K. H. Lee, K. Hennessy, H. Kim, and E. Hu, "Wavelength- and material-dependent absorption in GaAs and AlGaAs microcavities," *Applied Physics Letters* **90**, 051108 (2007).
- [165] O. Painter, J. Vuckovic, and A. Scherer, "Defect modes of a two-dimensional photonic crystal in an optically thin dielectric slab," *Journal of the Optical Society of America B-Optical Physics* **16**, 275 (1999).
- [166] S. Strauf, K. Hennessy, M. T. Rakher, Y. S. Choi, A. Badolato, L. C. Andreani, E. L. Hu, P. M. Petroff, and D. Bouwmeester, "Self-tuned quantum dot gain in photonic crystal lasers," *Physical Review Letters* **96**, 127404 (2006).
- [167] M. Kaniber, A. Laucht, A. Neumann, J. M. Villas-Boas, M. Bichler, M. C. Amann, and J. J. Finley, "Investigation of the nonresonant dot-cavity coupling in two-dimensional photonic crystal nanocavities," *Physical Review B* **77**, 161303 (2008).
- [168] N. Chauvin, C. Zinoni, M. Francardi, A. Gerardino, L. Balet, B. Alloing, L. H. Li, and A. Fiore, "Controlling the charge environment of single quantum dots in a photonic-crystal cavity," *Physical Review B* **80**, 241306 (2009).
- [169] M. Winger, T. Volz, G. Tarel, S. Portolan, A. Badolato, K. J. Hennessy, E. L. Hu, A. Beveratos, J. Finley, V. Savona, and A. Imamoglu, "Explanation of photon correlations in the far-off-resonance optical emission from a quantum-dot-cavity system," *Physical Review Letters* **103**, 4 (2009).
- [170] A. Laucht, M. Kaniber, A. Mohtashami, N. Hauke, M. Bichler, and J. J. Finley, "Temporal monitoring of nonresonant feeding of semiconductor nanocavity modes by quantum dot multiexciton transitions," *Physical Review B* **81**, 241302 (2010).
- [171] A. Laucht, N. Hauke, A. Neumann, T. Gunthner, F. Hofbauer, A. Mohtashami, K. Muller, G. Bohm, M. Bichler, M. C. Amann, M. Kaniber, and J. J. Finley, "Nonresonant feeding of photonic crystal nanocavity modes by quantum dots," *Journal of Applied Physics* **109**, 102404 (2011).

Bibliography

- [172] Y. Ota, N. Kumagai, S. Ohkouchi, M. Shirane, M. Nomura, S. Ishida, S. Iwamoto, S. Yorozu, and Y. Arakawa, "Investigation of the spectral triplet in strongly coupled quantum dot-nanocavity system," *Applied Physics Express* **2**, 122301 (2009).
- [173] R. Ohta, Y. Ota, M. Nomura, N. Kumagai, S. Ishida, S. Iwamoto, and Y. Arakawa, "Strong coupling between a photonic crystal nanobeam cavity and a single quantum dot," *Applied Physics Letters* **98**, 173104 (2011).
- [174] K. Karrai, R. J. Warburton, C. Schulhauser, A. Hoge, B. Urbaszek, E. J. McGhee, A. O. Govorov, J. M. Garcia, B. D. Gerardot, and P. M. Petroff, "Hybridization of electronic states in quantum dots through photon emission," *Nature* **427**, 135 (2004).
- [175] Y. Toda, O. Moriwaki, M. Nishioka, and Y. Arakawa, "Efficient carrier relaxation mechanism in InGaAs GaAs self-assembled quantum dots based on the existence of continuum states," *Physical Review Letters* **82**, 4114 (1999).
- [176] J. J. Finley, A. D. Ashmore, A. Lemaître, D. J. Mowbray, M. S. Skolnick, I. E. Itskevich, P. A. Maksym, M. Hopkinson, and T. F. Krauss, "Charged and neutral exciton complexes in individual self-assembled In(Ga)As quantum dots," *Physical Review B* **63**, 073307 (2001).
- [177] A. Vasanelli, R. Ferreira, and G. Bastard, "Continuous absorption background and decoherence in quantum dots," *Physical Review Letters* **89**, 216804 (2002).
- [178] R. Oulton, J. J. Finley, A. I. Tartakovskii, D. J. Mowbray, M. S. Skolnick, M. Hopkinson, A. Vasanelli, R. Ferreira, and G. Bastard, "Continuum transitions and phonon coupling in single self-assembled stranski-krastanow quantum dots," *Physical Review B* **68**, 235301 (2003).
- [179] D. Englund, A. Majumdar, A. Faraon, M. Toishi, N. Stoltz, P. Petroff, and J. Vuckovic, "Resonant excitation of a quantum dot strongly coupled to a photonic crystal nanocavity," *Physical Review Letters* **104**, 073904 (2010).
- [180] B. Ellis, M. A. Mayer, G. Shambat, T. Sarmiento, J. Harris, E. E. Haller, and J. Vuckovic, "Ultralow-threshold electrically pumped quantum-dot photonic-crystal nanocavity laser," *Nature Photonics* **5**, 297 (2011).
- [181] G. Tarel and V. Savona, "Linear spectrum of a quantum dot coupled to a nanocavity," *Physical Review B* **81**, 075305 (2010).

-
- [182] Y. Ota, S. Iwamoto, N. Kumagai, and Y. Arakawa, "Impact of electron-phonon interactions on quantum-dot cavity quantum electrodynamics," ArXiv e-prints (2009).
- [183] P. Kaer, T. R. Nielsen, P. Lodahl, A. P. Jauho, and J. Mørk, "Non-markovian model of photon-assisted dephasing by electron-phonon interactions in a coupled quantum-dot-cavity system," *Physical Review Letters* **104**, 157401 (2010).
- [184] K. H. Madsen, P. Kaer, A. Kreiner-Møller, S. Stobbe, A. Nysteen, J. Mørk, and P. Lodahl, "Measuring the effective phonon density of states of a quantum dot in cavity quantum electrodynamics," *Physical Review B* **88**, 045316 (2013).
- [185] A. Kavokin, J. Baumberg, G. Malpuech, and F. Laussy, *Microcavities* (OUP Oxford, 2011).
- [186] A. Kress, F. Hofbauer, N. Reinelt, M. Kaniber, H. J. Krenner, R. Meyer, G. Böhm, and J. J. Finley, "Manipulation of the spontaneous emission dynamics of quantum dots in two-dimensional photonic crystals," *Physical Review B* **71**, 241304 (2005).
- [187] A. Tandraechanurat, S. Ishida, D. Guimard, M. Nomura, S. Iwamoto, and Y. Arakawa, "Lasing oscillation in a three-dimensional photonic crystal nanocavity with a complete bandgap," *Nature Photonics* **5**, 91 (2011).
- [188] T. F. Krauss, R. M. DeLaRue, and S. Brand, "Two-dimensional photonic-bandgap structures operating at near infrared wavelengths," *Nature* **383**, 699 (1996).
- [189] D. M. Whittaker, I. S. Culshaw, V. N. Astratov, and M. S. Skolnick, "Photonic band structure of patterned waveguides with dielectric and metallic cladding," *Physical Review B* **65**, 073102 (2002).
- [190] A. A. Asatryan, K. Busch, R. C. McPhedran, L. C. Botten, C. M. de Sterke, and N. A. Nicorovici, "Two-dimensional green's function and local density of states in photonic crystals consisting of a finite number of cylinders of infinite length," *Physical Review E* **63**, 046612 (2001).
- [191] V. Zabelin, "Numerical investigations of two-dimensional photonic crystal optical properties, design and analysis of photonic crystal based structures," Ph.D. thesis (2009).
- [192] Q. Wang, S. Stobbe, and P. Lodahl, "Mapping the local density of optical states of a photonic crystal with single quantum dots," *Physical Review Letters* **107**, 167404 (2011).

Bibliography

- [193] M. Kaniber, A. Neumann, A. Laucht, M. F. Huck, M. Bichler, M. C. Amann, and J. J. Finley, “Efficient and selective cavity-resonant excitation for single photon generation,” *New Journal of Physics* **11**, 013031 (2009).
- [194] S. Ohno, S. Adachi, R. Kaji, S. Muto, and H. Sasakura, “Optical anisotropy and photoluminescence polarization in single inorganic quantum dots,” *Applied Physics Letters* **98**, 161912 (2011).
- [195] S. Reitzenstein, C. Bockler, A. Löffler, S. Hofling, L. Worschech, A. Forchel, P. Yao, and S. Hughes, “Polarization-dependent strong coupling in elliptical high-q micropillar cavities,” *Physical Review B* **82**, 235313 (2010).
- [196] M. Munsch, A. Mosset, A. Auffeves, S. Seidelin, J. P. Poizat, J. M. Gerard, A. Lemaître, I. Sagnes, and P. Senellart, “Continuous-wave versus time-resolved measurements of Purcell factors for quantum dots in semiconductor microcavities,” *Physical Review B* **80**, 115312 (2009).
- [197] A. Majumdar, A. Faraon, E. D. Kim, D. Englund, H. Kim, P. Petroff, and J. Vuckovic, “Linewidth broadening of a quantum dot coupled to an off-resonant cavity,” *Physical Review B* **82**, 045306 (2010).
- [198] A. Kiraz, S. Falth, C. Becher, B. Gayral, W. V. Schoenfeld, P. M. Petroff, L. Zhang, E. Hu, and A. Imamoglu, “Photon correlation spectroscopy of a single quantum dot,” *Physical Review B* **65**, 161303 (2002).
- [199] M. Qiu, “Effective index method for heterostructure-slab-waveguide-based two-dimensional photonic crystals,” *Applied Physics Letters* **81**, 1163 (2002).
- [200] M. H. Baier, A. Malko, E. Pelucchi, D. Y. Oberli, and E. Kapon, “Quantum-dot exciton dynamics probed by photon-correlation spectroscopy,” *Physical Review B* **73**, 205321 (2006).
- [201] M. Settnes, P. Kaer, A. Moelbjerg, and J. Mork, “Auger processes mediating the nonresonant optical emission from a semiconductor quantum dot embedded inside an optical cavity,” *Physical Review Letters* **111**, 067403 (2013).
- [202] H. J. Kimble, “The quantum internet,” *Nature* **453**, 1023 (2008).
- [203] M. F. Riedel, P. Bohi, Y. Li, T. W. Hansch, A. Sinatra, and P. Treutlein, “Atom-chip-based generation of entanglement for quantum metrology,” *Nature* **464**, 1170 (2010).
- [204] M. Gross and S. Haroche, “Super-radiance - an essay on the theory of collective spontaneous emission,” *Physics Reports-Review Section of Physics Letters* **93**, 301 (1982).

-
- [205] B. M. Garraway, "The dicke model in quantum optics: Dicke model revisited," *Philosophical Transactions of the Royal Society a-Mathematical Physical and Engineering Sciences* **369**, 1137 (2011).
- [206] S. Noda, "Seeking the ultimate nanolaser," *Science* **314**, 260 (2006).
- [207] J. Majer, J. M. Chow, J. M. Gambetta, J. Koch, B. R. Johnson, J. A. Schreier, L. Frunzio, D. I. Schuster, A. A. Houck, A. Wallraff, A. Blais, M. H. Devoret, S. M. Girvin, and R. J. Schoelkopf, "Coupling superconducting qubits via a cavity bus," *Nature* **449**, 443 (2007).
- [208] S. Reitzenstein, A. Löffler, C. Hofmann, A. Kubanek, M. Kamp, J. P. Reithmaier, A. Forchel, V. D. Kulakovskii, L. V. Keldysh, I. V. Ponomarev, and T. L. Reinecke, "Coherent photonic coupling of semiconductor quantum dots," *Optics Letters* **31**, 1738 (2006).
- [209] A. Laucht, J. M. Villas-Boas, S. Stobbe, N. Hauke, F. Hofbauer, G. Böhm, P. Lodahl, M. C. Amann, M. Kaniber, and J. J. Finley, "Mutual coupling of two semiconductor quantum dots via an optical nanocavity," *Physical Review B* **82**, 075305 (2010).
- [210] E. Gallardo, L. J. Martinez, A. K. Nowak, D. Sarkar, H. P. van der Meulen, J. M. Calleja, C. Tejedor, I. Prieto, D. Granados, A. G. Taboada, J. M. Garcia, and P. A. Postigo, "Optical coupling of two distant InAs/GaAs quantum dots by a photonic-crystal microcavity," *Physical Review B* **81**, 193301 (2010).
- [211] H. Kim, D. Sridharan, T. C. Shen, G. S. Solomon, and E. Waks, "Strong coupling between two quantum dots and a photonic crystal cavity using magnetic field tuning," *Optics Express* **19**, 2589 (2011).
- [212] A. Majumdar, M. Bajcsy, A. Rundquist, E. Kim, and J. Vuckovic, "Phonon-mediated coupling between quantum dots through an off-resonant microcavity," *Physical Review B* **85**, 195301 (2012).
- [213] F. Albert, K. Sivalertporn, J. Kasprzak, M. Strauß, C. Schneider, S. Höfling, M. Kamp, A. Forchel, S. Reitzenstein, E. A. Muljarov, and W. Langbein, "Microcavity controlled coupling of excitonic qubits," *Nature Communications* **4** (2013).
- [214] V. V. Temnov and U. Woggon, "Superradiance and subradiance in an inhomogeneously broadened ensemble of two-level systems coupled to a low-q cavity," *Physical Review Letters* **95**, 243602 (2005).

Bibliography

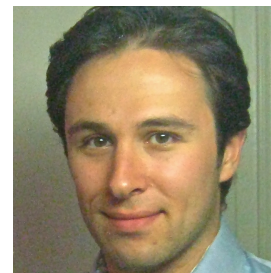
- [215] K. J. Xu and C. Piermarocchi, “Dynamics of elastic and inelastic energy transfer between quantum dots in a microcavity,” *Physical Review B* **84**, 115316 (2011).
- [216] A. Auffeves, D. Gerace, S. Portolan, A. Drezet, and M. F. Santos, “Few emitters in a cavity: from cooperative emission to individualization,” *New Journal of Physics* **13**, 093020 (2011).
- [217] Y. M. Su, D. Bimberg, and A. Knorr, “Collective light emission revisited: Reservoir induced coherence,” *Physical Review Letters* **110**, 113604 (2013).
- [218] N. Lambert, C. Emary, and T. Brandes, “Entanglement and the phase transition in single-mode superradiance,” *Physical Review Letters* **92**, 073602 (2004).
- [219] A. N. Poddubny, M. M. Glazov, and N. S. Averkiev, “Nonlinear emission spectra of quantum dots strongly coupled to a photonic mode,” *Physical Review B* **82**, 205330 (2010).
- [220] R. H. Dicke, “Coherence in spontaneous radiation processes,” *Physical Review* **93**, 99 (1954).
- [221] F. P. Laussy, A. Laucht, E. del Valle, J. J. Finley, and J. M. Villas-Boas, “Luminescence spectra of quantum dots in microcavities. iii. multiple quantum dots,” *Physical Review B* **84**, 195313 (2011).
- [222] M. Tavis and F. W. Cummings, “Exact solution for an n-molecule-radiation-field hamiltonian,” *Physical Review* **170**, 379 (1968).
- [223] K. Harkonen, F. Plastina, and S. Maniscalco, “Dicke model and environment-induced entanglement in ion-cavity qed,” *Physical Review A* **80**, 033841 (2009).
- [224] J. M. Fink, R. Bianchetti, M. Baur, M. Goppl, L. Steffen, S. Filipp, P. J. Leek, A. Blais, and A. Wallraff, “Dressed collective qubit states and the tavis-cummings model in circuit qed,” *Physical Review Letters* **103**, 083601 (2009).
- [225] E. del Valle, F. P. Laussy, and C. Tejedor, “Luminescence spectra of quantum dots in microcavities. ii. fermions,” *Physical Review B* **79**, 235326 (2009).
- [226] N. Quesada, “Strong coupling of two quantum emitters to a single light mode: The dissipative tavis-cummings ladder,” *arxiv* **86**, 013836 (2012).
- [227] T. E. Tessier, I. H. Deutsch, A. Delgado, and I. Fuentes-Guridi, “Entanglement sharing in the two-atom tavis-cummings model,” *Physical Review A* **68**, 062316 (2003).

- [228] V. V. Temnov and U. Woggon, "Photon statistics in the cooperative spontaneous emission," *Optics Express* **17**, 5774 (2009).
- [229] J. Ye, D. W. Vernooy, and H. J. Kimble, "Trapping of single atoms in cavity qed," *Physical Review Letters* **83**, 4987 (1999).
- [230] M. Keller, B. Lange, K. Hayasaka, W. Lange, and H. Walther, "Continuous generation of single photons with controlled waveform in an ion-trap cavity system," *Nature* **431**, 1075 (2004).
- [231] R. J. Schoelkopf and S. M. Girvin, "Wiring up quantum systems," *Nature* **451**, 664 (2008).
- [232] J. M. Fink, M. Goppl, M. Baur, R. Bianchetti, P. J. Leek, A. Blais, and A. Wallraff, "Climbing the jaynes-cummings ladder and observing its root n nonlinearity in a cavity qed system," *Nature* **454**, 315 (2008).
- [233] K. A. Atlasov, A. Rudra, B. Dwir, and E. Kapon, "Large mode splitting and lasing in optimally coupled photonic-crystal microcavities," *Optics Express* **19**, 2619 (2011).
- [234] D. Englund, A. Faraon, B. Y. Zhang, Y. Yamamoto, and J. Vuckovic, "Generation and transfer of single photons on a photonic crystal chip," *Optics Express* **15**, 5550 (2007).

Milan Ćalić

Avenue Recordon 15, CH-1004 Lausanne
Mobile: +41 76 447 86 60
Email: milancalic@gmx.net

Citizenship: Croatian
Born February 10, 1982



EDUCATION

Ph.D. in Physics, EPFL

2008 – Sept. 2013

- Specialized in semiconductor nanotechnology and nanophotonics.
- Thesis topic: Experimental studies with quantum dots, which are ultrasmall semiconductor light sources.
- Developed a scalable microfabrication method for integrating quantum dots into optical microcavities with nanometer precision, which is a significant improvement compared to other existing approaches.
- Measured the optical spectra from quantum dots in cavities and studied fundamental light-matter coupling effects at the microscopic level, which are important to understand for future information technology devices.
- Performed simulations with Matlab to compute the resonances of the optical cavities.

M.Sc. (Dipl.-Ing.) in Engineering Physics, Vienna University of Technology

2001 – 2008

- Master's project: Experimental investigation of ultrafast magnetization dynamics in ferromagnetic materials.

Erasmus exchange at ETH Zurich

2005 – 2006

- Received scholarship from the Erasmus exchange program to study at ETH Zurich for 1 academic year.

WORK EXPERIENCE

Master's project at IBM Research Zurich (6 months)

2007

- Conducted my Master's project in the Science & Technology department.
- Optically measured ultrafast magnetization dynamics in ferromagnetic films. The research was motivated by applications in future information processing devices that will be based on exploiting the spin of electrons.
- Created a simulation in Matlab to model the experimental data.

Internship at the International Atomic Energy Agency (IAEA) in Vienna (2 months)

2005

- Worked in the Department of Nuclear Sciences and Applications.
- Created an HTML-based platform for technical publications.
- Assisted in the organization of a scientific conference on fusion power plants.

Internship at the National University of Ireland, Galway (2 months)

2004

- Implemented an optimization algorithm in C++ to improve image sharpness in an adaptive optics system.
- The algorithm controlled a deformable mirror to correct for image aberrations, based on feedback from a CCD.

TECHNICAL SKILLS

Microfabrication and material characterization techniques

- Clean room processing, plasma etching, e-beam lithography, microscopy (SEM, AFM), optical spectroscopy.

IT software

- Matlab, C++, Origin, Photoshop, Illustrator, Microsoft Office, Latex, Dreamweaver.

LANGUAGE SKILLS

French: Professional working proficiency (B2)

German: Bilingual proficiency (C2)

English: Full professional proficiency (C1)

Armenian: Limited working proficiency (B1)

Persian: Limited working proficiency (B1)

EXTRACURRICULAR EXPERIENCE

Member of the board at IAESTE Vienna

2003-2005

- Assisted in the organization of the international internship placement program of IAESTE.
- Organized on-campus career fairs at Vienna University of Technology.